Constitutive modelling of filled rubbers and thermoplastic elastomers

Gordon Kumar

Keble College

Department of Engineering Science, University of Oxford

A thesis submitted for the degree of

Doctor of Philosophy

Michaelmas term 2024

Abstract

This thesis develops micromechanics-based constitutive models for the mechanical behaviour of filled rubbers and thermoplastic elastomers (TPEs) that are used across a range of industries. These materials are capable of large deformations and display various inelastic behaviours including viscoelasticity and the Mullins effect, a stress-softening phenomenon. The goal of this thesis is to model these behaviours generally and link them to microscale processes and parameters where possible. A general micromechanical framework capturing these behaviours is presented. The framework uses stretch amplification concepts and represents arbitrary inelastic behaviour in a Generalised Standard Materials approach on the chain level, which is averaged to yield macroscopic constitutive relations. Following specialisation of the framework to filled rubbers and TPEs, model predictions are compared to experimental data. Trends in the mechanical response with changes in hard phase volume fraction are described reasonably well. A separate model is developed for thermoplastic elastomers with hard phase in the form of cylinders. Distinct deformation mechanisms arise in TPEs with this microstructure. The model links the material composition to the large deformation and cyclic response of these TPEs. Analysis of the general framework reveals deficits in reproducing material behaviour under general biaxial loading conditions and in predicting Mullins softening with changes in loading direction. To address the first of these deficits, the role of the tube model of rubber elasticity is investigated. The assumptions behind tube models which lead to good fitting performance are identified and fitting performance is linked to dependence of the free energy function on the second invariant of the right Cauchy-Green deformation tensor. To better predict the anisotropy of the Mullins effect, a novel phenomenological extension to the micromechanical approach featuring a damage tensor and damage surface

is proposed. The model satisfyingly reproduces experimental data and is less computationally expensive than existing models. The model is implemented as a user subroutine in the commercial finite element software ABAQUS and numerical results are presented. The developed frameworks serve as a basis for modelling other behaviours exhibited by soft materials in the future.

Acknowledgements

First and foremost, I would like to give my sincere thanks to my supervisor Laurence Brassart for all of the support and guidance she has given me over the course of my studies. Her work ethic, ingenuity and depth of understanding have left me in awe over the years. My thanks also go to all of the other members of the Brassart group with whom I have shared the joys of research and whose company I have firmly enjoyed. I am grateful to the Engineering and Physical Sciences Research Council for funding my research. My time at Oxford has been extraordinarily special and it would be remiss of me not to acknowledge the friends that made it so - my flatmates, the members of Keble College MCR, all those that I have trained with and walked with, and a few others I've met along the way. I would also like to express my gratitude towards my family for (among many things) their unfailing support for me over the course of my educational journey. A special mention goes towards my late Mother, without whose encouragement I never would have embarked upon this work.

Contents

1 Introduction **1**

2 Theoretical background **11**
2.1 Preliminaries . . . 11
2.2 The phenomenological approach to rubber elasticity . . . 16
2.2.1 Invariant based models . . . 17
2.2.2 Principal stretch-based models . . . 19
2.3 The micromechanical approach to rubber elasticity . . . 22
2.3.1 The individual rubber chain . . . 22
2.3.2 The rubber network . . . 24
2.4 Modelling soft matrix/hard inclusions composites . . . 29
2.5 Modelling damage and the Mullins effect . . . 33
2.6 Viscoelasticty and viscoplasticity . . . 38

3 Micromechanical modelling of filled rubbers and thermoplastic elastomers **42**
3.1 Introduction . . . 42
3.2 Framework . . . 44
3.2.1 Kinematics . . . 45
3.2.2 Thermodynamics . . . 47
3.3 Application to filled rubbers . . . 49
3.3.1 Specialisation of the constitutive response . . . 49
3.3.2 Comparison to experimental data . . . 54
3.4 Application to thermoplastic polyurethanes . . . 59
3.4.1 Specialisation of the constitutive response . . . 59
3.4.2 Comparison to experimental data . . . 65
3.5 Conclusion . . . 71

4 Capturing I_2 dependence with the tube model **73**
4.1 Introduction . . . 73
4.2 Constitutive framework . . . 74
4.2.1 The tube model . . . 74
4.2.2 Macroscopic free energy . . . 78
4.2.3 Macroscopic stress-strain response. . . . 81
4.3 Evaluation of I_2 dependence . . . 82
4.4 Results . . . 86
4.4.1 Data of Kawabata et al. (1981) . . . 86
4.4.2 Data of Dechnarong et al. (2021) . . . 94
4.4.3 Data of Bechir et al. (2006) . . . 96

4.5 Discussion . . . 97
4.6 Conclusion . . . 106
4.7 Dissemination . . . 107

5 Modelling cylinder-forming thermoplastic elastomers 108
5.1 Introduction . . . 108
5.2 Framework . . . 111
5.2.1 Kinematics . . . 112
5.2.2 Thermodynamics . . . 114
5.3 Results . . . 120
5.3.1 Comparison to experimental data of Gregory et al. (2020) . . . 120
5.3.2 Grain level analysis . . . 124
5.4 Conclusion . . . 126

6 Anisotropic damage model for the Mullins effect 128
6.1 Introduction . . . 128
6.2 Constitutive framework . . . 132
6.2.1 Preliminaries . . . 132
6.2.2 Thermodynamics . . . 133
6.2.3 Damage surface and flow rule . . . 136
6.3 Specialisation of the free energy . . . 137
6.3.1 Elastic contribution . . . 138
6.3.2 Damage contribution . . . 141
6.3.3 Geometric interpretation . . . 142
6.4 Numerical implementation . . . 144
6.4.1 Constitutive updates . . . 144
6.4.2 Internal Newton-Raphson . . . 146
6.4.3 Consistent tangent . . . 147
6.5 Results . . . 148
6.5.1 Cyclic uniaxial tension response . . . 148
6.5.2 Response under different loading modes . . . 149
6.5.3 Comparison to experimental data of Diani and Le Tallec (2019) . . . 151
6.5.4 Comparison to experimental data of Machado et al. (2012) . . . 154
6.6 Finite element implementation . . . 157
6.7 Conclusion . . . 157
6.8 Dissemination . . . 159

7 Conclusions 160
7.1 Summary . . . 160
7.2 Future work . . . 162

Bibliography 167

A Incremental variational formulation of inelastic full-network framework 180

B Equivalence of plastic dissipation potential to yield function 183

C Analytic full network averaging 185
C.1 Variance of line-stretch in terms of invariant . . . 185

C.2 Variance of the area-stretch in terms of invariants 186

D Series expansions of the full-network tube free energy **189**

E Anisotropic Mullins effect model **193**
E.1 Equivalent formulation based on a variational principle 193
E.2 Consistent tangent operator 195
E.3 Finite element implementation 202
E.3.1 Compressible regularisation 202
E.3.2 Simulation of plate with central hole under sequential stretching . . 204

Chapter 1

Introduction

Rubber-like materials are soft materials used in a variety of engineering applications, ranging from car tyres to replacement heart valves (Yoda, 1998). Unlike other conventional engineering materials, rubbers undergo large deformations near elastically, which makes them suitable for applications where metals, ceramics and hard polymers are inappropriate. Particular use cases include seals and gaskets, where the deformability of the rubber allows close, leakproof contact to be made between components (Treloar, 1975); vibration isolation, where the low stiffness and viscoelastic behaviour of the rubber limit the transmission of load between a vibrating body and its mounting (Ciesielski, 1999); and for traction devices, such as tyres and shoe soles, which provide grip by deforming to match the (macroscopic) ruggedness of the surface which they grip (Lorenz et al., 2013). The characteristic large deformation behaviour of rubbers arises from a key difference in how they deform on a microscale compared to other materials. Stress arises in hard materials when the spacing between the atoms changes due to deformation. The origin of this form of elasticity is energetic. In contrast, the origin of elasticity in rubbers is entropic in nature.

Rubbers are made up of long, flexible polymer chains covalently bonded together to form a rubbery network (Treloar, 1975). The sites where different chains are bonded together are called crosslinks and they constrain the end positions of the polymer chains. As the chains are flexible, each chain can arrange itself in a number of different configurations for a given

separation between the ends of the chain without any change in internal energy. When the ends of the chain are pulled further apart (i.e. when the rubber network is deformed) the number of possible chain conformations decreases, which reduces the entropy of the chain and comes at a free energy penalty. This implies that a force must be exerted to pull the ends of the chain apart. In the absence of external forces, chains arrange in highly coiled configurations such that their end-to-end separation is a small fraction of their contour length. For a small end-to-end difference, the number of possible chain conformations is large and the chain is in a state of high entropy. This small end-to-end distance in the reference state allows the material to be stretched to several times its original length. This can be observed in the stress-strain response of the material. A typical stress-stretch curve for a rubber is shown in Fig. 1.1. It is 'S'-shaped, featuring an initial linear regime, where the rubber chains first begin to be uncoiled, and later features an upturn where it sharply rises as chains become fully extended and approach their contour length (Treloar, 1975). When a chain is fully extended, only one conformation of the chain is possible. This corresponds to a zero entropy state that can only be approached asymptotically, and gives rise to a singularity in the chain force-extension relationship. As all polymer chains above a certain temperature (the glass transition temperature) are flexible, all crosslinked polymers will display rubber-like elasticity in a particular temperature range.

For many popular engineering applications requiring soft materials (e.g. car tyres, seals, belts and hoses), the strength and stiffness of pure rubbers fall short of design requirements and rubbers with enhanced mechanical properties are required (Steck et al., 2023). One means to achieve this enhancement is through reinforcement of the rubber - by adding a phase of filler particles to the material (Medalia, 1987). These filler particles are most frequently carbon black or silica, which are effectively rigid in comparison to the rubber, and are nanometre-sized. Filler particles tend to aggregate together and the microstructure of a filled rubber consists of a soft matrix embedded with these hard inclusions. The precise mechanisms of reinforcement are not fully understood to date (Robertson and Hardman, 2021) but it is accepted that interactions between the filler particles and the polymer through mechanical, physical and sometimes chemical means may all contribute

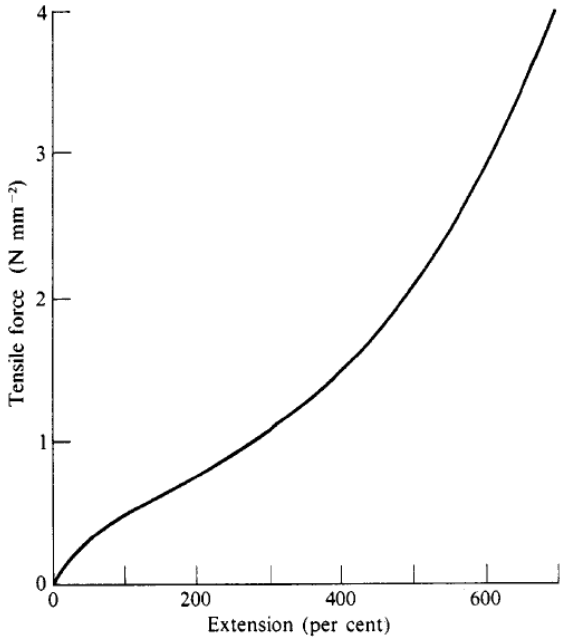


Figure 1.1: Nominal stress - extension curve for a vulcanised rubber. Figure reprinted from Treloar (1975), *The Physics of Rubber Elasticity*, Oxford University Press, with permission from Oxford Academic Publishing.

to reinforcement (Kraus, 1978; Medalia, 1987). Mechanically, fillers act to concentrate strain in the rubber for a given macroscopic deformation. Physically, rubber chains can be adsorbed on the surface of filler particles, constraining the rubber network and thus reducing the entropy of the chains, making the material stiffer (Kraus, 1978). Chemically, covalent bonding between the polymer and filler particles can give rise to a similar constraining effect and additionally filler particles may promote the formation of additional crosslinks within the rubber matrix during vulcanisation (Robertson and Hardman, 2021), altering the underlying properties of the matrix.

In addition to improving the stiffness and strength of a rubber, the presence of the filler particle phase heightens or gives rise to a number of interesting mechanical behaviours (Harwood et al., 1965; Bergström and Boyce, 2000). Most rubbers (quite notably natural rubber) exhibit a degree of viscoelastic behaviour that becomes more pronounced in the presence of a filler phase (Bergström and Boyce, 2000). This time-dependent behaviour can be observed during paused loading tests as shown in Fig. 1.2 for a rubber undergoing uniaxial compression. At each pause, the strain is held constant and it can be observed that the stress gradualllly relaxes from an initial value towards some equilibrium value as

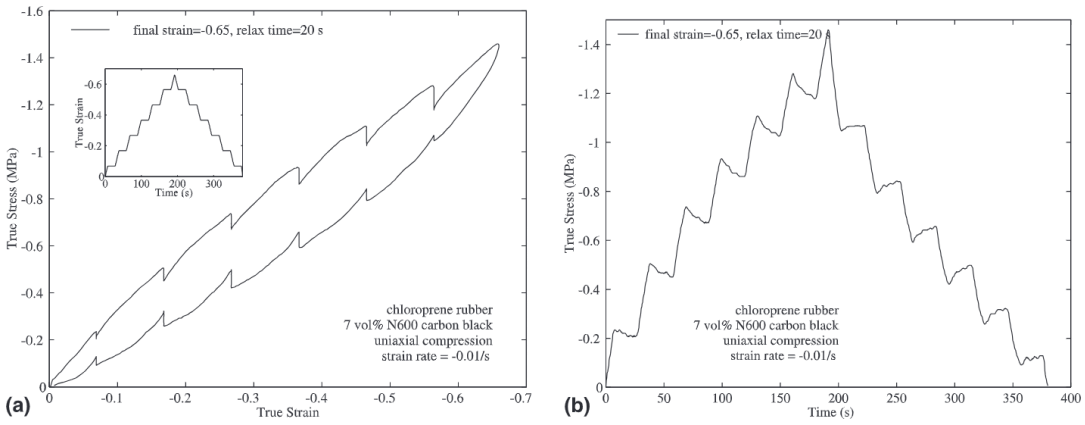


Figure 1.2: Loading-unloading response of a filled rubber under uniaxial compression with pauses at constant strain for 20 s (a) stress-strain response and (b) stress-time response. When held at constant strain, the stress in the rubber varies approximately exponentially with time. Figure reprinted from Bergström and Boyce (2000), 'Large strain time-dependent behavior of filled elastomers', *Mechanics of Materials* **32**(11), 627-644, with permission from Elsevier.

time progresses. This viscoelasticity is observed in many loading scenarios such as cyclic loading and during monotonic loading at different strain rates.

Another interesting behaviour that is exhibited by filled rubbers is the Mullins effect (see the review of Diani et al. (2009)). The Mullins effect is a rate-independent softening phenomenon where the apparent stiffness of the material decreases after it is subjected to deformations to which it has not previously been subjected. An example of the Mullins effect is shown in Fig. 1.3. The primary loading curve is followed when the material is experiencing 'new' deformations. During unloading and reloading below the maximum stretch previously reached, the response of the material is much softer. Further softening does not occur until the envelope of previous deformations is exceeded.

While filled rubbers offer good mechanical performance in many scenarios, they are a thermoset polymer and cannot be processed as a melt, which not only limits the choice of manufacturing processes for making components from filled rubbers but means that they cannot easily be recycled (Holden, 2011). This is a pressing issue for environmentally-conscious engineers, chemists and material scientists and motivates the use of alternative types of elastomers (Gregory et al., 2020). Thermoplastic elastomers (TPEs) are a family of rubber-like materials with similar microstructure and properties to filled rubbers but

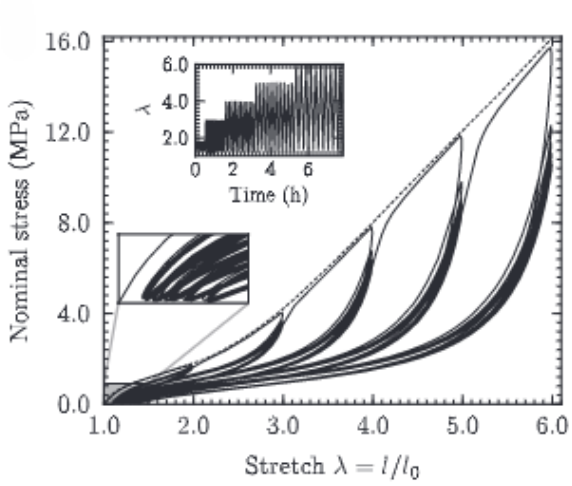


Figure 1.3: An example of the Mullins effect in a carbon black reinforced styrene butadiene rubber subjected to uniaxial tension. The load required to deform the material to a given stretch is appreciably lower during re-loading in comparison to the first loading, and further drops when the material is deformed to higher stretches than previously. Figure reprinted from Merckel, Brieu, Diani and Caillard (2012), 'Constitutive modeling of the anisotropic behavior of Mullins softened filled rubbers', *Journal of the Mechanics and Physics of Solids* **53**(10), 2231-2258, with permission from Elsevier.

with the advantage of melt processability at high temperatures. In contrast to traditional elastomers where chains are connected together through covalent bonds to form a network, TPEs achieve a crosslinking effect through phase separation. TPEs are block copolymers. Each TPE chain is constructed from strands of polymers in the rubbery state and the glassy state connected together. Similar segments display a tendency to group together, and the rubbery (soft) segments are tethered into a network by aggregates of non-rubbery (hard) segments. Above the glass transition of the hard segments, the system loses its pseudo-network architecture and flows in response to shearing (i.e. the system is thermoplastic). From recycling and processing points of view, this thermoplasticity is desirable in that it enables various economically-appealing processing methods, such as injection moulding and extrusion (Holden, 2011), to be used to manufacture soft components.

The mechanical behaviour of TPEs is similar but not identical to that of filled rubbers. Like filled rubbers, TPEs undergo large deformations, display rate sensitive behaviour, and exhibit the Mullins effect (Qi and Boyce, 2005). Furthermore, the mechanics of both materials are sensitive to their composition, in particular to the molecular weight of the soft phase and the volume fraction of the hard phase. Indeed, the stress-strain curve of a TPE

resembles that of a filled rubber to a first approximation (Scetta et al., 2021). Figure 1.4 shows a side-by-side comparison of stress-strain curves for a thermoplastic polyurethane (TPU) - a type of TPE - and a reinforced styrene-butadiene rubber demonstrating these shared behaviours. The key difference in the material responses is that more residual strain is accumulated during the loading of the TPE than in the loading of the filled rubber. The mechanical behaviour of TPEs (and filled rubbers) is highly dependent on their composition and can be altered by varying the proportional of hard phase in the material. Fig. 1.5 shows the stress-strain response of three thermoplastic polyurethane elastomers (TPUs) of different compositions subjected to uniaxial compression under three different strain rates (Cho et al., 2017). All three TPEs show a rate-sensitive response and considerable residual strain, which both become more pronounced as the proportion of hard phase in the TPE is increased.

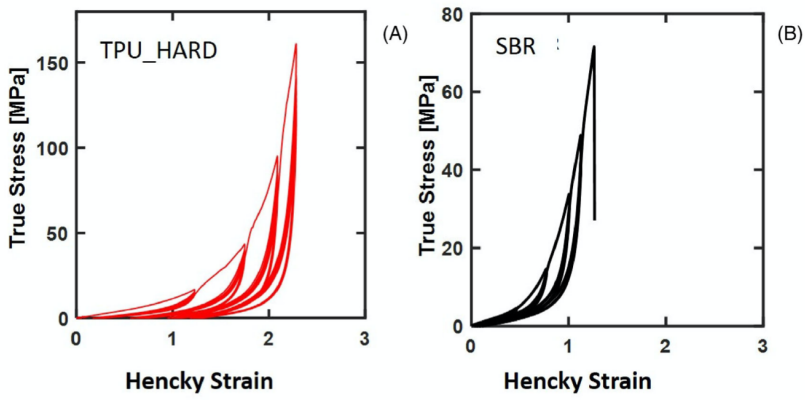


Figure 1.4: Comparison of uniaxial stress-strain curves for a TPU (Elastolan) and carbon black-reinforced styrene-butadiene rubber. Both materials show the Mullins effect and accommodate large deformations. More residual strain is accumulated in the deformation of the TPU. Figure reprinted from Scetta, Ju, Selles, Heuillet, Ciccotti and Creton (2021), 'Strain induced strengthening of soft thermoplastic polyurethanes under cyclic deformation', *Journal of Polymer Science* **59**(8), 685-696, with permission from John Wiley and Sons.

It is common practice in modern engineering to conduct finite element simulations of solid mechanics problems. These require accurate continuum level models of material behaviour. Ideally, these models should be constructed in a micromechanical approach and link mechanical behaviour to material composition and all underlying deformation mechanisms. There remain gaps in our knowledge of the micromechanical approach to

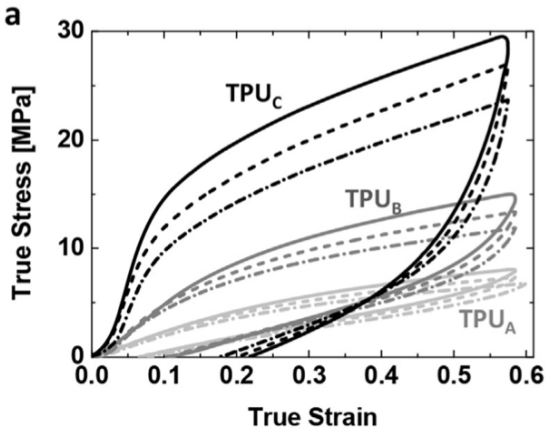


Figure 1.5: Uniaxial compression (negative stresses/strains shown) of TPUs with varying proportion of hard segments (A - 30%, B - 43% and C - 56% wt hard segments). Strain rates: $0.001\,s^{-1}$ (dot-dashed lines); $0.01\,s^{-1}$ (dashed lines); $0.1\,s^{-1}$ (solid lines). Higher hard phase volume fraction TPUs are stiffer and show more pronounced hysteresis and rate-sensitivity. Figure reprinted from Cho, Mayer, Pöselt, Susoff, in 't Veld, Rutledge and Boyce (2017), 'Deformation mechanisms of thermoplastic elastomers: Stress-strain behavior and constitutive modeling', *Polymer* **128**, 97-99, with permission from Elsevier.

rubber modelling, in particular surrounding the application of the approach to different rubber-like materials, to the modelling the response of rubbers under general triaxial loading conditions and to describing inelastic behaviour. This thesis seeks to formulate and systematically investigate models to fill these gaps.

To this end, we construct a general micromechanical modelling framework for filled rubbers and thermoplastic elastomers. The framework takes into account considerations of material microstructure and mechanisms of damage and viscoplasticity on the level of the rubber chain, extending upon the modelling of the elastic rubber chain in isolation, and links it to continuum-level behaviour. The framework is specialised separately to filled rubbers and thermoplastic polyurethanes, and comparisons to experimental data are conducted. In a second application, the micromechanical approach is applied in the context of cylinder-forming thermoplastic elastomer systems. These materials display a grain-like microstructure where the hard phase forms a series of long thin cylinders within each grain (Honeker and Thomas, 1996). Limited modelling work has been previously carried out on these materials. This motivates the development of a model which takes into account this microstructure and again links the macroscopic material behaviour to the composition of

the TPE.

In a third study, the fitting performance of micromechanical models in general multiaxial loading states (general plane stress conditions) is investigated. In the phenomenological theory of rubber elasticity, it is accepted that the free energy density must feature dependence on both the invariants I_1 and I_2 of the right Cauchy-Green deformation tensor $\boldsymbol{C}$ to predict the response in uniaxial tension, equibiaxial tension and planar extension with a single set of parameters. In the micromechanical approach, the tube model (which takes into account additional network constraints in the chain behaviour) usually needs to be incorporated to achieve good fitting performance for these loading conditions. However, tube models vary in their formulation and the suitability of different tube models to reproduce the stress-strain response of rubber-like materials in arbitrary states of deformation has not been systematically investigated previously. To address this gap, we compare the predictions of different tube models to experimental data for different rubber-like materials under general loading conditions, and analyse the ingredients needed to give rise to good fitting performance. In particular fitting performance is explained by linking tube models to dependence of the free energy function on the invariant I_2 through the use of universal relations.

The final contribution of this thesis is a novel modelling approach for capturing the anisotropy of the Mullins effect. It has long been reported that the Mullins effect is an anisotropic damage phenomenon, with anisotropy first reported by Mullins himself in the 1940's (Mullins, 1948). Micromechanical approaches struggle to accurately predict this anisotropy and are often computationally expensive, featuring many internal variables and decompositions of the material into several parallel co-acting deformation mechanisms. In this thesis, a novel semi-phenomenological extension to the micromechanical framework for capturing the Mullins effect is proposed, where a translating damage surface is introduced to describe the evolution of the internal variable inspired by kinematic hardening in the theory of plasticity. Compared to other models in the literature, the developed model is computationally less expensive and requires the use of fewer parameters. The model is

implemented as a user subroutine in ABAQUS/standard for finite element simulations, for which an illustrative example is provided.

This thesis is structured as follows. An overview of rubber modelling is provided in Chapter 2. In Chapter 3 extensions to the micromechanical framework for modelling thermoplastic elastomers and filled rubbers are outlined. The framework is subsequently specialised to two representative systems and confronted against various experimental data for cyclic and rate-varying loading. In Chapter 4, extensions to model the mechanical behaviour of rubbers under general loading conditions are analysed and the modelling assumptions leading to good fitting performance are studied. In Chapter 5, a model for thermoplastic elastomers with cylindrical microstructures is developed in the micromechanical approach. In Chapter 6, the anisotropic stress-softening exhibited by filled-rubbers undergoing the Mullins effect is investigated and the proposed model described and applied. Following this, the thesis is concluded in Chapter 7 where possible future directions for this work are also suggested.

Supporting publications

- G. Kumar, L. Brassart *On tube models of rubber elasticity: fitting performance in relation to sensitivity to the invariant I_2.* Mechanics of Soft Materials 5.1 (2023): 6.

- G. Kumar, L. Brassart *An anisotropic full-network model with damage surface for the Mullins effect in filled rubbers.* International Journal of Solids and Structures 304 (2024): 113030.

Chapter 2

Theoretical background

In this Chapter, the theoretical background underlying rubber modelling will be outlined, with a particular focus on the micromechanical approach to rubber modelling. We will begin our discussion of rubber modelling with rubber elasticity, progressing from the fundamental basis to the state-of-the-art. Micromechanical approaches to modelling damage and viscoelasticity in elastomers are built on this foundation and will be discussed in later sections.

2.1 Preliminaries

We follow standard notation and conventions throughout as much as possible. Bold-face letters are used for vector and second-order tensor quantities. With some exceptions, vectors are denoted with lower case letters and second-order tensors with upper case letters. Higher-order tensors are written in calligraphy typeface. The Einstein summation convention is followed unless explicitly stated otherwise. The trace and determinant of a second order tensor are denoted 'tr' and 'det' respectively. The operator ':' between two tensors denotes their double contraction and '$\otimes$' denotes the outer product. The subscript $()_0$ is used to denote the deviatoric part of a second-order tensor. The second-order identity and fourth-order identities are denoted $\mathbf{1}$ and $\mathbb{I}$ respectively. The deviatoric fourth-order identity is denoted $\mathbb{I}^{dev}$ and is defined such that $\boldsymbol{A}_0 = \mathbb{I}^{dev} : \boldsymbol{A}$ for any second-order tensor $\boldsymbol{A}$.

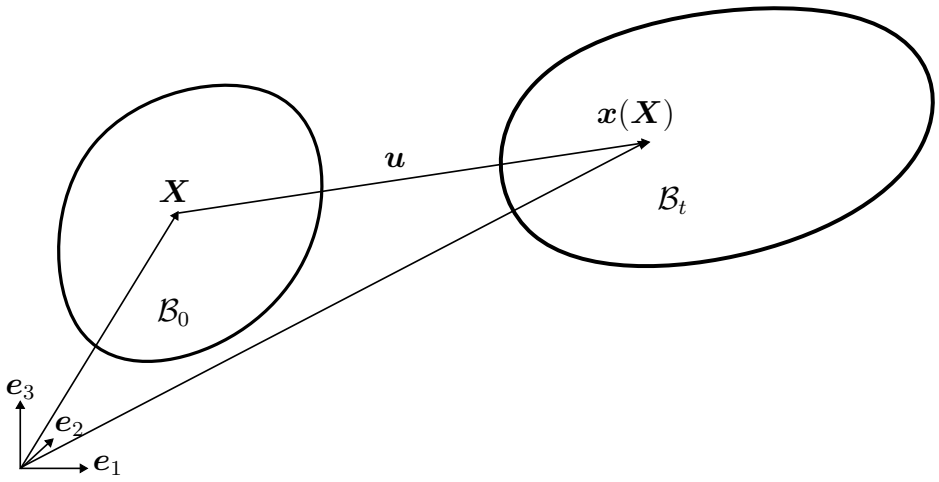


Figure 2.1: An illustration of the mapping $\boldsymbol{x}(\boldsymbol{X})$ from the reference configuration $\mathcal{B}_0$ to the current configuration $\mathcal{B}_t$ in finite deformation continuum mechanics.

Consider a macroscopically homogeneous body $\mathcal{B}_0$ in a reference state occupying a fixed region of space. Each point in the body can be identified by its position $\boldsymbol{X}$. Following deformation, the points occupy the current positions $\boldsymbol{x}$ in the body $\mathcal{B}_t$ which can be mapped from the reference positions. We describe this in the notation $\boldsymbol{x}(\boldsymbol{X})$. The displacement $\boldsymbol{u} := \boldsymbol{x} - \boldsymbol{X}$ is the difference between the current and reference vectors. The deformation gradient $\boldsymbol{F}$ is the gradient of $\boldsymbol{x}(\boldsymbol{X})$:

$$\boldsymbol{F} := \frac{\partial \boldsymbol{x}}{\partial \boldsymbol{X}}. \tag{2.1}$$

We define the right Cauchy-Green deformation tensor $\boldsymbol{C}$ and the left Cauchy-Green deformation tensor $\boldsymbol{B}$ as follows:

$$\boldsymbol{C} := \boldsymbol{F}^T\boldsymbol{F}, \quad \boldsymbol{B} := \boldsymbol{F}\boldsymbol{F}^T, \tag{2.2}$$

where ^{T} denotes the transpose. The following notation is used for the right and left polar decompositions of the deformation gradient into the rotation $\boldsymbol{R}$ and respectively right stretch tensor $\boldsymbol{U}$ and left stretch tensor $\boldsymbol{V}$:

$$\boldsymbol{F} = \boldsymbol{R}\boldsymbol{U} = \boldsymbol{V}\boldsymbol{R}. \tag{2.3}$$

The orthonormality of $\boldsymbol{R}$ implies $\boldsymbol{C} = \boldsymbol{U}^2$ and $\boldsymbol{B} = \boldsymbol{V}^2$. The spectral decomposition

allows $\boldsymbol{C}$ to be split into the principal stretches $\lambda^{(i)}$ and reference principal stretching directions $\boldsymbol{N}^{(i)}$, and similarly allows $\boldsymbol{B}$ to be split into the principal stretches and current stretching directions $\boldsymbol{n}^{(i)}$:

$$\boldsymbol{C} = \sum_{i=1}^{3} (\lambda^{(i)})^2 \boldsymbol{N}^{(i)} \otimes \boldsymbol{N}^{(i)}, \quad \boldsymbol{B} = \sum_{i=1}^{3} (\lambda^{(i)})^2 \boldsymbol{n}^{(i)} \otimes \boldsymbol{n}^{(i)}, \tag{2.4}$$

where the squares of the principal stretches are the eigenvalues of the tensors, and the reference and current stretching directions are the eigenvectors of $\boldsymbol{C}$ and $\boldsymbol{B}$ respectively. The principal directions are not unique when any of the principal stretches are repeated but can always be chosen to form an orthonormal basis in $\mathbb{R}^3$ such that:

$$\sum_{i=1}^{3} \boldsymbol{N}^{(i)} \otimes \boldsymbol{N}^{(i)} = \sum_{i=1}^{3} \boldsymbol{n}^{(i)} \otimes \boldsymbol{n}^{(i)} = \mathbf{1}. \tag{2.5}$$

Constitutive relations must be derived in a manner that satisfies the principles of thermodynamics. For materials undergoing isothermal processes whose only observable state variable is the deformation gradient, the first and second laws require that the change in the free energy of the system Ψ minus any work done on the system must not be positive. This can expressed in the following inequality:

$$\dot{\Psi} - \boldsymbol{P} : \dot{\boldsymbol{F}} \leq 0, \tag{2.6}$$

where $\boldsymbol{P}$ is the first Piola-Kirchhoff stress which forms a work conjugate pair with the deformation gradient. The thermodynamic inequality must hold for all admissible deformations to which the material can be subjected. State laws for stresses (and general thermodynamic forces) can be derived by enforcing these requirements following the Coleman-Noll procedure (Coleman and Noll, 1974), as will now be discussed in the case of hyperelasticity.

Hyperelastic materials feature a free energy density that depends only on the deformation gradient $\boldsymbol{F}$ and only deform elastically. For elastic deformations, the inequality becomes

a strict equality:

$$\left(\frac{\partial \Psi}{\partial \boldsymbol{F}} - \boldsymbol{P}\right) : \dot{\boldsymbol{F}} = 0, \tag{2.7}$$

which must hold true for any admissible changes in the deformation gradient $\dot{\boldsymbol{F}}$ at any current state described by $\boldsymbol{F}$. It is often assumed that rubber-like materials deform without changing volume i.e. are incompressible. The incompressibility constraint means that only variations in $\boldsymbol{F}$ where $J := \det \boldsymbol{F} = 1$ are admissible, which are such that $\dot{J} = J\boldsymbol{F}^{-T} : \dot{\boldsymbol{F}} = 0$. Considering these deformations yields the condition:

$$\boldsymbol{P} = \frac{\partial \Psi}{\partial \boldsymbol{F}} - P\boldsymbol{F}^{-T}, \tag{2.8}$$

which is the state law for stress. Here P is an arbitrary multiplier arising from the incompressibility constraint and corresponds to a pressure that cannot be determined from $\boldsymbol{F}$ alone. Similarly, the Cauchy stress $\boldsymbol{\sigma}$ and second Piola-Kirchhoff stress $\boldsymbol{S}$ can be expressed through the equivalent relations:

$$J\boldsymbol{\sigma} = \frac{\partial \Psi}{\partial \boldsymbol{F}}\boldsymbol{F}^T - P\mathbf{1}, \quad \boldsymbol{S} = 2\frac{\partial \Psi}{\partial \boldsymbol{C}} - P\boldsymbol{C}^{-1}, \tag{2.9}$$

which can be derived by again considering the thermodynamic inequality by replacing $\boldsymbol{P} : \dot{\boldsymbol{F}}$ with the appropriate power-conjugate pairings for each stress ($\boldsymbol{P} : \dot{\boldsymbol{F}} = J\boldsymbol{\sigma} : \dot{\boldsymbol{F}}\boldsymbol{F}^{-1} = \frac{1}{2}\boldsymbol{S} : \dot{\boldsymbol{C}}$).

Various physical considerations and assumptions restrict the nature of the free energy function. For all materials, the principle of objectivity must hold. Many rubber-like materials are isotropic. These principles can be embedded directly in the mathematical model as is commonly done in the phenomenological approach to rubber elasticity, or enforced in later assumptions as often happens in the development of physical models of rubber elasticity.

The principle of objectivity (or material frame indifference) states that the material response is independent of an arbitrary rotation $\boldsymbol{Q}$ of the spatial frame $\boldsymbol{x}$. This implies that

the free energy density written as a function of $\boldsymbol{F}$ must have the following property:

$$\Psi(\boldsymbol{F}) = \Psi(\boldsymbol{Q}\boldsymbol{F}). \tag{2.10}$$

for arbitrary right-orthogonal transformations $\boldsymbol{Q}$. Restricting the free energy density to depend only on the deformation gradient through the right Cauchy-Green deformation tensor $\boldsymbol{C}$ ensures that the principal of objectivity is satisfied.

Material isotropy is a commonly invoked modelling assumption that states that the material response does not depend on the direction in which it is stretched i.e. a rotation $\boldsymbol{Q}$ of the reference frame $\boldsymbol{X}$ for a given spatial configuration $\boldsymbol{x}$ does not change the free energy. Mathematically, this is reflected in the condition $\Psi(\boldsymbol{F}) = \Psi(\boldsymbol{F}\boldsymbol{Q})$. In combination with the principal of objectivity, material isotropy implies that the free energy is further restricted to depend on $\boldsymbol{C}$ only through its principal invariants:

$$I_1 = \mathrm{tr}\boldsymbol{C}, \quad I_2 = \frac{1}{2}\left(I_1^2 - \mathrm{tr}\boldsymbol{C}^2\right), \quad I_3 = \det \boldsymbol{C}, \tag{2.11}$$

or alternatively through the principal stretches $\lambda^{(i)}$, whose squares are the eigenvalues of $\boldsymbol{C}$ and which are also invariant measures of deformation. Note that the invariants can be expressed in terms of the principal stretches as follows:

$$I_1 = (\lambda^{(1)})^2+(\lambda^{(2)})^2+(\lambda^{(3)})^2, \quad I_2 = (\lambda^{(1)}\lambda^{(2)})^2+(\lambda^{(1)}\lambda^{(3)})^2+(\lambda^{(2)}\lambda^{(3)})^2, \quad I_3 = (\lambda^{(1)}\lambda^{(2)}\lambda^{(3)})^2. \tag{2.12}$$

Incompressibility restricts the range of admissible deformations to those where $I_3 = 1$, which means that the free energy density can effectively be considered a function of I_1 and I_2 only, or again equivalently as a function of the principal stretches with a constraint on their product:

$$\Psi = \Psi(I_1, I_2) \text{ with } I_3 = 1 \quad \text{or} \quad \Psi = \Psi(\lambda^{(1)}, \lambda^{(2)}, \lambda^{(3)}) \text{ with } \lambda^{(1)}\lambda^{(2)}\lambda^{(3)} = 1. \tag{2.13}$$

Following these assumptions, the Cauchy stress may be expressed as:

$$\boldsymbol{\sigma} = 2\frac{\partial \Psi}{\partial I_1}\boldsymbol{B} - 2\frac{\partial \Psi}{\partial I_2}\boldsymbol{B}^{-1} - P\mathbf{1} = \left(\sum_{i=1}^{3} \lambda^{(i)} \frac{\partial \Psi}{\partial \lambda^{(i)}} \boldsymbol{n}_i \otimes \boldsymbol{n}_i\right) - P\mathbf{1}, \tag{2.14}$$

As a consequence of invariance, I_1 and I_2 can equivalently be expressed in terms of $\boldsymbol{B}$, i.e. $I_1 = \mathrm{tr}\boldsymbol{B}$, $I_2 = \frac{1}{2}(I_1^2 - \mathrm{tr}\boldsymbol{B}^2)$. This choice is often convenient as it permits the Cauchy stress to be written as a function of $\boldsymbol{B}$ directly.

2.2 The phenomenological approach to rubber elasticity

Rubber-like materials are materials capable of undergoing large deformations with near complete reversibility (at least in some circumstances) and in these cases can be described within the framework of hyperelasticity. One approach to modelling rubber-like materials is the phenomenological approach, where a free energy function of convenient mathematical form is postulated to describe the material behaviour. The free energy function must satisfy the principle of objectivity, and in many cases is taken to be isotropic. Typically, phenomenological models of rubber elasticity are grouped into the invariant-based models and principal stretch-based models based on the arguments of their free energy function. All invariant-based models can quite simply be expressed in terms of principal stretches. However the computation of principal stretches requires the solution of an eigenvalue problem. This is unavoidably more expensive than the computation of the invariants defined in Eqs. $(2.11)_1$ - $(2.11)_3$ as these can simply be evaluated using elementary matrix manipulations. A great number of models of each type have been proposed in the literature (see the reviews of Marckmann and Verron (2006); Steinmann et al. (2012); Hossain et al. (2015); Dal et al. (2021); Ricker and Wriggers (2023)). A non-exhaustive selection these models, limited to the incompressibile case, are presented and discussed in this Section.

2.2.1 Invariant based models

Invariant-based models of rubber elasticity either depend on one or both of the invariants I_1 and I_2. We will begin by outlining first some I_1-based models before progressing to I_2-based models. The simplest and earliest invariant-based model is the neo-Hookean model. It has a free energy density that is proportional to I_1:

$$\Psi = \frac{1}{2}\mu(I_1 - 3), \tag{2.15}$$

where μ is the shear modulus. The neo-Hookean model has limited capabilities to capture the quantitative detail of the mechanical response of a material outside of the low-to-moderate deformation regime (provided it is well calibrated) (Marckmann and Verron, 2006) but is frequently used for its simplicity. It does not predict an upturn in the stress-strain response as is observed in most rubbers at higher stretches. Phenomenological models with a free energy that only depends on I_1 are often referred to as *generalised neo-Hookean* models after the neo-Hookean model.

The Gent model (Gent, 1996) is another very popular I_1-based model. In addition to a shear modulus μ, it is parameterised by the limiting extension parameter J_m:

$$\Psi = -\frac{\mu}{2} J_m \log\left(1 - \frac{I_1 - 3}{J_m}\right). \tag{2.16}$$

At low-to-moderate deformations (specifically when I_1 is much smaller than J_m), the Gent model predicts the same stress-strain response as the neo-Hookean model. However at larger stretches, the Gent model predicts an upturn in the stress-strain curve. As I_1 tends towards the limiting extensibility parameter J_m, the Gent model predicts a singularity in the free energy and in the stress-strain curve.

Lopez-Pamies (2010) proposed a free energy function that consists of a summation of power-law terms:

$$\Psi = \sum_{i=1}^{N} \frac{3^{1-\alpha_i}}{2\alpha_i} \mu_i \left(I_1^{\alpha_i} - 3^{\alpha_i}\right), \tag{2.17}$$

where μ_i and α_i are fitting parameters. This model can predict an upturn in the stress-stretch curve at large deformations but does not predict a singularity or limiting extensibility in the stress-stretch response.

A long-standing topic in the phenomenological theory of rubber elasticity is the role of the invariant I_2 in the free energy function. While I_2 did not appear in early formulations of the micromechanical theory of rubber elasticity, there has been strong experimental evidence gathered for a variety of rubber-like materials indicating the need for models with dependence on both strain invariants (see the experiments of Rivlin and Saunders (1951) and the analysis of Wineman (2005); Horgan and Smayda (2012); Anssari-Benam et al. (2021)) motivating the development of various I_2-based contributions to the free energy. Dependence on I_2 was first inferred by Mooney (1940) to explain the normal stresses observed in simple shear deformations. Further evidence for I_2-dependence in real rubber-like materials comes from inferences of the $\partial\Psi/\partial I_2$ derivative based on analysis of the material behaviour in general plane stress conditions (Rivlin and Saunders, 1951; Kawabata et al., 1981), and also arises in several other loading conditions (see Wineman (2005)). Quite often, models featuring dependence on invariants admit an additive decomposition of the free energy function into separate contributions from each invariant:

$$\Psi = f(I_1) + g(I_2), \tag{2.18}$$

where the I_1 contribution is often selected from existing I_1-based models in the literature. Popular choices include the neo-Hookean free energy and the Gent free energy. Various functional forms have been suggested for the I_2 contribution $g(I_2)$.

The Mooney-Rivlin model (Mooney, 1940) features a linear contribution to the free energy from I_2 in addition to a neo-Hookean term:

$$\Psi = C_1(I_1 - 3) + C_2(I_2 - 3), \tag{2.19}$$

where C_1 and C_2 are two fitting parameters that are related to material stiffness. Like

the neo-Hookean model, the Mooney-Rivlin model describes the mechanical response of rubber-like materials reasonably well at small-to-moderate deformations but does not accurately predict the response at larger strains.

An alternative I_2-contribution following a logarithmic term comes from Gent and Thomas (1958):

$$g(I_2) = C_2 \log \frac{I_2}{3}. \tag{2.20}$$

As the logarithm grows more slowly than the linear term, the Gent-Thomas model predicts a larger contribution from I_2 at low-to-moderate deformations than at large deformations. Another I_2-based functional form was suggested by Carroll (2011) based on a systematic fitting of Treloar's data (Treloar, 1943):

$$g(I_2) = C\sqrt{I_2}, \tag{2.21}$$

which was postulated in combination with an I_1 contribution of the form $f(I_1) = AI_1 + BI_1^4$. When calibrated against the same data, Carroll's model predicts very similar responses to the Gent-Thomas model (Carroll, 2011) (which may be reflected in comparisons of their series expansions) and offers good predictive ability in multiaxial loading conditions (Hossain and Steinmann, 2013).

2.2.2 Principal stretch-based models

The principal stretch-based models serve as an alternative to the invariant-based models where the free energy function is written as a symmetric function of the principal stretches to ensure material objectivity and isotropy. While principal stretch-based models are more computationally expensive than their invariant-based counterparts due to the need to solve eigenvalue problems and possible singularities in constitutive models as the principal stretches tend to one (Rivlin and Saunders, 1951; Carroll, 2011), it has been argued that they are simpler to analyse (Ogden, 1972) and easier to link to experimental behaviour (Valanis and Landel, 1967). Fitting principal stretch-based free energy func-

tions to experimental data can be made simpler by invoking further assumptions about the mathematical form of the free energy function. The Valanis-Landel hypothesis states that the free energy function can be additively split into a summation of a function of each of the principal stretches independently, i.e.:

$$\Psi(\lambda^{(1)}, \lambda^{(2)}, \lambda^{(3)}) = \sum_{i=1}^{3} \psi(\lambda^{(i)}). \tag{2.22}$$

This decoupling simplifies the problem of determining the functional form of the free energy density (Valanis and Landel, 1967; Kearsley and Zapas, 1980) as now only one function with a single independent variable needs to be determined, which can be done exactly from a simple shear test (Valanis and Landel, 1967). The Valanis-Landel hypothesis has been shown to reflect the behaviour of many rubber-like materials at moderate deformations (Valanis and Landel, 1967) but not when limiting extension is reached. The hypothesis implies that limiting extension is governed by the maximum principal stretch while experimental evidence suggests that the mode of deformation impacts limiting extensibility as well as the maximum principal stretch (Gent, 2005; Tkachuk and Linder, 2012). In their original paper, Valanis and Landel (1967) propose the single-parameter free energy density (featuring the shear modulus μ):

$$\Psi = 2\mu \sum_{i=1}^{3} \lambda^{(i)} \left(\log(\lambda^{(i)}) - 1 \right), \tag{2.23}$$

based on the analysis of the simple shear mode of deformation.

Perhaps the most used and most well-known principal stretch-based model is the Ogden model (Ogden, 1972) which also follows the Valanis-Landel hypothesis. In this model, the free energy function is a summation of power law terms:

$$\Psi = \sum_{i=1}^{N} \frac{\mu_i}{\alpha_i} \sum_{j=1}^{3} \left(\lambda^{(j)} \right)^{\alpha_i}, \tag{2.24}$$

where μ_i and α_i are fitting parameters and N is the number of terms in the series (chosen by the modeller). Convexity conditions require $\mu_i \alpha_i > 0$ for each i, which means that

negative μ_i terms are permitted in the model. Typically, the Ogden model is used with 2 or 3 terms to achieve good agreement with experimental data.

Another summation form principal stretch-based model was proposed by Shariff (2000):

$$\Psi = E \sum_{j=1}^{3} \sum_{i=0}^{N} \alpha_i \phi_i(\lambda^{(j)}), \tag{2.25}$$

where E and α_i are fitting parameters and the functions ϕ_i in the summation take on different forms depending on where they appear in the series:

$$\phi_0 = \frac{2\log\lambda^{(j)}}{3},\ \phi_1 = \exp(\lambda^{(j)} - 1) + \lambda^{(j)} - 2, \phi_2 = \exp(\lambda^{(j)} - 1) - \lambda^{(j)},$$
$$\phi_3 = \frac{(\lambda^{(j)} - 1)^3}{(\lambda^{(j)})^{3.6}},\ \phi_{i,\, i>3} = \left(\lambda^{(j)} - 1\right)^j - 1. \tag{2.26}$$

A very general principal stretch-based model was recently proposed by Anssari-Benam (2023), from which many other models can be recovered as special cases:

$$\Psi = \frac{3(n-1)}{2n}\mu N \left(\frac{\sum_{j=1}^{3} \left(\lambda^{(j)}\right)^{\alpha_i} - 3}{3N(n-1)} - \log\left(\frac{\sum_{j=1}^{3} \left(\lambda^{(j)}\right)^{\alpha_i} - 3N}{3 - 3N} \right) \right). \tag{2.27}$$

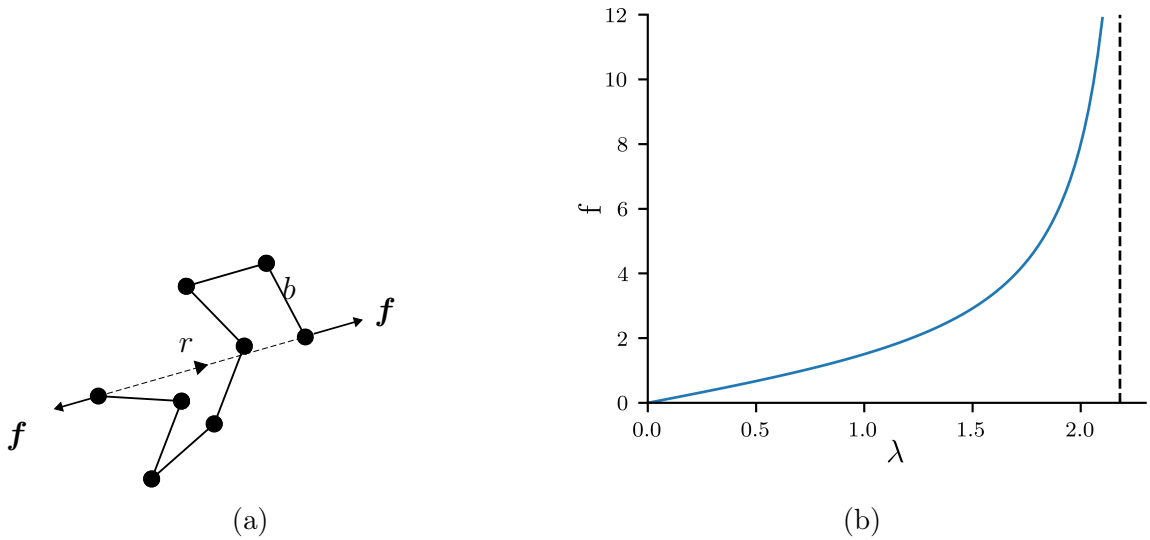
The Gent model can be recovered setting $\alpha = 2$; considering $N \to \infty$ recovers the Ogden model, from which the neo-Hookean and Mooney-Rivlin model can be recovered as further special cases.

A common problem encountered with summation-type models such as the Ogden model, the Shariff model, the Anssari-Benam model and the Lopez-Pamies model lies in calibration. If too many terms are included in the model, these models may lack a unique set of best fit parameters for a given dataset (Ogden et al., 2004). This arises as the parameter space features many local minimisers of the fitting error which implies the degeneracy of the best fit parameters. This non-uniqueness is not problematic if the model is only used for making predictions close to the datapoints which it was calibrated against however the predictions in other types of deformation or outside the calibrated stretch range may be unrealistic (Carroll, 2011).

The phenomenological modelling of rubber-like materials in hyperelasticity continues to be an active topic of research to date, with new models still appearing in the literature today (e.g. Anssari-Benam (2023)). While some models perform better than others (some models are better able to predict differences between different loading types at moderate and large deformations than others, some models have fewer parameters), many offer largely similar performance (Marckmann and Verron, 2006; Dal et al., 2021; Ricker and Wriggers, 2023) and there is a degree of choice in the particular selection of a rubber model from those available in the literature (Carroll, 2011). Fundamentally, all of the phenomenological models of rubber elasticity lack physical interpretation and may not be robust outside of their calibrated range. An alternative modelling approach which aims to bypass these difficulties is the micromechanical approach which links the macroscopic response of the rubber to its microstructure.

2.3 The micromechanical approach to rubber elasticity

2.3.1 The individual rubber chain



(a) (b)

Figure 2.2: (a) The freely-jointed chain model concept and (b) force-extension relationship with singularity as the chain is fully extended ($\lambda = 2.2$ in this case).

The starting point of the micromechanical approach to rubber elasticity is the isolated

rubber chain and its entropic character (Rubinstein et al., 2003). The freely-jointed chain model depicted in Fig. 2.2(a) is an idealisation of a real chain in the rubbery state that is sufficiently realistic for explaining the mechanical behaviour of rubbers including limiting extension effects. Chains are long and mobile and consist of a large number of segments. Segments freely orient themselves and chains can configure in a number of different ways in space. The maximum entropy principle dictates that the macroscopic equilibrium state of the system is such that the number of microscopic (macroscopically indistinguishable) configurations of the system and surroundings combined is maximised. This means that, when relaxed, chains arrange in highly-coiled configurations and the distance between the ends of the chain is far less than the contour length of the chain. Stretching a chain uncoils it and reduces the number of configurations it can adopt, resulting in a drop in entropy and increase in free energy. This reduction in entropy opposes stretching. It comes with a force penalty and is the origin of stress in rubber systems. Ideal rubbers are unlike other engineering materials in that deformation proceeds almost entirely through entropic mechanisms, without any change in chain internal energy.

The free energy of the freely-jointed chain ψ is parameterised by the number of Kuhn segments in each chain N, the length of each segment b, the absolute temperature T, the Boltzmann constant k_B, reference chain end-to-end distance r_0 and chain stretch λ (Treloar, 1975):

$$\psi(\lambda) = Nk_BT\left(\beta\frac{\lambda r_0}{Nb} + \log\frac{\sinh\beta}{\beta}\right), \tag{2.28}$$

$$\text{where } \beta = \mathcal{L}^{-1}\left(\frac{\lambda r_0}{Nb}\right) \text{ and } \mathcal{L}(x) = \coth x - \frac{1}{x}. \tag{2.29}$$

The chain stretch is defined on the micro-scale as the ratio of current chain end-to-end distance r to reference chain end-to-end distance:

$$\lambda = \frac{r}{r_0}. \tag{2.30}$$

The chain force-extension relationship can be found from the derivative $\partial\psi/\partial r$. The

thermodynamic force associated with chain stretching $f := \partial\psi/\partial\lambda$ is another commonly evaluated quantity. In Fig. 2.2(b), the force length-extension relationship is plotted for illustration. The relationship is initially linear but features an upturn as the chain reaches its extensibility limit, where it is extended to near its contour length. It is often assumed that the reference length of the chain scales is given by the root mean square chain end-to-end distance:

$$r_0 = \sqrt{N}b. \tag{2.31}$$

Though this assumption is widely followed, it is not necessary to close the model and does always accurately reflect the reference state of the chain in the network (Alamé and Brassart, 2020). If the number of Kuhn segments in the chain is large, such that the chain is only subjected to stretches far below its limiting extensibility, the freely-jointed chain can be approximated by the Gaussian chain model:

$$\psi(\lambda) \approx \frac{3}{2}k_B T\lambda^2 \quad \text{if } \lambda << \frac{Nb}{r_0}, \tag{2.32}$$

which does not take into account limiting extension effects but is a simpler expression than Eq. (2.28). Differences between the Gaussian chain model and the freely-jointed chain model are generally not appreciable for stretches $\lambda < 0.3Nb/r_0$. Other chain models have been proposed in the literature which take into account more realistic descriptions of chain configurations, such as the freely-rotating chain model , or account for the energetic contribution to the free energy from bond angle e.g. the worm-like chain model (see Rubinstein et al. (2003) for a summary of ideal chain models). Alternatively, purely phenomenological chain models have also been used in the literature (Govindjee et al., 2019) where the physical nature of the chain behaviour is not of interest.

2.3.2 The rubber network

A rubber-like material consists of a series of chains linked together at crosslinking points. Further modelling is required to relate macroscopic network behaviour to individual chain behaviour (Treloar, 1975). One basic assumption of rubber elasticity is that the free

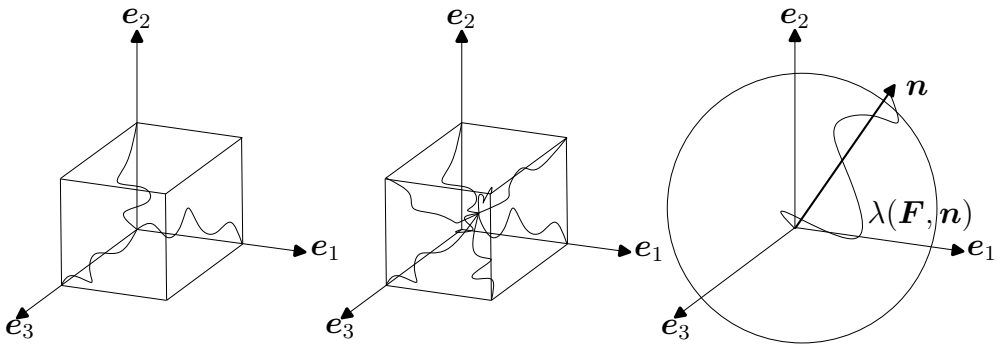


Figure 2.3: Schematic representations of (a) the three-chain (3C) model, where chains are aligned with principal stretching directions; (b) eight-chain (8C) model, where chains are aligned with diagonals of cube in principal stretch space; and (c) full-network (FN) model, where chains are oriented in all spatial directions.

energy of the network is simply the sum of the free energies of the individual chains in isolation:

$$\Psi = \frac{1}{V} \sum_{\text{network}} \psi(\lambda) \tag{2.33}$$

where λ needs to be related to the macroscopic deformation gradient.

The summation over all chains that compose the network is generally not feasible. One approach to address this problem is to replace the summation over chains with the orientational average behaviour of the chains. Chains are identified by their reference orientation, and chains with the same reference orientation are assumed to undergo the same stretch under macroscopic deformation. The full network approach, originally suggested by Treloar (1954) and later more fully explored by Wu and Van Der Giessen (1993), considers a continuous distribution of chains over all orientations (illustrated in Fig. 2.3(c)) with the same reference end-to-end lengths and properties, such that the free energy density is given by the integral over all reference chain orientations:

$$\Psi = \frac{n}{4\pi} \int_{\mathcal{S}} \psi(\lambda) d\mathcal{S}. \tag{2.34}$$

Here n is the number of chains per unit volume. $\mathcal{S}$ is the set of all unit reference directions and represents the unit sphere. For conciseness of notation, we later use angle brackets

$\langle\rangle$ to represent this integral:

$$\langle \bullet \rangle := \frac{1}{4\pi} \int_{\mathcal{S}} \bullet d\mathcal{S}. \tag{2.35}$$

The most frequently used rule to relate the chain stretch to the macroscopic deformation is the affine rule, which equates the chain stretch with the continuum line stretch $\bar{\lambda}$. A fibre embedded in the continuum with unit direction $\boldsymbol{n}$ is stretched according to:

$$\bar{\lambda} = |\boldsymbol{F}\boldsymbol{n}|. \tag{2.36}$$

The affine rule states that a chain with reference orientation $\boldsymbol{n}$ deforms like a fibre with reference orientation $\boldsymbol{n}$:

$$\lambda = \bar{\lambda}. \tag{2.37}$$

This measure of chain stretch is invariant to rotations of the current frame and ensures the model satisfies the principle of objectivity.

A more general family of chain stretch rules can be found by considering the chain stretch written as a to-be-specified function of the macroscopic deformation gradient and the (unit) reference direction vector of the chain $\boldsymbol{n}$:

$$\lambda = \lambda(\boldsymbol{F}, \boldsymbol{n}). \tag{2.38}$$

Micro-macro transitions deviating from the affine rule (2.37) but maintaining the form (2.38) are often used when modelling composite elastomers, such as filled rubbers and thermoplastic elastomers where chains are generally more deformed more than they would be in an affine network, as is later discussed. A family of rules of the form of Eq. (2.38) were also proposed by Fried (2002) in an attempt to recover the phenomenological Mooney-Rivlin model from the micromechanical approach to rubber elasticity. Later, a non-affine rule of the form $\lambda = \boldsymbol{U} : \boldsymbol{n} \otimes \boldsymbol{n}$ was proposed by Zhan et al. (2023*b*) and Amores et al. (2021) independently. In both cases, the non-affine deformation rule results in models which achieve good agreement with the experimental stress-strain behaviour however the precise physical interpretation of the rule remains unclear, whereas the physical meaning

of the affine rule remains unambiguous.

In practice, the full-network integral (2.34) is not analytically tractable for many loading cases and chain models, and must be approximated. The three-chain (James and Guth, 1943) and eight-chain (Arruda and Boyce, 1993) schemes are two analytical approaches to approximating the network free energy and are depicted alongside the exact full-network in Figure 2.3. The three-chain model represents the network through the deformation of three chains aligned with the principal axes of deformation (Treloar, 1975). The free energy is given by:

$$\Psi^{3C} = \frac{n}{3}\sum_{i=1}^{3}\psi(\lambda^{(i)}). \tag{2.39}$$

The eight-chain model (Arruda and Boyce, 1993) is a highly-celebrated model in the theory of rubber elasticity. A cube with freely-jointed chains spanning from the centre of the cube in principal stretch space to its vertices represents the network under deformation. The cube only undergoes principal deformations (i.e. it remains a cuboid) which implies that the stretch of each of the eight chains $\lambda^{(8C,i)}$ is the same and given by:

$$\lambda^{(8C,i)} = \sqrt{\frac{\left(\lambda^{(1)}\right)^2 + \left(\lambda^{(2)}\right)^2 + \left(\lambda^{(3)}\right)^2}{3}} =: \lambda^{8C}. \tag{2.40}$$

As all eight chains see the same stretch, the free energy is that of a single chain multiplied by a factor n (the number of chains per unit volume) to reflect the network connectivity:

$$\Psi^{8C} = n\sum_{i=1}^{8}\psi(\lambda^{(8C,i)}), \tag{2.41}$$

$$= n\psi(\lambda^{8C}). \tag{2.42}$$

The three-chain and eight-chain schemes can be considered reduced integration approaches to evaluating Eq. (2.33), where the integral is evaluated by summing the chain free energies at the three-chain and eight-chain orientations respectively. More precise approximations of the integral come from higher-order integration schemes. A number of such

discretisation schemes are applicable to this integration e.g. Bažant and Oh (1986); Fliege and Maier (1999). In this case, the full-network free energy becomes:

$$\Psi^{FN} = \sum_{i=1}^{N_{int}} w_i \psi(\lambda_i), \tag{2.43}$$

where w_i is the weight associated with the i^{th} integration point, λ_i is the stretch at that point and N_{int} is the number of integration points associated with the integration scheme.

The Cauchy stress for the full network model is given by:

$$\boldsymbol{\sigma} = n \left\langle \frac{\partial \psi}{\partial \lambda} \frac{\partial \lambda}{\partial \boldsymbol{F}} \boldsymbol{F}^T \right\rangle - P\mathbf{1}, \tag{2.44}$$

$$= n \left\langle \frac{1}{\lambda} \frac{\partial \psi}{\partial \lambda} \boldsymbol{F}\boldsymbol{n} \otimes \boldsymbol{F}\boldsymbol{n} \right\rangle - P\mathbf{1}. \tag{2.45}$$

To avoid the numerical issues associated with discretised full-network models, analytical approximations of the affine full-network integral were proposed independently by Puso (2003) and Beatty (2003). This approach entirely bypasses the need for numerical integration and results in significant reduction in computational cost. However, this comes with a loss in accuracy for non-quadratic chain free energy functions. First, note that the root mean square stretch Λ in a network of affinely-deforming chains can be expressed analytically using the identity $\langle \boldsymbol{n} \otimes \boldsymbol{n} \rangle = \mathbf{1}/3$:

$$\Lambda = \left(\langle \boldsymbol{C} : \boldsymbol{n} \otimes \boldsymbol{n} \rangle \right)^{0.5} = \left(\boldsymbol{C} : \langle \boldsymbol{n} \otimes \boldsymbol{n} \rangle \right)^{0.5} = \sqrt{\frac{I_1}{3}} \tag{2.46}$$

In the average-stretch approach, the full-network free energy is simply the chain free energy evaluated at the average stretch:

$$\langle \psi \rangle \approx \psi(\Lambda). \tag{2.47}$$

This approximation can be justified based on the Taylor expansion of the chain free energy

about the average stretch, where it can be observed that $\psi(\Lambda)$ is the zeroth-order term in the series and the first-order term is zero. A full derivation of this result is provided in Appendix D. As noted by Beatty (2003); Puso (2003), the average stretch coincides with the chain stretch sampled in the eight chain model and offers some explanation for the success of the eight-chain model. This approach has been extended to account for anisotropic chain orientation distributions by Khiêm and Itskov (2016) based on a parameterisation of the chain distribution in terms of a preferred direction which influences the average stretch.

2.4 Modelling soft matrix/hard inclusions composites

This thesis focusses on the modelling of two-phase elastomers such as thermoplastic elastomers and filled rubbers. Key to modelling these behaviours is a treatment for their composite structure which is generally characterised by the volume fractions of each phase. One approach to accounting for the heterogeneous microstructure of filled rubbers is based on homogenisation theory, where some averaging process is carried out that results in a description of the material as an equivalent single phase system with properties and behaviours derived from its constituent phases. In linear elasticity, various expressions exist for the approximate effective moduli of the homogenised material. For example Einstein (1906) derives the expression:

$$E = (1 + 2.5f)E_m, \tag{2.48}$$

relating the effective Young's modulus E to the Young's modulus of the rubber matrix E_m for composites with small volume fractions of added rigid filler particles. Further expressions have been developed in linear elasticity for higher volume fractions (Guth, 1945; Budiansky, 1965) and also for bounds on the effective elastic moduli (e.g. the Reuss and Voigt bounds, the Hashin-Shtrikman bounds (Hashin and Shtrikman, 1963)). The homogenisation approach has been extended to capture non-linear behaviour in filled elastomers by Lopez-Pamies, Goudarzi and Nakamura (2013); Lopez-Pamies, Goudarzi and Danas (2013), who derive a closed-form expression for the effective free energy Ψ

in terms of the matrix free energy Ψ_m (which is assumed to be I_1-based only) through a non-linear comparison medium technique assuming rigid fillers and a matrix with an I_1-based free energy function:

$$\Psi = (1-f)\Psi_m((1-f)^{-3.5}(I_1-3)+3), \tag{2.49}$$

which they validate against finite element results.

Whilst homogenisation approaches yield useful insight into the behaviour of filled rubbers and TPEs, these approaches face a number of roadblocks. Extending homogenisation theory to non-linear, inelastic and rate-dependent behaviour is very challenging and active field of research (c.f. the works of Castañeda and Tiberio (2000); Bleiler et al. (2021)). Furthermore, challenges arise in modelling behaviours which result from the interaction of the phase (for example, the Mullins effect in TPUs has been attributed to a process where soft segments initially impinged on the surface of hard domains become released). Many cutting-edge models assume highly idealised soft phase behaviour (hyperelasticity (Furer and Castañeda, 2020), nonlinear viscoelasticiy with Neo-Hookean elasticity and Newtonian viscosity (Ghosh et al., 2021)), which may be too much of an idealisation of the true system. More fundamentally, the validity of the continuum assumption in modelling filled rubbers and TPEs comes into question as the characteristic size of hard domains can be of the order of nanometres.

A simpler more heuristic approach to addressing the composite nature of the microstructure is through stretch amplification (Mullins and Tobin, 1957; Govindjee, 1997; Bergstrom and Boyce, 1999; Domurath et al., 2017). In this approach, the filled rubber is treated as a pure rubber that is subjected to a higher stretch than the material sees overall (i.e. the stretch is amplified) to reflect the rigid fillers not undergoing any deformation. The concept was first introduced considering rubbers undergoing uniaxial tension by Mullins and Tobin (1957), where it was proposed to amplify the nominal uniaxial strain $\Lambda - 1$ by

some factor X to yield the strain of the pure rubber:

$$\lambda = X(\Lambda - 1) + 1. \tag{2.50}$$

Subsequently, this concept has been generalised with different strain measures and used extensively in modelling filled rubbers, with various expressions existing for the amount by which a stretch measure is increased over the macroscopic in the literature (Govindjee, 1997; Bergstrom and Boyce, 1999).

Derivations of amplification factors vary primarily in whether or not the rubbery phase is treated as a continuum phase or just as a series of rubbery chains connecting filler particles. When the phases are treated on the continuum level, it is generally implied that the strain in the soft phase varies spatially. The hard particles act as stress concentration features which means that the matrix is more stressed and more stretched in these regions. This treatment is not consistent with the statistical mechanics treatment of chains where chains are averaged to springs which can only undergo homogeneous deformations. There is no notion of strain gradients on the chain length scale. As each single chains connects a hard particle to another hard particle, it is unclear what variation in strain implies in the statistical treatment.

One continuum approach is that of Govindjee and Simo (1991) where the deformation gradient itself is amplified based on considerations on volume averaging constraints on the deformation gradient. Following Hill (1963), they invoke the following relationship between the macroscopic gradient $\boldsymbol{F}$ and the volume average gradients in the rubber phase $\boldsymbol{F}^m$ and the filler phase $\boldsymbol{F}^f$:

$$\boldsymbol{F} = (1 - f)\boldsymbol{F}^m + f\boldsymbol{F}^f. \tag{2.51}$$

As the fillers are rigid, they suppose that the average deformation gradient in the filler phase is simply equal to the macroscopic rotation ($\boldsymbol{F}^f = \boldsymbol{R}$) and infer from Eq. (2.51) that the average deformation gradient in the rubber can be expressed in the following

relation:

$$\boldsymbol{F}^m = \frac{\boldsymbol{F} - f\boldsymbol{R}}{1-f}. \tag{2.52}$$

Bergstrom and Boyce (1999) propose that the appropriate extension of the one-dimensional amplification of Mullins and Tobin (1957) should be based on the invariant I_1:

$$I_1^s = X(I_1 - 3) + 3, \tag{2.53}$$

which they justify on the grounds that I_1 reflects the average chain stretch as per the eight-chain model. They suggest an expression for the amplification factor based on the Guth-Gold result for the effective modulus of a matrix consisting of a linear elastic matrix embedded with rigid inclusions (Guth and Gold, 1938), following a survey of other factors derived from these assumed phase behaviours. This expression reads:

$$X = 1 + 3.5f + bf^2, \tag{2.54}$$

where b is a material parameter that depends on the specific rubber system at hand. Lopez-Pamies, Goudarzi and Nakamura (2013); Lopez-Pamies, Goudarzi and Danas (2013) in their homogenisation approach alluded to earlier provide a more rigorous grounding for I_1-based amplification and suggest the following form for the amplification factor:

$$X = (1-f)^{-3.5}, \tag{2.55}$$

which yields similar predictions to the Guth-Gold expression for small volume fractions. This can be observed by considering the Taylor series expansion of Eq. (2.55).

The idea of using stretch amplification factors on the level of individual chains (where the chain stretch λ is amplified) was first suggested by Bueche (1960), who suggested an amplification factor based on kinematic grounds. By assuming that filler particles are rigid and that their spacing changes in a manner affine to the macroscopic deformation,

he finds that the effective chain stretch λ^s is given by:

$$\lambda^s = \frac{\lambda - f^{\frac{1}{3}}}{1 - f^{\frac{1}{3}}}, \tag{2.56}$$

which has subsequently been corroborated by X-ray scattering studies tracking the average displacement of filler particles (Rault et al., 2006). This approach has been followed in the literature in the context of full-network modelling by Dargazany and Itskov (2009, 2013).

While the stretch amplification factor should ideally be expressed in terms of microstructural material parameters, it is often expedient to simply treat it as a fitting parameter and forego any direct physical interpretation. This is the approach followed by Merckel et al. (2013) in order to achieve better agreement with experimental data.

2.5 Modelling damage and the Mullins effect

The basic framework for modelling the Mullins effect is damage mechanics. An internal variable is introduced to describe the damage state of the material. As the damage variable evolves, the effective elastic properties of the material drop, causing a Mullins effect to arise in the model. In phenomenological models, the internal variable has no physical interpretation, whereas in micromechanical models the internal variable is linked to some physical quantity and its evolution is linked to some physical mechanism.

Many of the early phenomenological frameworks for modelling the Mullins effect fall under the umbrella of continuum damage mechanics (CDM) (e.g. Simo (1987)), a framework originally developed for modelling the evolution of microscopic cracks in metals (Lemaitre and Chaboche, 1994). In this framework, the free energy of the system is proportional to the free energy of the undamaged system multiplied by a factor of $(1 - d)$, where d is a damage variable.

$$\Psi(\boldsymbol{F}, d) = (1 - d)\Psi(\boldsymbol{F}). \tag{2.57}$$

In the pristine state $d = 0$ and in a fully damaged state $d = 1$. Various criteria controlling the evolution of the damage variable have been proposed which each have different implications on the fitting performance of CDM models for the Mullins effect (Chagnon et al., 2004). Chagnon et al. (2004) note that, as the damage variable impacts the free energy multiplicatively in CDM models, the stress-strain curves during reloading obey a scaling relationship: all re-loading curves (which describe the material response at fixed extents of damage) are the same within a multiplicative factor. Unfortunately, real rubbers do not show this scaling property implying more sophisticated damage models are required to accurately capture the material response (Chagnon et al., 2004; Diani et al., 2009). A recent model from Zhan et al. (2023*a*) makes use of the chain level analogue of the damage rule (2.57):

$$\psi(\lambda) = (1 - d)\psi_0(\lambda), \tag{2.58}$$

where d is a damage variable associated with chains in a particular direction.

The pseudo-elastic approach is an alternative phenomenological approach proposed by Ogden and Roxburgh (1999). In their framework, the material response is effectively switched between a primary response (i.e. the virgin loading response) and a damaged response based on a damage variable which is equal to one in the former case and varies between zero and one during reloading processes.

$$\Psi(\boldsymbol{F}, d) = d\Psi_0(\boldsymbol{F}) + \phi(d). \tag{2.59}$$

While the damage variable in the pseudo-elastic approach varies during elastic processes and has no clear meaning, the modelling approach is popular and gets good agreement with experimental data for monotonic cyclic loading. The model was originally formulated in an isotropic setting and did not predict the accumulation of residual strain with Mullins softening, but has been extended to incorporate both anisotropy (Anssari-Benam et al., 2023; Anssari-Benam and Hossain, 2024), residual strain (Dorfmann and Ogden, 2004) and to occur alongside other physics (see e.g. Angela Mihai and Goriely (2020)).

Though these models may be well suited to describing the mechanical response of many rubbers following appropriate calibration against experimental data, they do not offer physical interpretation and or necessarily make reasonable predictions outside of the domain of the data they are calibrated against, and furthermore are often restricted to describing isotropic damage only. These shortcomings can be addressed in physical approaches for the Mullins effect. Various explanations for the physical origin of the Mullins effect have been put forward in the past and models have in turn sprung from each of these hypotheses (Diani et al., 2009).

Micromechanical models for the Mullins effect typically feature a damage variable on the level of the individual chain (or distribution of chains) that is related to a postulated mechanism for the Mullins effect. There is a long and at times seemingly contradictory history of investigations into the fundamental physical origins of the Mullins effect (Diani et al., 2009; Diaz et al., 2014; Zhan et al., 2024). The hypothesised mechanisms can generally be grouped into three categories depending on where the damage mechanism is believed to take place. Theories can be classified as polymer matrix theories (such as entanglement release (Hanson et al., 2005)), filler cluster theories (Klüppel and Schramm, 2000; Plagge and Klüppel, 2017) and filler-polymer theories (including bond breakage (Bueche, 1961), molecular slippage (Dannenberg, 1975) and surface adsorption/de-adsorption (Dannenberg and Brennan, 1966) theories). Modelling approaches for different supposed mechanisms can be similar and models for the Mullins effect general fall under the umbrella of those which treat the Mullins effect as a network breakdown, be it through polymer-filler processes or matrix processes, and those which treat it as a hard-to-soft phase transition following an early hypothesis from Mullins and Tobin (1957).

The hard-to-soft transition models assume that the rubber consists of a stiff phase and a soft phase and that softening arises from an increase in the proportion of soft phase at the expense of hard phase. This causes softening of the material by increasing the relative contribution to the free energy from the soft phase (with a reduction in the contribution from the hard phase) and through a decrease in the degree of stretch amplification in the

soft phase. Models of this type feature evolving stress amplification factors or effective volume fractions. Johnson and Beatty (1993) propose a one-dimensional model in this framework where the amplification factor is a function of the maximum stress previously applied to the material. A major development in models of this type comes from Qi and Boyce (2004, 2005), who model an evolving stretch amplification factor in an eight-chain model with I_1-based strain amplification. They suggest that the amplification factor depends on the effective volume fraction of hard phase through the Guth-Gold relationship (2.54) and write an evolution law for the effective volume fraction based on the historic maximum eight-chain stretch that the material has been subjected to:

$$\dot{f} = A(f_\infty - f)\frac{\Lambda_L - 1}{(\Lambda_L - \lambda_{\max})^2}\dot{\lambda}_{\max}, \tag{2.60}$$

which has subsequently been adopted by Wang and Chester (2018) in a Mullins effect model with thermal recovery and Alkhoury et al. (2024) in a coupled Mullins softening and viscoelasticity model.

The effect of the break up of filler clusters has also been modelled through evolving stretch amplification factors or evolving distribution of amplification factors. Plagge and Klüppel (2017) suppose that filler clusters cause varying degrees of stretch amplification in the rubber network, which entails that the free energy function is given the following integral:

$$\Psi(I_1 - 3, I^* - 3, X_{\max}) = \int_{X_{\min}}^{X_{\max}} P_X(X)\Psi_X(X(I_1 - 3), X(I^* - 3))dX, \tag{2.61}$$

where P_X is the fraction of rubber under degree of amplification X per unit volume, Ψ_X is the free energy density and $I^* := (\lambda^{(1)})^\beta + (\lambda^{(2)})^\beta + (\lambda^{(3)})^\beta$ is an invariant term that appears in the free energy function of their underlying rubber matrix. In their model, the maximum amplification factor $X_{\max}$ decreases as filler clusters breakdown, giving rise to softening.

A landmark model following the network breakdown theory is that of Govindjee and

Simo (1991). They propose the splitting the free energy of the system into a contribution from chains than span from crosslink to crosslink in the network (the CC contribution) and a contribution from chains that connect filler particles to filler particles (the PP contribution). Damage arises from the debonding of chains spanning between filler particles, affecting the latter contribution to the free energy. In their theoretical formulation, chains cease to contribute to the free energy once they have been stretched to their contour length, reflecting the chains tearing free from the particle surfaces when overly extended. Following the Govindjee and Simo (1991) model, Miehe and Göktepe (2005) construct a microsphere model assuming the same damage mechanism in a filler-filler chain contribution to the free energy, with a chain level phenomenological damage parameter. The filler-filler contribution is parallel to a pure network contribution which follows from a p-root averaged full network model with a tube contribution.

Dargazany and Itskov (2009) advance this framework by considering the variation in chain length in the particle-particle network. In a given direction, the chains that connect particles together vary in their contour length but are assumed to be stretched by the same amount for a given macroscopic deformation. Dargazany and Itskov (2009) argue that the chains debond from the particles in order from shortest-to-longest. They parameterise the chain length distribution in each direction and assume that the lower bound increases to reflect chain desorption or sliding processes. This means that the directional free energy ψ is expressed through the following integral:

$$\psi(\lambda, \lambda_m) = \int_{h(\lambda_m)}^{N_m} n(\lambda_m) p(N) \psi(\lambda, N) dN, \tag{2.62}$$

where N is the number of Kuhn segments per soft chain, $n(\lambda_m)$ is the number of chains per unit volume in a particular direction, $p(N)$ is the proportion of chains with N segments in the pristine state and λ_m is the maximum stretch chains in a particular direction have ever experienced. In a later work, Dargazany and Itskov (2013) extend the network decomposition to include a particle-crosslink contribution in addition to the crosslink-crosslink and particle-particle contributions to account for the breakup and reformation

of filler aggregates. This gives rise to further hysteresis in the material response. Itskov and Knyazeva (2016) consider a more physically-sound representation of the distribution $p(N)$ based on a generalisation of the Flory distribution of chain length that arises in a random polymerisation process.

Another modelling concept which has been widely followed in the literature is the network alteration theory (Marckmann et al., 2002). The network alteration theory explains the Mullins effect through the breakdown of crosslinks or effective crosslinks in the network without being specific about their precise physical meaning (e.g. whether true crosslinks between chains are broken, filler-polymer bonds are broken or entanglements are released). Consider a crosslink between two separate polymer strands. From a mechanical point of view, there are four chains that meet at this crosslink. When the crosslink breaks, the four chains become two disconnected chains that are now longer. Based on these considerations, Marckmann et al. (2002) suggest that the mechanism for the Mullins effect can be modelled through a process where the average chain length increases. This causes softening as longer chains are have a higher extensibility limit and so are more compliant than shorter chains at large stretches. The breaking of the links between chains also causes a decrease in the number of chains per unit volume in the material. The authors suggest that the increase in chain length and decrease in chain density are balanced such that the total number of elastically active monomers per unit volume remains constant i.e.:

$$n(t)N(t) = n_0 N_0. \tag{2.63}$$

This concept has been invoked in a number of later Mullins effect models, including those of Chagnon et al. (2006), Diani et al. (2006), Diani and Le Tallec (2019), Xiao et al. (2021), Zhan and Xiao (2022) amongst others.

2.6 Viscoelasticty and viscoplasticity

The mechanical response of most rubbers shows some rate-sensitivity. This is classically addressed in the theory of finite viscoelasticity following a multiplicative split of the

deformation gradient into elastic and viscous parts:

$$\boldsymbol{F} = \boldsymbol{F}^e \boldsymbol{F}^v, \tag{2.64}$$

and by postulating flow rules for the evolution of the viscous part of the deformation gradient (see the framework of Reese and Govindjee (1998)). In the context of rubber-modelling, phenomenological expressions are often followed for the evolution of the viscous part of the deformation gradient, though some concepts from the field of polymer physics have been introduced to this framework. Bergström and Boyce (2000) propose a flow rule based on the Doi-Edwards reptation theory (Doi and Edwards, 1988), where the viscous strain is related to the release of dangling strands and loops in the rubber network. Another physical concept for rubber viscoelasticity is the transient network theory of Green and Tobolsky (1946), where the formation and breaking of crosslinks in the network gives rise to the time-dependent behaviour of the material.

The micromechanical approach has also been applied to the problem of rubber viscoelasticity, where the elastic network theory is extended in either phenomenological or physical ways to account for viscous effects. A simple extension to viscoelasticity can be achieved by adding a dashpot element parallel to the rubber chain, similarly to the spring-dashpot analogy used for macroscopic viscoelasticity (Göktepe and Miehe, 2005; Linder et al., 2011; Govindjee et al., 2019; Bresolin and Vassoler, 2022). In this case, the chain stretch is split into viscous λ^v and elastic parts λ^e:

$$\lambda = \lambda^e \lambda^v, \tag{2.65}$$

The multiplicative decomposition of stretch implies the additive split of the logarithmic stretch rate d into elastic and viscous parts d^e and d^v respectively:

$$d = d^e + d^v, \tag{2.66}$$

where $d^{()} = \dot{\lambda}^{()}/\lambda^{()} = \overline{\log \lambda^{()}}^{\cdot}$. The free energy features an additional contribution from

the viscoelastic branch:

$$\psi(\lambda, \lambda^e) = \psi^{(1)}(\lambda) + \psi^{(2)}(\lambda^e). \tag{2.67}$$

It should be noted that this is one possible formulation of viscoelasticity of many, and various free energy decompositions may be chosen. We follow this formulation for illustration. Some thermodynamically-consistent rule must be written to describe the evolution of the viscous stretch to render the framework complete. To this end, we may consider the thermodynamic inequality and identify the thermodynamic forces conjugate to $\dot{\boldsymbol{F}}$ and d^v:

$$\dot{\Psi} - \boldsymbol{P} : \dot{\boldsymbol{F}} = \left\langle \frac{\partial \psi^{(1)}}{\partial \lambda}\dot{\lambda} + \frac{\partial \psi^{(2)}}{\partial \lambda^e}\dot{\lambda}^e \right\rangle - \boldsymbol{P} : \dot{\boldsymbol{F}}, \tag{2.68}$$

$$= \left\langle \left(\frac{\partial \psi^{(1)}}{\partial \lambda} + \frac{\partial \psi^{(2)}}{\partial \lambda^e}\frac{\lambda^e}{\lambda} \right) \frac{\partial \lambda}{\partial \boldsymbol{F}} \right\rangle : \dot{\boldsymbol{F}} - \left\langle \left(\lambda^e \frac{\partial \psi^{(2)}}{\partial \lambda^e} d^v \right) \right\rangle - \boldsymbol{P} : \dot{\boldsymbol{F}}, \tag{2.69}$$

where we have made us of the relation between stretch rates $\dot{\lambda}^e = \lambda^e(\dot{\lambda}/\lambda - \dot{\lambda}^v/\lambda^v) = \lambda^e(d - d^v)$ and assumed that $\lambda = \lambda(\boldsymbol{F}, \boldsymbol{n})$. Considering the thermodynamic inequality and applying the Coleman-Noll procedure (e.g. requiring the inequality to hold for all virtual deformations $\{\dot{\boldsymbol{F}}, d^v\}$ and be a strict equality during elastic processes), we recover the state law for stress (factoring in the incompressibility constraint):

$$\boldsymbol{P} = \left\langle \left(\frac{\partial \psi^{(1)}}{\partial \lambda} + \frac{\partial \psi^{(2)}}{\partial \lambda^e}\frac{\lambda^e}{\lambda} \right) \frac{\partial \lambda}{\partial \boldsymbol{F}} \right\rangle - P\boldsymbol{F}^{-T}, \tag{2.70}$$

and the following inequality for dissipation:

$$\left\langle \frac{\partial \psi^{(2)}}{\partial \lambda^e}\lambda^e d^v \right\rangle \geq 0, \tag{2.71}$$

which must be satisfied for any virtual deformation. It must therefore hold locally (in each direction individually):

$$\frac{\partial \psi^{(2)}}{\partial \lambda^e}\lambda^e d^v \geq 0. \tag{2.72}$$

The framework of Generalised Standard Materials (GSM) (see Halphen and Son Nguyen (1975); Germain et al. (1983)) is called upon to ensure this condition is satisfied. A

dissipation potential $\phi(d^v)$ is introduced. In the original GSM framework, the inelastic driving force derives from the potential:

$$\frac{\partial \psi^{(2)}}{\partial \lambda^e} \lambda^e = \frac{\partial \phi}{\partial d^v}. \tag{2.73}$$

By imposing the conditions that the ϕ is convex, non-negative and passes through the origin, the thermodynamic inequality is satisfied:

$$\frac{\partial \psi^{(2)}}{\partial \lambda^e} \lambda^e d^v = \frac{\partial \phi}{\partial d^v} d^v \geq 0. \tag{2.74}$$

Models of this framework include that of Miehe and Göktepe (2005) who propose the use of a general power-law expression for the viscous potential:

$$\phi = \frac{a}{\eta(1+a)} \left(\eta |d^v|\right)^{(1+a)/a}, \tag{2.75}$$

which achieves good agreement with their experimental data for a filled hydrogenated nitrile rubber. A similar expression is later used by Govindjee et al. (2019) and Bresolin and Vassoler (2022) in their variational full-network frameworks. While this viscoelastic overstress is implemented in the micromechanical framework, it does not relate to specific deformation mechanisms and is phenomenological in nature, and it is generally introduced from a theoretical standpoint with limited comparisons to experimental data.

Chapter 3

Micromechanical modelling of filled rubbers and thermoplastic elastomers

3.1 Introduction

In this Chapter, a micromechanical model for filled rubbers, thermoplastic elastomers and similar two-phase elastomer systems is presented. While these materials may vary in their chemistry, from a mechanical perspective they have a great deal in common, sharing similar microstructures and displaying a number of the same mechanical behaviours, including damage phenomena such as the Mullins effect. These grounds motivate us to present a common modelling framework for these systems with sufficient generality to capture the details of the mechanics of each individual system. The framework is specialised in turn to filled rubbers and thermoplastic polyurethanes (TPUs).

In the past, some models have been developed for the mechanical behaviour of thermoplastic elastomers but modelling frameworks which generalise the behaviour of both filled rubbers and thermoplastic elastomers have not previously been investigated. Furthermore, existing TPE models often have loose connections to physical parameters and are not always suitable for finite element analyses as they do not capture all of the necessary behaviours of TPEs under finite deformation conditions (see e.g. Hotta et al. (2002); Buckley et al. (2011); Fernandes Arruebarrena (2016)), or are too computationally ex-

pensive to be used in simulations of real world problems (e.g. molecular dynamics models Aoyagi (2016); Kodama et al. (2024)). Constitutive models for TPEs include that of Qi and Boyce (Qi and Boyce, 2004, 2005) previously mentioned in Section 2.5 which focusses on describing the Mullins effect through an evolving stretch amplification concept. A later model was developed by the same group following a network alteration hypothesis (Cho et al., 2017). While both of these models are able to fit experimental data for TPEs reasonably well and describe the material response in a general setting, the models require complete re-fitting to the experimental data when any material parameters (in particular the hard phase volume fraction) are changed. Another TPE modelling framework was developed by Drozdov (2006); Drozdov and Christiansen (2007) based on the transient description of network junctions (where viscoelastic chain pull-out processes occur). They consider Gaussian chains and invoke statistical arguments to impose the excluded volume effect arising from hard domain presence. The model achieves good fit for moderate deformations but does not incorporate chain limiting extension effects so is not suitable for large deformation. Furthermore, the model does not describe the Mullins effect in TPEs. Other models have been developed for specific aspects of the mechanical response of TPEs, such as the Mullins effect in one dimension (Buckley et al., 2011) and the stress relaxation response (Hotta et al., 2002), but are not trivially extended to general loading conditions. There are additionaly further models neglect important aspects of the material response such as the Mullins effect (Yu et al., 2010; Wang et al., 2020).

Here, a micromechanical framework is introduced to address these deficits. The Generalised Standard Materials (GSM) approach is followed to describe inelastic behaviour on the chain level. Stretch amplification is used to describe the effects of hard phase volume fraction on the material response. A specialisation of the framework to filled rubbers is then carried out, and from comparisons to experimental data the fitting performance of the model is evaluated. Deficits of the model in describing the response of rubbers under general loading conditions are motivation for the study on tube models of rubber elasticity in Chapter 4, and deficits in predicting the anisotropy of the Mullins effect serve as motivation for work of Chapter 6. A separate specialisation is carried out with respect

to thermoplastic polyurethanes and the ability of the model to predict changes in the mechanical response with varying hard phase volume fraction in relation to experimental data is evaluated.

3.2 Framework

We will begin with some general considerations for modelling composite materials. Consider a representative volume element (RVE) of the material subjected to a deformation gradient $\boldsymbol{F}$. The volume average free energy density of the system is a function of $\boldsymbol{F}$ and a list of possible internal variables ξ_i and can be expressed as a sum of the volume average over each phase. Specifically for filled rubbers and TPEs, the free energy density of the system Ψ is the sum of the volume average free energy density in the soft phase Ψ^s and the volume average free energy density in the hard phase Ψ^h, each weighted by their respective volume fractions (Hill, 1963):

$$\Psi(\boldsymbol{F}, \xi) = (1 - f)\Psi^s + f\Psi^h, \tag{3.1}$$

where f is the hard phase volume fraction.

Due to the stiffness disparity between the soft rubbery phase and the near rigid hard phase, it can be assumed that the hard phase effectively does not deform. As the hard does not deform (i.e. no strain or change in strain occurs with macroscopic deformation), the contribution to the elastic free energy from the hard phase can be taken as an arbitrary constant and be set to zero. This means that the free energy depends only on the soft phase free energy:

$$\Psi = (1 - f)\Psi^s. \tag{3.2}$$

We follow the micromechanical approach and assume that in the soft phase, all chains with the same orientation are subjected to the same stretch and have the same properties. This allows the contribution to the free energy to be written as the orientational average

of all of the chains in the system:

$$\Psi^s = \frac{1}{4\pi}\int_{\mathcal{S}} \psi^s(\lambda, \xi_i) d\mathcal{S}, \tag{3.3}$$

where ψ^s is the total contribution to the free energy from all chains in the reference direction $\boldsymbol{n}$. The stretch of the soft segments λ is a function of the deformation gradient and the reference orientation $\boldsymbol{n}$:

$$\lambda = \lambda(\boldsymbol{F}, \boldsymbol{n}). \tag{3.4}$$

3.2.1 Kinematics

Another implication of treating the hard phase as rigid is that deformation of the soft phase is larger than the macroscopic deformation (as discussed in Section 2.4). This can be accounted for in the micromechanical relationship through the functional form of Eq. (3.4), which we will specify based on considerations of the material microstructure. There are three kinematic measures on three different lengthscales that should be considered. The chain stretch λ is a true measure of chain deformation, considering the ratio of the current end-to-end distance of the chain r to the reference end-to-end distance r_0:

$$\lambda = \frac{r}{r_0}. \tag{3.5}$$

The stretch Λ represents the change in length of the vector spanning the centres of hard domains:

$$\Lambda = \frac{R}{R_0}, \tag{3.6}$$

where R and R_0 are respectively the current and reference distance between the centres of two hard domains. The continuum line stretch $\bar{\lambda}$ is the change in length of a unit vector $\boldsymbol{n}$ embedded in a continuum medium deformed by deformation gradient $\boldsymbol{F}$:

$$\bar{\lambda} = |\boldsymbol{F}\boldsymbol{n}|. \tag{3.7}$$

We assume that the filler centres are transplaced affinely with the macroscopic deformation:

$$\Lambda = \bar{\lambda}. \tag{3.8}$$

The fact that the fillers are effectively rigid and are connected together by rubbery chains can be used to relate these deformation measures. Using the geometry depicted in Fig. 3.1, observe that the distance between the centres of two filler particles is the sum of the filler diameter D and the current chain end-to-end distance:

$$R = D + r, \tag{3.9}$$

which implies that the reference quantities follow the relation $R_0 = D + r_0$. If fillers are not perfectly spherical, D can be interpreted as characteristic lengthscale for the particles. As the fillers are rigid, D is deformation independent. The current configuration quantities in Eq. (3.9) can be replaced with stretches and reference quantities using Eqs. (3.5)-(3.6) to give:

$$\lambda = (\Lambda - 1)\frac{R_0}{r_0} + 1, \tag{3.10}$$

which is a simple relation between the chain stretch λ and the particle-particle stretch Λ. As discussed in Section 2.4, rules of this form were first proposed by Bueche (1961) and have been experimentally verified (Rault et al., 2006) and used in a variety of models (see e.g. Dargazany and Itskov (2009)). However, there is a problem with Eq. (3.10) under compression ($\Lambda < 1$) - it can predict negative chain stretches (depending on the magnitude of Λ and R_0/r_0), which are inadmissible.We modify Eq. (3.10) to follow a power law under compression to bypass this problem, such as that used by Merckel et al. (2013). The exponent of the power law is chosen to ensure the rule is smooth and continuous

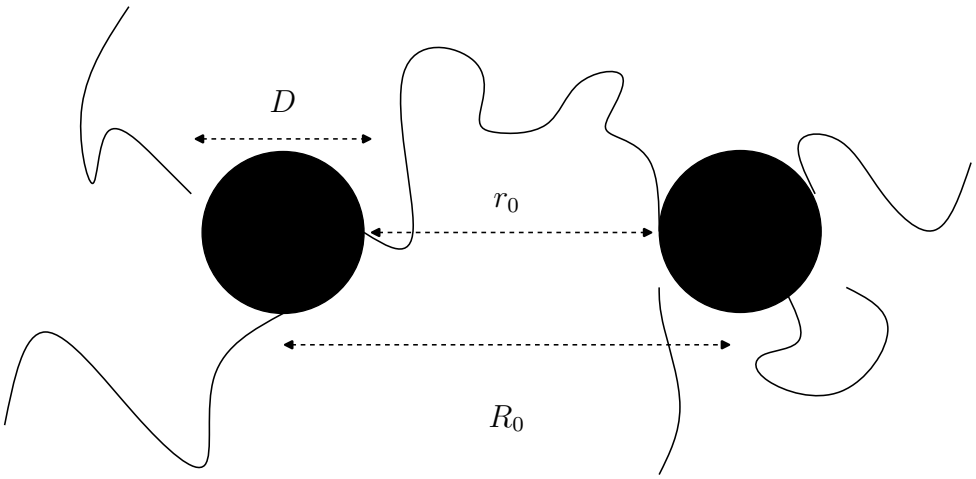


Figure 3.1: Hard inclusions/filler particles within soft matrix. Rubbery chains with reference end-to-end distance r_0 connect particles of diameter D together.

around $\Lambda = 1$.

$$\lambda = \begin{cases} \frac{R_0}{r_0}(\Lambda - 1) + 1 & \Lambda \geq 1, \\ \Lambda^{\frac{R_0}{r_0}} & \Lambda < 1. \end{cases} \tag{3.11}$$

By assuming a lattice-like arrangement of fillers, we can relate the ratio R_0/r_0 to the volume fraction:

$$\frac{R_0}{r_0} = \frac{1}{1 - \left(\frac{6f}{n\pi}\right)^{\frac{1}{3}}}. \tag{3.12}$$

This follows from the assumption that there are n spherical fillers within a cubic unit cell of edge length R_0:

$$f = \frac{\pi n}{6} \frac{(R_0 - r_0)^3}{R_0^3}. \tag{3.13}$$

Note that n can be treated as a fitting parameter when fillers do not follow a well-ordered arrangement.

3.2.2 Thermodynamics

We model a variety of inelastic behaviours (such as viscoelasticity, viscoplasticity and damage) on the microscale. We follow the Generalised Standard Materials (GSM) frame-

work (Halphen and Son Nguyen, 1975; Germain et al., 1983) to define these behaviours, which we shall now outline in a general sense. Under isothermal processes, the relevant thermodynamic inequality reads:

$$\dot{\Psi} - \boldsymbol{P} : \dot{\boldsymbol{F}} \leq 0. \tag{3.14}$$

Introducing the microscopic soft phase free energy through Eqs. (3.2) and (3.3), the left hand side becomes:

$$\dot{\Psi} - \boldsymbol{P} : \dot{\boldsymbol{F}} = (1-f)\left\langle \frac{\partial \psi^s}{\partial \lambda}\frac{\partial \lambda}{\partial \boldsymbol{F}} : \dot{\boldsymbol{F}} + \frac{\partial \psi^s}{\partial \xi_i}\dot{\xi}_i \right\rangle - \boldsymbol{P} : \dot{\boldsymbol{F}}, \tag{3.15}$$

$$= \left((1-f)\left\langle \frac{\partial \psi^s}{\partial \lambda}\frac{\partial \lambda}{\partial \boldsymbol{F}} \right\rangle - \boldsymbol{P} \right) : \dot{\boldsymbol{F}} + (1-f)\left\langle \frac{\partial \psi^s}{\partial \xi_i}\dot{\xi}_i \right\rangle. \tag{3.16}$$

We follow the Coleman-Noll procedure to determine state laws and thermodynamic restrictions on dissipative processes. Considering arbitrary virtual deformations $\{\dot{\boldsymbol{F}}, \dot{\xi}_i\}$ at any current state of the system, the state law for stress (factoring in the incompressibility constraint giving to the hydrostatic pressure P) is derived:

$$\boldsymbol{P} = (1-f)\left\langle \frac{\partial \psi^s}{\partial \lambda}\frac{\partial \lambda}{\partial \boldsymbol{F}} \right\rangle - P\boldsymbol{F}^{-T}, \tag{3.17}$$

and furthermore the following inequality for dissipation is also derived:

$$-\left\langle \frac{\partial \psi^s}{\partial \xi_i}\dot{\xi}_i \right\rangle \geq 0, \tag{3.18}$$

which must be satisfied for any virtual deformation. That is, it must hold in each direction individually and for each inelastic mechanism:

$$-\frac{\partial \psi^s}{\partial \xi_i}\dot{\xi}_i \geq 0 \qquad \text{(no summation)}. \tag{3.19}$$

Following the Generalised Standard Materials framework, which is outlined for the specific case of viscoelasticity in Section 2.6, a dissipation potential $\phi(\dot{\xi}_i)$ from which the driving

forces conjugate to the internal variables derive is introduced:

$$-\frac{\partial \psi^s}{\partial \xi_i} = \frac{\partial \phi}{\partial \dot{\xi}_i}. \tag{3.20}$$

Requiring the dissipation potential ϕ to be convex, non-negative and pass through the origin ensures that the thermodynamic inequality is satisfied:

$$-\frac{\partial \psi^s}{\partial \xi_i}\dot{\xi}_i = \frac{\partial \phi}{\partial \dot{\xi}_i}\dot{\xi}_i \geq 0 \qquad \text{(no summation)}. \tag{3.21}$$

Alternatively, the flux of the internal variable can be determined through a variational principle equivalent to the condition (3.21) following Ortiz and Stainier (1999):

$$\inf_{\dot{\xi}_i} \left\{ \dot{\psi}^s + \phi \right\}. \tag{3.22}$$

One easily verifies that the stationary conditions are equivalent to (2.74). The variational principle is convenient for the formulation of incremental constitutive updates, as shown in Appendix A.

3.3 Application to filled rubbers

3.3.1 Specialisation of the constitutive response

To specialise the framework to filled rubbers, it remains to identify the relevant deformation mechanisms and define the directional potentials ψ^s and ϕ corresponding to these mechanisms, which are orientationally averaged to yield the macroscopic constitutive relation for the material, Eq. (3.3). We will focus on describing the Mullins effect in filled rubbers and follow a network alteration assumption - that softening results from a breakdown of effective crosslinks in the network, increasing the number of segments per elastically active chain - to explain the effect. The state of the chain is then described by two state variables, the chain stretch λ and a damage parameter ξ, which imply that ϕ

and ψ^s have the following dependence:

$$\psi^s = \psi^s(\lambda, \xi), \quad \phi = \phi(\dot{\xi}, \xi), \tag{3.23}$$

where $\xi = 0$ corresponds to the pristine state. In contrast to some damage model formulations (see e.g. Lemaitre and Chaboche (1994)), we do not link $\xi = 1$ to a fully damaged state but allow ξ to increase indefinitely. We follow the freely-jointed chain model for the free energy function where the number of segments in the chain is a function of the damage variable ξ following the network alteration hypothesis. As the free energy ψ^s is the free energy density contribution in the reference direction $\boldsymbol{n}$, the freely-jointed chain model is weighted by n, the number of chains per unit volume with reference orientation $\boldsymbol{n}$. Following Marckmann et al. (2002), we include the constraint that the number of chains in a particular direction decreases when effective crosslinks break such that the total number of Kuhn segments per unit volume is constant. This is reflected in the product of n and the number of Kuhn segments per chain i.e. $n(\xi)N(\xi) = n_0 N_0$. The free energy then becomes:

$$\psi^s(\lambda, \xi) = n_0 N_0 k_B T \left(\beta \frac{\lambda r_0}{N(\xi) b} + \log \frac{\beta}{\sinh \beta} \right), \quad \beta = \mathcal{L}^{-1} \left(\frac{\lambda r_0}{N(\xi) b} \right). \tag{3.24}$$

We furthermore assume that the reference length of the chains is given by their average when undergoing an unconstrained random walk in the pristine state:

$$r_0 = \sqrt{N_0} b, \tag{3.25}$$

and does not evolve as damage occurs. We invoke a general form of the dissipation potential:

$$\phi(\dot{\xi}, \xi) = \begin{cases} \Gamma(\xi)\dot{\xi} & \dot{\xi} \geq 0, \\ +\infty & \dot{\xi} < 0, \end{cases} \tag{3.26}$$

where $\Gamma(\xi)$ will be specified later. This form of the dissipation potential in combination with the variational principle dictates that the evolution of ξ is irreversible (i.e. ξ can

only increase). The dissipation potential is infinite when $\dot{\xi} < 0$. The energy functional is therefore never minimised for negative $\dot{\xi}$ and such values are prohibited in the framework. As only damage evolutions where $\dot{\xi} \geq 0$ are admitted in the model, the damage process is always progressive.

Using the specific form of the dissipation potential, the variational principle implies that the following functional is minimised with respect to $\dot{\xi}$:

$$J(\dot{\xi}) = \left(\frac{\partial \psi^s}{\partial \xi} + \Gamma(\xi) \right) \dot{\xi}. \tag{3.27}$$

Taking into account the prohibition of negative $\dot{\xi}$, the variational principle dictates that when damage occurs, it is such that:

$$\frac{\partial \psi^s}{\partial \xi} + \Gamma(\xi) = 0, \tag{3.28}$$

which is independent of $\dot{\xi}$ and does not for a given state (described by λ and ξ) allow $\dot{\xi}$ to be determined immediately. Some light can be shed on this and on the role of the function $\Gamma(\xi)$ by considering the sign of the term $\partial J/\partial \dot{\xi} = \partial \psi^s/\partial \xi + \Gamma(\xi)$ which enters the functional (3.27). If the current state of the material is such that $\partial J/\partial \dot{\xi} < 0$, the infimum conditions imply $\dot{\xi} \to \infty$. An instantaneous damage process occurs that brings the state of the material to satisfy the condition $\partial J/\partial \dot{\xi} = 0$. If $\partial J/\partial \dot{\xi}$ is positive, the minimising value of $\dot{\xi}$ is zero (as $\dot{\xi} < 0$ is prohibited) and no damage occurs. These inequalities mean that $\partial J/\partial \dot{\xi}$ acts like a yield surface, with $\Gamma(\xi)$ mirroring the yield strength (including hardening) and $-\partial \psi^s/\partial \xi$ acting like the effective stress.

Owing to the progressive nature of the damage process, we expect that the function $\Gamma(\xi)$ will either grow with damage or remain constant as ξ increases:

$$\frac{d\Gamma}{d\xi} \geq 0. \tag{3.29}$$

For simplicity, we assume a linear form of $\Gamma(\xi)$:

$$\Gamma(\xi) = \Gamma_0 + \alpha\xi. \tag{3.30}$$

The internal variable evolution is connected to N through the following relation:

$$N(\xi) = N_{ss} - (N_{ss} - N_0)\exp(-\xi), \tag{3.31}$$

where N_{ss} and N_0 are respectively the steady state and initial numbers of Kuhn segments per chain. The rule (3.31) implies that in the pristine state, the chain has N_0 segments per chain and tends towards N_{ss} as damage progresses. Owing to the network alteration theory of Marckmann et al. (2002), it is implied that $n(\xi)$ drops during this process.

The relation (3.31) together with the chain free energy function implies the following inequality:

$$\frac{\partial^2\psi^s}{\partial\lambda\partial\xi} < 0, \tag{3.32}$$

which implies that the chain force $\partial\psi^s/\partial\lambda$ drops as damage occurs, which is of course partly by design in this model. It is interesting to note that the conditions in Eqs. (3.29) and (3.32) together with the variational principle imply that damage only occurs when chain stretch reaches a value greater than any value it has previously reached:

$$\dot{\xi} > 0 \iff \lambda(t) = \max_{\tau\in[0,t]} \lambda(\tau). \tag{3.33}$$

To illustrate the meaning of this model on a chain level, we plot the number of Kuhn segments (normalised by N_0) associated with particular maximum stretch in Fig. 3.2. We fix the free energy related parameters $N_0 = 11$, $N_{ss}/N_0 = 1.5$, $n_0 k_B T = 1$ MPa and vary the dissipative parameters, Γ_0 and α, from baseline values of $\Gamma_0 = -\partial\psi^s(1,0)/\partial\xi$ (the driving force for damage evaluated in the pristine undeformed state) and $\alpha = 0$ to show their impact on the relationship between N and the maximum stretch. From Eq. (3.28), it can be seen that setting $\Gamma_0 \geq -\partial\psi^s(1,0)/\partial\xi$ ensures that no damage occurs without

deformation. We only consider Γ_0 in compliance with this constraint and introduce the quantity $\Delta\Gamma_0$, defined through:

$$\Delta\Gamma_0 := \Gamma_0 - \partial\psi^s(1,0)/\partial\xi, \tag{3.34}$$

for readability.

The choice of the parameters Γ_0 and α has a significant impact on the evolution of N. Fig. 3.2 shows that the parameter Γ_0 acts like a damage threshold: the maximum stretch must surpass a particular value controlled by Γ_0 for damage to occur. Increasing Γ_0 increases this value. The parameter α controls the degree of softening that occurs for a given maximum stretch. As α increases, the amount of damage that occurs for a given stretch is greater. Both parameters can significantly alter the shape of the curve, changing it from concave to convex. Ultimately, the relation (3.31) limits the maximum value of N to N_{ss} and it appears that regardless of the specific choice of Γ_0 and α, N_{ss} is reached at around a stretch $\lambda^c_{max} = 4$.

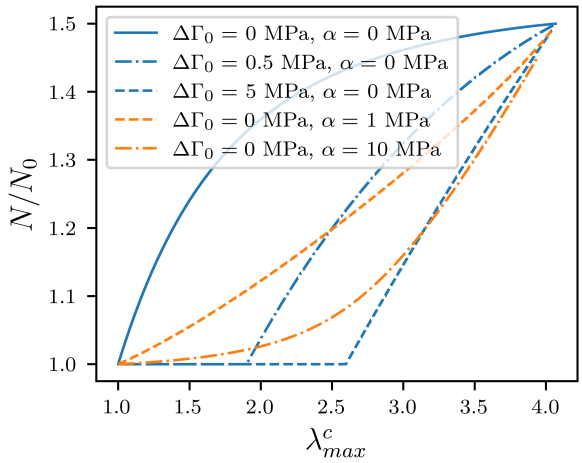


Figure 3.2: Evolution of Kuhn segments with different damage model parameters.

As the chain level behaviour has been specified, the model is now closed and the macroscopic material behaviour is found from the orientational average of the chain behaviour

following Eq. (3.3). Equation (3.17) implies that the first Piola-Kirchhoff stress reads:

$$\boldsymbol{P} = (1-f)\left\langle \frac{\partial \psi^s}{\partial \lambda^s}\frac{\partial \lambda^s}{\partial \boldsymbol{F}} \right\rangle - P\boldsymbol{F}^{-T}, \tag{3.35}$$

where the derivative $\partial\psi^s/\partial\lambda^s$ is found from Eq. (3.24) and the state of each chain is updated following Eq. (3.28). We will now consider the identification of material parameters and then evaluate the predictions of the model in relation to experimental data for a family of filled rubbers.

3.3.2 Comparison to experimental data

We compare the model predictions to the data of Diani and Le Tallec (2019) for carbon black filled styrene butadiene rubbers subjected to cyclic uniaxial tension. Four rubbers of 30, 40, 50 and 60 phr (per hundred rubber - the mass of filler in the system relative to the mass of polymer) are considered. These mass-related fractions correspond to filler volume fractions of approximately 0.16, 0.20, 0.24 and 0.28 respectively. They are cycled to progressively higher stretches and demonstrate the Mullins effect. The experimental data are not reported alongside error bars or further statistical information and it is not clear how much noise the data contain.

The model is fitted to the stress-strain response of the 30 phr and 40 phr rubbers simultaneously using a trial-and-error method and the responses of the higher volume fraction rubbers are predicted. Data for rubbers at two different volume fractions are needed for calibration of the parameter n which relates the volume fraction to the degree of stretch amplification. To fit the data, physically reasonable values were picked for the parameters $n_0 k_B T$, N_0 and $N_s s$ and the damage parameters were set such that damage initiates as soon as the material is deformed from the pristine state ($\Delta\Gamma = 0$ MPa) and without hardening ($\alpha = 0$ MPa). The resulting model responses were then compared to the experimental data visually and adjusted to improve the response. The adjustment of the parameters was based on parametric studies (not shown) which indicate the role of different parameters on the material response. The parameter $n_0 k_B T$ controls the (pristine)

$n_0 k_B T$	N_0	N^{ss}	$\Delta\Gamma_0$	α	n
0.38 MPa	5	21.25	0 MPa	1.9 MPa	1.27

Table 3.1: Parameters for model calibrated against Diani and Le Tallec (2019) data for 30 and 40 phr carbon filled styrene butadiene rubbers undergoing cyclic uniaxial tension.

initial elastic stiffness of the material and was adjusted to change the overall slope of the stress-strain response. The parameters N_0 and N_{ss} control the stretch at which there is an upturn in the stress-stretch response. The damage parameter α influences the hysteresis loop observed and n controls the scaling of the material response across different volume fractions. The resulting best-fit parameters are listed in Table 3.1.

The fits and predictions of the model stress-strain response are shown in Fig. 3.3 alongside the data of Diani and Le Tallec (2019). The model is able to fully capture the cyclic response of the material at lower volume fractions. The changes in the slope of the stress-stretch curve and size of the hysteresis loops are close to the experimental response. A slight upturn in the response at larger stretches is also reproduced. Moving to higher volume fractions, the model predicts an increase in stiffness with the proportion of filler that is consistent with the experimental data however the model underpredicts the hysteresis at larger stretches. There are various possible explanations for why the model underpredicts this hysteresis. The model assumes that the mechanism of damage is essentially the same at all volume fractions and is only more pronounced at higher volume fractions because of stretch amplification. In reality, the volume fraction may influence the damage mechanism through additional effects, e.g. by increasing the amount of filler-polymer interactions (due to increased surface area of filler particles) or through the breaking up or alteration of the filler particle network. These dependencies could potentially be incorporated in the framework through introducing volume fraction dependence on the specific forms of the potentials chosen in the specialisation of the model, thought more work needs to be done to determine appropriate forms either empirically or from physical considerations.

Another aspect of the model response that we shall consider is the anisotropy of the softening, which can be demonstrated in uniaxial tensile tests conducted in sequentially

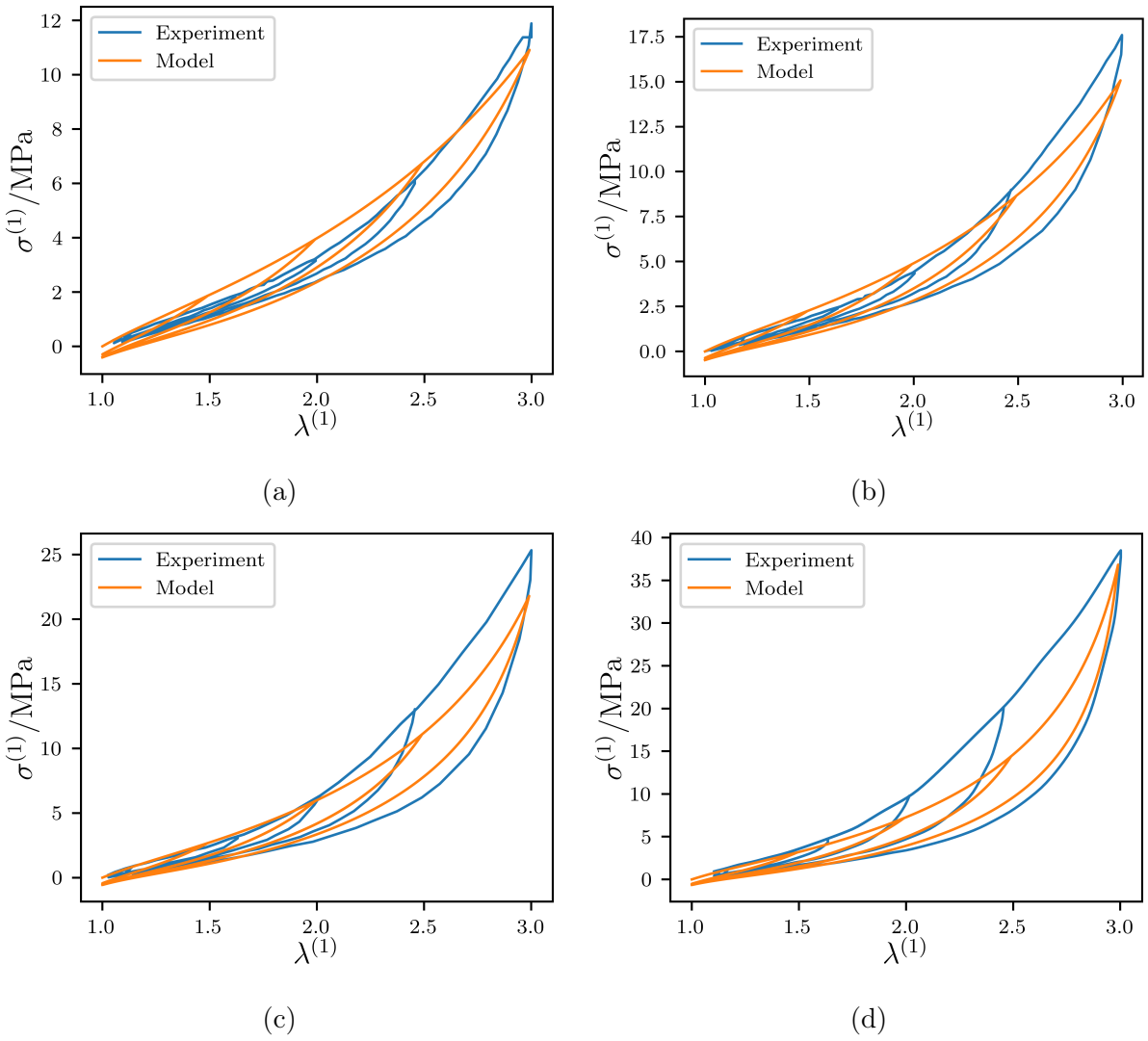


Figure 3.3: Model predictions against experimental data of Diani and Le Tallec (2019) for response of carbon black filled styrene butadiene rubbers. The rubbers contain filler particles in the proportions (a) 30 phr (b) 40 phr (c) 50 phr and (d) 60 phr corresponding to volume fractions of approximately 0.16, 0.20, 0.24 and 0.28 respectively.

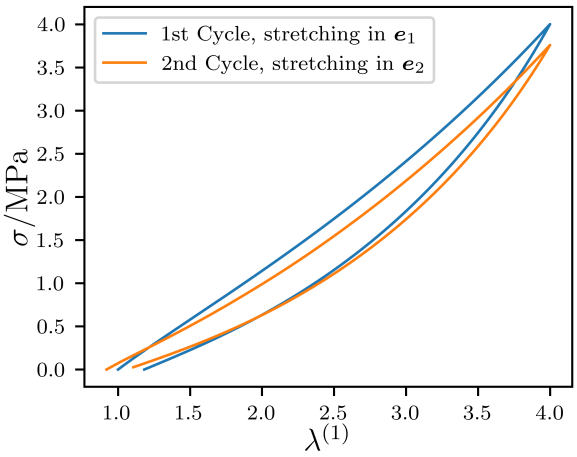


Figure 3.4: Model response for material subjected to uniaxial tension (UT) in direction $\boldsymbol{e}_1$ followed by $\boldsymbol{e}_2$ (orthogonal to the original stretching direction). The model predicts that UT induces softening not only in the stretching direction but also in the transverse directions.

different directions. The stress-stretch response during such a loading scenario for the 40 phr carbon black-filled SBR is shown in Fig. 3.4. In this case, the rubber is stretched to $\lambda^{(1)} = 3$ and fully unloaded in the direction $\boldsymbol{e}_1$, then deformed in the same manner in the direction $\boldsymbol{e}_2$. The model predicts that the material does not return to the reference configuration when unloaded to a stress-free state after damage has occurred - some residual strain is present in the damaged stress-free state. Under uniaxial tension, the chains more aligned with stretching direction deform more than those less aligned with the stretching direction. Reaching a larger stretch, these chains therefore undergo more damage than the others, and the material becomes anisotropic. While the chains most aligned with the stretching direction undergo the most damage, the damaging of chains between the stretching direction and the plane transverse to the stretching direction means that some softening also occurs in the transverse direction. That is, the model predicts that when the material is subsequently stretched at 90° to the original loading direction, a softer response will be observed than if deformed from the pristine state. This is not in qualitative agreement with the experimental data of e.g. Hanson et al. (2005); Machado et al. (2012); Merckel et al. (2012) among others for the sequential uniaxial response of filled rubbers, where it is found that the response during the 90° loading essentially coincides with the pristine loading response.

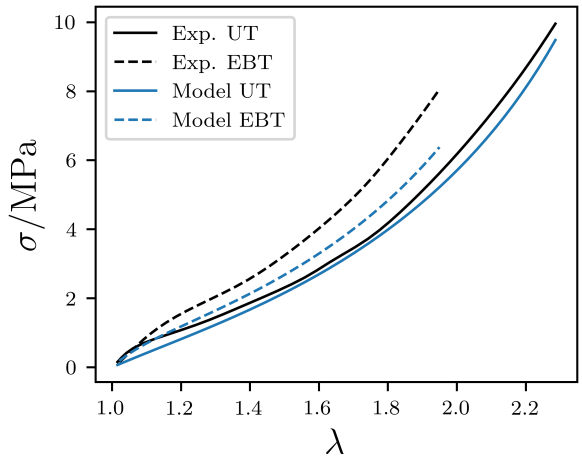


Figure 3.5: Comparison of model predictions to experimental data of Fernandes Arruebarrena (2016) for carbon black filled chloroprene under uniaxial tension (UT) and equibiaxial tension (EBT) with a single set of parameters. When fitted to the uniaxial response, the equibiaxial response is underpredicted by the model.

The Mullins effect is displayed not only in uniaxial tension (UT), which we have so far investigated, but additionally in general deformation states such as equibiaxial tension (EBT). To evaluate the performance of the model in predicting the mechanical response in such conditions, we confront the model to the uniaxial tension and equibiaxial tension data of Fernandes Arruebarrena (2016) for a carbon black filled chloroprene rubber. The model is calibrated against the uniaxial data using least squares minimisation on the difference between the true experimental stress and the model true stress. The response under equibiaxial tension is then predicted using these parameters and compared to the experimental response. The fitted and predicted curves alongside the experimental data are shown in Fig. 3.5 and the best-fit parameters are reported in Table 3.2. The model struggles to predict the equibiaxial response of the material. This can be observed from Fig. 3.5 where the experimental stress in EBT is much greater than the model prediction. This indicates that while the model is well-suited to predicting the material behaviour in a single loading condition (such as uniaxial tension), the outlined framework does not trivially apply to general conditions. Further investigation is required to understand the poor performance of the model in this situation.

$n_0 k_B T$	N_0	N^{ss}	$\Delta\Gamma_0$	α	n
1.85 MPa	2.5	6.375	0 MPa	3.91 MPa	1.27

Table 3.2: Parameters for model calibrated against Fernandes Arruebarrena (2016) data for a 36 phr carbon black filled chloroprene rubber undergoing uniaxial tension.

3.4 Application to thermoplastic polyurethanes

3.4.1 Specialisation of the constitutive response

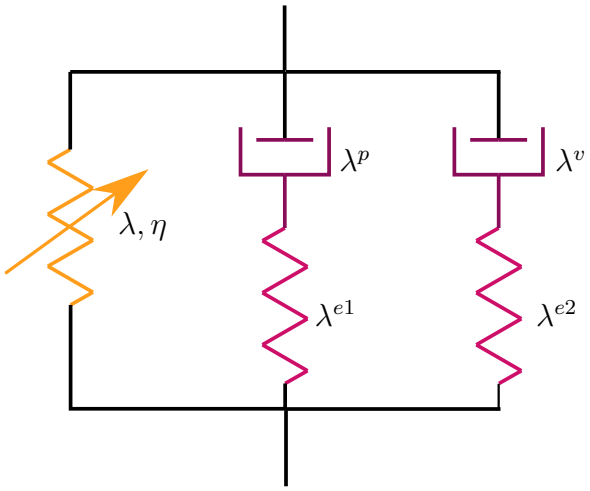


Figure 3.6: Representation of TPU chains in the spring-dashpot analogy.

We shall now specialise our modelling framework to thermoplastic polyurethanes. TPUs are linear, segmented block copolymers. They again demonstrate rubber-like elasticity and a composition-dependent Mullins effect (Prisacariu, 2011) but also exhibit striking plastic behaviour (Scetta et al., 2021). We will describe this behaviour on the chain level using the GSM framework. We assume that only the soft segments connecting hard domain to hard domain contribute to the free energy of the system. Following the investigations of Sui et al. (2015, 2017) on stress-softening in TPUs, we assume that a damage process occurs where chain segments that are impinged on the hard domain surface become freed over the course of deformation. We assume that on top of the damage part of the response, there are additional plastic and viscoelastic mechanisms, which motivate the split of the chain free energy into three parts corresponding to these mechanisms:

$$\psi^s(\lambda, \xi) = \psi^{(1)}(\lambda, \xi) + \psi^{(2)}(\lambda^{e1}) + \psi^{(3)}(\lambda^{e2}). \tag{3.36}$$

Here we have introduced the split of the chain stretch λ into elastic and plastic parts λ^{e1} and λ^p and elastic and viscous parts λ^{e2} and λ^v respectively:

$$\lambda = \lambda^{e1}\lambda^p = \lambda^{e2}\lambda^v, \tag{3.37}$$

and identified the damage parameter ξ, the plastic stretch λ^p and the viscous stretch λ^v as internal state variables for damage, plasticity and viscoelasticity respectively. The multiplicative decomposition of stretch implies the additive split of the logarithmic stretch rate d into elastic and viscous parts d^e and d^v respectively:

$$d = d^e + d^v, \tag{3.38}$$

where $d^{()} = \dot{\lambda}^{()}/\lambda^{()} = \overline{\log \lambda^{()}}^{\cdot}$. It is assumed that the dissipation potential accordingly splits into three independent contributions reflecting the damage and inelastic deformation mechanisms:

$$\phi = \phi^{(1)}(\dot{\xi}, \xi) + \phi^{(2)}(d^p) + \phi^{3)}(d^v). \tag{3.39}$$

In the spring-dashpot analogy, this model corresponds to the parallel variable stiffness spring/spring-dashpot system shown in Fig. 3.6.

The decomposition depicted in Fig. 3.6 was chosen for simplicity and to allow the main ideas of the framework to be presented clearly. It should be noted however that the framework permits an arbitrary number of spring dashpot elements to be used, and that the use of more elements would give more degrees of freedom for model calibration, potentially allowing for improved fitting performance.

Damage contribution

In the pristine state of the material some of soft segments are impinged on the surface of the hard domain (Sui et al., 2015, 2017). This reduces the effective number of segments in the chain. As damage occurs, the effective number of segments increases and the chain becomes softer. This mechanism is depicted in Fig. 3.7. We assume that the rubbery

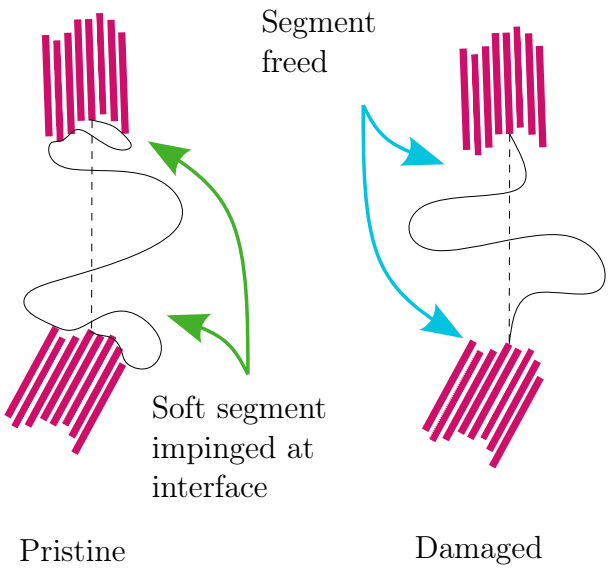


Figure 3.7: Damage mechanism where soft segments are released from impingement sites on hard domain surface.

chain connecting the hard domains is effectively a freely-jointed chain with an evolving number of Kuhn segments. We follow the same free energy and dissipation potential for the TPU model as in the filled rubber model:

$$\psi^{(1)}(\lambda,\xi) = N(\xi)k_BT\left(\beta\frac{\lambda r_0}{N(\xi)b} + \log\frac{\beta}{\sinh\beta}\right), \quad \beta = \mathcal{L}^{-1}\left(\frac{\lambda r_0}{N(\xi)b}\right), \tag{3.40}$$

$$\phi^{(1)}(\dot{\xi},\xi) = \begin{cases} \Gamma(\xi)\dot{\xi} & \dot{\xi} \geq 0, \\ +\infty & \dot{\xi} < 0. \end{cases} \tag{3.41}$$

We again choose the same linear form for $\Gamma(\xi)$ for simplicity:

$$\Gamma(\xi) = \Gamma_0 + \alpha\xi, \tag{3.42}$$

and saturation relation for $N(\xi)$:

$$N(\xi) = N_{ss} - (N_{ss} - N_0)\exp(-\xi). \tag{3.43}$$

Plastic contribution

In plasticity theories, the dissipation potential usually depends on the plastic strain rate through the accumulated plastic strain rate $\dot{p}$ to take into account hardening effects (see e.g. Brassart and Stainier (2012)). Following this approach, we split the plastic strain rate into $\dot{p}$ and a direction N:

$$d^p = \dot{p}N, \tag{3.44}$$

where $\dot{p} \geq 0$ and $N = \pm 1$ to render the split unique. We introduce the following forms of the free energy and dissipation potentials for simplicity:

$$\psi^{(2)}(\lambda^{e1}) = \frac{1}{2}\mu^{e1}(\log \lambda^{e1})^2, \tag{3.45}$$

$$\phi^{(2)}(\dot{p}, p) = \begin{cases} (\sigma_y + hp)\,\dot{p}, & \dot{p} \geq 0, \\ 0, & \dot{p} < 0, \end{cases} \tag{3.46}$$

corresponding to a log linear elastic response with linear plastic hardening.

As outlined in the general framework, the updating of the plastic state of the material is the solution of a minimisation problem. In this case, the minimisation is with respect to $\dot{p}$ and N instead of just d^p. Introducing the Lagrange multiplier Π to enforce the constraint on the magnitude of N, the evolution of plastic strain minimises the following functional with respect to $\dot{p}$, N and Π:

$$J(\dot{p}, N, \Pi, \lambda) = \frac{\partial \psi^{(2)}}{\partial \lambda^{e1}}\lambda^{e1}\left(d - \dot{p}N\right) + \left(\sigma_y + hp\right)\dot{p} + \Pi\left(|N| - 1\right). \tag{3.47}$$

From the resulting Euler-Lagrange equations, it can be shown that (see Appendix B):

$$N = \operatorname{sgn}\left(\lambda^{e1}\frac{\partial \psi^{(2)}}{\partial \lambda^{e1}}\right), \tag{3.48}$$

and:

$$f_y := \left|\frac{\partial \psi}{\partial \lambda^{e1}}\lambda^{e1}\right| - \sigma_y - hp \leq 0, \quad \dot{p} \geq 0, \quad f_y\dot{p} = 0. \tag{3.49}$$

such that plastic flow only occurs when the yield function f_y is zero i.e. this choice of inelastic variables and dissipation recover a one-dimensional yield function formulation of plasticity (similar to that of the damage branch - see Section 3.3 in addition to Appendix B).

Viscoelastic contribution

TPUs also exhibit a degree of viscoelasticity separately from plasticity and damage, as can be observed from the cyclic unloading-loading response. During this loading no further softening takes place, which implies that no damage occurs, and no increase in residual strain occurs, indicating that the mechanism is not viscoplastic. We assume the below potentials to describe this mechanism:

$$\psi^{(3)} = \frac{1}{2}\mu^e(\log \lambda^e)^2, \tag{3.50}$$

$$\phi^{(3)} = \eta \left(d_0^v\right)^2 \log\left(\cosh\left(\frac{d^v}{d_0^v}\right)\right). \tag{3.51}$$

The dissipation potential defined in Eq. (3.51) corresponds to a dashpot that is approximately linear at small strain rates but saturates at higher strain rates. This can be inferred from the derivative of the dissipation potential, which reads:

$$\frac{\partial \phi^{(3)}}{\partial d^v} = \eta d_0^v \tanh \frac{d^v}{d_0^v}. \tag{3.52}$$

Taking the limits $d^v/d_0^v \to 0$ and $d^v/d_0^v \to \pm\infty$, we find:

$$\lim_{d^v \to 0} \frac{\partial \phi^{(3)}}{\partial d^v} = \eta d^v, \quad \lim_{d^v \to \pm\infty} \frac{\partial \phi^{(3)}}{\partial d^v} = \pm \eta d_0^v, \tag{3.53}$$

which reflects this saturation. To analyse the influence of the parameter d_0^v on the mechanical response, the stress-stretch response of the viscoelastic branch on its own under uniaxial tension at two different strain rates (0.05 s^{-1} and 0.01 s^{-1}) is shown in Fig 3.8 for different values of d_0^v. The values of d_0^v are chosen to be below, similar to, and above these strain rates. The viscosity and elastic modulus are set to arbitrary reasonable values and

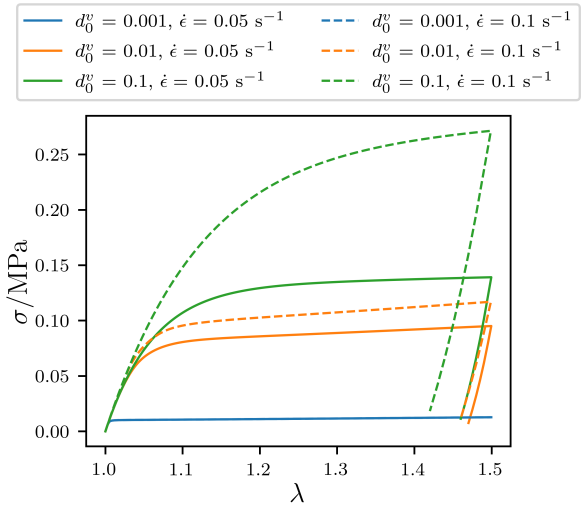


Figure 3.8: Predictions of viscoelastic branch under uniaxial tension at different strain rates for different values of d_0^v.

held constant. Specifically, we choose $\eta = 26.7$ MPa s and $\mu^{e2} = 10.7$ MPa.

Fig. 3.8 reveals that the parameter d_0^v controls the rate-sensitivity of the viscous branch and the magnitude of the viscous stress contribution. The impact on rate-sensitivity is demonstrated by considering the different responses solicited for different magnitudes of d_0^v relative to the applied strain rate. When d_0^v is much below the applied strain rate, increasing the strain rate does not impact the stress-stretch response. When d_0^v is similar to the applied strain rate, increasing the strain rate increases the stress outputted by the model. The model shows further heightened rate sensitivity when d_0^v is greater than the applied strain rate. In addition, increasing d_0^v increases the contribution of the viscous branch.

As all of the constitutive functions have now been selected, it only remains to identify the material parameters through calibration of the model against experimental data before the model can be evaluated. From Eqs (3.17), (3.40), (3.45) and (3.50) it follows that the first Piola-Kirchhoff stress reads:

$$\boldsymbol{P} = (1-f)\left\langle \left(\frac{\partial \psi^{(1)}}{\partial \lambda} + \frac{\partial \psi^{(2)}}{\partial \lambda^{e1}} \frac{\lambda^{e1}}{\lambda} + \frac{\partial \psi^{(3)}}{\partial \lambda^{e2}} \frac{\lambda^{e2}}{\lambda} \right) \frac{\partial \lambda^s}{\partial \boldsymbol{F}} \right\rangle - P\boldsymbol{F}^{-T}. \tag{3.54}$$

3.4.2 Comparison to experimental data

Parameter	Value	Parameter	Value
$\nu_0 k_b T$	20 MPa	σ_y	0.53 MPa
$r_0/(N_0 b)$	0.2	h	0 MPa
N_{ss}/N_0	2	μ^{e2}	18.7 MPa
α	6.7 MPa	η	46.7 MPa s
$\Delta\Gamma$	0 MPa	d_0^v	0.05 s^{-1}
μ^{e1}	1.3 MPa	n	2

Table 3.3: Fitting parameters for data of Cho et al. (2017)

To demonstrate the predictive power of the model, we fit it to the data of Cho et al. (2017) for three TPUs of different hard phase volume fractions (A - 27%, B - 39% and C - 52%) undergoing uniaxial compression. The TPUs are deformed at three different strain rates and subjected to cyclic loading. The data for the tests conducted at a nominal strain rate of $\dot{\epsilon} = -0.01$ s^{-1} are used for parameter identification and the data at the nominal strain rates $\dot{\epsilon} = -0.1$ s^{-1} and $\dot{\epsilon} = -0.001$ s^{-1} are used for validation. Fig. 3.9(a) shows the model response against experimental data under cyclic uniaxial compression at different volume fractions at a nominal strain rate of $\dot{\epsilon} = -0.01$ s^{-1} (used for calibration). Figs. 3.9(b)-(d) show the model and experimental comparisons of the uniaxial response of the three different TPUs respectively each at three different strain rates (used for model validation).

A heuristic, iterative procedure was followed for fitting the model to the data of Cho et al. (2017). First, initial guesses for the parameter values were set. The microstructural parameters $\nu_0 k_B T$, relating to the number of soft chains per unit volume; $r_0/(N_0 b)$, which relates to the initial level of extension of the chains; n, which relates to the structure of the hard phase; and N_{ss}/N_0, the ratio of final chain length to initial chain length were set to physically-reasonable values based on microstructural information from Cho et al. (2017). The chain moduli μ^{e1} and μ^{e2} were initially set equal to $\nu_0 k_B T$ (which reflects the initial soft chain modulus) as these terms are expected to be the same order of magnitude. The other viscous and plastic parameters η, h and d_0^v were set such that viscous and plastic effects would initially be negligible. As it is believed damage initiates as soon as the

material is deformed, $\Delta\Gamma$ was set to 0 MPa and (as an initial guess) the parameter α was set to 0 MPa. Then, the parameters relating to $\psi^{(1)}$ and $\phi^{(1)}$ (the hyperelastic-damage branch) were modified to approximately match the initial loading-unloading response of the material. The viscous parameters were then adjusted to match the hysteresis loop observed during the *second* loading-unloading cycle (as opposed to the first, which is expected to be significantly impacted by the hyperelastic-damage branch). Finally, the plastic parameters were altered to attempt to match the residual strain observed in the material response. The parameter n was adjusted to improve the scaling of the material responses across volume fractions. As all aspects of the mechanical response are altered (to a greater or lesser degree) by all of the mechanical properties, this process was performed iteratively and the quality of the fits was assessed by inspection. The fitted model parameters are shown in Table 3.3.

As can be seen from Fig. 3.9(a), the model is broadly able to capture changes in the mechanical response observed with changing volume fraction. The increased stiffness and hysteresis observed at large volume fractions is captured. Across all volume fractions, the model predicts a rate-sensitivity in qualitative agreement with the experimental data as shown in Figs. 3.9(b)-(d). Larger strain rates are associated with higher stresses, and at higher volume fractions the rate-sensitivity of the model appears to become more pronounced i.e. the difference between the high-rate and low-rate predictions is bigger at larger volume fractions than at lower volume fractions. This is again in agreement with the experimental data.

Some aspects of the model fitting performance show room for improvement. The model predicts an initial linear stress-stretch response followed by a plateau region whereas the experimental data show a more gradual decrease in gradient across all strain rates and volume fractions. Another difference between the model and the experimental data lies in the unloading. The experimental data do not show much difference during unloading at different strain rates despite showing significant rate-sensitivity during loading. The model shows a similar degree of rate sensitivity during both loading and unloading.

To further analyse the model performance, we compare model predictions to the experimental data of Cho et al. (2017) for the response of the same TPUs as before under paused cyclic uniaxial compression. The paused compression tests consist of loading the material to a true strain of -1 where the material is held at constant strain for 60 s at various points in the deformation during loading and unloading. During these pauses, the material undergoes stress relaxation. The model predictions (using the parameters listed in Table 3.3) are shown in Fig. 3.10(a) alongside the experimental data in Fig. 3.10(b). While the model somewhat captures the response at the volume fraction $f = 0.27$, it struggles to capture the experimental response at larger volume fractions, particularly during the unloading and during stress relaxation. The model predicts that at a given fixed strain, more stress relaxation occurs for the higher volume fraction TPUs, in line with the experimental data. The data however show more relaxation occurs at larger strains than at small strains, which is not predicted by the model. This perhaps arises from having only a single viscous mechanism in the model and only calibrating the model against cyclic data at various strain rates. There are some reports in the literature that multiple viscoelastic branches are needed to capture the material response of many glassy polymers under stress relaxation and under cyclic loading simultaneously (Ricker et al., 2023) under the postulate that different deformation mechanisms (following different relaxation times) dominate the material response in the respective cases. Extending the framework to have further viscoelastic branches could quite easily be done in the future.

In future, it would be useful to re-examine this work using a more rigorous fitting procedure. As it stands, the poor model performance is equally likely to be due to a poor calibration procedure as it is due to poor modelling choices. Typical fitting procedures for complex elastomer models with a large number of parameters seek to fit parameters sequentially, where parameters are fitted in-turn based on links between the parameters and specific parts of the material response. For example, Cho et al. (2017) fit their model to experimental data by (in order) extracting modulus-like parameters from stress relaxation data, identifying viscoplastic parameters from yield stress data (at different strain rates) and determining damage parameters from cyclic uniaxial data (all fits are evalu-

ated by inspection and no details of how the parameter space is searched are provided). Alkhoury et al. (2024) conduct model calibration by partitioning the parameters into rate-independent and rate-dependent groups. The rate-independent parameters are fitted to quasi-static experimental data and the rate-dependent parameters are fitted to time-dependent data (in both cases using least squares regression). In both of these examples, parameters are fitted in smaller groups instead of all at once to more efficiently arrive at global minima and reduce the computational expense of the fitting procedure.

A drawback of full-network based models featuring additive decompositions of the free energy function (i.e., spring-dashpot models) is that it is challenging to uncover independent links between the material parameters and the material response, which has significant implications for following sequential model calibration procedures. Consider fitting the initial slope of the stress-strain response. In a full-network model, there is a contribution to the initial slope from each chain direction and each spring-dashpot mechanism, which means that is immediately not trivial to link chain parameters to the macroscopic behaviour. This issue is exacerbated as chains in different direction are subjected to different strains and strain rates (depending on how closely they align with the stretching direction), and this have very different contributions to the mechanical response. For these reasons, it may not be possible to follow a sequential fitting procedure for this type of model. The fitting procedure ought to follow the minimisation of some error function, such as the least squares difference between the experimental and model data points. A method that is effective in higher dimensional spaces would be required owing to the number of model parameters present. There is a vast literature on possible optimisation methods which could be applied to the problem of material parameter extraction (and have been applied in other contexts - see e.g. Balázs et al. (2021)). Methods based on genetic algorithms, which are able to handle optimisation problems in high-dimensional spaces, have recently found success for TPU modelling (Reyes et al., 2024) and could readily be applied to model calibration in this case too.

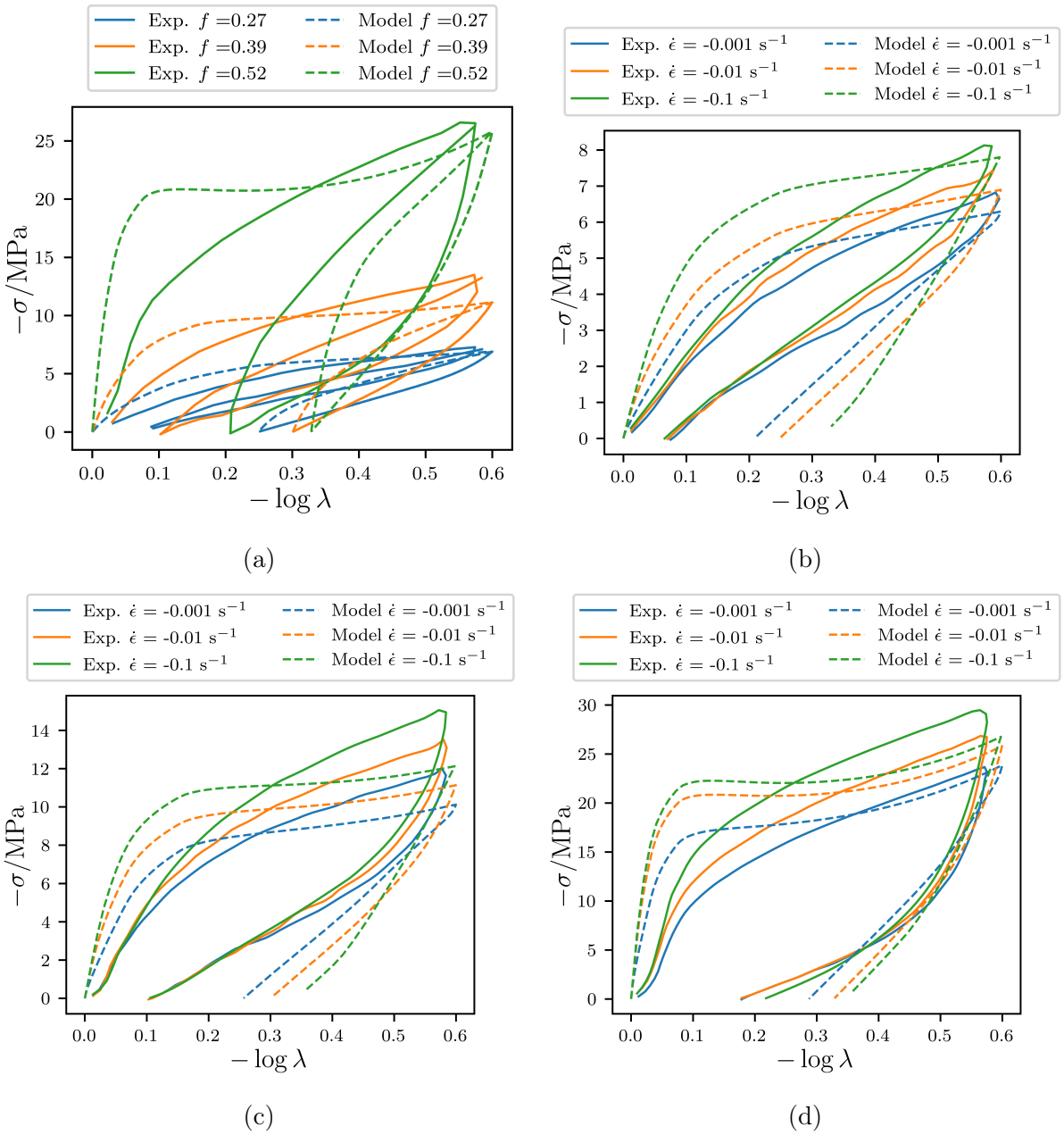
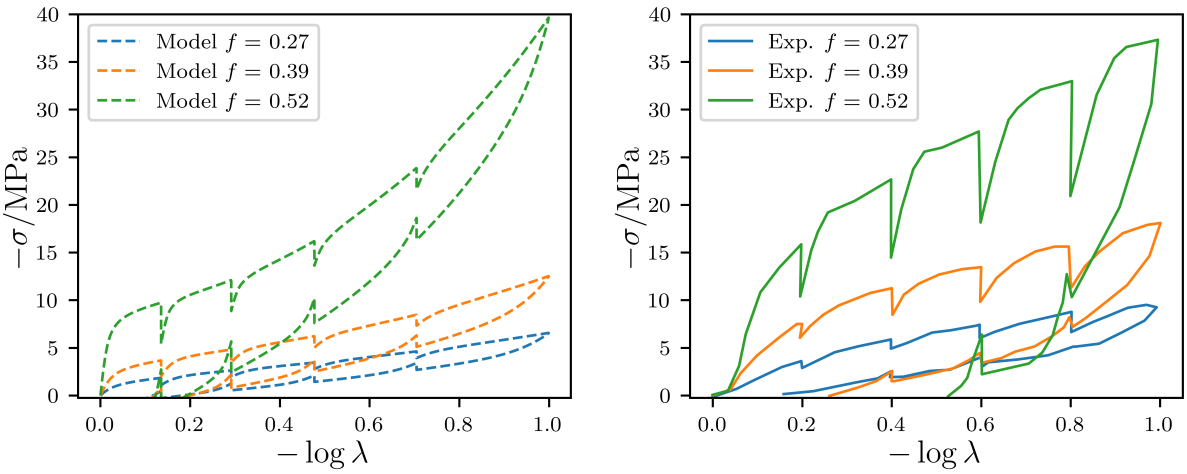


Figure 3.9: Comparison of model to the cyclic uniaxial compression data of Cho et al. (2017) for (a) three TPUs (of different volume fractions) at a nominal strain rate of -10^{-2} s^{-1} and (b) - (d) TPUs with hard phase volume fractions 0.27, 0.39 and 0.52 respectively under different strain rates.



(a) (b)

Figure 3.10: Comparison of (a) model predictions to the (b) experimental data of Cho et al. (2017) for three TPUs of different volume fractions undergoing uniaxial compression at a nominal strain rate of -10^{-2} s^{-1} with pauses of 60 s duration at various strains.

3.5 Conclusion

In this Chapter, a modelling framework for two-phase elastomers has been presented in a general sense and applied to experimental data for filled rubbers and thermoplastic polyurethanes as illustrative examples. The framework is based on the full-network approach to rubber elasticity with extensions to allow a variety of inelastic behaviours to be described on a chain level including the Mullins effect, plasticity and viscoelasticity. It features a simple treatment of the hard-soft microstructure based on the assumption that the hard phase is rigid, which places kinematic constraints on the deformation of the soft phase, and is able to link changes in the hard phase volume fraction to changes in the macroscopic response. The framework is specialised to filled rubbers with a focus on capturing the Mullins effect by following a network alteration assumption where effective crosslinks in the network breakdown. It is subsequently specialised to thermoplastic polyurethanes by incorporating plastic and viscoelastic mechanisms in addition to the damage mechanism.

In both cases, the model is able to achieve a degree of agreement with experimental data at low volume fractions and predict the general trends in the mechanical behaviour with increasing volume fraction. However, the model underpredicts of the degree of damage and viscous effects that take place at larger volume fractions. In future, it would serve to re-evaluate the fitting of the model following a more complete set of experimental data (with quantified errors) and after developing a more rigorous fitting procedure. These developments would allow conclusions to be drawn about the model fitting performance with more confidence and give a clearer indication of the underlying deficits of the model.

As revealed in the analysis of the framework specialised to filled rubbers, the framework has some limitations in describing the anisotropy developed during Mullins softening and in predicting the response of the material under general loading conditions with a single set of material parameters. These limitations motivate two of the later studies in this thesis. In Chapter 4, the assumptions leading to good fitting performance of micromechanical

models under general multiaxial loading conditions are examined and in Chapter 6, an approach to modelling the anisotropy developed during the Mullins effect is proposed. The approach is based on the full-network concept with an alternative approach to describing damage in the material.

Chapter 4

Capturing I_2 dependence with the tube model

4.1 Introduction

In the literature, a great number of constitutive models have been proposed for the capturing the large deformation stress-strain response of rubber-like materials. One factor influencing the choice of rubber model is the ability of the model to accurately describe the behaviour under general loading conditions (i.e. under arbitrary triaxial deformations). In Section 3.3, a constitutive model for filled rubbers was developed in the micromechanical approach and compared to the experimental data of Fernandes Arruebarrena (2016) for the uniaxial and equibiaxial tensile responses of a filled rubber. The model struggled to capture both responses of the material with a single set of parameters. It turns out that this is a common deficit of many micromechanical models even in the hyperelastic setting (Marckmann and Verron, 2006).

Restricting ourselves to hyperelasticity, we will explore one extension to the micromechanical approach – the tube model – which has been found to improve fitting performance in the past (Marckmann and Verron, 2006; Hossain et al., 2015; Dal et al., 2021). Differing from past works, we separate tube models into two families based on their kinematic description as we find this has a determining role in fitting performance. In approaching

the problem from a phenomenological perspective, it has become accepted that invariant-based phenomenological models must feature dependence on both invariants I_1 and I_2 to reproduce the mechanical response of rubber under general loading conditions accurately (Destrade et al., 2017; Dal et al., 2021; Anssari-Benam et al., 2021). It would therefore seem plausible that tube models lead to the emergence of I_2 dependency in the micromechanical models. However, a link between the tube model and dependence on I_2 has not previously been investigated.

In this Chapter, the modelling assumptions in the micromechanical framework that lead to good fitting performance in general loading conditions are investigated. In the process of this investigation, links between fitting performance and the invariant I_2 are highlighted, motivated by the important role this functional dependence plays in the context of phenomenological models. Specifically, the kinematics of tube deformation and their interplay with different network-averaging schemes and their relationship with the emergence of the invariant I_2 and good fitting performance are elucidated. Model performance is benchmarked against experimental datasets encompassing various loading modes for the same material (e.g. uniaxial tension - biaxial tension, uniaxial tension - uniaxial compression, generic biaxial loading) and tests are developed to infer I_2 dependence as it is not always explicitly obvious from inspection of the free energy function.

4.2 Constitutive framework

4.2.1 The tube model

Micromechanical models begin with the behaviour of an individual rubber chain and arrive at the behaviour of a macroscopic rubber network by averaging this behaviour over the constitutive chains. The behaviour of a rubber chain in isolation is a well-understood problem in polymer physics, and can be modelled through the freely-jointed chain model. As is written in Eq. (2.33), it is assumed that the free energy of the network is the sum of the isolated chain free energies. However in a rubber network chains do not

behave the same way as they do in isolation. For a given end-to-end distance, the number of conformations accessible to a single chain is constrained in the network due to the presence of neighbouring chains (McLeish, 2002). This means that the (Helmholtz) free energy differs between a chain in a network and a chain in isolation, which impacts both chain and network behaviour. A modification of the chain free energy function ψ in Eq. (2.33) is therefore required to capture the network response.

A simple means to do this is through the tube concept (Doi and Edwards, 1988; McLeish, 2002). The constraints imposed on a chain by its neighbours are considered to be equivalent to the restrictions placed upon the chain if it were constrained within a fictitious tube of deformation-dependent cross-sectional area. Chain conformations where any part of the chain is outside the tube are no longer admissible. This model of the constraints placed upon the chain can be incorporated by adding a contribution to the free energy of the freely-jointed chain that penalises inadmissible chain conformations, and which can be written as a function of the tube diameter.

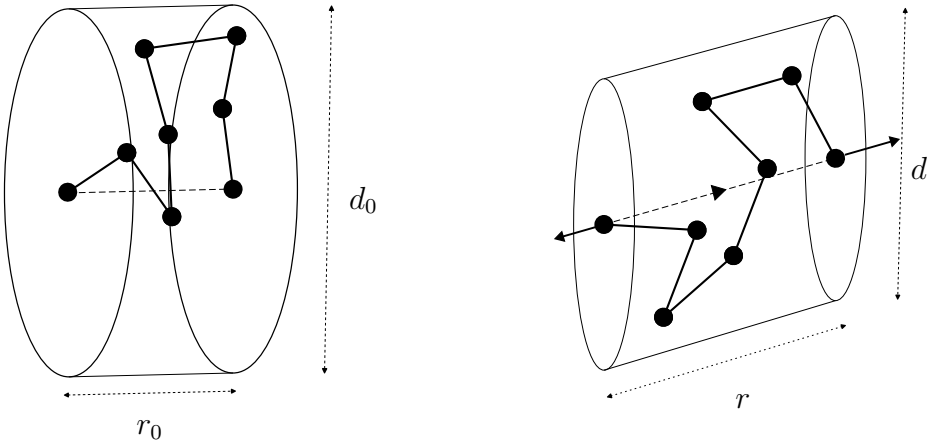


Figure 4.1: The tube model in the reference and current configurations. Only chain conformations entirely within the tube are admissible.

The tube model admits an additive decomposition of the chain free energy into an isolated chain free energy contribution ψ_p (commonly referred to as the *phantom* contribution) and a constraint term ψ_c (Miehe et al., 2004; Darabi and Itskov, 2021):

$$\psi(\nu, \lambda) = \psi_f(\lambda) + \psi_c(\nu). \tag{4.1}$$

The argument of the phantom contribution is the chain stretch λ and the argument of the tube contribution is the tube area stretch ν. Microscopically, λ is the ratio of current to reference chain end-to-end distance and ν is the ratio of tube reference area (proportional to d_0^2) to tube current area (proportional to d^2):

$$\lambda = \frac{r}{r_0}, \quad \nu = \left(\frac{d_0}{d}\right)^2. \tag{4.2}$$

The free energy of the phantom contribution can be obtained from the freely-jointed chain model, see Eq. (2.28):

$$\psi_f = Nk_BT\left(\beta\frac{\lambda r_0}{Nb} + \log\frac{\sinh\beta}{\beta}\right), \quad \beta = \mathcal{L}^{-1}\left(\frac{\lambda r_0}{Nb}\right). \tag{4.3}$$

The free energy contribution associated with the reduction in conformational entropy arising from the tube constraint is taken of the following form (Doi and Edwards, 1988; Miehe et al., 2004):

$$\psi_c(\nu) = \alpha Nk_BT\left(\frac{b}{d_0}\right)^2\nu, \tag{4.4}$$

where α is a geometry factor pertaining to the shape of the tube cross section.

The microscopic deformation measures must be related to the macroscopic deformation to close the model. Two macroscopic deformation measures of interest are the continuum line stretch $\bar{\lambda}$ (of a line of unit length and direction $\boldsymbol{n}$):

$$\bar{\lambda} = |\boldsymbol{F}\boldsymbol{n}|, \tag{4.5}$$

and the continuum area stretch $\bar{\nu}$ given by Nanson's formula (for a plane of unit area and normal $\boldsymbol{n}$):

$$\bar{\nu} = J|\boldsymbol{F}^{-T}\boldsymbol{n}|. \tag{4.6}$$

It is often assumed that the chain stretch is given by the continuum line stretch through the affine rule:

$$\lambda = \bar{\lambda}. \tag{4.7}$$

Tube models vary in their statistical mechanics treatments and in the assumed relationship between the tube dimensions and the macroscopic deformation. Most tube models express the change in tube diameter in terms of the chain stretch λ. Examples include affine tube models (Edwards, 1967; Gaylord, 1979), constant volume tube models (Marrucci, 1981; Gaylord, 1982), and non-affine tube models (Heinrich et al., 1988; Rubinstein and Panyukov, 1997). A selection of these models are presented in Table 4.1. A general presentation, which encompasses the previously-mentioned models as special cases, has recently been proposed by Darabi and Itskov (2021), in combination with three-chain averaging. We refer to tube models that relate the change in tube dimensions to the chain stretch, and hence to the line-stretch of the continuum, as "λ-based" tube models. In contrast, Miehe et al. (2004) maintain the tube area contraction ν as a second *independent* micro-kinematic variable, and further propose a (non-affine) relationship between the tube area contraction and the area-stretch of the continuum. These authors implement their tube model within a full-network averaging scheme. This approach was recently simplified by considering eight-chain averaging (or, equivalently, area-stretch averaging in the sense of Beatty (2003)), see Kroon (2011); Khiêm and Itskov (2016); Anssari-Benam et al. (2021). We call tube models that relate the tube area contraction to the area-stretch of the continuum as "ν-based" tube models.

In this Chapter, we will compare tube models from each family following a power-law relation between the tube diameter and the macroscopic deformation:

$$\nu = \begin{cases} \bar{\lambda}^{\beta} & \text{for } \lambda\text{-based models,} \\ \bar{\nu}^{\beta} & \text{for } \nu\text{-based models.} \end{cases} \tag{4.8}$$

To make clear the distinction between the two forms of model, we adopt the following notation for the constraint contribution to the free energy:

$$\psi_c^{(\lambda)}(\bar{\lambda}) = k\bar{\lambda}^{\beta} \quad \text{for } \lambda\text{-based models,} \tag{4.9}$$

$$\psi_c^{(\nu)}(\bar{\nu}) = k\bar{\nu}^{\beta} \quad \text{for } \nu\text{-based models.} \tag{4.10}$$

Tube model	ψ_c
Affine tube (Edwards, 1967; Gaylord, 1979)	$k\bar{\lambda}^{-2}$
Constant volume tube (Marrucci, 1981; Gaylord, 1982)	$k\bar{\lambda}$
Heinrich et al. (1988)	$k\bar{\lambda}^{\beta}$
Rubinstein and Panyukov (1997)	$k(\bar{\lambda}+\bar{\lambda}^{-1})$
Darabi and Itskov (2021)	$k(\bar{\lambda}^{\beta}+\bar{\lambda}^{\gamma})$

Table 4.1: Overview of λ-based tube models of the literature.

4.2.2 Macroscopic free energy

As described in Section 2.3.2, the macroscopic free energy Ψ of the network is obtained by averaging the chain free energy over representative orientations. We consider three averaging schemes, respectively corresponding to the full-network, three-chain and eight-chain models.

Full-network averaging. The full-network (FN) approach to rubber elasticity considers a uniform distribution of chain orientations in the reference configuration. The macroscopic free energy is given by:

$$\Psi^{FN} = n\langle\psi\rangle, \quad \langle\bullet\rangle := \frac{1}{4\pi}\int_{\mathcal{S}} \bullet \, d\mathcal{S}, \tag{4.11}$$

where n is the number density of polymer chains and integration is carried out over the unit sphere $\mathcal{S}$. Using Eq. (4.1), the macroscopic free energy can be additively split into its phantom and tube contributions:

$$\Psi^{FN} = n\langle\psi_f\rangle + n\langle\psi_c\rangle \equiv \Psi_f^{FN} + \Psi_c^{FN}, \tag{4.12}$$

where Ψ_f^{FN} and Ψ_c^{FN} respectively represent the phantom and tube contributions to the macroscopic free energy. The macroscopic phantom contribution is independent of the the specific tube model being considered. The macroscopic tube contribution differs

depending on whether a λ-based or ν-based tube model is used. For a λ-based model:

$$\Psi_c^{FN(\lambda)} = n\langle\psi_c^{(\lambda)}\rangle, \tag{4.13}$$

where $\psi_c^{(\lambda)}$ is a function of the line-stretch and is given by Eq. (4.9), while for a ν-based tube model:

$$\Psi_c^{FN(\nu)} = n\langle\psi_c^{(\nu)}\rangle, \tag{4.14}$$

where $\psi_c^{(\nu)}$ is a function of the area-stretch and is given by Eq. (4.10).

Evaluation of the integral over all the orientations generally requires numerical quadrature. Here, we adopt the 900-point scheme proposed by Fliege and Maier (1999). While this scheme is costly, it is associated with very low numerical integration errors (Verron, 2015; Itskov, 2016) and can be treated as a very accurate benchmark for the response of a full-network model.

Three-chain averaging. The macroscopic free energy of the three-chain (3C) model is obtained by restricting the orientation averaging to chains that are initially aligned with the principal stretch directions. Recall that $\lambda^{(i)}$ $(i = 1, 2, 3)$ are the principal stretches, and let $\nu^{(i)}$ be the area-stretches in the principal directions. According to Eq. (4.6), the latter are given by: $\nu^{(1)} = \lambda^{(2)}\lambda^{(3)}$, $\nu^{(2)} = \lambda^{(1)}\lambda^{(3)}$ and $\nu^{(3)} = \lambda^{(1)}\lambda^{(2)}$. The macroscopic free energy of the three-chain model is given by:

$$\Psi^{3C} = \frac{n}{3}\sum_{i=1}^{3}\psi^{(i)} = \frac{n}{3}\sum_{i=1}^{3}\psi_f^{(i)} + \frac{n}{3}\sum_{i=1}^{3}\psi_c^{(i)} \equiv \Psi_f^{3C} + \Psi_c^{3C}, \tag{4.15}$$

where the superscript (i) refers to a chain aligned with the i^{th} principal direction. More explicitly, the macroscopic phantom contribution to the free energy is given by:

$$\Psi_f^{3C} = \frac{n}{3}\sum_{i=1}^{3}\psi_f(\lambda^{(i)}), \tag{4.16}$$

The macroscopic tube contribution for the λ-based and ν-based tube models are respectively given by:

$$\Psi_c^{3C(\lambda)} = \frac{n}{3}\sum_{i=1}^{3}\psi_c^{(\lambda)}(\lambda^{(i)}), \tag{4.17}$$

and:

$$\Psi_c^{3C(\nu)} = \frac{n}{3}\sum_{i=1}^{3}\psi_c^{(\nu)}(\nu^{(i)}). \tag{4.18}$$

Eight-chain averaging. The eight-chain (8C) model only considers chains aligned with the diagonals of a cube with edges aligned with the principal directions. In a coordinate system aligned with the principal axes, $\boldsymbol{n} = (\pm 1/\sqrt{3}, \pm 1/\sqrt{3}, \pm 1/\sqrt{3})$. Direct application of formulas (4.5) and (4.6) in each of the eight-chain directions gives:

$$\lambda^{(8C,i)} = \sqrt{\frac{(\lambda^{(1)})^2 + (\lambda^{(2)})^2 + (\lambda^{(3)})^2}{3}} \equiv \lambda^{8C}, \tag{4.19}$$

and:

$$\nu^{(8C,i)} = \sqrt{\frac{(\lambda^{(2)}\lambda^{(3)})^2 + (\lambda^{(1)}\lambda^{(3)})^2 + (\lambda^{(1)}\lambda^{(2)})^2}{3}} \equiv \nu^{8C}, \tag{4.20}$$

where the superscript $(8C, i)$ refers to the i^{th} chain ($i = (1, 8)$). Equations (4.19) and (4.20) show that all the representative chains experience the same line-stretch and the same area-stretch, and therefore all representative chains have the same energy. Averaging of the chain energy over the eight directions then directly gives:

$$\Psi^{8C} = n\psi = n\psi_f + n\psi_c \equiv \Psi_f^{8C} + \Psi_c^{8C}. \tag{4.21}$$

The macroscopic phantom contribution is given by:

$$\Psi_f^{8C} = n\psi_f(\lambda^{8C}). \tag{4.22}$$

The macroscopic tube contributions in the λ-based and ν-based schemes are respectively given by:

$$\Psi_c^{8C(\lambda)} = n\psi_c^{(\lambda)}(\lambda^{8C}), \tag{4.23}$$

and

$$\Psi_c^{8C(\nu)} = n\psi_c^{(\nu)}(\nu^{8C}). \tag{4.24}$$

4.2.3 Macroscopic stress-strain response.

In this work we assume that the material is incompressible ($J = 1$). Recall that the Cauchy stress is given by:

$$\boldsymbol{\sigma} = \frac{\partial \Psi}{\partial \boldsymbol{F}} \boldsymbol{F}^T - P\mathbf{1}, \tag{4.25}$$

where P is an arbitrary scalar to be determined from boundary conditions. The principal stresses are obtained from Eq. (4.25) as:

$$\sigma_i = \frac{\partial \Psi}{\partial \lambda^{(i)}} \lambda^{(i)} - P. \tag{4.26}$$

The shear modulus G obtained with the different models can be calculated from the stress-stretch response in a uniaxial tensile test along direction 1 as:

$$3G = \lim_{\lambda^{(1)} \to 1} \frac{d\sigma_1}{d\lambda^{(1)}}. \tag{4.27}$$

The shear modulus can be additively decomposed into a phantom contribution G_f and a tube contribution G_c. Assuming that the Gaussian limit holds in the reference configuration, which is the case if $N \gtrapprox 11$, then the phantom modulus is simply given by $G_f = nk_BT$, which holds for the full-network, three-chain and eight-chain averaging methods (for a smaller number of Kuhn segments N, chains are pre-stretched beyond their Gaussian regime in the reference configuration, so that finite extensibility effects must be included in the expression of the modulus). In contrast, the tube contribution to the shear modulus depends on the chosen averaging method. These contributions may be evaluated by taking inserting the tube contribution into the relevant averaging scheme and then evaluating the limit (4.27) analytically. For the full-network, three-chain and

eight-chain models, we respectively find:

$$G_c^{FN} = nk\beta\left(\frac{\beta}{15} + \frac{1}{5}\right), \tag{4.28}$$

$$G_c^{3C} = \frac{nk\beta^2}{6}, \tag{4.29}$$

$$G_c^{8C} = \frac{nk\beta}{3}. \tag{4.30}$$

Note that identical expressions are found for the λ-based and ν-based tube models. When the tube energy is quadratic, i.e. $\beta = 2$, all three moduli coincide: $G_c = \frac{2nk}{3}$.

4.3 Evaluation of I_2 dependence

We seek to evaluate the sensitivity of tube models to the invariant I_2. In most models, I_2 does not explicitly appear and we need other means to probe sensitivity to it. The most direct way to evaluate the I_2 dependence of a hyperelastic model or experimental data is to calculate the partial derivative $\partial\Psi/\partial I_2$. However, the partial derivatives of the free energy with respect to the invariants are sensitive to experimental and numerical noise for small but still finite deformations (Rivlin and Saunders, 1951; Anssari-Benam et al., 2021). For an incompressible, hyperelastic material in a state of plane stress ($\sigma_3 = 0$), the partial derivatives of the free energy with respect to the invariants can be expressed in terms of the principal stretches and stresses as (Rivlin and Saunders, 1951; Anssari-Benam et al., 2021):

$$\frac{\partial\Psi}{\partial I_1} = \frac{1}{2((\lambda^{(1)})^2 - (\lambda^{(2)})^2)}\left(\frac{(\lambda^{(1)})^2\sigma_1}{(\lambda^{(1)})^2 - (\lambda^{(3)})^2} - \frac{(\lambda^{(2)})^2\sigma_2}{(\lambda^{(2)})^2 - (\lambda^{(3)})^2}\right), \tag{4.31}$$

$$\frac{\partial\Psi}{\partial I_2} = \frac{1}{2((\lambda^{(2)})^2 - (\lambda^{(1)})^2)}\left(\frac{\sigma_1}{(\lambda^{(1)})^2 - (\lambda^{(3)})^2} - \frac{\sigma_2}{(\lambda^{(2)})^2 - (\lambda^{(3)})^2}\right), \tag{4.32}$$

Note that these expressions are only valid when all three principal stretches are distinct, i.e. they do not apply to uniaxial tension or equibiaxial tension. Furthermore, numerical problems arise for smaller deformations. Considering small deformations, where $\lambda^{(i)} \to 1$, the stresses σ_1 and σ_2 must approach zero at an appropriate rate for a finite value of

$\partial\Psi/\partial I_1$ and $\partial\Psi/\partial I_2$ to be reached, as otherwise $\partial\Psi/\partial I_2$ cannot be inferred. Numerical or experimental noise can interfere with this limit and renders it challenging to make statements about the I_2 dependence with confidence. Rivlin and Saunders in their seminal work found excessive noise in applying Eqs. (4.31)-(4.32) to their experimental data for deformations where $I_1, I_2 < 5$, preventing the analysis of I_2-dependence over small-to-moderate deformations.

Universal relations offer an alternative means to assess the emergence of I_2 dependence. Universal relations are relationships between stress and deformation that hold true for a family of materials with free energy functions of a particular type regardless of the specific form of the function. If a model predicts a stress-strain response for which a universal relation for a particular class of materials does not hold, the model does not belong to that class of materials. Several universal relations have been proposed for the class of free energy functions defined as $\Psi = \Psi(I_1)$ (i.e. where I_2 dependence of the free energy function is excluded) (Wineman, 2005; Anssari-Benam et al., 2021). This class is sometimes referred to as the family of generalised neo-Hookean models. In the following, a universal relation based on general biaxial loading (where all three principal stretches are distinct) proposed in the literature is recounted, and two novel universal relations respectively applicable to uniaxial and equibiaxial loading, and to uniaxial tension and compression, are introduced.

General biaxial tension. Consider first a general biaxial loading with $\sigma_3 = 0$. Then the general stress-strain relation (2.14) gives:

$$\sigma_1 = 2\left((\lambda^{(1)})^2 - \frac{1}{(\lambda^{(1)})^2(\lambda^{(2)})^2}\right)\left(\frac{\partial\Psi}{\partial I_1} + \lambda_2^2\frac{\partial\Psi}{\partial I_2}\right), \tag{4.33}$$

$$\sigma_2 = 2\left((\lambda^{(2)})^2 - \frac{1}{(\lambda^{(1)})^2(\lambda^{(2)})^2}\right)\left(\frac{\partial\Psi}{\partial I_1} + \lambda_1^2\frac{\partial\Psi}{\partial I_2}\right), \tag{4.34}$$

If the free energy only depends on I_1, then the following universal relation holds (Wineman, 2005; Anssari-Benam et al., 2021):

$$\frac{\sigma_1}{\sigma_2} = \frac{(\lambda^{(1)})^4(\lambda^{(2)})^2 - 1}{(\lambda^{(1)})^2(\lambda^{(2)})^4 - 1}. \tag{4.35}$$

This universal relation is applicable when the three principal stretches are distinct and under a plane stress state. This somewhat limits its applicability, as experimental data for general biaxial loading require specialised equipment to obtain and are not commonly reported in the literature. Experimental data are much more readily available for uniaxial and equibiaxial tension and compression, which are considered in the subsequent universal relations.

Uniaxial and equibiaxial tension. Consider uniaxial tension (UT) and equibiaxial tension (EBT). In these two loading cases, the non-zero stresses are respectively given by:

$$\sigma_{UT} = 2\left(\lambda_{UT}^2 - \frac{1}{\lambda_{UT}}\right)\left(\frac{\partial \Psi}{\partial I_1} + \frac{1}{\lambda_{UT}}\frac{\partial \Psi}{\partial I_2}\right), \tag{4.36}$$

$$\sigma_{EBT} = 2\left(\lambda_{EBT}^2 - \frac{1}{\lambda_{EBT}^4}\right)\left(\frac{\partial \Psi}{\partial I_1} + \lambda_{EBT}^2\frac{\partial \Psi}{\partial I_2}\right). \tag{4.37}$$

If the free energy depends only on I_1, and if λ_{UT} and λ_{EBT} are evaluated at the same value of I_1, then the following relation between principal stresses and stretches holds:

$$\frac{\sigma_{UT}}{\sigma_{EBT}} = \frac{\left(\lambda_{UT}^2 - \lambda_{UT}^{-1}\right)}{\left(\lambda_{EBT}^2 - \lambda_{EBT}^{-4}\right)}. \tag{4.38}$$

The condition that the stretches in the two loading cases correspond to the same I_1 requires that:

$$\lambda_{UT}^2 + 2\lambda_{UT}^{-1} = 2\lambda_{EBT}^2 + \lambda_{EBT}^{-4}. \tag{4.39}$$

Factorising the above relation gives:

$$(\lambda_{UT} - \lambda_{EBT}^{-2})(\lambda_{UT}^2 + \lambda_{EBT}^{-2}\lambda_{UT} - 2\lambda_{EBT}^2)\lambda_{UT}^{-1} = 0. \tag{4.40}$$

Therefore, the tensile stretches in the uniaxial and equibiaxial tension tests which give the same I_1 are related by:

$$\lambda_{UT} = \frac{1}{2\lambda_{EBT}^2}\left(\sqrt{1+8\lambda_{EBT}^6}-1\right). \tag{4.41}$$

The other admissible root $\lambda_{UT} = \lambda_{EBT}^{-2}$ maps to a uniaxial compression test and is not considered. The universal relation (4.39) can be used to assess I_2 dependence from uniaxial and equibiaxial tensile data in the following way. For each tensile stretch value in the equibiaxial test, calculate the stretch in the uniaxial tension test which gives the same I_1 using relation (4.41). Next evaluate condition (4.38). If it is not satisfied, it implies that the free energy function depends on I_2. Note that the converse is generally not true: satisfaction of condition (4.38) at a given I_1 does not necessarily guarantee that Ψ is independent of I_2.

Uniaxial tension and compression. Now consider the non-zero stresses under uniaxial tension (UT) and uniaxial compression (UC):

$$\sigma_{UT} = 2\left(\lambda_{UT}^2 - \frac{1}{\lambda_{UT}}\right)\left(\frac{\partial\Psi}{\partial I_1} + \frac{1}{\lambda_{UT}}\frac{\partial\Psi}{\partial I_2}\right), \tag{4.42}$$

$$\sigma_{UC} = 2\left(\lambda_{UC}^2 - \frac{1}{\lambda_{UC}}\right)\left(\frac{\partial\Psi}{\partial I_1} + \frac{1}{\lambda_{UC}}\frac{\partial\Psi}{\partial I_2}\right). \tag{4.43}$$

Evaluating these expressions at the same value of I_1, and assuming that the free energy is independent of I_2, the following is obtained:

$$\frac{\sigma_{UT}}{\sigma_{UC}} = \frac{\lambda_{UT}^2 - \frac{1}{\lambda_{UT}}}{\lambda_{UC}^2 - \frac{1}{\lambda_{UC}}}. \tag{4.44}$$

The axial stretches in uniaxial tension and compression tests which give the same value of I_1 are related by:

$$\lambda_{UT} = \frac{\lambda_{UC}}{2}\left(\sqrt{1+\frac{8}{\lambda_{UC}^3}}-1\right). \tag{4.45}$$

which is readily obtained from Eq. (4.41) by noting the correspondence between the stretches in a tensile equibiaxial test and in a compressive uniaxial test: $\lambda_{UC} = \lambda_{EBT}^{-2}$.

The universal relation (4.44) can be verified graphically using the Mooney stress, which is defined as:

$$\mathcal{M} = \frac{\sigma}{\lambda^2 - \lambda^{-1}}, \tag{4.46}$$

The universal relation (4.44) means that the Mooney stress $\mathcal{M}$, when represented as a function of I_1, is the same in uniaxial tension and uniaxial compression if the material response is independent of I_2.

4.4 Results

To assess fitting performance, we fit models to three literature datasets for the mechanical response of rubber-like materials under distinct states of deformation, and make comparisons based on the quality of these fits. In each case, we find that the quality of the model fits correlates to the degree of I_2-dependence the model exhibits.

4.4.1 Data of Kawabata et al. (1981)

To begin the experimental data of Kawabata et al. (1981) for an isoprene rubber vulcanisate under general biaxial tension are considered. The rubber is under plane stress with $\sigma_3 = 0$. During loading, the stretch $\lambda^{(1)}$ is held constant and the other stretch $\lambda^{(2)}$ is varied, allowing states of deformation ranging from unaxial tension to equibiaxial tension to be probed. To investigate fitting performance, the λ-based and ν-based micromechanial models are fitted to the experimental data for uniaxial and equibiaxial tension simultaneously using least squares minimisation. The models calibrated using these data are then used to predict the material response in intermediate deformation states. The fitting error to be minimised is defined as:

$$\epsilon = \sum_{i=1}^{N_p} \left(\sigma_e^{(i)} - \sigma_m^{(i)}\right)^2. \tag{4.47}$$

where N_p represents the number of data points, $\sigma_e^{(i)}$ the i^{th} experimental stress data point and $\sigma_m^{(i)}$ the corresponding stress calculated using the model. Other choices of objective

function are possible, such as those based on absolute differences between points, differences in areas between curves among others, those where error in both the independent and dependent variable are considered (see Birkes and Dodge (2011) for an overview of alternative curve fitting methods). The data do not feature any obvious outliers (which if were present pollute the results of least squares approaches) and the data are originally reported point-wise by Kawabata et al. (1981), and so a point difference method was followed here. The least squares error is minimised using the minimize function in the Python Scipy optimisation toolbox following the Broyden-Fletcher-Goldfarb-Shanno (BFGS) method (Fletcher, 1987). This is a quasi-Newton method and achieves a good rate of convergence without requiring the evaluation of a Jacobian matrix at every increment. Best-fit parameters and the minimised fitting error for each model are reported in Table 4.2.

Figure 4.2 shows the full-network model predictions considering λ-based (Fig. 4.2(a)) and ν-based (Fig. 4.2(b)) tube models, along with experimental data for uniaxial and equibiaxial tension. Both models predict a stiffer response under equibiaxial tension than under uniaxial tension. However, the λ-based full-network fails to capture the response under equibiaxial tension accurately. In contrast, the ν-based full-network tube model provides an excellent fit (note that modelling and experimental curves for equibiaxial tension practically coincide). Model predictions for general biaxial loading using the same set of parameters are compared to experimental data in Fig. 4.3. In the figures, each line corresponds to a constant value of the principal stretch $\lambda^{(1)}$, as indicated. The λ-based model predictions (Figs 4.3(a) and (b)) deviate significantly from the experimental data, particularly at the highest values of $\lambda^{(1)}$. For a given value of $\lambda^{(1)}$, the error is the smallest under uniaxial states of deformation, and increases monotonically with $\lambda^{(2)}$. In contrast, the ν-based model captures the general biaxial response well for all modes of deformation and all degrees of deformation. Both σ_1 and σ_2 are well predicted. Note that Kawabata et al. (1981) also reported experimental data for $1.04 \leq \lambda^{(1)} \leq 1.12$. For these smaller $\lambda^{(1)}$ values, the agreement between experimental data and theoretical predictions increases for both models. For clarity of presentation, here we only show results for the highest $\lambda^{(1)}$

values.

The relative performance of the λ-based and ν-based full-network models can be correlated to their I_2 sensitivity. To this end, we first consider the universal relation (4.38), which applies to uniaxial and equibiaxial tension data. For convenience, we define the following indicator function as a measure of deviation from the universal relation:

$$\mathcal{G}_1(I_1) := \frac{\left(\lambda_{UT}^2 - \lambda_{UT}^{-1}\right)}{\left(\lambda_{EBT}^2 - \lambda_{EBT}^{-4}\right)} - \frac{\sigma^{UT}}{\sigma^{EBT}}, \tag{4.48}$$

so that an I_2 independent response implies $\mathcal{G}_1 = 0$. In Eq. (4.48), λ_{UT} and λ_{EBT} are tensile stretches calculated from I_1 for uniaxial and equibiaxial tension, respectively. The indicator function calculated for experimental and modelling data reported in Fig. 4.2 is shown in Fig. 4.4. Experimental data show a clear deviation from the universal relation, which is well reproduced by the ν-based full-network model. In contrast, the λ-based full-network model is much less sensitive to I_2 (the magnitude of the indicator function is smaller). We also note that the experimental indicator function corresponding to the ν-based model tends to a plateau at large stretches, which is in agreement with experimental data, whereas the indicator function for the λ-based model keeps increasing as the stretches increase.

Alternatively, we may also consider the universal relation (4.35), which applies to general biaxial tension with distinct principal stretches. Similarly to the previous case, we define an indicator function:

$$\mathcal{G}_2(\lambda^{(1)}, \lambda^{(2)}) := \frac{\left((\lambda^{(1)})^4(\lambda^{(2)})^2 - 1\right)}{\left((\lambda^{(1)})^2(\lambda^{(2)})^4 - 1\right)} - \frac{\sigma_1}{\sigma_2}, \tag{4.49}$$

so that an I_2 independent response corresponds to $\mathcal{G}_2 = 0$. The indicator function calculated based on the experimental data for general biaxial loading (neglecting data points with repeated principal stretches) and model predictions for the λ-based and ν-based models are shown in Fig. 4.5. Again, the experimental data show I_2 dependence ($\mathcal{G}_2$ is non-zero). The ν-based model (Fig. 4.5(b)) is able to recover the experimental I_2

dependence at large values of $\lambda^{(1)}$ and $\lambda^{(2)}$, where the λ-based model shows little sign of I_2 dependence (Fig. 4.5(a)). For smaller values of $\lambda^{(1)}$, both models fail to recover the experimental trend. However, in this regime the indicator function is extremely sensitive to measurement errors as both denominators in Eq. (4.49) tend to zero.

We next consider the three-chain and eight-chain averaging schemes as a simplification of the full-network model. Model parameters obtained by fitting the experimental data for uniaxial and equibiaxial tension are shown in Table 4.2. Comparisons between experimental data and model fits are shown in Figs 4.6(a) and (b) for the λ-based and ν-based models, respectively. Corresponding values of the indicator function (4.48) are shown in Figs 4.6(c) and (d). The eight-chain λ-based model, similarly to the the λ-based full-network model, is unable to predict both responses simultaneously. However, the λ-based three-chain model is able to achieve good agreement with the data for both loading modes. In contrast, the ν-based models are able to predict the experimental response equally well under any averaging scheme. The ability of all of these models to capture simultaneously the uniaxial and equibiaxial responses is reflected in the indicator function. The λ-based three-chain model and all of the ν-based models are able to capture the experimental curve, whereas the λ-based full-network model shows limited I_2 dependence. The eight-chain λ-based model is independent of I_2.

Tube model	Integration	nk_BT/MPa	N	nk/MPa	β	Error/(MPa)^2
$\psi_c^{(\lambda)} = k\bar{\lambda}^\beta$	Full-network	0.32	2500	0.12	−3.5	0.42
	Three-chain	0.27	2500	2.0	−0.55	0.011
	Eight-chain	0.21	12	740	0.00079	0.69
$\psi_c^{(\nu)} = k\bar{\nu}^\beta$	Full-network	0.28	620	0.56	0.66	0.016
	Three-chain	0.27	630	2.3	0.52	0.012
	Eight-chain	0.29	630	0.36	0.73	0.017

Table 4.2: Best-fit parameters for models fitted simultaneously to the uniaxial and equibiaxial tensile data of Kawabata et al. (1981) under different averaging schemes.

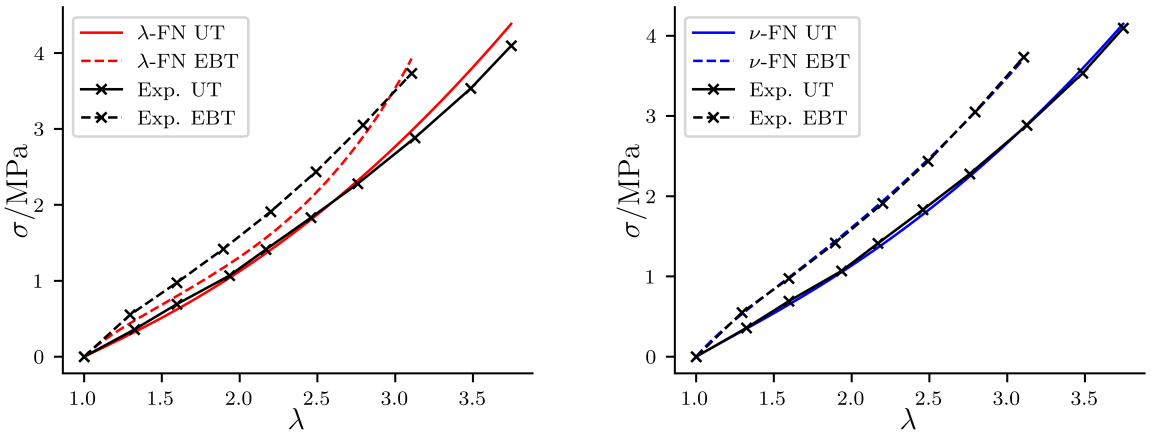


Figure 4.2: Comparison between model predictions and experimental data of Kawabata et al. (1981) for uniaxial (UT) and equibiaxial tension (EBT). Non-affine tube models are considered, with (a) λ-based and (b) ν-based tube models. Full-network averaging is used.

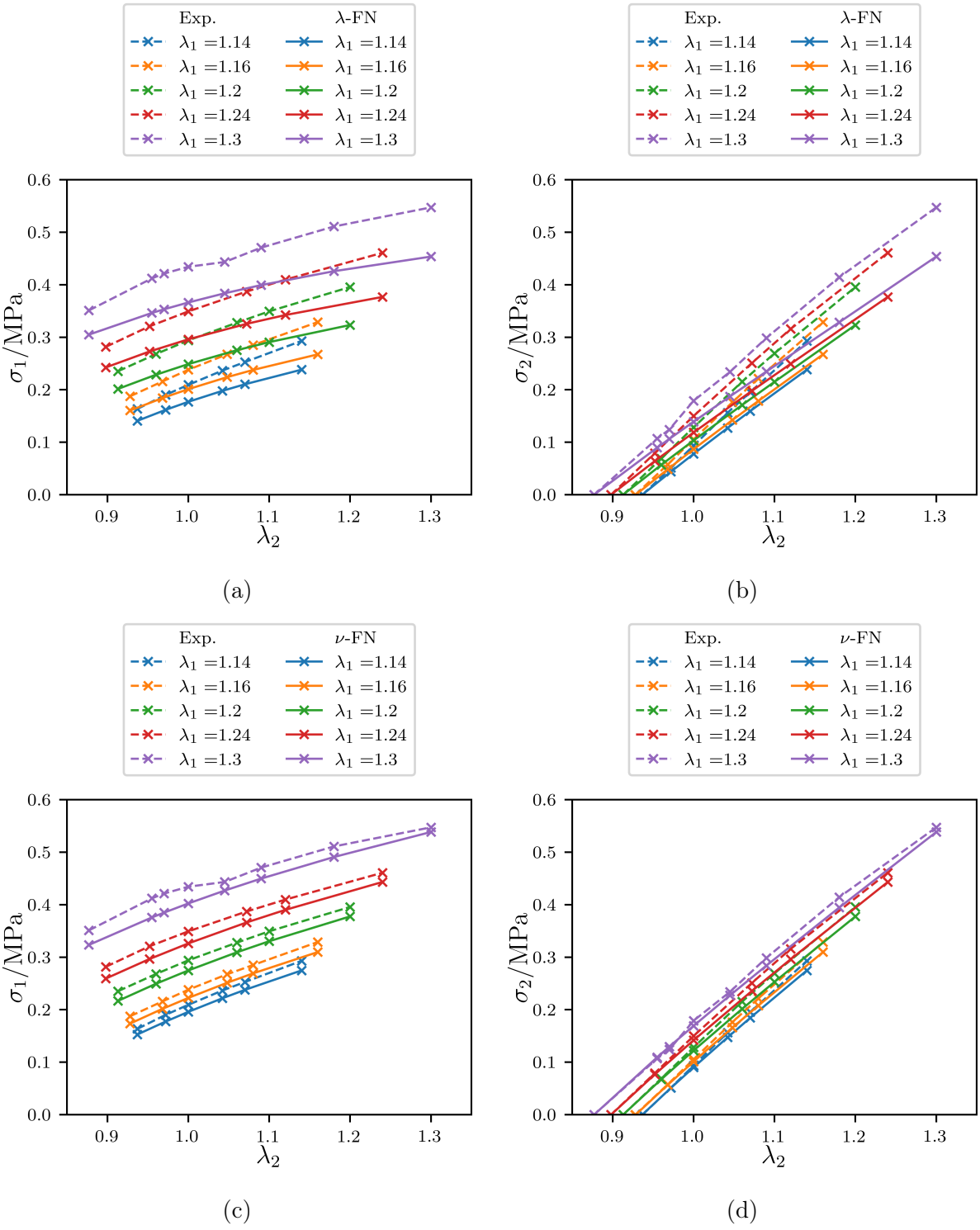


Figure 4.3: Comparison between the prediction of the full-network (a)-(b) λ-based tube model and (c)-(d) ν-based tube model, and the experimental data of Kawabata et al. (1981) for general biaxial loading.

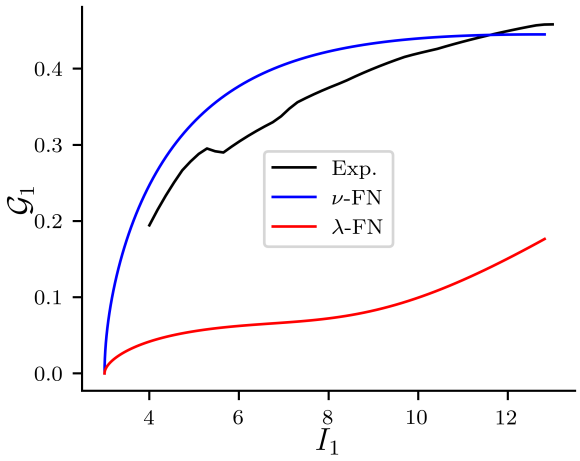
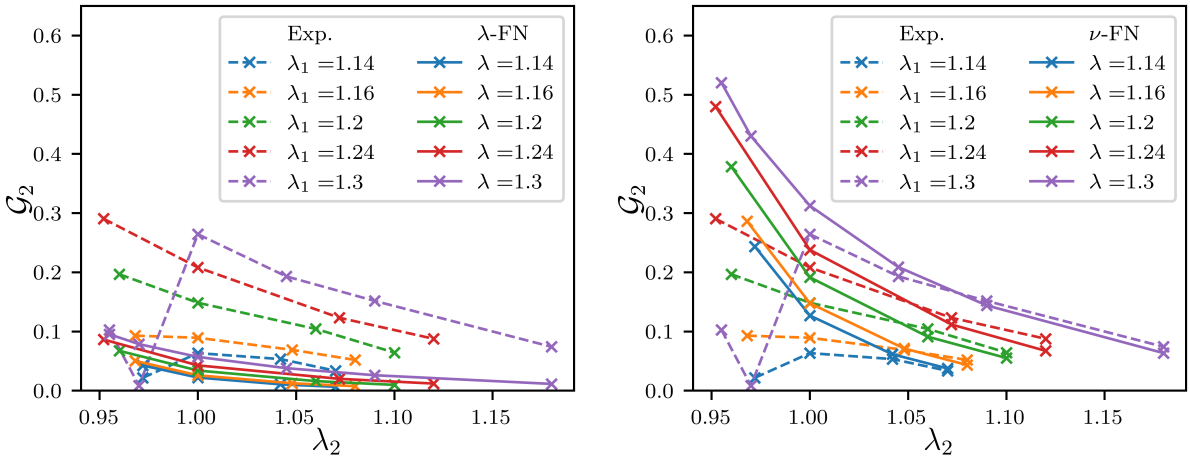


Figure 4.4: The I_2 indicator function $\mathcal{G}_1(I_1)$ for uniaxial and equibiaxial tension, Eq. (4.48), applied to the experimental data of Kawabata et al. (1981) and to model predictions using full-network λ-based and ν-based tube models.



(a) (b)

Figure 4.5: The I_2-indicator function $\mathcal{G}_2(\lambda^{(1)}, \lambda^{(2)})$ for general biaxial loading, Eq. (4.49), applied to the experimental data of Kawabata et al. (1981) and model predictions using full-network (a) λ-based and (b) ν-based tube models.

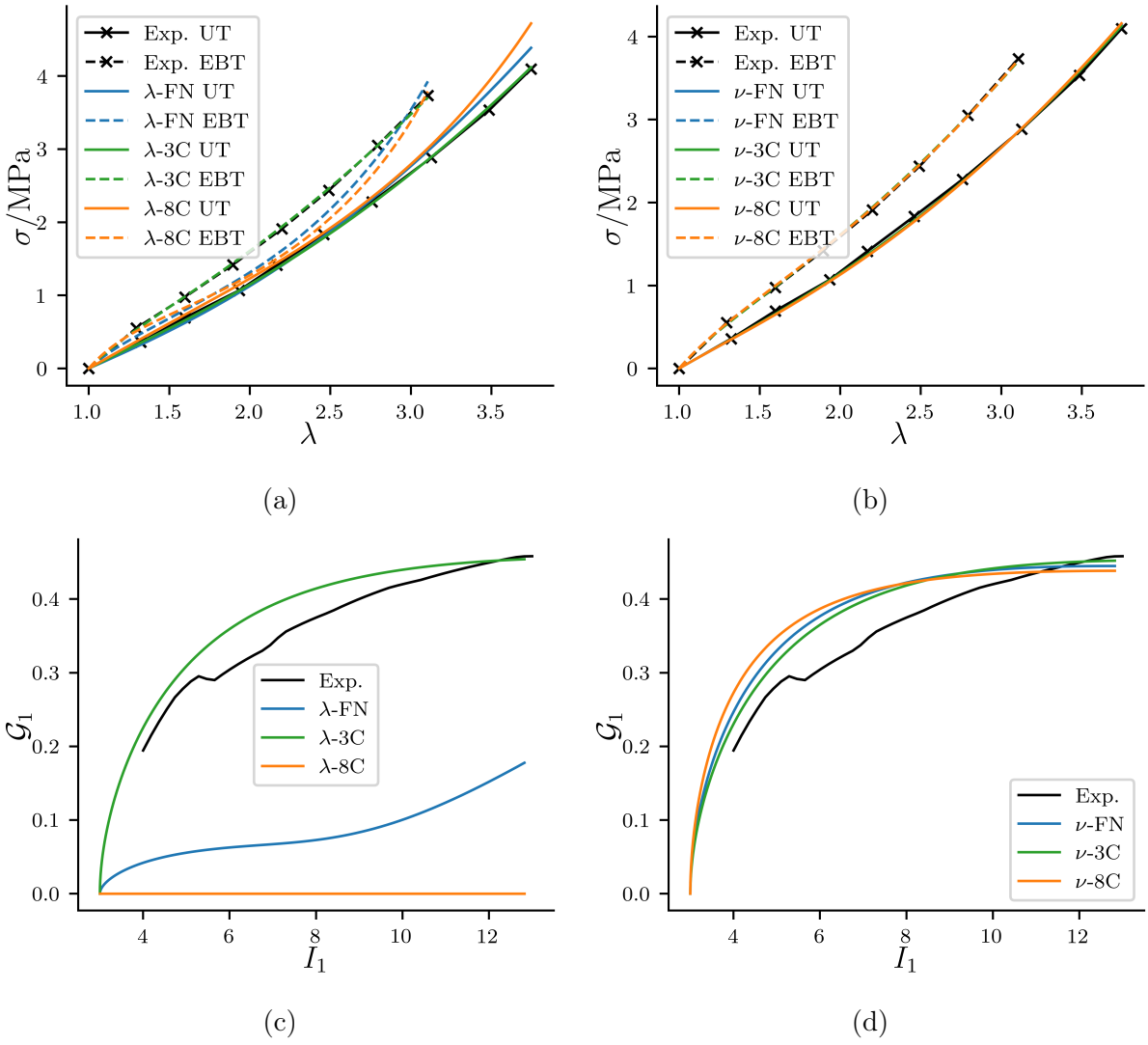


Figure 4.6: Comparison between model predictions and experimental data of Kawabata et al. (1981) for uniaxial (UT) and equibiaxial tension (EBT), using (a) λ-based tube models and (b) ν-based tube models in combination with the full-network (FN), three-chain (3C) and eight-chain (8C) averaging schemes. I_2 indicator function (4.48) for (c) λ-based and (d) ν-based tube models.

4.4.2 Data of Dechnarong et al. (2021)

We next consider experimental data reported by Dechnarong et al. (2021) for a thermoplastic elastomer (SEBS) subjected to uniaxial and equibiaxial tension. A similar fitting procedure was adopted as in the previous section, and best-fit parameters for the various tube models are reported in Table 4.3.

Figs 4.7(a) and (b) show the model predictions along with the experimental data. The λ-based models show different fitting performances under the different averaging schemes. The full-network model describes the uniaxial response well at small deformations, but departs from the experimental curve at large deformation and underpredicts the equibiaxial response up to moderate deformation. The eight-chain λ-based model insufficiently distinguishes the different responses and underpredicts the initial slope of the stress-stretch curve. In contrast, the three-chain λ-based model achieves near perfect agreement. The ν-based model gives good agreement with the experimental data under all of the averaging schemes considered.

Figs 4.7(c) and (d) show the indicator function (4.48) corresponding to the results in Figs 4.7(a) and (b). The full-network λ-based model shows I_2 dependence only at moderate stretches, whereas the three-chain λ-based model shows I_2 dependence consistent with experimental data. The eight-chain λ-based model is independent of I_2. The indicator function calculated for the ν-based models is very close to the experimental one for all averaging schemes. The degree of I_2 dependence exhibited by all of these schemes correlates with their ability to distinguish between uniaxial and equibiaxial tension.

Tube model	Integration	nk_BT/MPa	N	nk/MPa	β	Error/(MPa)^2
$\psi_c^{(\lambda)} = k\bar{\lambda}^\beta$	Full-network	0.28	2500	0.46	-3.0	39
	Three-chain	0.18	2500	1.1	-0.98	1.1
	Eight-chain	0.48	1700	3200	-0.00054	100
$\psi_c^{(\nu)} = k\bar{\nu}^\beta$	Full-network	0.15	39	0.95	0.88	0.89
	Three-chain	0.15	85	1.5	0.91	1.1
	Eight-chain	0.15	21	1.0	0.76	0.32

Table 4.3: Best-fit parameters for models fitted simultaneously to the uniaxial and equibiaxial tensile data of Dechnarong et al. (2021) under different averaging schemes.

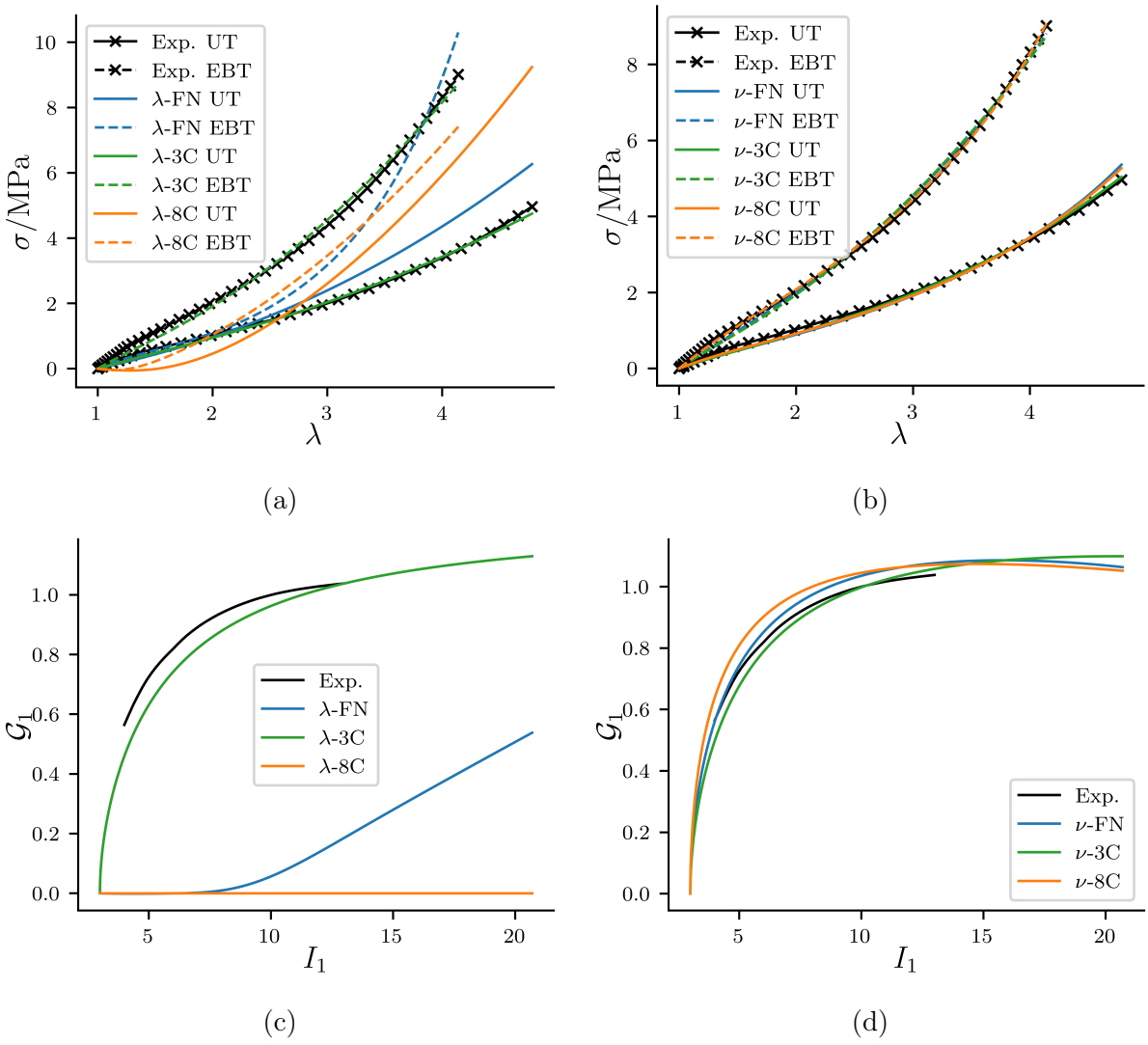


Figure 4.7: Comparison between model predictions and experimental data of Dechnarong et al. (2021) for uniaxial (UT) and equibiaxial tension (EBT), using (a) λ-based tube models and (b) ν-based tube models in combination with the full-network (FN), three-chain (3C) and eight-chain (8C) averaging schemes. I_2 indicator function (4.48) for (c) λ-based and (d) ν-based tube models.

4.4.3 Data of Bechir et al. (2006)

Finally, we consider the tension-compression data reported by Bechir et al. (2006) for a carbon black-filled natural rubber. In the experiment, the material has been pre-conditioned to render it effectively hyperelastic and eliminate the Mullins effect. The data are shown in Fig 4.8 with model predictions obtained with the λ- and ν-based models under different averaging schemes. Corresponding best-fit parameters are shown in Table 4.4.

All models are able to capture the upturns in the stress-stretch curve under tension and compression and achieve broadly similar fits in the moderate stretch region except for the λ-based eight-chain model, which fails to capture the stress upturn in compression. Close inspection of the phantom and tube contributions for each model reveals that the stress upturn in tension arises from the extensibility limit in the freely-jointed chain model (as expected), whereas the stress upturn in compression is due to the tube contribution, which in the λ-based eight-chain model is unable to capture the experimental trend.

I_2 dependence is investigated by plotting the Mooney stress (4.46) against I_1, see Figs 4.9 (a) and (b). Experimental curves show a different response under uniaxial tension and compression, which indicates I_2 dependence according to the universal relation (4.44). This is well predicted by the λ-based full-network and three-chain models. However, the λ-based eight-chain model shows the same Mooney stress under uniaxial tension and compression, implying that this model is I_2 independent. In contrast, all three ν-based formulations predict significant I_2 dependence in general agreement with the experimental data.

Equivalently, we may define an additional indicator function measuring deviation from the universal relation (4.44):

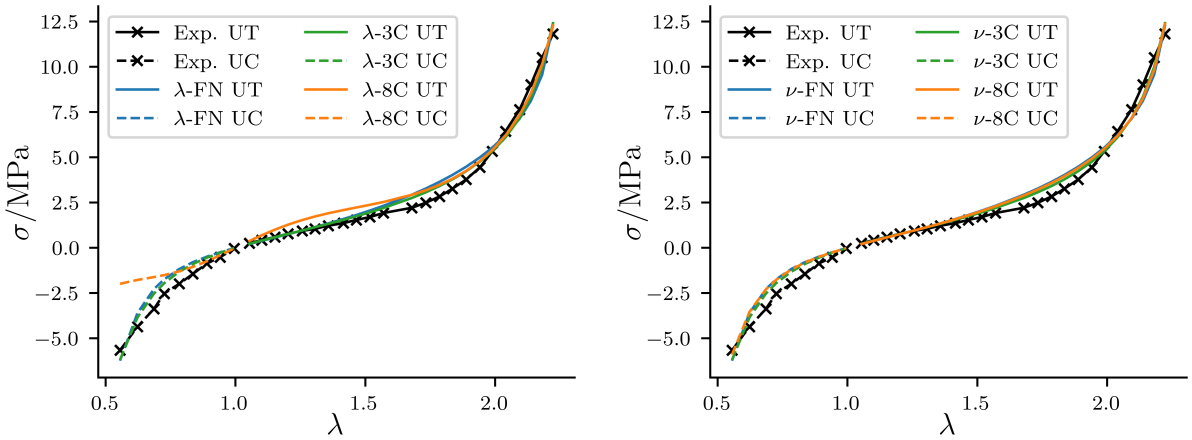
$$\mathcal{G}_3 := \frac{\lambda_{UT}^2 - \lambda_{UT}^{-1}}{\lambda_{UC}^2 - \lambda_{UC}^{-1}} - \frac{\sigma_{UT}}{\sigma_{UC}}. \tag{4.50}$$

such that I_2 independence implies $\mathcal{G}_3 = 0$. Figs 4.9 (c)-(d) show this indicator for the

data of Bechir et al. (2006). As expected, Figs 4.9 (c)-(d) convey the same information as Figs 4.9 (a)-(b): all models are able to recover the experimental I_2 dependence, except the λ-based eight-chain model, which is independent of I_2. Here we included both the Mooney-I_1 plot and the indicator function plot for the sake of illustration, as to the best of our knowledge, neither of these tests had previously been used to assess I_2 dependence from uniaxial tension and compression data.

Tube model	Integration	nk_BT/MPa	N	nk/MPa	β	Error/(MPa)^2
$\psi_c^{(\lambda)} = k\bar{\lambda}^\beta$	Full-network	0.54	5.1	0.20	−8.7	9.9
	Three-chain	0.35	5.6	0.32	−4.3	5.7
	Eight-chain	0.52	2.3	−0.48	−9.7	31
$\psi_c^{(\nu)} = k\bar{\nu}^\beta$	Full-network	0.54	5.1	0.20	5.7	10
	Three-chain	0.35	5.6	0.32	4.3	5.7
	Eight-chain	0.18	2.1	0.59	5.4	8.4

Table 4.4: Best-fit parameters for models fitted simultaneously to the uniaxial and equibiaxial tensile data of Bechir et al. (2006) under different averaging schemes.



(a) (b)

Figure 4.8: Comparison between model predictions and experimental data of Bechir et al. (2006) for uniaxial tension (UT) and compression (UC), using (a) λ-based tube models and (b) ν-based tube models in combination with the full-network (FN), three-chain (3C) and eight-chain (8C) averaging schemes.

4.5 Discussion

Main findings from the comparison of model predictions to experimental data can be summarised as follows:

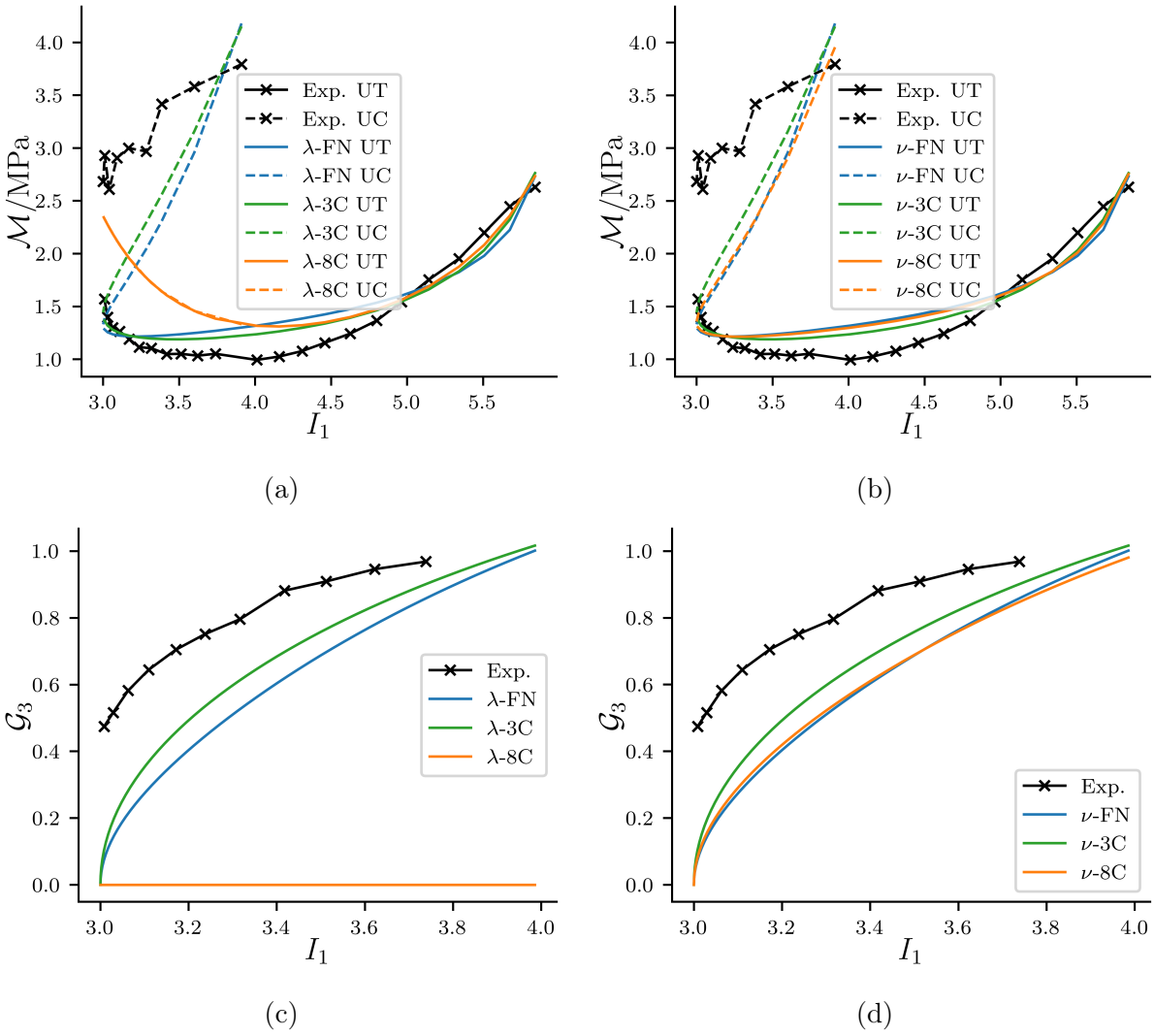


Figure 4.9: (a)-(b) Comparison of Mooney stress-I_1 responses obtained using various orientation averaging schemes to the experimental data of Bechir et al. (2006). (c)-(d) Corresponding I_2 indicator functions, Eq. (4.50).

1. ν-based tube models are able to provide a good fit for a range of experimental data under various loading conditions, regardless of the orientation-averaging scheme used (full-network, three-chain or eight-chain averaging).

2. λ-based tube models can only provide a good fit under various loading modes when used in conjunction with three-chain averaging.

3. Fitting ability of all the models is directly correlated to their I_2 sensitivity, as measured via their departure from universal relations valid for I_2-independent behaviour.

As our main findings hinge on the validity of our fitting procedure, we will begin the

discussion of the results by first exploring whether or not our findings hold true when other fitting approaches are followed. It is often the case when calibrating large deformation constitutive models to experimental data that the objective function is not convex and features several local minima such that best fit parameters are not necessarily unique and a true global minimum is challenging to identify. In the field of optimisation, the Basin-hopping algorithm (Wales and Doye, 1997) is a method developed for determining global minima in such circumstances. It is an iterative two-step procedure where firstly a random step is taken in the parameter space and then a local minimisation step takes place to determine the nearest minimum to that point. This point and the corresponding value of the objective function are stored. These steps are repeated a sufficient number of times and an estimate of the global minimum is determined from the collection of local minima.

To explore whether or not the best fit parameters identified are near the global minimum, a Basin-hopping search is conducted using the SciPy Optimize basinhopping function over 100 iterations for fitting both formulations of tube model to the data of Kawabata et al. (1981) under all three of the integration schemes considered. The original best fit parameters quoted in Table 4.2 (found using the BFGS method) are used to initialise the scheme, and the least squares objective function Eq. (4.47) is minimised. The best fit parameters found using the basin hopping did not differ from those found the least squares/BFGS method. We take this to indicate that our findings based on the BFGS method are fairly robust.

To check if our findings hold true using alternative objective functions to the least squares function, we also fit the data using the absolute difference error. That is, we consider minimisation of the error $\epsilon^{(abs)}$:

$$\epsilon^{(abs)} = \sum_{i=1}^{N_p} \left| \sigma_e^{(i)} - \sigma_m^{(i)}) \right|, \tag{4.51}$$

where again N_p represents the number of data points, $\sigma_e^{(i)}$ the i^{th} experimental stress data

point and $\sigma_m^{(i)}$ the corresponding stress calculated using the model. We minimise this error again for the data of Kawabata et al. (1981) using the BFGS method following the SciPy Optimize minimise function (Fletcher, 1987). The resulting best-fit parameters are reported in Table 4.5. Inspection of the reported error values again support the conclusion that the ν-based tube models generally perform better than the λ-based models. However in this approach, the three-chain λ-based model did not perform comparably to the ν-based three-chain model (as it did following the least squares approach). Despite this fact, we assume our general findings using the least squares approach are generally robust and attribute this discrepancy to problems with minimising the absolute error difference. As we shall discuss later, it can be shown that in the case of the three-chain scheme, both families of tube model can be made equivalent by an appropriate choice of material parameters, thus indicating a problem with minimising the error function in this scenario. This is perhaps due to the non-smoothness of the absolute value operator.

Tube model	Integration	nk_BT/MPa	N	nk/MPa	β	Error/(MPa)^2
$\psi_c^{(\lambda)} = k\bar{\lambda}^\beta$	Full-network	0.32	2500	0.082	-3.5	2.07
	Three-chain	0.32	2500	0.00021	-3.46	2.18
	Eight-chain	0.32	2500	-0.040	-3.46	3.11
$\psi_c^{(\nu)} = k\bar{\nu}^\beta$	Full-network	0.28	620	0.56	0.66	0.41
	Three-chain	0.28	630	0.82	0.74	0.48
	Eight-chain	0.2	630	0.72	0.51	0.64

Table 4.5: Best-fit parameters for models fitted simultaneously to the uniaxial and equibiaxial tensile data of Kawabata et al. (1981) under different averaging schemes using an error function based on absolute differences rather than squared differences.

To further explore the I_2 sensitivity of various tube formulations, we calculated the partial derivatives of the tube contribution to the free energy, $\partial\Psi_c/\partial I_1$ and $\partial\Psi_c/\partial I_2$, as described in Section 4.3. Partial derivatives (normalised by (nk)) are shown as a function of the exponent β for a state of pure shear with $\lambda^{(1)} = 2$, $\lambda^{(2)} = 0.5$ and $\lambda^{(3)} = 1$ in Fig. 4.10. Pure shear was considered because the three principal stretches are distinct and formulas (4.31) and (4.32) can be used. The range of exponent values was chosen to be representative of best-fit exponent values obtained in the previous section. For the λ-based full-network model (Figs 4.10 (a) and (b)), both $\partial\Psi_c/\partial I_1$ and $\partial\Psi_c/\partial I_2$ are small relative to (nk) and have a similar order of magnitude across the considered range of

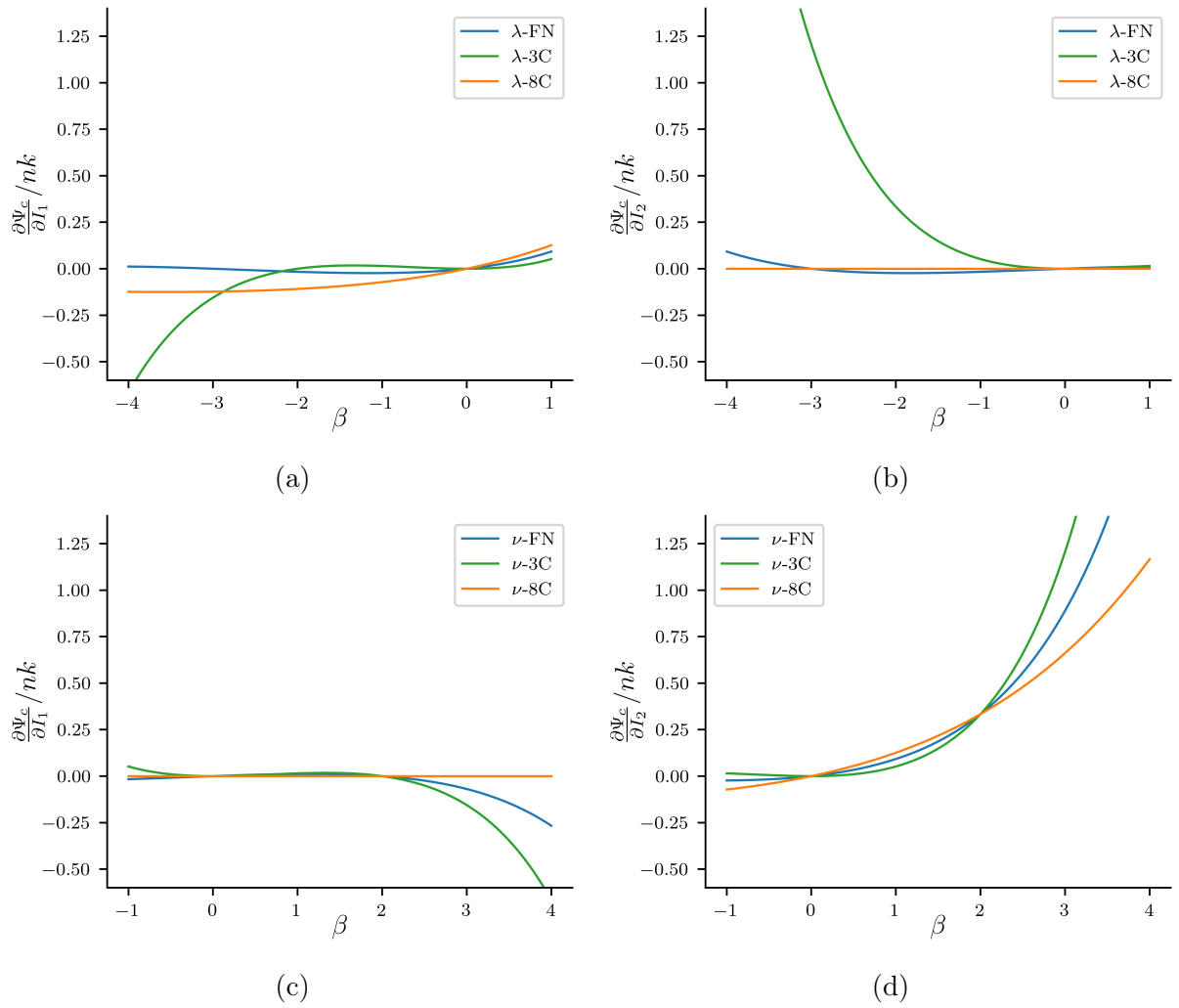


Figure 4.10: Direct evaluation of the normalised partial derivatives $\partial\Psi_c/\partial I_1$ and $\partial\Psi_c/\partial I_2$ as a function of the tube exponent β in a pure shear test ($\lambda^{(1)} = 2$, $\lambda^{(2)} = 0.5$ and $\lambda^{(3)} = 1$), as predicted by (a)-(b) λ-based and (c)-(d) ν-based tube models combined with full-network (FN), three-chain (3C) and eight-chain (8C) averaging.

β-values. The λ-based eight-chain model shows zero I_2 dependence. In contrast, the λ-based three-chain model shows significant I_2 dependence at large negative values of β. Regarding ν-based models, all three averaging schemes lead to significant $\partial\Psi_c/\partial I_2$, which increases as β increases (Fig. 4.10(d)). The three-chain and full-network models also show significant negative $\partial\Psi_c/\partial I_1$ at large positive values of β, while the tube model is independent of I_1 when used in combination with eight-chain averaging (Fig. 4.10(c)). These observations for a broader range of β-values are consistent with results of Section 4.4.

The I_2 (resp. I_1) independence of the λ-based (resp. ν-based) eight-chain model is easily

understood. Using Expression (2.12) of the invariants in terms of the principal stretches, Eq. (4.19) directly gives the line-stretch of the representative chains in the λ-based tube model as $\lambda^{8C} = \sqrt{I_1/3}$, and Eq. (4.20) gives the area-stretch of the representative chains in the ν-based tube model as $\nu^{8C} = \sqrt{I_2/3}$. Therefore, Eq. (4.21) provides, for the λ-based tube model:

$$\Psi_c^{8C(\lambda)} = n\psi_c^{(\lambda)}\left(\sqrt{\frac{I_1}{3}}\right) = nk\left(\frac{I_1}{3}\right)^{\beta/2}, \tag{4.52}$$

and for the ν-based tube model:

$$\Psi_c^{8C(\nu)} = n\psi_c^{(\nu)}\left(\sqrt{\frac{I_2}{3}}\right) = nk\left(\frac{I_2}{3}\right)^{\beta/2}, \tag{4.53}$$

Thus, λ-based tube models only bring I_1 dependence in the eight-chain averaging approximation, while ν-based tube models only bring I_2 dependence in this averaging scheme. Note that identical expressions are obtained by adopting the stretch-average full-network approximation proposed by Beatty (2003). In this approach, the macroscopic tube energy is obtained by evaluating the λ-based tube energy using the full-network average of the squared line-stretch as argument:

$$\Psi_c^{(\lambda)} = n\psi_c^{(\lambda)}\left(\sqrt{\langle\bar{\lambda}^2\rangle}\right) = nk\langle\bar{\lambda}^2\rangle^{\beta/2}, \tag{4.54}$$

and, for the ν-based tube energy, using the full-network average of the squared area-stretch as argument:

$$\Psi_c^{(\nu)} = n\psi_c^{(\nu)}\left(\sqrt{\langle\bar{\nu}^2\rangle}\right) = nk\langle\bar{\nu}^2\rangle^{\beta/2}. \tag{4.55}$$

Expressions (4.54) and (4.55) are respectively identical to Expressions (4.52) and (4.53), recalling the identities (Kearsley, 1989) (see also Appendix C.1 and C.2):

$$\langle\bar{\lambda}^2\rangle = \frac{I_1}{3}, \quad \langle\bar{\nu}^2\rangle = \frac{I_2}{3}. \tag{4.56}$$

The I_2 dependence of ν-based eight-chain tube formulations has previously been pointed

out by several authors (Kroon, 2011; Ehret, 2015; Khiêm and Itskov, 2016; Anssari-Benam et al., 2021). Setting $\beta = 2$ in Eq. (4.53), one recovers the C_2-term of the Mooney-Rivlin model, with $C_2 = nk/3$. For $\beta = 1$, one recovers the phenomenological Carroll model (Carroll, 2011). In general, the model (4.53) is of the Rivlin-Saunders type (Rivlin and Saunders, 1951).

Regarding the three-chain models, one should first recognise that λ-based and ν-based tube formulations are in fact mathematically equivalent. Their contributions to the macroscopic free energy are respectively given by:

$$\Psi_c^{3C(\lambda)} = \frac{nk}{3}\left((\lambda^{(1)})^{\beta} + (\lambda^{(2)})^{\beta} + (\lambda^{(3)})^{\beta}\right), \tag{4.57}$$

and:

$$\Psi_c^{3C(\nu)} = \frac{(nk)'}{3}\left((\lambda^{(1)})^{-\beta'} + (\lambda^{(2)})^{-\beta'} + (\lambda^{(3)})^{-\beta'}3\right), \tag{4.58}$$

where we have used the condition of incompressibility to express the principal area-stretches in Eq. (4.15) as: $\nu^{(1)} = \lambda^{(2)}\lambda^{(3)} = (\lambda^{(1)})^{-1}$, $\nu^{(2)} = \lambda^{(1)}\lambda^{(3)} = (\lambda^{(2)})^{-1}$ and $\nu^{(3)} = \lambda^{(1)}\lambda^{(2)} = (\lambda^{(3)})^{-1}$. Expressions (4.57) and (4.58) are identical provided that $\beta' = -\beta$ (and that $(nk) = (nk)'$). This is consistent with expression (4.29) of the tube shear modulus, which involves β^2. In light of this, the same level of performance exhibited by the two three-chain formulations was expected. The best-fit parameters reported in Tables 4.2-4.4 indeed show the expected correspondence between λ-based and ν-based tube parameters. The expected relations $\beta' = -\beta$ and $(nk) = (nk)'$ are however not exactly satisfied in Tables 4.2 and 4.3, which is attributed to the fact that best-fit parameters are non-unique (Ogden et al., 2004). This is confirmed by the fact that the fitting error associated with λ-based and ν-based models is the same in these two examples. Using the set of parameters identified using the λ-based model to predict results with the ν-based model (upon switching the sign of β) does predict an identical response for all data sets, as expected. The mathematical equivalence between λ-based and ν-based three-chain tube models does not however explain their stronger I_2 sensitivity, as compared to their full-network counterpart. We note however that the affine tube model, obtained taking

$\beta = -2$ in the λ-based model (i.e. $\beta = 2$ in the ν-based model) leads again to the C_2 term of the Mooney-Rivlin model with $C_2 = nk/3$. It is also worth pointing out the formal similarity between the three-chain tube model and the one-term Ogden model (Ogden, 1972), previously noted by Kaliske and Heinrich (1999).

Some insights into the I_2 sensitivity of λ-based and ν-based full-network models can be gained by considering Taylor series expansions of the macroscopic tube energy. Detailed derivations are provided in Appendix D, along with a numerical verification for small stretches. The λ-based macroscopic tube energy admits the following series expansion about the full-network average of the squared line-stretch, $\langle \bar{\lambda}^2 \rangle$:

$$\Psi_c^{FN(\lambda)} = n\psi_c^{(\lambda)}\left(\sqrt{\frac{I_1}{3}}\right) + n\frac{2}{45}\frac{d^2 w_c^{(\lambda)}}{d\Lambda^2}\left(\frac{I_1}{3}\right)(I_1^2 - 3I_2) + \text{h.o.t.}, \tag{4.59}$$

where $\Lambda := \bar{\lambda}^2$ and $w_c^{(\lambda)}(\Lambda) := \psi_c^{(\lambda)}(\bar{\lambda})$. Therefore, to the lowest order, $\Psi_c^{FN(\lambda)}$ only depends on I_1 and coincides with the eight-chain model (4.52). The second invariant I_2 appears in the second-order term, but is coupled with I_1. Similarly, the series expansion of the ν-based full-network tube energy about the average squared area-stretch $\langle \bar{\nu}^2 \rangle$ is given by:

$$\Psi_c^{FN(\nu)} = n\psi_c^{(\nu)}\left(\sqrt{\frac{I_2}{3}}\right) + n\frac{2}{45}\frac{d^2 w_c^{(\nu)}}{d\Gamma^2}\left(\frac{I_2}{3}\right)(I_2^2 - 3I_1) + \text{h.o.t.}, \tag{4.60}$$

where we have used the notation $\Gamma := \bar{\nu}^2$ and $w_c^{(\nu)}(\Gamma) := \psi^{(\nu)}(\bar{\nu})$. This expression shows that, to the lowest order, the tube contribution to the macroscopic energy only depends on I_2 and is identical to the eight-chain expression (4.53). The comparison between Eqs (4.59) and (4.60) suggests that the stronger I_2 sensitivity in the ν-based full-network model arises from its lowest order term.

Similar series expansions can be constructed for the three-chain models, as detailed in

Appendix D. For the λ-based model, the tube energy can be expressed as:

$$\Psi_c^{3C(\lambda)} = n\psi_c^{(\lambda)}\left(\sqrt{\frac{I_1}{3}}\right) + n\frac{1}{9}\frac{d^2w_c^{(\lambda)}}{d\Lambda^2}\left(\frac{I_1}{3}\right)(I_1^2 - 3I_2) + \text{h.o.t.}, \tag{4.61}$$

and for the ν-based three-chain model:

$$\Psi_c^{3C(\nu)} = n\psi_c^{(\nu)}\left(\sqrt{\frac{I_2}{3}}\right) + n\frac{1}{9}\frac{d^2w_c^{(\nu)}}{d\Gamma^2}\left(\frac{I_2}{3}\right)(I_2^2 - 3I_1) + \text{h.o.t.}. \tag{4.62}$$

Expressions (4.61) and (4.62) only differ from their full-network counterparts (4.59) and (4.60) by a numerical factor in the second-order term (and by higher-order terms). Invoking the same argument as in the full-network case, one would conclude that the three-chain λ-based model is dominated by I_1, and the three-chain ν-based model is dominated by I_2. However, as demonstrated above, the two models are formally equivalent. This highlights the importance of higher-order terms on the role of invariants in the free energy function.

In addition to fitting performance, the ν-based tube model is also superior in that its best-fit parameters (nk) and β obtained from a given experimental data set are fairly consistent across all three integration schemes (under the caveat of non-uniqueness of best-fit parameters). This is not the case for the λ- based models, where best-fit parameters show a much larger variation across the different integration schemes for the same experimental data set, see Tables 4.2-4.4. Given the molecular basis of the tube model, one would hope for a low sensitivity of the parameters on the orientation averaging scheme used for the parameters to have a physical meaning, considering the three-chain and eight-chain averaging schemes as cost-effective simplifications of the full-network averaging. ν-based models fulfill this requirement to some extent, whereas λ-based models clearly do not.

Best-fit parameters predicted by the ν-based models can also be compared to theoretical values derived from statistical mechanics considerations. The non-affine tube model of the form $\psi_c^{(\lambda)} = k\bar{\lambda}^\beta$ was derived by Heinrich and coworkers (Heinrich et al., 1988; Kaliske and Heinrich, 1999), where three-chain averaging was used. These authors expressed the

kinematic relation for the tube deformation as $d = d_0 \bar{\lambda}^{\alpha\beta'}$, where $\alpha = 1/2$ and β' is an empirical fit parameter in the range $0 < \beta' \leq 1$. The original non-affine model is recovered from our formulation by setting $\beta = -2\alpha\beta' = -\beta'$. According to these authors, a value $\beta' = 1$ ($\beta = -1$) is relevant for unswollen, well-connected networks (Kaliske and Heinrich, 1999). The actual exponent value may however differ due to various constraint release mechanisms during deformation, or due to the presence of rigid fillers leading to strain amplification (Kaliske and Heinrich, 1999). For the experimental data considered in this work, the three-chain λ-based model provides $\beta = -0.55$ (data of Kawabata et al. (1981)), $\beta = -0.98$ (data of Dechnarong et al. (2021)) and $\beta = -4.3$ (data of Bechir et al. (2006)). The first two β-values are consistent with theoretical predictions. The larger exponent value (in magnitude) in the third example might be attributed to strain amplification required to capture the composite effect.

4.6 Conclusion

In this work, we have systematically investigated the ability of two classes of tube formulation to capture the response of rubber-like incompressible materials under different modes of deformation. The two classes were defined based on the assumed relationship between the (microscopic) tube-area contraction and the deformation of the macroscopic continuum. In λ-based approaches, the tube contraction is expressed in terms of the line-stretch of the continuum, while in ν-based approaches it is expressed in terms of the area-stretch. To describe the free energy contribution associated with the tube topological constraints, a power-law expression was adopted, which encompasses a broad range of tube formulations proposed in the literature. In addition, three popular orientation averaging schemes were considered, namely the full-network, three-chain and eight-chain averaging methods.

Comparisons between model predictions and experimental data suggest that ν-based formulations are in general superior to λ-based formulation, in the sense that 1) they can fit experimental data for any orientation-averaging scheme, 2) associated best-fit parameters

are similar, and thus potentially more amenable to a physical interpretation. In contrast, we found that λ-based formulations can only fit experimental data when used together with the three-chain averaging scheme. We also found that the fitting performance of the various models was directly correlated to their sensitivity to the second invariant I_2. This confirms previous findings that I_2 dependence is necessary for good fitting performance against experimental data for different modes of deformation. Our study further identifies the combinations of tube kinematic assumption and orientation averaging scheme that lead to I_2 dependence, which had not been investigated before.

In this Chapter, we focused on the mathematical structure of micromechanics-based hyperelastic models in relation to fitting performance and I_2 sensitivity. To this end, the power law description of the tube free energy was effectively treated as a phenomenological model, and we did not attempt to link the parameters k and β to specific molecular processes, nor did we attempt to propose a new tube formulation based on molecular considerations. The present study could however be helpful in guiding the development of improved tube models which combine a good fitting ability with physically-based parameters. We also limited our analysis to the classical freely-jointed chain model under the assumption of affine chain stretch to describe the elasticity of the phantom network. Other models could be considered, in particular models that relax the assumption of the affinity of the chain stretch. Such considerations are left for future work.

4.7 Dissemination

This work in this Chapter features in the publication: "G. Kumar, L. Brassart *On tube models of rubber elasticity: fitting performance in relation to sensitivity to the invariant* I_2. Mechanics of Soft Materials 5.1 (2023): 6."

Chapter 5

Modelling cylinder-forming thermoplastic elastomers

5.1 Introduction

We now turn our focus to modelling thermoplastic elastomers where the hard phase forms highly-ordered cylinders within the soft matrix. Cylinders are formed due to a phase separation process that takes place on the molecular scale. This phase separation is caused by thermodynamic incompatibility between the hard and soft blocks in each molecule, which drives the formation of distinct regions of each phase. However, molecular connectivity constraints limit separation to a microscopic scale (Bates and Fredrickson, 2000). The cylindrical morphology is one of many possible morphologies that TPEs can exhibit and occurs when the hard phase volume fraction and molecular weight fall in a particular range. For a given material composition, a morphology which minimises the sum of the free energies of mixing and stretching is obtained. The various equilibrium morphologies exhibited by TPEs are illustrated in Fig. 5.1 in order of increasing hard phase volume fraction. For small amounts of hard phase, the microstructure consists of hard spheres within a soft matrix. As the amount of hard phase is increased, it becomes favourable instead for the hard phase to form long cylinders connected by the soft phase. Increasing this ratio further, the double gyroid morphology is observed (where both phases

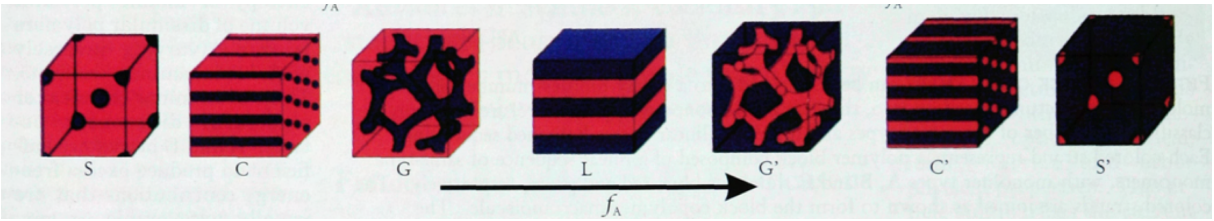


Figure 5.1: TPE morphologies for (left-to-right) increasing hard phase volume fraction. Figure reprinted from Bates and Fredrickson (2000), 'Block Copolymers - Designer Soft Materials', *Physics Today* **52**(2), 32-28, with permission from the American Institute of Physics.

are continuous). For near equal amounts of hard and soft phase, microstructure is lamellar. Cylindrical, gyroid and lamellar TPEs are generally granular materials, being made up of many grains which differ in the orientation of the hard phase (Honeker and Thomas, 1996).

Like filled rubbers and other thermoplastic elastomers, cylinder-forming TPEs show rate-sensitive hysteretic mechanical behaviour that is strongly dependent on their composition. Fig. 5.2(a) illustrates the compositional dependence of a family of four TPEs with increasing hard segment molecular weight alongside the cyclic loading response of one TPE, all from Gregory et al. (2020). All of these TPEs have a poly(cyclohexene-alt-phthalate) hard block and poly(ϵ-decalactone) soft block. These TPEs are cylinder-forming though TPE-8 and TPE-9 show a partially mixed morphology, featuring some spherical regions in addition to cylindrical regions. Clearly, increasing the proportion of hard phase results in a stiffer material with a lower failure stretch. Fig. 5.2(b) shows a hysteresis loop. A significant amount of dissipation occurs after the first loading cycle, and while further dissipation occurs during further cycles it is of a much smaller magnitude than during the first loading-unloading cycle.

While cylinder-forming TPEs show many of the same mechanical behaviours as other two-phase elastomers, the presence of these hard cylinders motivates a separate modelling framework from filler rubbers as the deformation of the hard phase plays a much larger role in the mechanics of these TPEs. Under tensile deformation, the hard cylinders have been reported to neck and eventually break up, giving rise to various inelastic

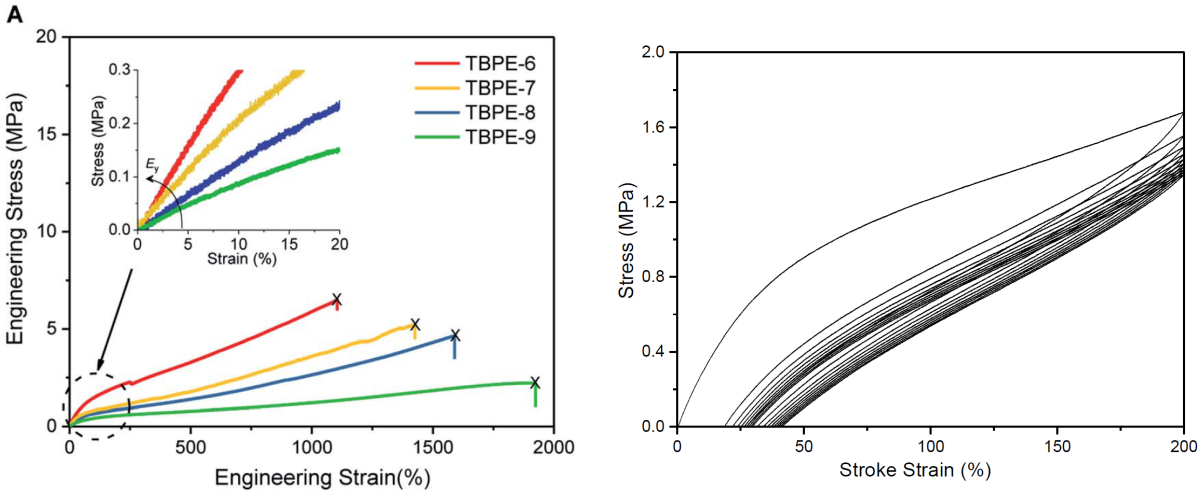


Figure 5.2: Mechanical behaviour of (a) a family of TPEs of the same soft segment molecular weight but different volume fractions (TPE-6 - 29%, TPE-7 - 24 %, TPE-8 - 19%, TPE-9 - 12%) (b) a TPE under cyclic uniaxial tension. Figure reprinted from Gregory, Sulley, Carrodeguas, Chen, Santmarti, Terrill, Lee and Williams (2020), 'Triblock polyester thermoplastic elastomers with semi-aromatic polymer end blocks by ring-opening copolymerization', *Chemical Science* **11**(25), 6567-6581, under CC-BY-NC 3.0. licence.

behaviours on a macroscale (Keller and Odell, 1985; Pakula et al., 1985), while under compression the cylinders are reported to buckle and form a chevron pattern (Honeker and Thomas, 1996; Mamodia et al., 2008). Some modelling work has been done previously on cylinder-forming TPEs and also on lamellar TPEs, which share some deformation mechanisms with cylindrical TPEs. With some exceptions, past micromechanical approaches have focussed on modelling single TPE grains and have neglected to treat the phase behaviours appropriately for large deformation. The anisotropy of single grain TPEs has been analysed in small strain by Keller and Odell (1985), where each phase is assumed to exhibit linear elastic behaviour. Another continuum treatment for analysing the buckling of cylinders under contraction is presented by Read et al. (1999), again for single grain TPEs. This phenomenon has more generally been addressed in theories for microbuckling in fibre-reinforced composites (see e.g. Aboudi and Gilat (2022)). A two-step approach following a tangent second order homogenisation method was pursued by Lopez-Pamies et al. (2008) for modelling the behaviour of polygranular lamellar TPEs but was limited to a generalised neo-Hookean description of the soft phase behaviour and an elastic description of the hard phase behaviour.

In this work, a physically-motivated constitutive model for cylindrical TPEs following the micromechanical approach to rubber elasticity is developed. The model takes the TPE microstructure into account and considers contributions from both the soft segments and hard phase to the mechanical response. The model is confronted to the large deformation and cyclic loading data of Gregory et al. (2020) for four TPEs of different compositions, and the ability of the model to predict changes in the mechanical response with varying hard phase volume fraction is analysed.

5.2 Framework

We follow a micromechanical approach to model cylindrical TPEs. Our model features three microstructural features on different structural length scales. The largest feature is the TPE grain. During cooling from the melt, cylinder formation initiates with any preferred orientation, such that on a micrometre scale, TPE grains (regions where cylinders locally have the same orientation) are formed (Honeker and Thomas, 1996). The mechanical behaviour of each individual grain is highly anisotropic, being much stiffer along the direction of the cylinders than in the transverse direction (Daniel et al., 2000). The next largest microstructural feature we consider is the hard cylinder. Under tension cylinders breakup and reform (Pakula et al., 1985; Honeker and Thomas, 1996), introducing inelastic behaviour to the material. Under compression, cylinders buckle at a critical threshold. We model both of these behaviours through the specification of the hard phase free energy function and dissipation potential, following the framework of Generalised Standard Materials (GSM). The final features we discuss are the soft rubbery segments that span between the hard cylinders. These give rise to the large deformation elasticity exhibited by the material and can be modelled using classical tools from the theory of rubber elasticity.

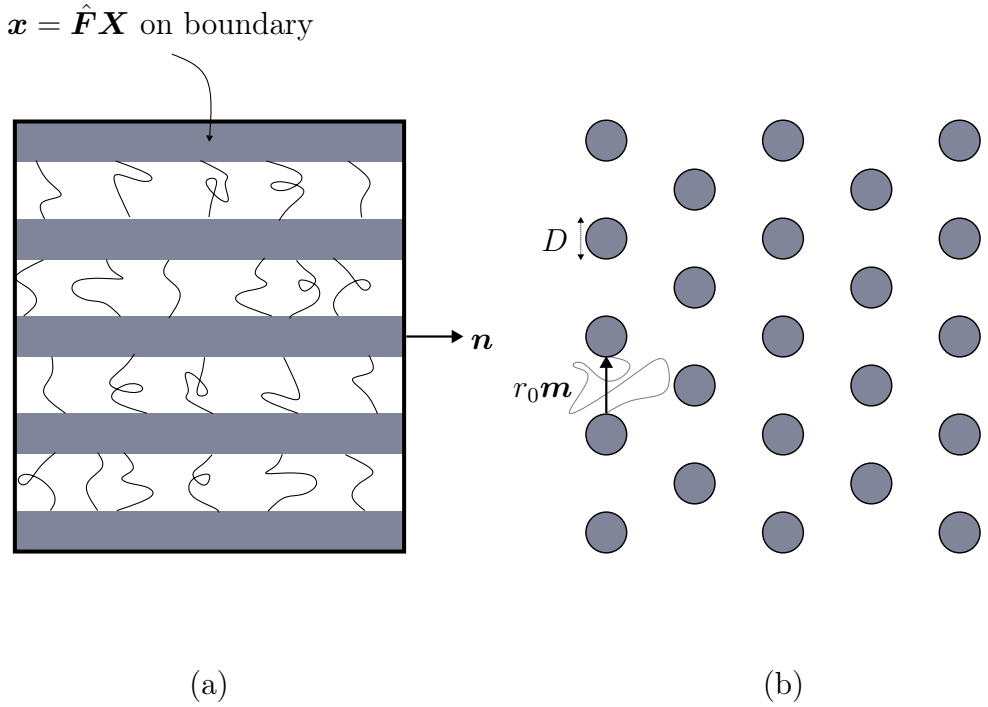


Figure 5.3: Projection views of TPE grain. (a) View of grain showing direction of cylinders (b) View of grain looking down cylinder long axis.

5.2.1 Kinematics

We will begin by examining the deformation of an individual TPE grain, as the way in which each grain deforms gives an indication of how the hard cylinders and soft segments within it deform. Consider a grain with edges displaced by some deformation gradient $\hat{\boldsymbol{F}}$ as shown in Fig. 5.3. Each grain consists of many hard cylinders oriented in a single direction, and many more soft segments connecting theses cylinders together in the transverse plane. Hard cylinders span from one edge of the grain to the other. When the edges of the grain are displaced, the ends of the hard cylinders are displaced by the same amount. Thus the cylinders aligned in the reference direction $\boldsymbol{n}$ are subjected to an axial stretch λ^h given by:

$$\lambda^h(\hat{\boldsymbol{F}}, \boldsymbol{n}) = |\hat{\boldsymbol{F}}\boldsymbol{n}|. \tag{5.1}$$

We assume that hard cylinders effectively only undergo uniaxial deformations which are fully described by the axial stretch λ^h. Deformations in the transverse plane (normal to the long axis of the cylinders) are borne mostly by the soft phase, as the strain is

split between the two phases according to their respective stiffnesses in a series-like coupling. As the hard phase is much stiffer than the soft phase, load in the transverse plane largely does not influence the deformation of the cylinders and is secondary to their axial deformation.

The initial end-to-end vectors of the soft segments all lie within the plane normal to the cylinders. The stretch that a soft segment spanning between two cylinders sees can be derived following an argument similar to that outlined in Section 3.2. As shown in Fig. 5.3(b), the cylinders are described by their diameter D which does not change with deformation and are distributed periodically within each grain. This periodicity implies that in the transverse plane, the centres of the cylinders are displaced by the deformation gradient $\hat{\boldsymbol{F}}$. The centres of each cylinder are separated by a reference vector $(r_0+D)\boldsymbol{m}$, where r_0 is the reference length of the chain (which coincides with the cylinder separation) and $\boldsymbol{m}$ is reference orientation of the chain (which again coincides with the cylinder separation and lies within the plane normal to $\boldsymbol{n}$). In the deformed configuration, the separation is given by the sum of the current soft segment length r and the cylinder diameter D:

$$r + D = |\hat{\boldsymbol{F}}\boldsymbol{m}|(r_0 + D). \tag{5.2}$$

Writing $r = \lambda^s(\hat{\boldsymbol{F}}, \boldsymbol{m})r_0$, this leads to the following expression for soft segment stretch:

$$\lambda^s(\hat{\boldsymbol{F}}, \boldsymbol{m}) = \left(\frac{D + r_0}{r_0}\right)\Big(|\hat{\boldsymbol{F}}\boldsymbol{m}| - 1\Big) + 1. \tag{5.3}$$

As in Section 3.2 we modify this to ensure positive stretches are always predicted under compression:

$$\lambda^s = \begin{cases} \left(\frac{D+r_0}{r_0}\right)\Big(|\hat{\boldsymbol{F}}\boldsymbol{m}| - 1\Big) + 1 & |\hat{\boldsymbol{F}}\boldsymbol{m}| \geq 1, \\ |\hat{\boldsymbol{F}}\boldsymbol{m}|^{\frac{D+r_0}{r_0}} & |\hat{\boldsymbol{F}}\boldsymbol{m}| < 1. \end{cases} \tag{5.4}$$

The fraction $(D+r_0)/r_0$ is related to the volume fraction of the hard phase. As $(D+r_0)/r_0$ is a ratio of length scales we assume that the volume fraction scales with its cube through

an unknown proportionality factor k:

$$f = k\left(\frac{D}{r_0 + D}\right)^3. \tag{5.5}$$

For simplicity, we will assume that all grains are subjected to the macroscopic deformation gradient $\boldsymbol{F}$:

$$\hat{\boldsymbol{F}} = \boldsymbol{F}. \tag{5.6}$$

This iso-strain assumption is a gross simplification of the mechanics of a true polygranular system but at this stage remains sufficiently accurate for our purposes, and is challenging to replace with a more realistic scale transition given the lack of detailed information about the grain structure of TPEs. Furthermore, Eq. (5.6) is the simplest micro-macro transition that satisfies the equality constraint between the macroscopic deformation gradient and the volume average microscopic deformation gradient (Hill, 1963).

5.2.2 Thermodynamics

We will now express the macroscopic free energy of the system in terms of the contributions of the hard and soft phases that compose it. Recall that the free energy density of the system is the sum of the volume average free energy density in the soft phase Ψ^s and the volume average free energy density in the hard phase Ψ^h, each weighted by their respective volume fractions (Hill, 1963):

$$\Psi = (1 - f)\Psi^s + f\Psi^h, \tag{5.7}$$

where f is the hard phase volume fraction. Each free energy contribution can be found by considering the average contribution for each phase within each grain, and then averaging these contributions over the distribution of grains in the system.

We have assumed that within each grain, the deformation of the hard phase is uniform and depends on the orientation of the grain and the macroscopic deformation gradient. We will further assume that the distribution of grain orientation is isotropic. This means

that the volume average of the hard phase free energy density is simply the unweighted orientational average of the hard phase free energy density ψ^h, which depends on the stretch of the cylinders and a list of possible internal variables ξ_i^h which will be specified later:

$$\Psi^h = \frac{1}{4\pi}\int_{\mathcal{S}} \psi^h(\lambda^h(\boldsymbol{F},\boldsymbol{n}),\xi_i^h)d\mathcal{S}, \tag{5.8}$$

where the stretch depends on the orientation $\boldsymbol{n}$ and integration is over all unit $\boldsymbol{n}$ which make up the set $\mathcal{S}$.

As we have made the assumption that all grains are subjected to the macroscopic deformation gradient, Eq. (5.4) tells us that the soft segment stretch is the same for all soft segments with the same reference orientation, regardless of which grain they are in. Thus the volume average soft phase free energy density is equal to the orientational average free energy density of the soft segments. The orientational distribution of soft segments is isotropic as the distribution of grains is isotropic. Therefore, the volume average soft phase free energy density is given by:

$$\Psi^s = \frac{n^{ss}}{4\pi}\int_{\mathcal{S}} \psi^{ss}(\lambda^s(\boldsymbol{F},\boldsymbol{n}),\xi_i^s)d\mathcal{S}, \tag{5.9}$$

where ψ^{ss} is the soft segment free energy which takes the soft segment stretch and a list of possible internal variables ξ_i^s for the soft phase as its arguments. Here we have also introduced the number of soft segments per unit soft volume n^{ss}, which can be expressed in terms of the number of Kuhn segments per chain N and the segment volume v:

$$n^{ss} = \frac{1}{Nv}. \tag{5.10}$$

Usually, the soft segment molecular weight $M_{w,ss}$ and density of soft phase ρ_s are more readily available than the Kuhn parameters, as correct calculation of chain parameters requires additional knowledge of the chain flexibility (Rubinstein et al., 2003). The number

of soft chains per unit reference volume can instead be expressed:

$$n^{ss} = \frac{\rho_s \mathcal{N}_A}{M_{w,ss}}, \tag{5.11}$$

where $\mathcal{N}_A$ is Avogadro's constant. It should be stressed that while we write the soft segment free energy per chain ψ^{ss}, ψ^h is the free energy per unit reference hard volume, not the free energy per hard cylinder.

Following the Coleman-Noll procedure applied to the full-network framework (as outlined in Section 3.2.2), it can be shown that the first Piola-Kirchhoff stress reads:

$$\boldsymbol{P} = (1-f)\left\langle \nu^{ss} \frac{\partial \psi^s}{\partial \lambda^s} \frac{\partial \lambda^s}{\partial \boldsymbol{F}} \right\rangle + f \left\langle \frac{\partial \psi^h}{\partial \lambda^h} \frac{\partial \lambda^h}{\partial \boldsymbol{F}} \right\rangle - P\boldsymbol{F}^{-T}, \tag{5.12}$$

and that satisfaction of the thermodynamic inequality at the chain level for each inelastic mechanism requires:

$$-\frac{\partial \psi^h}{\partial \xi_i^h}\dot{\xi}_i^h \geq 0, \quad -\frac{\partial \psi^s}{\partial \xi_i^s}\dot{\xi}_i^s \geq 0. \qquad \text{(No summations)} \tag{5.13}$$

Once again we use the framework of Generalised Standard Materials to ensure inelastic behaviour is specified in accordance with the above inequalities. Dissipation potentials $\phi^h(\dot{\xi}_i^h, \xi_i^h)$ and $\phi^s(\dot{\xi}_i^s, \xi_i^s)$ for the hard and soft phases respectively are introduced. These are required to be positive, convex and pass through the origin to ensure satisfaction of the reduced thermodynamic inequalities $(5.13)_1$ and $(5.13)_2$. The rates of change of the internal variables are found from the solution of the following equations:

$$\frac{\partial \psi^h}{\partial \xi_i^h} + \frac{\partial \phi^h}{\partial \dot{\xi}_i^h} = 0, \quad \frac{\partial \psi^{ss}}{\partial \xi_i^s} + \frac{\partial \phi^s}{\partial \dot{\xi}_i^s} = 0. \qquad \text{(No summations)} \tag{5.14}$$

Soft phase behaviour

We assume that the soft segments deform by two deformation mechanisms. The first of these is the entropic mechanism classically described in the theory of rubber elasticity -

there is a contribution to the free energy based on the number of conformations chains can explore for a given distance between their ends. We assume that there is a viscoelastic overstress in addition to this contribution arising from the intrinsic monomer viscosity. This contribution is assumed be enthalpic in origin rather than entropic, as it pertains to changes in monomer spacing rather than to the uncoiling of chains. We therefore split the free energy as follows:

$$\psi^{ss}(\lambda^s) = \psi^{(1)}(\lambda^s) + \psi^{(2)}(\lambda^{e1}), \tag{5.15}$$

where $\psi^{(1)}$ is the free energy contribution of the entropic mechanism and $\psi^{(2)}$ is the contribution from the viscoelastic mechanism, which takes the elastic stretch λ^{e1} as its argument. This is based on a split of the soft segment stretch into elastic and viscous parts λ^{e1} and λ^v :

$$\lambda^s = \lambda^{e1}\lambda^v. \tag{5.16}$$

We model the entropic contribution through the freely-jointed chain model described in Section 2.3.1:

$$\psi^{(1)}(\lambda^s) = Nk_BT\left(\beta\frac{\lambda^s r_0}{Nb} + \log\frac{\sinh\beta}{\beta}\right), \tag{5.17}$$

$$\text{where } \beta = \mathcal{L}^{-1}\left(\frac{\lambda^s r_0}{Nb}\right) \text{ and } \mathcal{L}(x) = \coth x - \frac{1}{x}, \tag{5.18}$$

where symbols are defined in Section 2.3.1.

For simplicity, we assume that the viscoelastic contribution can be described by the following pair of potentials:

$$\psi^{(2)}(\lambda^{e1}) = \frac{1}{2}N\mu^{e1}\left(\log\lambda^{e1}\right)^2, \tag{5.19}$$

$$\phi^{(2)}(d^v) = \frac{1}{2}N\eta\left(d^v\right)^2, \tag{5.20}$$

where μ^{e1} is a modulus-like parameter and η is a viscosity-like parameter. The number of Kuhn segments N appears in these expressions as we have assumed that viscoelastic

mechanism is based on monomer motion. We assume that there is an average contribution to the free energy per monomer which can be multiplied by the number of Kuhn segments to yield the chain contribution, which $\psi^{(2)}$ represents. These potentials correspond to (log-)linear viscoelasticity, which can be shown by considering solution of the evolution equation in the GSM framework. In this case it states:

$$\frac{\partial \psi^s}{\partial \log \lambda^v} + \frac{\partial \phi}{\partial d^v} = -N\mu^{e1} \log \lambda^{e1} + N\eta d^v = 0, \tag{5.21}$$

where we have made use of the fact that $\partial \psi^s / \partial \log \lambda^v = -\lambda^e \partial \psi^{(2)} / \partial \lambda^{e1}$. Recognising that $\log \lambda^e = \log \lambda - \log \lambda^v$, it can be observed that Eq. (5.21) is a first order linear ordinary differential equation for $\log \lambda^v$, and thus describes linear viscoelasticity.

During the calculation of the full-network integrals for evaluating the soft phase free energy, the free energy contribution $\psi^{(2)}$ is multiplied by the number of chains per unit volume n^{ss}. Using Eq. (5.10), it can be observed that the model response depends only on the parameters μ^{e1} and η through the ratios μ^{e1}/v and η/v, which have dimensions of stress. The ratios μ^{e1}/v and η/v are reported when the model is fitted rather than the parameters themselves for conciseness.

Hard phase behaviour

The hard phase appears to exhibit different behaviours under tension and compression, with mechanisms of shear plasticity appearing to dictate the response under tension and elastic buckling appearing to take place under compression. We seek to model these behaviours in a simple manner. To this end, we begin with the tensile behaviour of the hard phase in mind and introduce the theory of plasticity to describe it. We follow the GSM plasticity framework outlined in Section 3.4 to describe the plastic response of the hard segments. The hard phase stretch is split into elastic and plastic parts λ^{e2} and λ^p:

$$\lambda^h = \lambda^{e2} \lambda^p, \tag{5.22}$$

Name	Volume fraction	$M_{w,ss}$/kg mol^{-1}
TBPE-6	0.29	78.3
TBPE-7	0.24	69.8
TBPE-8	0.19	87.0
TBPE-9	0.12	97.2

Table 5.1: Composition of TPEs produced by Gregory et al. (2020)

and the logarithmic plastic strain rate is split into a non-negative magnitude $\dot{p}$ and direction N^p which has a magnitude constrained to unity ($|N^p| = 1$) to render the split unique:

$$d^p := \frac{\dot{\lambda}^p}{\lambda^p} = \dot{p} N^p. \tag{5.23}$$

The plastic dissipation potential takes $\dot{p}$ as its argument and is chosen to follow a linear form:

$$\phi^h(\dot{p}, p) = \begin{cases} (\sigma_y + hp)\,\dot{p} & \dot{p} \geq 0, \\ +\infty & \dot{p} < 0, \end{cases} \tag{5.24}$$

which features the yield stress σ_y and a hardening parameter h.

We assume that the buckling of the hard cylinders limits their contribution to the effective hard phase free energy under compression and assume a modified quadratic (in true strain) form of the free energy function:

$$\psi^h(\lambda^{e2}) = \begin{cases} \frac{1}{2}\mu^h (\log \lambda^{e2})^2 & \lambda^{e2} \geq 1, \\ \frac{1}{2} a \mu^h (\log \lambda^{e2})^2 & \lambda^{e2} < 1, \end{cases} \tag{5.25}$$

where μ^h is the hard phase shear modulus and a is a parameter heuristically introduced to reflect the reduced compressive contribution to the free energy from the hard phase due to the buckling of the cylinders. Accordingly, a is restricted such that $0 \leq a \leq 1$.

5.3 Results

5.3.1 Comparison to experimental data of Gregory et al. (2020)

We apply the model to the TPEs produced by Gregory et al. (2020). The dataset consists of monotonic uniaxial tensile tests carried out at nominal strain rates of 0.017 s^{-1} for four TPEs with compositions outlined in Table 5.1, and cyclic uniaxial tensile tests for three of the TPEs. Each TPE has a large soft segment molecular weight and so contains a large number of Kuhn segments. This fact can be used to simplify the expression for the soft segment free energy to that of Gaussian chain model as in Eq. (2.32) in Section 2.3.1. We fit the Gregory et al. (2020) data after first fixing the compositional parameters of the model to the large deformation response of TPE-6 and TPE-7, and the cyclic response of TPE-6. These data make up the calibration data, and the monotonic and cyclic responses for TPE-8 and TPE-9 are used for validation. We arrive at the fits for monotonic uniaxial tension in Fig. 5.4 and cyclic uniaxial tension in Fig. 5.5.

The fitting procedure is similar to that outlined in Section 3.4.2. First, the physical parameters are set based on the compositional data provided by Gregory et al. (2020). The remaining fitting parameters are k (which features in the relation (5.5) between the degree of stretch amplification and the volume fraction) and the viscoelastic parameters. At large deformations, the free energy contribution $\psi^{(1)}$ is much greater than that of $\psi^{(2)}$ or of ψ^{h} due to the elastic-inelastic splits in these branches. All of the parameters controlling $\psi^{(1)}$ aside from k are either physical constants, or are set by the material composition or temperature. This means that there is essentially a single degree of freedom in the model for capturing the trend in the large deformation response of the TPEs. The monotonic tensile data provided by Gregory et al. (2020) for TPE-6 and TPE-7 go up to a stretch of 20. This is an extremely large deformation, from which the model suggests k can be extracted near independently from the other fitting parameters. The value is determined by through an iterative trial-and-error approach where an estimate of the parameter is manually adjusted to achieve a fit which by inspection is sufficient. As no

measures of the variation in the experimental data are provided, it is unclear whether or not exact quantitative agreement with the data is expected or desired (as the data are not necessarily representative of the material behaviour). The model fits for the large deformation response of TPE-6 and TPE-7 are shown in Fig. 5.4 alongside predicted responses for TPE-8 and TPE-9. The viscoelastic parameters are determined using a similar trial-and-error methodology applied to the cyclic response of TPE-6, where initial values are such that the moduli-like terms μ^{e1} and μ^{h} are initially set equal to $\nu k_B T$ and then adjusted alongside the other parameters to match the hysteresis loop during the second loading-unloading cycle. The parameters used for these fits are shown in Table 5.2.

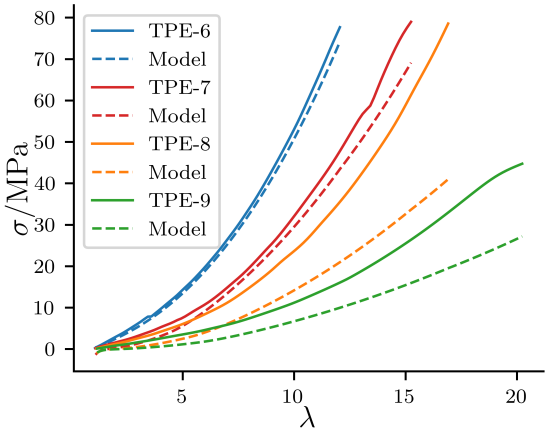


Figure 5.4: TPE model fitted to the monotonic uniaxial tensile data of Gregory et al. (2020) for four TPEs of different volume fractions.

Fig. 5.4 demonstrates the ability of the model to describe trends in the mechanical response up to very large strains across a range of volume fractions. While the model is able to describe the response of the two higher volume fraction TPEs very well, the prediction of the response of the two smaller volume fraction TPEs is not as satisfying at large strains, which perhaps reveals a limitation of the stretch amplification approach we have followed. This could also be due to the fact that TPE-8 and TPE-9 are reported to show a mixed spherical and cylindrical morphology (Gregory et al., 2020).

The model is able to capture the key features of the cyclic response of the material. The model captures the accumulation of residual strain observed after the first cycle, and also

captures a hysteresis loop that the data show during subsequent loading cycles. The changes in the mechanical response with volume fraction are reasonably well captured going from the calibrated response of TPE-6 to TPE-9 though less well so for TPE-8. This is in contrast to some of our findings for the prediction of the large deformation response, where the response of TPE-9 was not well described. Whereas the contribution of $\psi^{(1)}$ is more significant than the hard phase and soft phase viscoelastic contributions at large strains, the small-to-moderate deformation response is strongly affected by all contributions. This could perhaps reflect that the trend in the hard phase contribution with volume fraction is better predicted than the trend in the soft phase contribution.

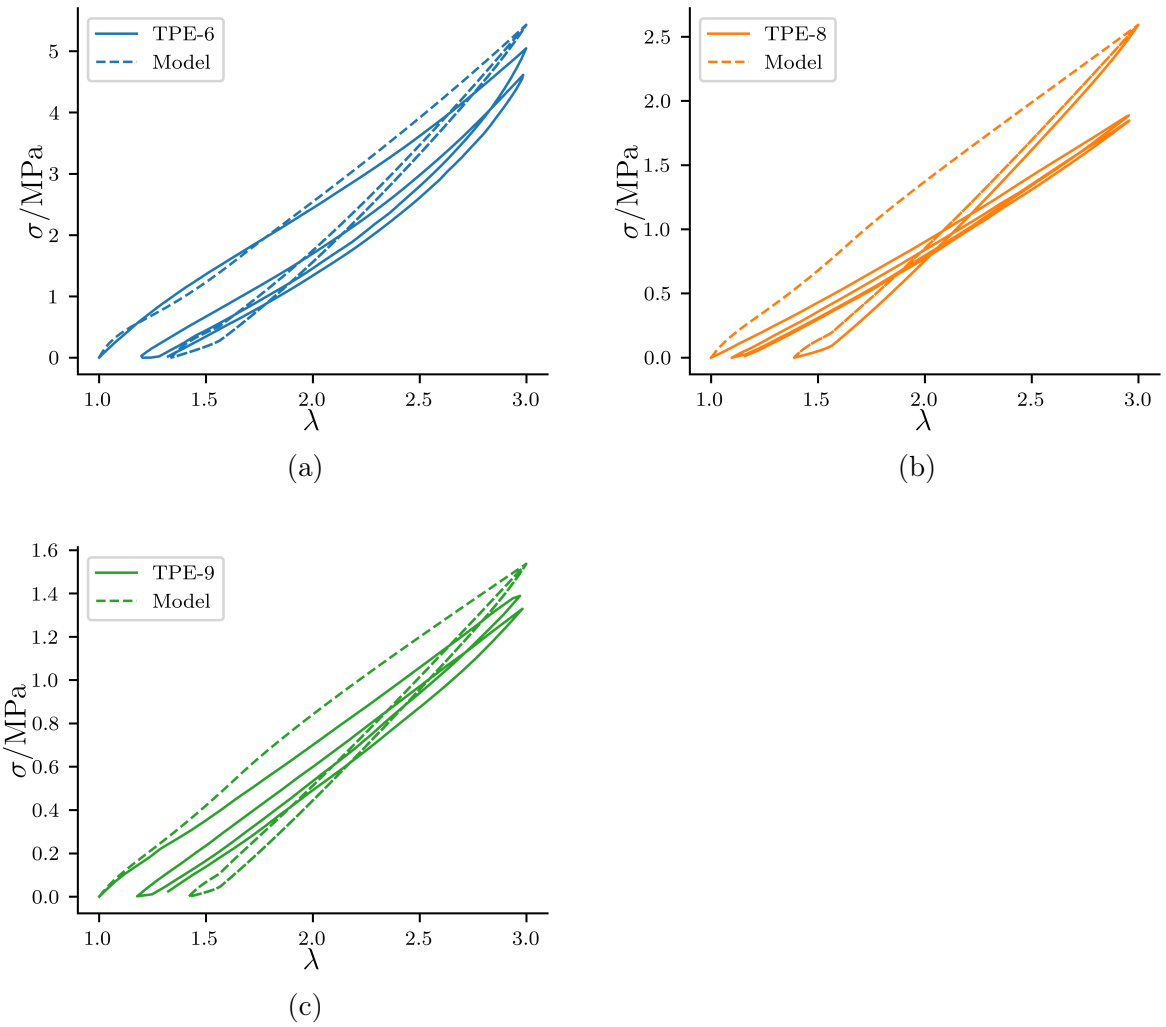


Figure 5.5: TPE model fitted to the cyclic uniaxial tensile data of Gregory et al. (2020) for three TPEs of different volume fractions.

k	μ^{e1}/v	η/v	μ^h	σ_y	h	a
0.425	0.5 MPa	3 MPa s	30 MPa	5 MPa	10 MPa	0.1

Table 5.2: Fitting parameters for data of Gregory et al. (2020).

To further investigate the model performance, we predict the stress-relaxation responses and paused cyclic loading responses of the three TPEs tested under cyclic uniaxial tension by Gregory et al. (2020). In Fig. 5.6(a), the stress elicited when the material is held at a stretch of $\lambda = 3$ against time is predicted, following a ramp loading at a nominal strain rate of 1 s^{-1}, and in Fig. 5.6(b) the cyclic response under the same strain rate up to a maximum stretch $\lambda = 3$ with pauses of 15 s at the selected stretches $\lambda = 1.5$, $\lambda = 2$ and $\lambda = 2.5$ is shown. In Fig. 5.6(a), we can see that larger hard phase volume fraction TPEs are predicted to undergo greater stress relaxation than the TPEs containing less hard phase. The heightening of this viscous behaviour can also be observed in the paused loading shown in Fig. 5.6 where more relaxation is seen in the higher volume fraction TPE at all stretches. The paused loading response further reveals that across all volume fractions, the degree of stress relaxation for a given TPE becomes slightly less pronounced at higher stretches where the non-viscous mechanisms contribute more to the mechanical response.

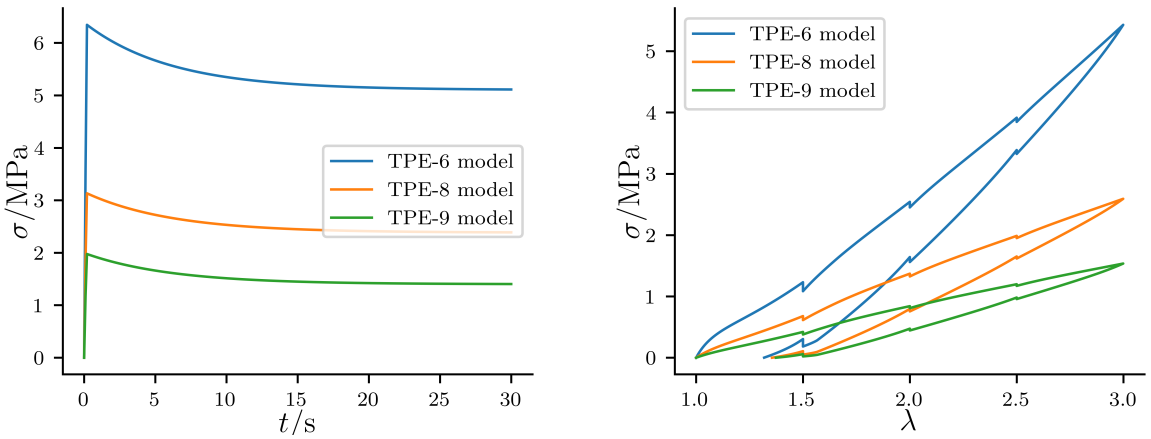


Figure 5.6: Model predictions for the response of TPEs from Gregory et al. (2020) under (a) a constant stretch of $\lambda = 3$ following a ramp loading from the pristine state at a strain rate of 1 s^{-1} and (b) paused cyclic loading at a strain rate of 1 s^{-1} where the material is held at constant strain for 15 s at stretch increments of 0.5.

5.3.2 Grain level analysis

Another aspect of the model which is interesting to analyse is the contribution of grains in different orientations to the observed mechanical response. In each grain, all hard phase is aligned in a single direction and the soft segments lie in the plane normal to the cylinders. It therefore follows that the volume average free energy contribution from the hard phase is simply given by ψ^h without the need for orientational averaging, and that the soft phase free energy is given by the orientational average contribution for all soft segments in the plane normal to n (i.e., following integration over directions in the unit circle). We can express the free energy per unit volume of the grain as:

$$\Psi^G = (1-f)\left\langle n^{ss}\psi^{ss}\right\rangle_{\boldsymbol{m}} + f\psi^h, \tag{5.26}$$

where $\langle()\rangle_{\boldsymbol{m}}$ denotes the orientational average over the plane normal to the direction $\boldsymbol{m}$. The contribution to the initial modulus can be computed from the limit (Ogden, 1997):

$$\mu = \lim_{\lambda\to 1}\frac{\sigma}{\lambda^2-\lambda^{-1}}. \tag{5.27}$$

In Fig. 5.7(a), we plot the contribution of grains oriented at an angle θ to the stretching direction to the initial modulus of the system as a whole. The contribution to the modulus μ is normalised by the maximum contribution $\mu_{\max}$, which occurs when the cylinders are aligned with the stretching direction. The grains which contribute least to the elastic modulus of the material are curiously not those whose cylinders are perpendicular to the stretching direction, but instead those at an intermediate orientation. This is qualitatively in line with the experimental results of Keller and Odell (1985) who find that in single grain cylindrical TPEs, the lowest apparent elastic modulus under uniaxial tension occurs at an angle of approximately 55° to the stretching direction. Their results are plotted in Fig. 5.7 for comparison. In our framework, this minimal compliance arises at an intermediate angle as it has been assumed that the reference orientations of the hard cylinders and soft segments are perpendicular to each other. This means that neither

constituent is well aligned with the stretching direction when the sample is strained at intermediate angles and thus results in a lower apparent modulus.

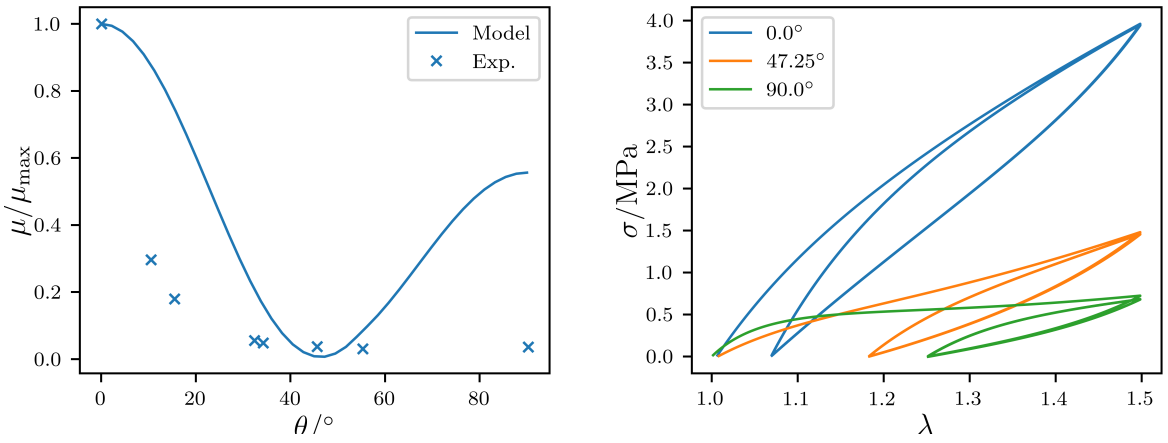


Figure 5.7: (a) The normalised contributions to the initial modulus from grains at an angle θ to the stretching direction under uniaxial tension, shown alongside experimental measurements of the initial modulus of single grain samples stretched in different directions relative to the hard cylinders from Keller and Odell (1985), and (b) the stress-strain response of grains at specific orientations relative to the stretching direction under macroscopic uniaxial tension.

In Fig. 5.7(b), the stress component acting directly in the stretching direction is plotted against the macroscopic uniaxial stretch for grains aligned with the stretching direction, perpendicular to the stretching direction and at 47.25° to the stretching direction. The angle 47.25° corresponds to the smallest initial modulus contribution as shown in Fig. 5.7(a). While it can be observed that the initial slope of the stress-strain curve is lower for the 47.25° grain than the fully aligned and perpendicular grains, the stress in this grain drops below that of the perpendicular grain at a stretch $\lambda \approx 1.15$. A possible explanation for this transition lies in the rotation of hard and soft segments at intermediate angles to the stretching direction. When the material is deformed, the current orientation of both the soft segments and hard segments is related to the affine displacement and rotation of their reference orientation vector $\boldsymbol{Fn}$. Vectors which are perpendicular or parallel to the uniaxial stretching direction do not rotate during this deformation but vectors in between these extremes become increasingly aligned with the stretching direction as deformation progresses. It is therefore expected in the model that as deformation progresses, the hard

and soft segments become increasingly recruited in grains at intermediate angles, which leads to higher stresses. This perhaps explains why the stress increases above that of the 90° grain.

5.4 Conclusion

A micromechanical model for cylinder-forming thermoplastic elastomers has been presented in this Chapter. The deformation behaviour of the material is explained in terms of the deformation of the hard cylinders and soft rubbery chains taking place on a microscale. The hard phase gives rise to plastic behaviour and the soft segments are assumed to be responsible for the material viscoelasticity and large deformation elasticity. An affine micro-macro relation is assumed for the hard segments and a stretch amplification rule is developed for the soft segments. These rules and the split of the free energy account for the effects of changing material composition in the model. The model is compared to experimental data for four TPEs of varying composition subjected to monotonic uniaxial tension up to large stretches and cyclic uniaxial tension, and is able to describe some of the trends observed in the mechanical response with varying composition. The model predicts that grains aligned obliquely (neither perpendicular nor parallel) to the stretching direction contribute least to the initial modulus of the material, qualitatively in line with the data of Keller and Odell (1985).

In this work a number of simplifying assumptions have been invoked to render the model tractable which could later be revisited in future. For example, it has been assumed that all grains in the system are subjected directly to the macroscopic deformation gradient. The modelling of polygranular and polycrystalline materials (featuring transitions from single crystal behaviour) has been researched extensively in the past following homogenisation techniques, which could in future be applied to the modelling of TPEs. Considering the modelling of grains themselves, further experiments on well oriented TPE samples could shed light on more appropriate descriptions of the hard and soft phase behaviours, which would improve the model fitting performance. Similar to the modelling of Chapter

3, it would serve to explore the fitting of the model using a more rigorous procedure to allow the deficits of the model fitting performance to be inferred more precisely.

Chapter 6

Anisotropic damage model for the Mullins effect

6.1 Introduction

The Mullins effect is a stress softening phenomenon exhibited by many rubber-like materials, where the effective elastic properties of the material drop when it is deformed for the first time (Mullins, 1969; Diani et al., 2009). The effect occurs under a variety of loading conditions and broad range of soft materials (Zhan et al., 2024), and has presented the mechanics community with a rich and multi-faceted problem from both a characterisation and modelling point of view. As discussed in Section 2.5 the origins of the Mullins effect in these materials have historically been attributed to processes taking place in the rubber (Mullins and Tobin, 1965) (e.g. entanglement release (Hanson et al., 2005)), to the breakdown of clusters of filler particles (Klüppel and Schramm, 2000; Plagge and Klüppel, 2017), or to changes in polymer-filler interactions at the interface, including polymer-filler bond breakage (Bueche, 1960), molecular slippage (Dannenberg, 1975) or adsorption/de-adsorption of chains from the filler surface (Dannenberg and Brennan, 1966; Diaz et al., 2014).

Existing constitutive models for the Mullins effect can be characterised as either phenomenological or micromechanical, and within each of these categories as either isotropic

or anisotropic (see the excellent recent review of Zhan et al. (2024) for an overview of many Mullins effect models). Micromechanical models are rooted in the physical picture of rubber elasticity - that the behaviour of the rubber network can be explained by breaking it down to the chains that compose it - whereas phenomenological models are chosen for convenient mathematical form. Isotropic models of both types are numerous (see Govindjee and Simo (1991); Marckmann et al. (2002); Chagnon et al. (2006) and Simo (1987); Ogden and Roxburgh (1999); Dorfmann and Ogden (2004) for a small selection of models of each respective type, as discussed in Section 2.5) and have shown to be successful at describing behaviour under a single mode of proportional loading. However, the Mullins effect is highly anisotropic (Mullins, 1948). The anisotropy of the effect is clearly demonstrated in sequential uniaxial tensile tests, where the material is subjected to uniaxial tension in one direction, unloaded and then subjected to uniaxial tension in another direction. Softening in one direction under uniaxial stretching is often reported to induce negligible softening in the perpendicular direction, with samples showing almost the exact same stress-strain curve in the 90° loading as in the original loading in a variety of experiments (Hanson et al., 2005; Merckel et al., 2012; Machado et al., 2012; Mai et al., 2017).

Phenomenological anisotropic models include those based on the concept of structural tensors (Horgan et al., 2004; Peña and Doblaré, 2009; Dorfmann and Pancheri, 2012; Shariff, 2014) (or preferred directions, where typically the underlying free energy is assumed to be orthotropic) and those based on principal directions (e.g. Anssari-Benam et al. (2023); Anssari-Benam and Hossain (2024)). These models perform well under proportional loading, in which directions that the material damages are clear, however the material response when damage directions or principal stretching directions change has not been fully elaborated (especially if damage directions change in a manner that cannot easily be tracked), or require storage of the entire deformation histories (Shariff, 2006, 2014). Micromechanical damage models are usually based on the full-network concept where the behaviour of the rubber network is found from the directional average of the chain behaviour (Wu and Van Der Giessen, 1993), usually assuming that chains follow

an isotropic distribution of orientations in the reference configuration. A number of such models can be cast in the form where the state of each chain is described by a stretch parameter λ and a damage parameter which we will call ξ. As ξ increases, the effective chain properties change, resulting in softening. The damage parameter ξ may be linked for example to the number of Kuhn segments in each chain (Diani et al., 2006; Marckmann et al., 2016; Diani and Le Tallec, 2019), the stretch amplification factor (Merckel et al., 2013) or the directional number density of chains (Göktepe and Miehe, 2005; Dargazany and Itskov, 2009, 2013).

While the full-network approach is often adopted in modelling the anisotropic behaviour of rubbers, it may lead to a pathological behaviour where unphysical transverse softening occurs during uniaxial deformation, as we previously encountered in the filled rubber model developed in Section 3.3. As illustrated in Fig. 6.1, during uniaxial tension, chains with orientations between the stretching direction and the perpendicular directions are also stretched, and therefore also undergo local damage. When the material is subsequently stretched in a transverse direction, the material is softer than in the pristine state, as these already-damaged chains are again recruited in transverse deformation. As previously mentioned, such transverse softening is generally not observed in experiments where in most cases the transverse response of the damaged material is close to the response of the pristine material (Hanson et al., 2005; Merckel et al., 2012; Machado et al., 2012; Mai et al., 2017). This pathological behaviour is inherent to full-network models where it is assumed that the degree of chain damage depends on chain deformation history only.

Alternative approaches to model anisotropic damage based on orientation averaging have been proposed. For example, Machado et al. (2014) proposed a two-network theory where softening in a given material direction is affected by both the maximum historic strain energy in that direction and the maximum historic strain energy in all directions. The model is able to reproduce experimental data by Machado et al. (2012) where the amount of stress softening depends on the angle between the first and second loading. However,

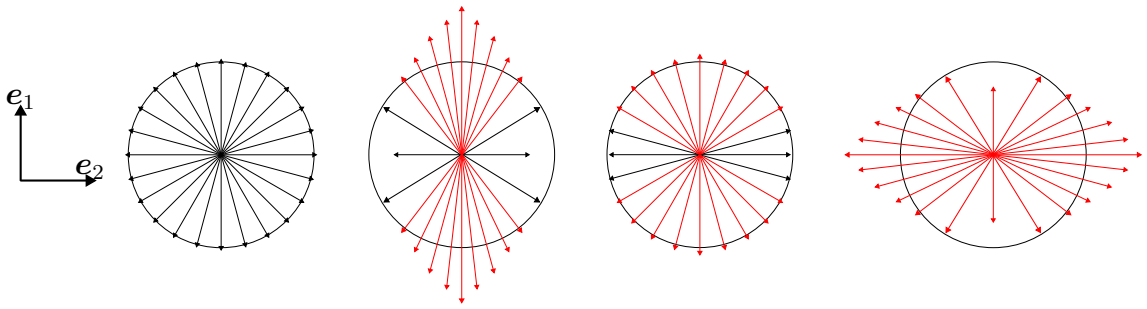


Figure 6.1: The evolution of chain damage in the $e_1 - e_2$ plane under uniaxial tensile tests in different directions for models with damage criteria based on the state of individual chains only. Damaged chains are shown in red.

the model is essentially phenomenological. Khiêm and Itskov (2017) developed a physics-based approach where the response is decomposed into elastic, damage and hysteresis contributions. Softening is captured via internal variables that depend on the historic values of the principal stretches and directions, as well as the current directions of loading. However, the model formulation comprises a large number of constitutive function, and its applicability to arbitrary loading conditions has not been fully explored.

In this Chapter, we propose a new constitutive framework to describe the anisotropy induced by the Mullins effect in rubber. Following the full-network approach, the elastic energy is calculated by averaging the energy of representative, damaging chains over orientations. However, we depart from the hypothesis that the state of an individual chain depends only on its own deformation history, and instead describe the global distribution of damage using a single tensor damage parameter, from which the damage of a given chain can be obtained, so that chain damage parameters do not need to be stored in each direction. The damage tensor evolves according to global damage conditions and flow rules, in a manner similar to the phenomenological theory of plasticity with kinematic hardening. The model satisfyingly captures key experimental observations for cyclic loading in different loading directions. We also implemented our model as a user subroutine UMAT for the finite element software ABAQUS to demonstrate its suitability for numerical simulations under arbitrary loading conditions.

6.2 Constitutive framework

6.2.1 Preliminaries

At the continuum level, we describe the deformation of the material with the right Cauchy-Green deformation tensor $\boldsymbol{C} = \boldsymbol{F}^T\boldsymbol{F}$ where $\boldsymbol{F}$ is the deformation gradient. We assume incompressible behaviour, so that $\det(\boldsymbol{C}) = 1$. Let $\lambda^{(i)}$ $(i = 1, 2, 3)$ be the principal stretches (i.e. $(\lambda^{(i)})^2$ are the principal values of $\boldsymbol{C}$) and $\boldsymbol{N}^{(i)}$ be the corresponding orthonormal set of principal stretch directions, which may or may not be unique depending on whether or not the principal stretches are repeated. The principal stretches are numbered following the convention $\lambda^{(1)} \geq \lambda^{(2)} \geq \lambda^{(3)}$. We define p as the number of tensile stretching directions with $\lambda^{(i)} > 1$. Due to incompressibility ($\lambda^{(1)}\lambda^{(2)}\lambda^{(3)} = 1$), p can only take values 0, 1 or 2.

For any symmetric second-order tensor $\boldsymbol{T}$, we define $\hat{\boldsymbol{T}}$ as the projection of $\boldsymbol{T}$ into the tensile stretching directions:

$$\hat{\boldsymbol{T}} = \sum_{i=1}^{p}\sum_{j=1}^{p}\left(\boldsymbol{T} : (\boldsymbol{N}^{(i)} \otimes \boldsymbol{N}^{(j)})\right)\boldsymbol{N}^{(i)} \otimes \boldsymbol{N}^{(j)} \tag{6.1}$$

$$= \sum_{i=1}^{p}\sum_{j=1}^{p}(\boldsymbol{N}^{(i)} \otimes \boldsymbol{N}^{(i)})\boldsymbol{T}(\boldsymbol{N}^{(j)} \otimes \boldsymbol{N}^{(j)}). \tag{6.2}$$

Note that the rank of $\hat{\boldsymbol{T}}$ is the number of tensile stretching directions p. For $p = 1$ and $p = 2$, the above expressions respectively specialise as:

$$\hat{\boldsymbol{T}} = \begin{cases} (\boldsymbol{N}^{(1)} \otimes \boldsymbol{N}^{(1)})\boldsymbol{T}(\boldsymbol{N}^{(1)} \otimes \boldsymbol{N}^{(1)}) & (p = 1) \\ (\boldsymbol{1} - \boldsymbol{N}^{(3)} \otimes \boldsymbol{N}^{(3)})\boldsymbol{T}(\boldsymbol{1} - \boldsymbol{N}^{(3)} \otimes \boldsymbol{N}^{(3)}) & (p = 2) \end{cases}, \tag{6.3}$$

where we have also used the fact that the principal stretch directions form an orthonormal basis: $\sum_{i=1}^{3} \boldsymbol{N}^{(i)} \otimes \boldsymbol{N}^{(i)} = \boldsymbol{1}$. The above expression shows that the projected tensor $\hat{\boldsymbol{T}}$ remains well-defined even in the case of repeated tensile principal stretches $\lambda^{(1)} = \lambda^{(2)} > 1$ (where $\boldsymbol{N}^{(1)}$ and $\boldsymbol{N}^{(2)}$ are not uniquely defined), since the third contractile principal

direction $\boldsymbol{N}^{(3)}$ is well defined.

Alternatively, the projection of tensor $\boldsymbol{T}$ in the tensile directions can also be expressed as:

$$\hat{\boldsymbol{T}} = \mathcal{N} : \boldsymbol{T}, \tag{6.4}$$

where $\mathcal{N}$ is the fourth-order projection tensor defined for $p = 1, 2$ as:

$$\mathcal{N} = \sum_{i=1}^{p} \sum_{j=1}^{p} \boldsymbol{N}^{(i)} \otimes \boldsymbol{N}^{(j)} \otimes \boldsymbol{N}^{(i)} \otimes \boldsymbol{N}^{(j)}. \tag{6.5}$$

6.2.2 Thermodynamics

The state of the material is described with the right Cauchy-Green deformation tensor $\boldsymbol{C}$ and a symmetric second-order tensor $\boldsymbol{A}$, which quantifies the amount of anisotropic damage in the material. The pristine state of the material corresponds to $\boldsymbol{A} = \boldsymbol{0}$. Let $\Psi = \Psi(\boldsymbol{C}, \boldsymbol{A})$ be the (Helmholtz) free energy density, and $\boldsymbol{S}$ be the second Piola-Kirchhoff stress tensor. The following thermodynamic inequality holds during isothermal deformations:

$$\dot{\Psi}(\boldsymbol{C}, \boldsymbol{A}) - \frac{1}{2}\boldsymbol{S} : \dot{\boldsymbol{C}} \leq 0, \tag{6.6}$$

which, applying the chain rule, may be re-written as:

$$\left(\frac{\partial \Psi}{\partial \boldsymbol{C}} - \frac{1}{2}\boldsymbol{S}\right) : \dot{\boldsymbol{C}} + \frac{\partial \Psi}{\partial \boldsymbol{A}} : \dot{\boldsymbol{A}} \leq 0. \tag{6.7}$$

The inequality should hold for any virtual deformations $\{\dot{\boldsymbol{C}}, \dot{\boldsymbol{A}}\}$ for a given current state $\{\boldsymbol{C}, \boldsymbol{A}\}$. Accounting for incompressibility, and considering that deformations where $\dot{\boldsymbol{A}} = \boldsymbol{0}$ are purely elastic, we arrive at the state law for the stress:

$$\boldsymbol{S} = 2\frac{\partial \Psi}{\partial \boldsymbol{C}} - P\boldsymbol{C}^{-1}, \tag{6.8}$$

where P is a hydrostatic pressure arising from the incompressibility constraint and is determined from boundary the conditions. The inequality (6.7) then reduces to:

$$\boldsymbol{Z} : \dot{\boldsymbol{A}} \geq 0, \tag{6.9}$$

where $\boldsymbol{Z}$ is the driving force for damage and is given by:

$$\boldsymbol{Z} = -\frac{\partial \Psi}{\partial \boldsymbol{A}}. \tag{6.10}$$

Eq. (6.9) which must be satisfied by the kinetic model for the evolution of the damage tensor $\boldsymbol{A}$.

We follow the full-network concept in rubber elasticity to describe the elastic energy of the network (Wu and Van Der Giessen, 1993). Accordingly, the rubber is represented by a distribution of randomly oriented representative chains with energy density $\psi(\lambda, \xi)$ where λ is the chain stretch and ξ is a scalar damage variable for the chain. The elastic energy of the rubber is given by the directional average of the chain free energy:

$$\Psi = \langle \psi(\lambda, \xi) \rangle, \quad \langle \cdot \rangle := \frac{1}{4\pi} \int_{\mathcal{S}} (\cdot) \, d\mathcal{S}, \tag{6.11}$$

where the integration is carried out over the unit sphere $\mathcal{S}$. The chain stretch λ is calculated using a simple affine deformation rule:

$$\lambda^2 = \boldsymbol{C} : \boldsymbol{n} \otimes \boldsymbol{n}, \tag{6.12}$$

where $\boldsymbol{n}$ is the unit orientation vector of the representative chain in the reference configuration. By analogy with Eq. (6.12), a similar localisation rule is adopted for the directional damage parameter:

$$\xi = \hat{\boldsymbol{A}} : \boldsymbol{n} \otimes \boldsymbol{n}, \tag{6.13}$$

where $\hat{\boldsymbol{A}}$ is the projection of the damage tensor $\boldsymbol{A}$ in the tensile direction: $\hat{\boldsymbol{A}} = \mathcal{N} : \boldsymbol{A}$, cf. Eq. (6.4). Eq. (6.13) means that the instantaneous chain damage only depends on

the components of $\boldsymbol{A}$ in the directions of tensile stretches. As shown later, this feature is key to capture directional softening in cyclic tests where the principal directions of stretch vary from one cycle to the next. Eq. (6.13) also shows that the damage parameter ξ does not depend on λ, but instead is calculated based on the macroscopic tensors $\boldsymbol{C}$ and $\boldsymbol{A}$. It follows that the model does not require storage of ξ in all directions.

Remark 1. *In our approach, the full-network representation should be considered as a mathematical tool used to describe anisotropic damage, rather than a realistic description of the real rubbery network. Similarly, the representative chains in the full-network model should not be be interpreted as real polymer chains. This is clear from the damage localisation law (6.13), which states that the damage state of a given representative chain depends on the global damage tensor $\boldsymbol{A}$ and the current principal stretch directions $\boldsymbol{N}^{(i)}$, independent of the deformation history of that particular representative chain. Nevertheless, the full-network representation remains useful in providing a physical picture, compared to a purely phenomenological approach.*

Remark 2. *We adopted the affine rule (6.12) for simplicity. Alternatively, a non-affine localisation rule could be used, noting that non-affine deformations exist in real networks. For example, non-affine "fully-relaxed" microsphere models have been proposed in the literature where the chain stretch is obtained from a minimisation principle (Miehe et al., 2004; Tkachuk and Linder, 2012; Govindjee et al., 2019; Diani and Le Tallec, 2019). In principle, a fully-relaxed approach could be incorporated within our framework. The localisation rule (6.12) could also be modified to account for strain amplification effects arising from the presence of fillers (Govindjee and Simo, 1991; Bergstrom and Boyce, 1999; Khiêm and Itskov, 2017; Plagge and Klüppel, 2017).*

Inserting Expression (6.11) of the free energy into Definition (6.10) of the damage driving force, and using the damage localisation rule (6.13), it can be verified that $\boldsymbol{Z} = \hat{\boldsymbol{Z}}$. Thus, the rank of $\boldsymbol{Z}$ coincides with the number of tensile directions p, and the spectral decomposition of $\boldsymbol{Z}$ is:

$$\boldsymbol{Z} = \sum_{i=1}^{p} \nu^{(i)} \boldsymbol{M}^{(i)} \otimes \boldsymbol{M}^{(i)}, \tag{6.14}$$

where $\nu^{(i)}$ are the eigenvalues of $\boldsymbol{Z}$ and $\boldsymbol{M}^{(i)}$ are the corresponding eigenvectors. In the case where $p = 1$, we have $\boldsymbol{M}^{(1)} = \boldsymbol{N}^{(1)}$ and $\nu^{(1)} = \boldsymbol{Z} : (\boldsymbol{N}^{(1)} \otimes \boldsymbol{N}^{(1)})$. In the case where $p = 2$, $\boldsymbol{M}^{(1)}$ and $\boldsymbol{M}^{(2)}$ lie in the $\boldsymbol{N}^{(1)}$-$\boldsymbol{N}^{(2)}$ plane (since $\boldsymbol{Z} \cdot \boldsymbol{N}^{(3)} = \boldsymbol{0}$), however they do not necessarily coincide with $\boldsymbol{N}^{(1)}$ and $\boldsymbol{N}^{(2)}$. In the particular case where $p = 2$ and $\nu^{(1)} = \nu^{(2)} \equiv \nu^{(1,2)}$, the eigenvectors $\boldsymbol{M}^{(1)}$ and $\boldsymbol{M}^{(2)}$ are not fully determinate (they can be chosen arbitrarily within the $\boldsymbol{N}^{(1)}$-$\boldsymbol{N}^{(2)}$ plane). However, the driving force remains well defined since Eq. (6.14) can be rewritten as $\boldsymbol{Z} = \nu^{(1,2)}(\boldsymbol{1} - \boldsymbol{N}^{(3)} \otimes \boldsymbol{N}^{(3)})$.

Finally, the dissipation (6.9) can be rewritten:

$$\boldsymbol{Z} : \dot{\boldsymbol{A}} = \boldsymbol{Z} : \hat{\dot{\boldsymbol{A}}} \geq 0. \tag{6.15}$$

6.2.3 Damage surface and flow rule

Following classical concepts in plasticity theory (Lemaitre and Chaboche, 1994; Neto et al., 2011), we postulate the existence of an elastic domain in the force space within which the response is elastic and no damage occurs. The elastic domain is assumed to be convex and to contain the origin $\boldsymbol{Z} = \boldsymbol{0}$. The elastic domain is defined through p convex damage functions $f^{(i)}(\boldsymbol{Z})$, defined as:

$$f^{(i)}(\boldsymbol{Z}) = \nu^{(i)} \leq 0, \quad i \in (1, p). \tag{6.16}$$

Damage can only occur when one (or several) of the principal values of the driving force $\boldsymbol{Z}$ are zero: $f^{(i)} = \nu^{(i)} = 0$ for any $i \in (1, p)$. In the case where $p = 2$ and $\nu^{(1)} = \nu^{(2)}$, we define the elastic domain as $f^{(1,2)} = \nu^{(1,2)} \leq 0$.

Flow rules for damage evolution are obtained using the maximum dissipation principle (see e.g. Lubliner (1984); Neto et al. (2011)). For given $\dot{\boldsymbol{A}}$, the force $\boldsymbol{Z}$ is such that the dissipation (6.9) is maximised under the constraints (6.16) set by the damage functions:

$$\max_{\boldsymbol{Z}} \{\boldsymbol{Z} : \dot{\boldsymbol{A}} - \sum_{i=1}^{p} \dot{\alpha}^{(i)} f^{(i)}\}, \tag{6.17}$$

where $\dot{\alpha}^{(i)}$ are the Lagrange multipliers enforcing the constraints (6.16). The stationary condition gives the normal flow rule:

$$\dot{\boldsymbol{A}} = \sum_{i=1}^{p} \dot{\alpha}^{(i)} \frac{\partial f^{(i)}}{\partial \boldsymbol{Z}}, \tag{6.18}$$

where either the Lagrange multiplier is zero (no damage) or non-negative with the corresponding damage functions equal to zero (Karush-Kuhn-Tucker conditions). Owing to convexity and passing through the origin, it can be verified that the dissipation inequality (6.9) is satisfied. Using the specific form (6.16) of the damage surface in the flow rule (6.18), and using the result $\frac{\partial \nu^{(i)}}{\partial \boldsymbol{Z}} = \boldsymbol{M}^{(i)} \otimes \boldsymbol{M}^{(i)}$ (Magnus, 1985), the flow rule becomes:

$$\dot{\boldsymbol{A}} = \sum_{i=1}^{p} \dot{\alpha}^{(i)} \boldsymbol{M}^{(i)} \otimes \boldsymbol{M}^{(i)}. \tag{6.19}$$

This relation also shows that $\dot{\boldsymbol{A}} = \hat{\dot{\boldsymbol{A}}}$. In the special case of repeated eigenvalues $\nu^{(1)} = \nu^{(2)}$, we assume that $\dot{\alpha}^{(1)} = \dot{\alpha}^{(2)} = \dot{\alpha}^{(1,2)}$, so that $\dot{\boldsymbol{A}} = \dot{\alpha}^{(1,2)}(\boldsymbol{1} - \boldsymbol{N}^{(3)} \otimes \boldsymbol{N}^{(3)})$.

In Appendix E.1, we show that the general constitutive equations obtained using the concept of the damage surface can alternatively be obtained as the solution of a variational problem subjected to kinematic constraints on the flow rule (Ortiz and Stainier, 1999; Brassart and Stainier, 2012).

6.3 Specialisation of the free energy

We specialise the model by decomposing the energy density of the representative chains into elastic and damage contributions:

$$\psi(\lambda, \xi) = \psi^e(\lambda, \xi) + \psi^d(\xi). \tag{6.20}$$

Using full-network averaging, the corresponding contributions to the macroscopic free energy are given by:

$$\Psi^e = \langle \psi^e \rangle, \quad \Psi^d = \langle \psi^d \rangle, \tag{6.21}$$

and:

$$\Psi = \Psi^e + \Psi^d. \tag{6.22}$$

We also define corresponding contributions to the damage driving force:

$$\boldsymbol{Y} := -\frac{\partial \Psi^e}{\partial \boldsymbol{A}}, \quad \boldsymbol{X} := \frac{\partial \Psi^d}{\partial \boldsymbol{A}}, \tag{6.23}$$

so that:

$$\boldsymbol{Z} = \boldsymbol{Y} - \boldsymbol{X}. \tag{6.24}$$

We also have that $\hat{\boldsymbol{Y}} = \boldsymbol{Y}$ and $\hat{\boldsymbol{X}} = \boldsymbol{X}$, by construction. By definition, the contribution $\boldsymbol{Y}$ represents the elastic energy release due to the damage, whereas the contribution $\boldsymbol{X}$ represents the increase in free energy as damage increases. Eq. (6.24) highlights their opposite contributions to the total driving force $\boldsymbol{Z}$, with $\boldsymbol{Y}$ promoting damage and $\boldsymbol{X}$ acting against damage development, being respectively conjugated with $\dot{\boldsymbol{A}}$ and $-\dot{\boldsymbol{A}}$ in the dissipation inequality (6.9). As illustrated in the following, $\boldsymbol{X}$ plays a role similar to a back stress in plasticity with kinematic hardening.

6.3.1 Elastic contribution

Inspiring from the phenomenological Gent model of rubber elasticity (Gent, 1996), the elastic energy of the representative chain is taken of the following form:

$$\psi^e(\lambda, \xi) = -\frac{3}{2} G \eta(\xi) \log\left(1 - \frac{(\lambda - 1)^2}{\eta(\xi)}\right), \tag{6.25}$$

where G is the elastic modulus and η represents a limiting strain. This can be observed from the chain force-extension relationship:

$$f = \frac{\partial \psi}{\partial \lambda} = 3G \frac{(\lambda - 1)}{\left(1 - \frac{(\lambda-1)^2}{\eta}\right)}, \tag{6.26}$$

where f is the force conjugate to λ and has dimensions of energy per volume. When the chain strain $(\lambda - 1)$ is much smaller in magnitude than η, the chain behaves like a linear spring with spring constant $3G$. When the chain strain approaches η, the chain force tends to infinity. The force-extension relationship (6.26) thus mimics that of the freely-jointed chain model in rubber elasticity, which is derived from the non-Gaussian statistics for a fluctuating chain, see e.g. (Rubinstein et al., 2003). Different from the classical freely-jointed chain model, no external force is required to maintain mechanical equilibrium in the unstretched configuration $\lambda = 1$. This ensures that the reference state is stress-free.

We assume that softening results from an increase in chain extensibility η with chain damage ξ. In a real network, this could be attributed to de-adsorption of network chains from the filler surface, increasing their contour length. The following empirical relation is adopted:

$$\eta(\xi) = \eta_0 e^{k_1 \xi}, \tag{6.27}$$

where η_0 represents the initial limiting chain strain. As ξ increases, so does the limiting strain of the chain η. The parameter k_1 quantifies the effect of damage on the chain behaviour, with an increase in k_1 leading to an increase in softening for a given degree of damage. The chain model (6.26) is illustrated in Fig. 6.2 for different values of η.

Remark 3. *Alternative softening descriptions could be considered within our framework. For example, one could consider that both the chain modulus and the limiting strain are functions of the damage parameter: $G = G(\xi)$ and $\eta = \eta(\xi)$, which would provide additional degrees of freedom when fitting model predictions to experimental data. Damage by chain scission could also be included in the full-network framework for example by considering an evolving, orientation-dependent density of chains in different directions based on a chain scission criterion (Mulderrig et al., 2021). In this Chapter, to focus on the main ideas, we adopted the simplest possible representation allowing us to capture softening at large deformations while limiting the number of constitutive functions and fitting parameters.*

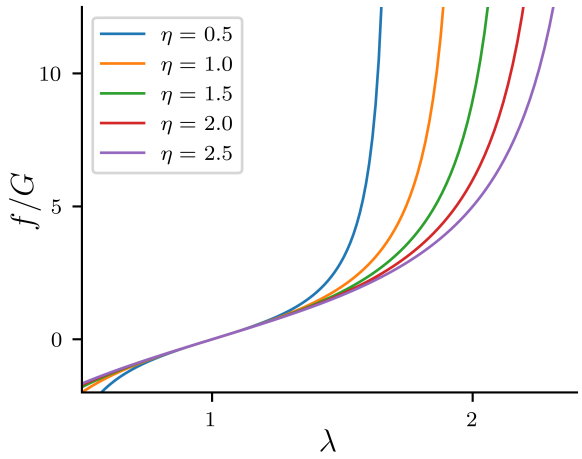


Figure 6.2: Illustration of normalised chain force-extension relationship for different chain limit strain parameter η. The chain force tends to infinity when the chain strain $(\lambda - 1)$ approaches η.

The elastic energy Ψ^e is calculated by numerical integration of the chain energy over the unit sphere:

$$\Psi^e(\boldsymbol{C}, \boldsymbol{A}) = \frac{1}{4\pi} \int_{\mathcal{S}} \psi^e(\lambda, \xi) d\mathcal{S} \approx \sum_{i=1}^{N_{int}} w_i \psi^e(\lambda_i, \xi_i), \tag{6.28}$$

where w_i is the integration weight associated with the i^{th} integration point on the unit sphere, (λ_i, ξ_i) represents the state of the representative chain with corresponding orientation on the sphere, and N_{int} is the number of integration points. Several integration schemes have been proposed with the intention to minimise the error associated with certain test functions or error under rigid body rotation (Bažant and Oh, 1986; Fliege and Maier, 1999), see also Verron (2015); Itskov (2016). Here, we adopted a conservative 900-point scheme of Fliege and Maier (1999) to ensure that the integrals are accurately evaluated and negligible rotational error is introduced to the material response. However, test cases (not shown here) comparing predictions using integration schemes developed by Fliege and Maier (1999) with N_{int} ranging from 36 to 900 suggest that schemes with a minimum of 144 points lead to acceptable rotational errors.

6.3.2 Damage contribution

For the damage contribution, we adopt the simple phenomenological expression:

$$\psi^d(\xi) = \frac{1}{2}k_2\xi^2, \tag{6.29}$$

where k_2 is a fitting parameter. As a result of this simple functional form, the orientational average of the damage contribution to the chain free energy can be evaluated analytically. To this end, we use the localisation rule (6.13) to express ξ in terms of $\hat{\boldsymbol{A}}$ and $\boldsymbol{n}$ in Eq. (6.29). Using Eq. (6.21), the macroscopic damage energy then writes:

$$\Psi^d = \frac{1}{2}k_2\hat{\boldsymbol{A}} : \langle \boldsymbol{n}\otimes\boldsymbol{n}\otimes\boldsymbol{n}\otimes\boldsymbol{n}\rangle : \hat{\boldsymbol{A}}. \tag{6.30}$$

Using the identity $\langle \boldsymbol{n}\otimes\boldsymbol{n}\otimes\boldsymbol{n}\otimes\boldsymbol{n}\rangle = \frac{1}{15}(2\mathbb{I}+\boldsymbol{1}\otimes\boldsymbol{1})$, where $\mathbb{I}$ is the symmetric fourth-order identity tensor (see e.g. Ken-Ichi (1984)), the damage contribution to the free energy becomes:

$$\Psi^d = \frac{k_2}{30}\left(2tr(\hat{\boldsymbol{A}}^2) + (tr(\hat{\boldsymbol{A}}))^2\right). \tag{6.31}$$

The corresponding contribution to the driving force is given by:

$$\boldsymbol{X} = \frac{k_2}{15}\left(2\hat{\boldsymbol{A}} + tr(\hat{\boldsymbol{A}})\sum_{i=1}^{p}\boldsymbol{N}^{(i)}\otimes\boldsymbol{N}^{(i)}\right). \tag{6.32}$$

The complete model has four parameters: G, η_0, k_1 and k_2. It can further be shown that k_1 and k_2 only play a role via the ratio k_2/k_1^2. To see this, we first define a scaled damage tensor as:

$$\hat{\boldsymbol{A}}' = k_1\hat{\boldsymbol{A}}. \tag{6.33}$$

Introducing the scaled damage tensor into Eq. (6.27) for the chain limiting strain, we obtain:

$$\eta = \eta_0 \exp\left(\hat{\boldsymbol{A}}' : \boldsymbol{n}\otimes\boldsymbol{n}\right), \tag{6.34}$$

which makes the network contribution to the free energy independent of k_1. The damage contribution to the free energy becomes:

$$\Psi^d = \frac{\kappa}{2}\left(2tr(\hat{\boldsymbol{A}}'^2) + (tr(\hat{\boldsymbol{A}}'))^2\right), \tag{6.35}$$

where $\kappa := \frac{k_2}{15k_1^2}$. This equation shows that parameters k_1 and k_2 impact the mechanical response only through the ratio k_2/k_1^2. In the following, we set $k_1 = 1$ so that $\hat{\boldsymbol{A}}' = \hat{\boldsymbol{A}}$ and only vary the parameter κ.

6.3.3 Geometric interpretation

In the case where the principal directions of the two contributions to the driving forces $\boldsymbol{X}$ and $\boldsymbol{Y}$ coincide, the damage surface admits a simple graphical representation in the principal space, similar to the Rankine yield surface. For $p = 2$, damage occurs when either of the principal values of $\boldsymbol{Y}$, $Y^{(1)}$ or $Y^{(2)}$, reaches the threshold sets by the corresponding principal values of $\boldsymbol{X}$, $X^{(1)}$ or $X^{(2)}$, so that $\nu^{(i)} = Y^{(i)} - X^{(i)} = 0$ (Fig. 6.3). The grey area represents the elastic region where the principal values of $\boldsymbol{Y}$ are less than those of $\boldsymbol{X}$. If the principal directions are fixed, as damage progresses the damage yield surface simply translates along the direction(s) in which damage is activated, similar to kinematic hardening. In the case where $p = 1$, the elastic domain reduces to the open interval $[-\infty, X^{(1)}]$ along the $Y^{(1)}$ axis.

An alternative and more general geometric representation of the damage criterion can be provided in the case where $p = 2$ regardless of whether the principal bases of $\boldsymbol{Y}$ and $\boldsymbol{X}$ coincide or not. The yield functions (6.16) constrain the eigenvalues of the driving force to be zero or negative. In the language of linear algebra, the tensor $\boldsymbol{Z}$ is thus negative semi-definite and the following inequality holds:

$$\boldsymbol{Z} : \boldsymbol{m} \otimes \boldsymbol{m} \leq 0, \tag{6.36}$$

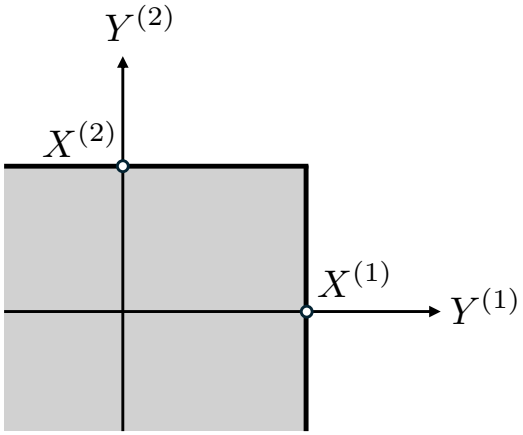


Figure 6.3: Representation of the damage surface in the principal space when the principal directions of $\boldsymbol{X}$ and $\boldsymbol{Y}$ coincide for $p = 2$. $X^{(i)}$ and $Y^{(i)}$ are the principal values of $\boldsymbol{X}$ and $\boldsymbol{Y}$.

where $\boldsymbol{m}$ is an arbitrary unit vector, which can be also expressed as:

$$(\boldsymbol{Y} - \boldsymbol{X}) : \boldsymbol{m} \otimes \boldsymbol{m} \leq 0. \tag{6.37}$$

We now consider a vector $\boldsymbol{m}$ in the $\boldsymbol{N}^{(1)} - \boldsymbol{N}^{(2)}$ plane where damage is admissible:

$$\boldsymbol{m} = \cos\theta \boldsymbol{N}^{(1)} + \sin\theta \boldsymbol{N}^{(2)}. \tag{6.38}$$

The parameterisation with arbitrary angle θ ensures that $|\boldsymbol{m}| = 1$. We may graphically represent the functions $\boldsymbol{Y} : \boldsymbol{m} \otimes \boldsymbol{m}$ and $\boldsymbol{X} : \boldsymbol{m} \otimes \boldsymbol{m}$ for all values of θ. By definition of the damage functions, the $\boldsymbol{X}$-curve always bounds the $\boldsymbol{Y}$-curve. During elastic deformations, the $\boldsymbol{Y}$-curve is fully inside the $\boldsymbol{X}$-curve and the two curves do not touch. If at any point the two curves touch, damage occurs.

The functions $\boldsymbol{Y} : \boldsymbol{m} \otimes \boldsymbol{m}$ and $\boldsymbol{X} : \boldsymbol{m} \otimes \boldsymbol{m}$ are represented as a function of θ in Fig. 6.4 in the cases where (a) the deformation is purely elastic and (b) damage occurs. Curves are represented for an arbitrary damage state $\boldsymbol{A} = 0.5\boldsymbol{e}_1 \otimes \boldsymbol{e}_1 + 0.25(\boldsymbol{e}_1 \otimes \boldsymbol{e}_2 + \boldsymbol{e}_2 \otimes \boldsymbol{e}_1) + 0.5\boldsymbol{e}_2 \otimes \boldsymbol{e}_2$. The material is subjected to a deformation $\boldsymbol{F} = \text{diag}(1.95, 1.95^{0.5}, 1.95^{-1.5})$ in Fig. 6.4(a) and $\boldsymbol{F} = \text{diag}(2.00, 2.00^{0.5}, 2.00^{-1.5})$ in Fig. 6.4(b). We use the arbitrary

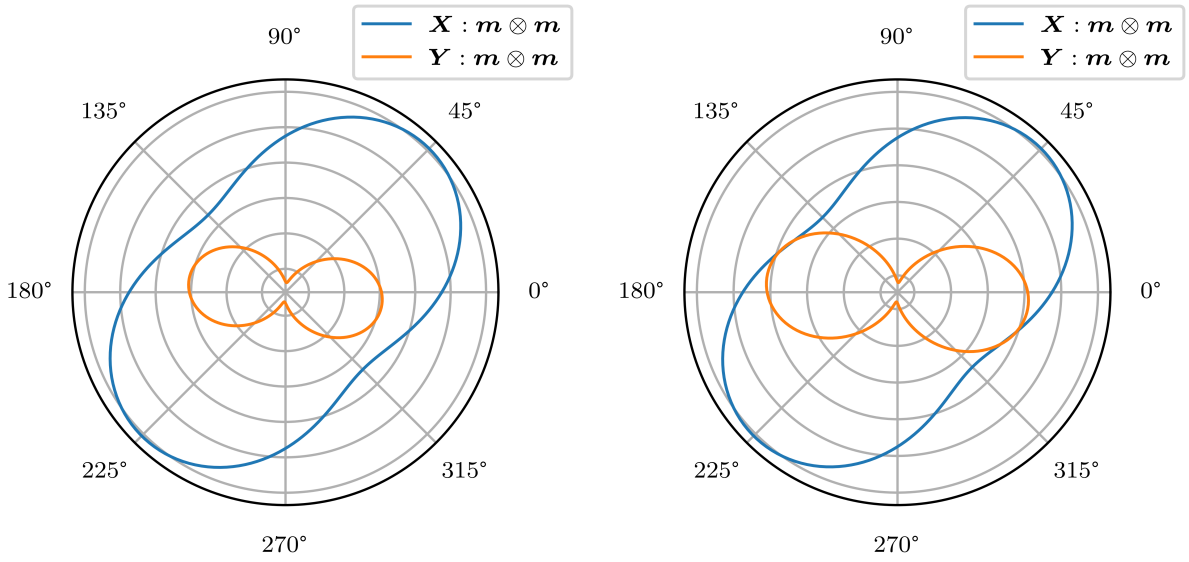


Figure 6.4: Functions $\boldsymbol{Y} : \boldsymbol{m} \otimes \boldsymbol{m}$ and $\boldsymbol{X} : \boldsymbol{m} \otimes \boldsymbol{m}$ for (a) an elastic deformation (the damage criterion is not met) and (b) a deformation involving further damage (the damage criterion is met). The $\boldsymbol{Y}$-curve is always inside the $\boldsymbol{X}$-curve with the two curves coming into contact only during damage.

material parameters $G = 5$ MPa, $\eta_0 = 0.5$, $\kappa = 0.25$ MPa.

6.4 Numerical implementation

6.4.1 Constitutive updates

We now consider the problem of integrating the constitutive relations over a time step $[t_n, t_{n+1}]$. The state at t_n is supposed to be known: $(\boldsymbol{C}_n, \boldsymbol{A}_n)$, as a well as the deformation at t_{n+1}: $\boldsymbol{C}_{n+1}$. The principal stretches $\lambda_{n+1}^{(i)}$ and principal directions $\boldsymbol{N}_{n+1}^{(i)}$ $(i = 1, 2, 3)$ can be calculated, and p is set as the number of tensile stretches $\lambda_{n+1}^{(i)} > 1$. In the case of repeated tensile stretches, only the principal direction $\boldsymbol{N}^{(3)}$ is needed.

Assuming that the rates of damage $\dot{\alpha}^{(i)}$ are constant over the time step, the damage flow rule (6.19) is discretised as:

$$\boldsymbol{A}_{n+1} = \boldsymbol{A}_n + \sum_{i=1}^{p} \Delta\alpha^{(i)} \boldsymbol{M}_{n+1}^{tr(i)} \otimes \boldsymbol{M}_{n+1}^{tr(i)}, \tag{6.39}$$

where $\Delta\alpha^{(i)} = \dot{\alpha}^{(i)}\Delta t$. In Eq. (6.39), to simplify the algorithm, we use damage directions $\boldsymbol{M}_{n+1}^{tr(i)}$ associated with a trial state $(\boldsymbol{C}_{n+1}, \boldsymbol{A}_n)$. The trial damage driving force is defined as:

$$\boldsymbol{Z}_{n+1}^{tr} = -\frac{\partial \Psi}{\partial \boldsymbol{A}}(\boldsymbol{C}_{n+1}, \boldsymbol{A}_n). \tag{6.40}$$

The trial directions $\boldsymbol{M}_{n+1}^{tr(i)}$ are the eigenvectors of $\boldsymbol{Z}_{n+1}^{tr}$. In the case where $p = 1$, we have that $\boldsymbol{M}_{n+1}^{tr(1)} = \boldsymbol{N}_{n+1}^{(1)}$. In the case where $p = 2$ and the eigenvalues $\nu_{n+1}^{tr(i)}$ are distinct, $\boldsymbol{M}_{n+1}^{tr(1)}$ and $\boldsymbol{M}_{n+1}^{tr(2)}$ are found by solving an eigenvalue problem. If $\nu_{n+1}^{tr(1)} = \nu_{n+1}^{tr(2)}$, then these eigenvectors are not needed since the incremental flow rule can be calculated as $\boldsymbol{A}_{n+1} = \boldsymbol{A}_n + \Delta\alpha^{(1,2)}(\boldsymbol{1} - \boldsymbol{N}_{n+1}^{(3)} \otimes \boldsymbol{N}_{n+1}^{(3)})$.

Elastic predictor. To determine whether damage takes place over the time step, we evaluate the damage functions $f^{(i)}$ for the trial driving force. The increment is purely elastic if the driving force satisfies the conditions:

$$f_{n+1}^{tr(i)} = \nu_{n+1}^{tr(i)} = \boldsymbol{Z}_{n+1}^{tr} : \boldsymbol{M}_{n+1}^{tr(i)} \otimes \boldsymbol{M}_{n+1}^{tr(i)} < 0, \tag{6.41}$$

for $i \in (1, p)$. In this case, the stress update is calculated as:

$$\boldsymbol{S}_{n+1} = \boldsymbol{S}_{n+1}^{tr} = 2\frac{\partial \Psi}{\partial \boldsymbol{C}}(\boldsymbol{C}_{n+1}, \boldsymbol{A}_n) - P_{n+1}\boldsymbol{C}_{n+1}^{-1}, \tag{6.42}$$

and $\boldsymbol{A}_{n+1} = \boldsymbol{A}_n$.

Damage correction. If the condition (6.41) is violated for any $i \in (1, p)$, then a damage correction step must be performed so that forces remain on the damage surface:

$$f_{n+1}^{(i)} = \nu_{n+1}^{(i)} = \boldsymbol{Z}_{n+1} : \boldsymbol{M}_{n+1}^{tr(i)} \otimes \boldsymbol{M}_{n+1}^{tr(i)} = 0. \tag{6.43}$$

In this expression, $\boldsymbol{Z}_{n+1} = -\frac{\partial \Psi}{\partial \boldsymbol{A}}(\boldsymbol{C}_{n+1}, \boldsymbol{A}_{n+1})$ where $\boldsymbol{A}_{n+1}$ is given by the discretised flow rule (6.39). Thus, Eq. (6.43) constitutes a nonlinear equation for the damage variable $\Delta\alpha^{(i)}$. When $p = 1$, only one nonlinear equation must be solved for $\Delta\alpha^{(1)}$. When $p = 2$, one or two damage directions may be active, giving either one or two (coupled) nonlinear

equations. The nonlinear equations are solved using the Newton-Raphson method detailed in the following section. After the updates $\Delta\alpha^{(i)}$ have been obtained, the damage tensor is updated using the discretised flow rule (6.39), and the stress update is calculated as:

$$\boldsymbol{S}_{n+1} = 2\frac{\partial \Psi}{\partial \boldsymbol{C}}(\boldsymbol{C}_{n+1}, \boldsymbol{A}_{n+1}) - P_{n+1}\boldsymbol{C}_{n+1}^{-1}. \tag{6.44}$$

6.4.2 Internal Newton-Raphson

In this section, we provide details on the numerical solution of Eq. (6.43) for $\Delta\alpha^{(i)}$ using a standard Newton-Raphson method. In the following, we omit the subscripts $n+1$ for brevity. In the case where there is only one active damage direction, Eq. (6.43) becomes:

$$f^{(1)} = \boldsymbol{Z} : \boldsymbol{N}^{(1)} \otimes \boldsymbol{N}^{(1)} = 0. \tag{6.45}$$

Using the subscript r to denote a quantity at the r^{th} iteration, the Newton-Raphson scheme is expressed as:

$$\Delta\alpha_{r+1}^{(1)} = \Delta\alpha_{r}^{(1)} - \left(\frac{\partial f^{(1)}}{\partial \Delta\alpha^{(1)}}\right)_r^{-1} f_r^{(1)}, \tag{6.46}$$

$$\left(\frac{\partial f^{(1)}}{\partial \Delta\alpha^{(1)}}\right)_r = \boldsymbol{N}^{(1)} \otimes \boldsymbol{N}^{(1)} : \left(\frac{\partial \boldsymbol{Z}}{\partial \boldsymbol{A}}\right)_r : \boldsymbol{N}^{(1)} \otimes \boldsymbol{N}^{(1)}, \tag{6.47}$$

where:

$$\left(\frac{\partial \boldsymbol{Z}}{\partial \boldsymbol{A}}\right)_r = -\frac{\partial^2 \Psi}{\partial \boldsymbol{A}^2}(\boldsymbol{C}, \boldsymbol{A}_r). \tag{6.48}$$

When there are two active damage directions with $\nu_{n+1}^{tr(1)} \neq \nu_{n+1}^{tr(2)}$, we need to solve the following system for the two unknowns $\Delta\alpha^{(1)}$ and $\Delta\alpha^{(2)}$:

$$f_{n+1}^{(i)} = \boldsymbol{Z}_{n+1} : \boldsymbol{M}^{tr(i)} \otimes \boldsymbol{M}^{tr(i)} = 0, \quad i = 1, 2. \tag{6.49}$$

Application of the Newton-Raphson method gives:

$$\Delta\alpha_{r+1}^{(i)} = \Delta\alpha_r^{(i)} - \left(\frac{\partial f^{(j)}}{\partial \Delta\alpha^{(i)}}\right)_r^{-1} f^{(j)}, \tag{6.50}$$

$$\left(\frac{\partial f^{(i)}}{\partial \Delta\alpha^{(j)}}\right)_r = \boldsymbol{M}^{tr(i)} \otimes \boldsymbol{M}^{tr(i)} : \left(\frac{\partial \boldsymbol{Z}}{\partial \boldsymbol{A}}\right)_r : \boldsymbol{M}^{tr(j)} \otimes \boldsymbol{M}^{tr(j)}, \tag{6.51}$$

where $i, j = 1, 2$. The solution method requires inversion of the 2×2 matrix $\frac{\partial f^{(i)}}{\partial \Delta\alpha^{(j)}}$, which we do analytically in our implementation.

In the particular case where $p = 2$ and $\nu_{n+1}^{tr(1)} = \nu_{n+1}^{tr(2)}$, we only need to solve one nonlinear equation for one unknown $\Delta\alpha^{(1,2)}$:

$$f_{n+1}^{(1,2)} = \boldsymbol{Z}_{n+1} : (\mathbf{1} - \boldsymbol{N}^{(3)} \otimes \boldsymbol{N}^{(3)}) = 0. \tag{6.52}$$

Application of the Newton-Raphson method gives:

$$\Delta\alpha_{r+1}^{(1,2)} = \Delta\alpha_r^{(1,2)} - \left(\frac{\partial f^{(1,2)}}{\partial \Delta\alpha^{(1,2)}}\right)_r^{-1} f_r^{(1,2)}, \tag{6.53}$$

$$\left(\frac{\partial f^{(1,2)}}{\partial \Delta\alpha^{(1,2)}}\right)_r = (\mathbf{1} - \boldsymbol{N}^{(3)} \otimes \boldsymbol{N}^{(3)}) : \left(\frac{\partial \boldsymbol{Z}}{\partial \boldsymbol{A}}\right)_r : (\mathbf{1} - \boldsymbol{N}^{(3)} \otimes \boldsymbol{N}^{(3)}). \tag{6.54}$$

The first guess for the Newton-Raphson can be taken as the undamaged solution, $\Delta\alpha^{(i)} = 0$, or as the damage increment of the previous time step.

6.4.3 Consistent tangent

The consistent tangent operator is calculated from the total derivative of the stress with respect to $\boldsymbol{C}_{n+1}$. The part of the stress independent of the pressure (i.e. the part related to the free energy derivative) derives as:

$$\frac{d^2\Psi}{d\boldsymbol{C}_{n+1}^2} = \frac{\partial^2\Psi}{\partial \boldsymbol{C}_{n+1}^2} + \frac{\partial^2\Psi}{\partial \boldsymbol{C}_{n+1} \partial \boldsymbol{A}_{n+1}} : \sum_{i=1}^{p} \left(\boldsymbol{M}_{n+1}^{tr(i)} \otimes \boldsymbol{M}_{n+1}^{tr(i)} \frac{\partial \Delta\alpha^{(i)}}{\partial \boldsymbol{C}_{n+1}} + \Delta\alpha^{(i)} \frac{\partial \boldsymbol{M}_{n+1}^{tr(i)} \otimes \boldsymbol{M}_{n+1}^{tr(i)}}{\partial \boldsymbol{C}_{n+1}} \right). \tag{6.55}$$

We calculate $\partial \Delta\alpha^{(i)} / \partial \boldsymbol{C}_{n+1}$ from the total derivatives of the damage functions $f^{(i)}$ with respect to $\boldsymbol{C}_{n+1}$ incorporating the update of $\Delta\alpha^{(i)}$. The damage direction derivatives are

found by differentiating the eigenvalue problem for $\boldsymbol{Z}$. Details of our calculations are provided in E.2. The pressure term $P_{n+1}\boldsymbol{C}_{n+1}^{-1}$ can be differentiated with respect to $\boldsymbol{C}_{n+1}$ leading to the following expression for the material tangent (Weiss et al., 1996):

$$\frac{d\boldsymbol{S}_{n+1}}{d\boldsymbol{C}_{n+1}} = 2\frac{d^2\Psi}{d\boldsymbol{C}_{n+1}^2} + \frac{1}{2}P_{n+1}\left(\boldsymbol{C}_{n+1}^{-1}\odot\boldsymbol{C}_{n+1}^{-1} + \left(\boldsymbol{C}_{n+1}^{-1}\odot\boldsymbol{C}_{n+1}^{-1}\right)^t\right), \tag{6.56}$$

where $()^t$ pertains to the transpose in the final two indices and $\odot$ is the tensor product $(\boldsymbol{A}\odot\boldsymbol{B})_{ijkl} = A_{ik}B_{jl}$.

6.5 Results

We first illustrate the capabilities of our model under simple cases of homogeneous deformation where the principal stretching directions do not change during the deformation history. In these cases, it can be easily verified from the damage flow rule (6.19) and Eq. (6.3) that $\boldsymbol{A} = \hat{\boldsymbol{A}}$. We first consider the cyclic uniaxial tension response, and analyse the role of the parameters κ and η_0 on the mechanical response. We then compare the predictions of the model under planar extension and equibiaxial tension to the response in uniaxial tension. Numerical results presented in this Section were obtained using an implementation of the model in Python.

6.5.1 Cyclic uniaxial tension response

Fig. 6.5 shows the model response under progressive cyclic uniaxial tension in the $\boldsymbol{e}_1$ direction for different values of κ and η_0. We set $G = 1.7$ MPa, $\eta_0 = 0.50$ and $\kappa = 0.50$ MPa as the baseline parameters. Figs 6.5(a) and (b) show that the model predicts a lower stress during unloading, compared to the stress during loading at the same strain. As the material is being reloaded, the stress-strain response follows the unloading path, before rejoining the original curve at the stretch at which unloading occurred. Further softening only occurs when the material is subjected to a stretch greater than that to which the material has previously been subjected. These are the typical features of the Mullins effect, which are well captured by the model.

Figs 6.5(c) and (d) show the corresponding evolution of the damage tensor component $A_{11} = \hat{A}_{11}$, which is the only non-zero component of the damage tensor for uniaxial loading according to the damage flow rule (6.19). During loading up to a stretch $\lambda^{(1)}_{max}$ not experienced by the material before, the damage parameter A_{11} is calculated from the condition that the damage state should remain on the damage surface: $Y^{(1)} - X^{(1)} = 0$. During unloading, $Y^{(1)} - X^{(1)} < 0$ and A_{11} remains constant. During reloading, A_{11} increases again when $Y^{(1)} - X^{(1)} = 0$, which is only satisfied for $\lambda^{(1)} = \lambda^{(1)}_{max}$ since $X^{(1)}$ is constant during unloading.

Increasing κ leads to a stiffer response of the material (Fig. 6.5(a)), which is attributed to an increase in the damage contribution to the free energy, and hence to an increase in the damage threshold as damage progresses. Indeed, as shown in Fig. 6.5(c), less damage is accumulated at a given stretch when κ is larger (A_{11} is smaller). Fig. 6.5(b) shows the effect of the initial limit strain η_0 on the mechanical response. This parameter controls the overall stiffening response in the undamaged state, with a smaller chain extensibility limit giving a higher stress for a given strain, which is apparent in the nonlinear regime of the chain response. Smaller values of η_0 also lead to an increase in the damage driving force $\boldsymbol{Y}$, which favours damage. As a result, the hysteresis loop is more pronounced when η_0 decreases. This is also reflected in the greater accumulation of damage for a given stretch as η_0 decreases in Fig. 6.5(d).

6.5.2 Response under different loading modes

We next compare model predictions under uniaxial tension (UT) ($\lambda^{(1)} > 1$, $\lambda^{(2)} = \lambda^{(3)} = 1/\sqrt{\lambda^{(1)}}$), planar extension (PE) ($\lambda^{(1)} > 1$, $\lambda^{(2)} = 1$, $\lambda^{(3)} = 1/\lambda^{(1)}$) and equibiaxial tension (EBT) ($\lambda^{(1)} = \lambda^{(2)} > 1$, $\lambda^{(3)} = 1/\lambda_1^2$), respectively. In all cases, the loading is up to a maximum principal stretch of 1.8. Material parameters are the same as in the previous section: $G = 1.7$ MPa, $\eta_0 = 0.5$ and $\kappa = 0.5$ MPa. In addition to predicted stress-strain curves, we also show the distribution of the chain limit strain η in the orientation space, as an indicator of the extent of damage. We chose to represent η, instead of the components of $\boldsymbol{A}$, because it has a clearer physical interpretation.

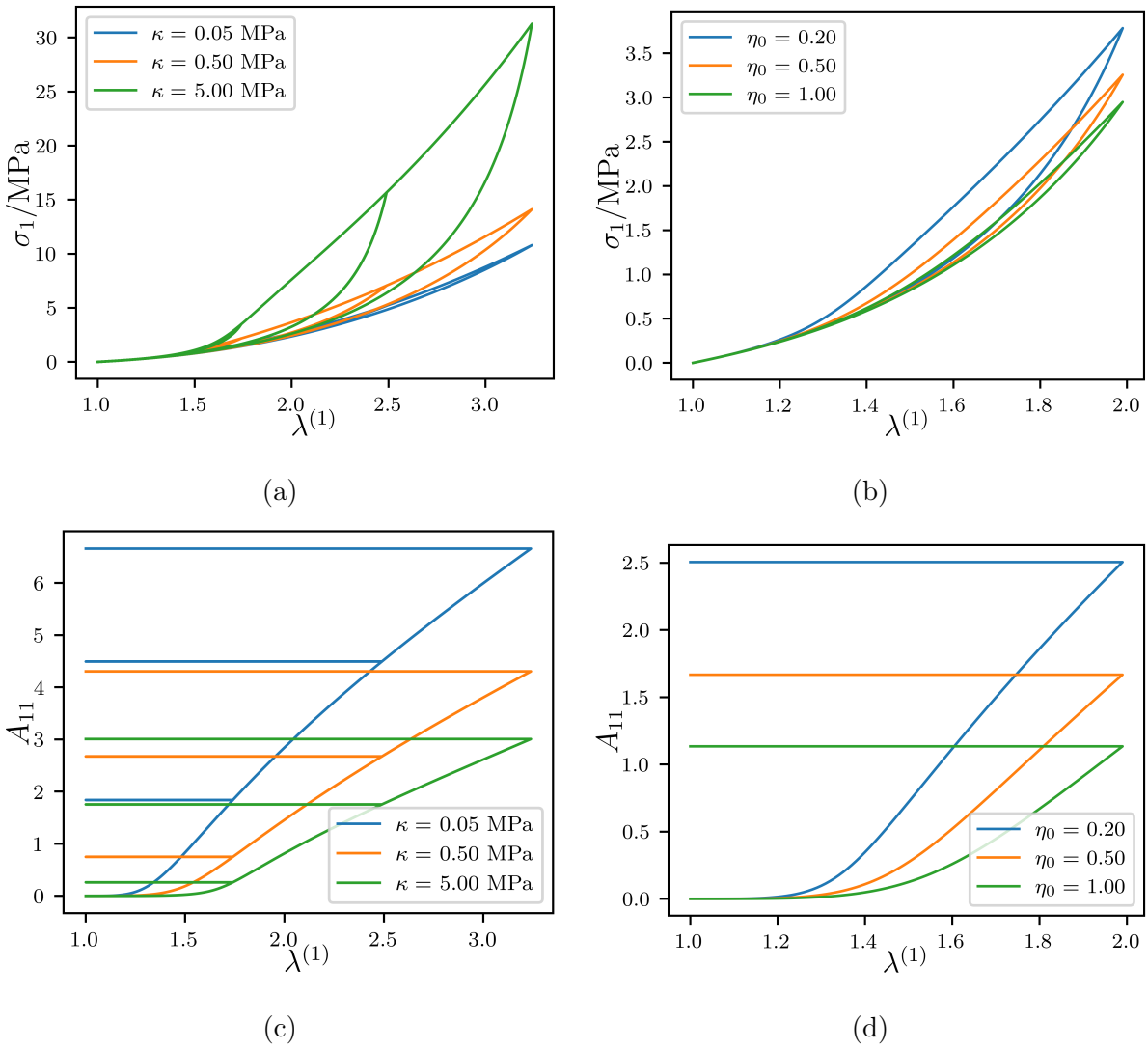


Figure 6.5: (a),(b): Influence of parameters κ and η_0 on the uniaxial stress-stretch response of the material subjected to loading in the $\boldsymbol{e}_1$-direction. (c),(d): Corresponding evolution of A_{11}.

Fig. 6.6(a) shows that the model predicts a clear Mullins effect in all loading modes. A similar damage distribution develops during loading under uniaxial tension and planar extension, cf. Figs 6.6(b) and (c). Both damage distributions appear similar and the maximum directional value of the damage parameter is approximately the same in both cases, i.e. $\eta_{max}^{UT} \approx \eta_{max}^{PE} \approx 1.2$. Under equibiaxial tension, Fig. 6.6(d), the damage distribution differs significantly in that damage proceeds over the entire plane of tensile stretching rather than in just one direction. It is interesting to consider the amount of damage the chains aligned with the stretching directions accumulate in equibiaxial tension compared to the other two cases. In equibiaxial tension, all the chains in a same $\boldsymbol{e}_1 - \boldsymbol{e}_2$

plane experience the same damage ξ. However, in equibiaxial tension these chains are more damaged ($\eta_{max}^{EBT} \approx 1.3$). This is due to the larger contribution $\boldsymbol{Y}$ to the damage driving force under equibiaxial tension, which causes more damage.

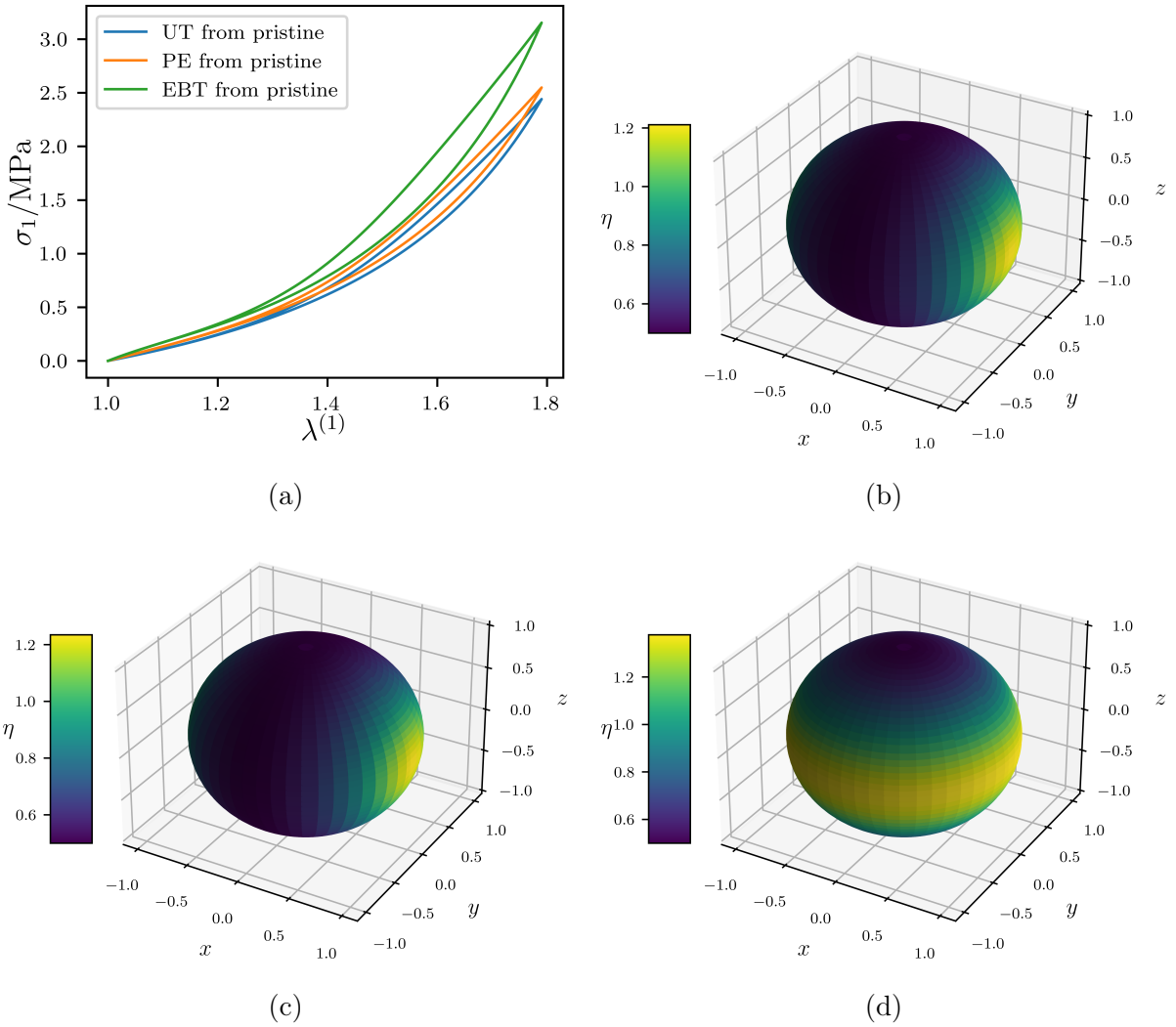


Figure 6.6: (a) Stress-stretch curves under different loading conditions and plots of the final distribution of η in the orientation space for: (b) uniaxial tension, (c) planar extension and (d) equibiaxial tension.

6.5.3 Comparison to experimental data of Diani and Le Tallec (2019)

We next compare model predictions to experimental data of Diani and Le Tallec (2019) for carbon-black reinforced styrene butadiene rubbers with varying proportions of added filler particles (30 phr, 40 phr, 50 phr and 60 phr). The rubbers are subject to cycles of uniaxial tension of progressively increasing magnitude. The amplitude of the maximum

stretch is increased by 0.5 each cycle for four cycles, with the first cycle taking place up to a stretch of 1.5. The data are provided for single experimental tests and no measurements of uncertainity or noise are provided. Fitting of the model parameters is done using least squares regression in the SciPy optimize module using the Broyden-Fletcher-Goldfarb-Shanno (BFGS) method (Fletcher, 1987), where the error is sum of the squares of the (unweighted) difference between the experimental true stress and model true stress over all experimental points in the deformation history. The least squares objective function is chosen for simplicity and expediency. The data show no obvious outliers and in the absence of further information it seems reasonable to assume the errors in the data are uniform (homoscedastic), which indicates that unweighted least squares offers an appropriate means to fit the data (Birkes and Dodge, 2011). The best-fit parameters are listed in Table 6.1 and the model fits are plotted against the experimental data in Fig. 6.7, along with predicted values of the (only non-zero) component of the damage tensor, A_{11}.

Composition	G/MPa	η_0	κ/MPa
30 phr	1.69	0.180	0.169
40 phr	1.92	0.178	0.526
50 phr	2.05	0.179	1.343
60 phr	2.61	0.179	2.669

Table 6.1: Parameters for fitting to Diani and Le Tallec (2019) data.

The model quantitatively captures the Mullins softening exhibited by each rubber. Hysteresis loops of appropriate size and shape are predicted and the slopes in the stress-strain curve are well predicted during both elastic and inelastic processes. However, the model does not predict behaviour of the material at small strains particularly well. This is attributed to our specific model of chain energy (6.25), where softening arises from an increase in the chain contour length, Eq. (6.27). In this formulation, damage only impacts the large deformation behaviour of the material, leaving the small strain response unaffected. Improved predictions could be achieved by linking the damage tensor to parameters related to the small strain response instead of, or in addition to, the chain extensibility, for example by considering a damage-dependent chain modulus $G(\xi)$. The fitting performance of the model could also be improved by considering viscoelasticity.

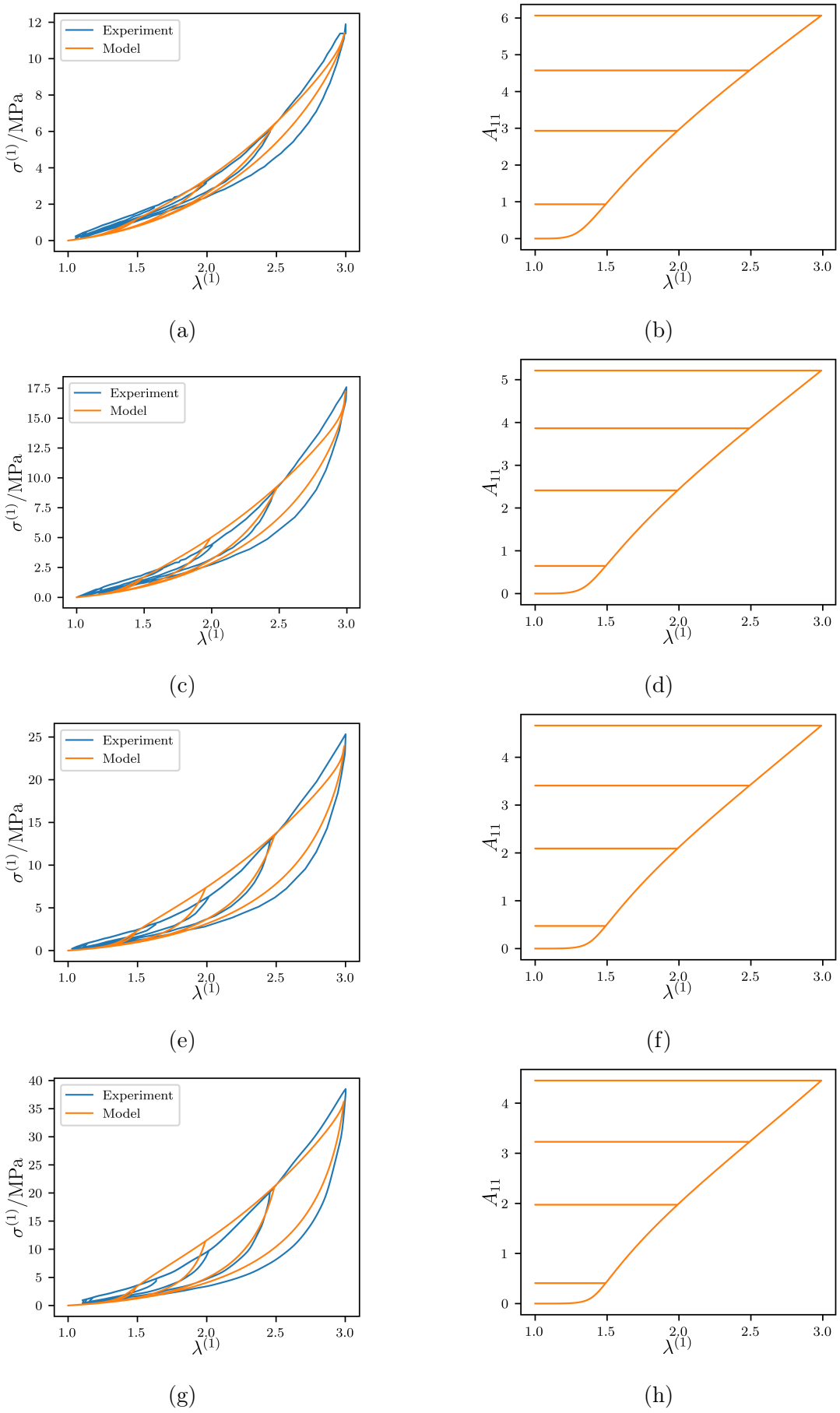


Figure 6.7: Model fitted to data of Diani and Le Tallec (2019) for filled rubbers with (a)-(b) 30 phr, (c)-(d) 40 phr, (e)-(f) 50 phr and (g)-(h) 60 phr filler particles added.

6.5.4 Comparison to experimental data of Machado et al. (2012)

We now consider loading scenarios where the loading directions change during deformation. As experimental validation, we consider the dataset of Machado et al. (2012) for filled silicone rubber. In the experiments, rectangular samples of the the rubber were first subjected to uniaxial loading-unloading cycle in direction $\boldsymbol{e}_1$. Smaller rectangular samples were then cut from the conditioned samples with different orientations to the original rectangular sample, and then subjected to uniaxial tension. Experimental results show that the amount of stress softening observed during reloading depends on the angle between the first and second loading (Fig. 6.8(a)). As the angle between the first and second loading increases, the amount of softening decreases. In particular, the stress-strain curve of samples cut at 90° almost coincides with the first loading curve. For all angles, the stress-strain curves of the second loading all rejoin the first loading curve at the same stretch, corresponding to the maximum tensile stretch reached during the first loading.

The predictions of our model under the same loading conditions are shown in Fig. 6.8(b), using the following parameter values: $G = 0.3$ MPa, $\eta_0 = 0.278$ and $\kappa = 0.216$ MPa. These parameter values were found from least squares minimisation applied to the loading-unloading response of the material in a single direction following the approach outlined in Section 6.5.3. The model well captures the orientation dependence of the stress softening. In particular, all the stress-strain curves during the second loading rejoin the first loading curve, with the curve at 90° coinciding exactly with the the first loading curve. However, our model also predicts that the stretch at which the first loading curve is rejoined also depends on orientation, which contradicts the experimental observation. As shown below, this feature is built in the formulation, and therefore cannot be fixed by fitting the constitutive functions. Nevertheless, the overall agreement is acceptable, considering the very small number of constitutive functions and fitting parameters.

Figs 6.8(c) and (d) show the component of the damage tensor $\hat{\boldsymbol{A}} : \boldsymbol{N}^{(1)} \otimes \boldsymbol{N}^{(1)}$ during the first loading/unloading cycle and the second loading, respectively. During the first

loading cycle, $\boldsymbol{N}^{(1)} = \boldsymbol{e}_1$ and $\hat{\boldsymbol{A}} : \boldsymbol{N}^{(1)} \otimes \boldsymbol{N}^{(1)} = \hat{A}_{11} = A_{11}$ is the only component of the tensor $\boldsymbol{A}$, since $\boldsymbol{A}$ only grows in the (unique) direction of tensile stretch, according to the flow rule (6.19). $\hat{A}_{11}$ grows during loading, and remains constant during unloading (Fig. 6.8(c)). At the start of the second loading at an angle θ about the $\boldsymbol{e}_3$ axis, $\boldsymbol{N}^{(1)} = \boldsymbol{e}'_1$, and the components of tensors $\boldsymbol{A}$ and $\hat{\boldsymbol{A}}$ in the rotated basis are given by:

$$[A]_{i'j'} = \begin{bmatrix} \cos^2\theta A_{11} & -\cos\theta\sin\theta A_{11} & 0 \\ -\cos\theta\sin\theta A_{11} & \sin^2\theta A_{11} & 0 \\ 0 & 0 & 0 \end{bmatrix}, \quad [\hat{A}]_{i'j'} = \begin{bmatrix} \cos^2\theta A_{11} & 0 & 0 \\ 0 & 0 & 0 \\ 0 & 0 & 0 \end{bmatrix}, \tag{6.57}$$

which shows that the projection of $\boldsymbol{A}$ onto the tensile stretch direction results (in the rotated basis) in the elimination of all components of $\boldsymbol{A}$ except the one in the direction of loading. The subsequent evolution of $\hat{\boldsymbol{A}} : \boldsymbol{N}^{(1)} \otimes \boldsymbol{N}^{(1)} = \hat{A}_{1'1'}$ during the second loading at an angle θ is shown in Fig. 6.8(d). When $\theta = 0°$, $\hat{A}_{1'1'}$ at the start of the second loading is the same as at the end of first loading, and remains constant during the second loading, until the stretch reaches the maximum historic stretch. The corresponding stress-stretch curve shows the strongest softening. At an intermediate angle $\theta \in [0°, 90°]$, $\hat{A}_{1'1'}$ at the start of the second loading is lower than at $0°$, and also remains constant during the second loading. Therefore, the softening is less prominent. Damage resumes when the reloading curve meets the original curve, where $Z_{1'1'} = Y_{1'1'} - X_{1'1'} = 0$. In particular, for $\theta = 90°$, $\hat{A}_{1'1'}$ is zero at the start of the second loading, so that the behaviour during the second loading coincides with the behaviour during the first loading.

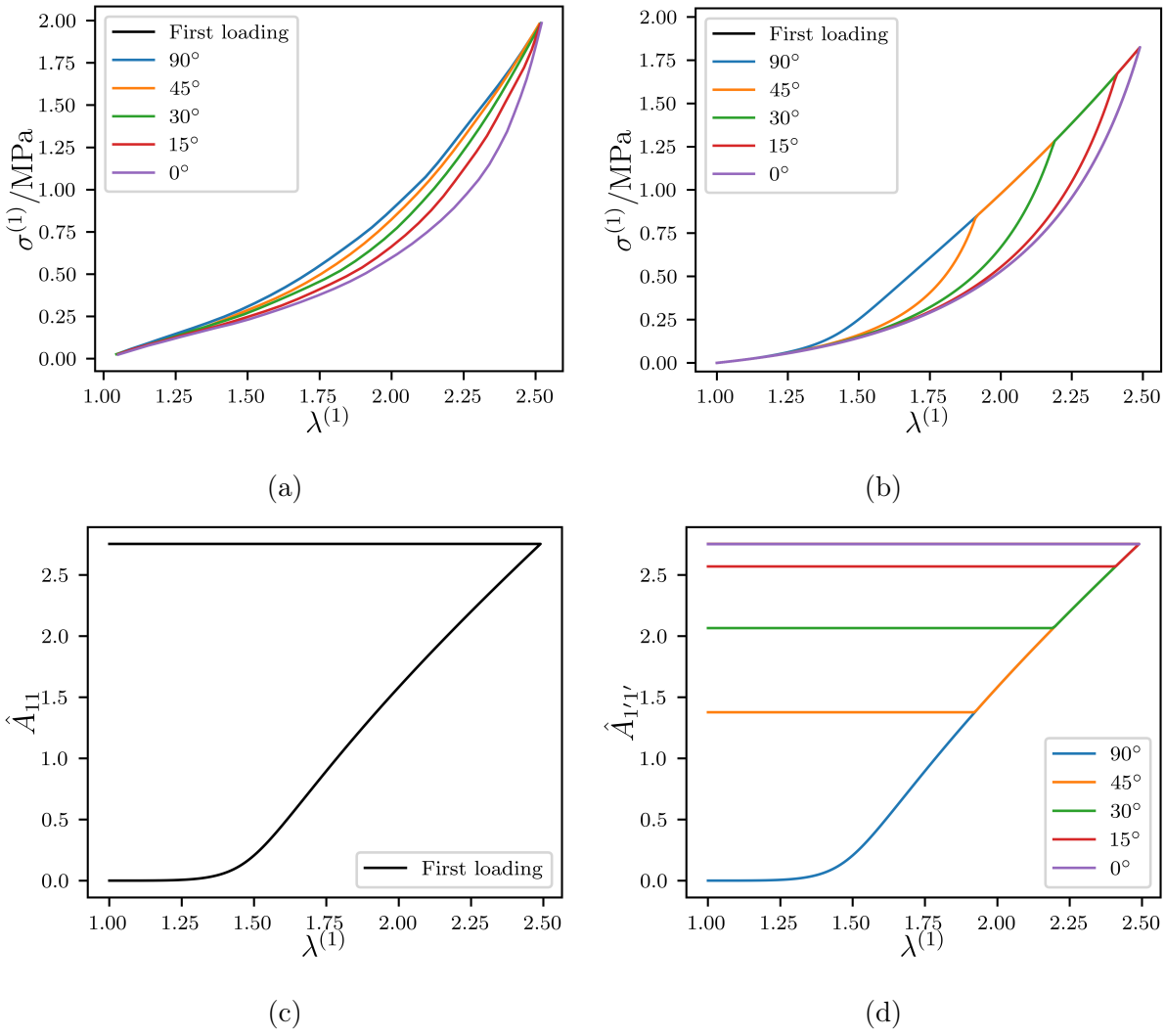


Figure 6.8: (a) Experimental data of Machado et al. (2012) for cyclic uniaxial tension in the $\boldsymbol{e}_1$-direction and subsequent loading at angles of 0°, 15°, 30°, 45° and 90° relative to the $\boldsymbol{e}_1$-direction. (b) Model predictions of the cyclic response. (c) Evolution of $\hat{A}_{11}$ during the first cycle. (d) Evolution of $\hat{A}_{1'1'}$ in the tensile direction during subsequent loading at different angles. Note that in Figs (a) and (b), the first loading curve coincides with the 90° curve and is not visible.

6.6 Finite element implementation

To demonstrate the ability of our model to consider arbitrary loading conditions in non-homogeneous cases, we have implemented our model in the finite element software ABAQUS as a user subroutine UMAT. For conciseness, the finite element implementation is detailed in E.3 alongside the numerical example of the loading of a holed plate in sequentially different directions. Our implementation treats the incompressibility constraint through a compressible regularisation to simplify the finite element problem. Note that our finite element implementation is not able to handle possible strain localisation due to strain softening (for example in the presence of a sharp notch), where unphysical mesh dependency is expected. In the numerical example considered, softening-induced localisation is not observed as no sharp notches are present. A more general implementation of our approach robust against softening-induced localisation would require a non-local approach such as a gradient-enhanced formulation, see e.g. Ferreira et al. (2017), which is outside the scope of this work.

6.7 Conclusion

We have presented a constitutive model for the Mullins effect under arbitrary loading conditions, including complex loading featuring changes in material stretching directions. The free energy function is based on the full-network representation, which involves the orientational averaging of the energy of a representative chain. Softening is captured by increasing the contour length (or chain limit extensibility) during deformation. Different from full-network damage models, the instantaneous chain damage is calculated based on a global damage tensor, and also depends on the current tensile stretching directions. The use of the tensor variable bypasses the need for storing individual damage parameters at the level of individual chains. The damage tensor evolves according to a damage criterion and flow rules, paralleling the treatment of plasticity with kinematic hardening. While the model may appear more complex than other full-network Mullins effect models in the literature, the updating of the internal state requires the solution of only one or two equa-

tions, compared to up to several hundred in full network models. Furthermore, the model is able to reproduce key experimental features for uniaxial tensile tests under sequentially different directions which other full-network models struggle to capture. In particular, the model predicts orientation-dependent softening with zero softening in the transverse direction. In addition, for all orientations of second loading, predicted curves rejoin the curve of the first loading, in agreement with experimental findings. The model has been implemented as a user subroutine UMAT in the finite element software ABAQUS and is suitable for solving boundary value problems in the absence of damage localisation.

While the model qualitatively captures experimental trends, some shortcomings have also been identified. First, regarding the tensile response in cyclic tests where the loading direction varies from one cycle to the next (the data from Machado et al. (2012)), the model predicts that the stretch at which the original curve is rejoined also depends on orientation, in contradiction with the experimental data. At this time, it is unclear to us whether this shortcoming can be addressed within the proposed framework. Another limitation of the proposed model is the poor fitting performance at low to moderate strain. This could most probably be addressed by considering more general constitutive functions for the free energy of the representative chain and its softening, in particular by also accounting for a dependence of the chain modulus on damage. Other specific choices for the damage contribution to the free energy could also be considered.

In this Chapter, we presented the constitutive framework in its simplest possible form, limiting the number of constitutive functions and fitting parameters to focus on the key features of the mathematical model. However, the constitutive framework is flexible and has the potential to be extended in several directions. First, the current model does not account for viscous effects which are exhibited by many soft materials over the timescales of the experiments. Viscoelasticity as well as rate-dependent damage could be considered within the current framework. Effects of topological constraints between the rubber chains (e.g. entanglements) could be taken into account using tube models of rubber elasticity, which consider an additional contribution to the chain free energy that involves

the area-stretch of the continuum in addition to the line stretch (Göktepe and Miehe, 2005). As shown in Chapter 4, full-network models where the chain behaviour depends on both the line-stretch and the area-stretch exhibit I_2-dependence, which is necessary for reproducing experimental data for various loading modes. Additional flexibility for fitting experimental data could also be achieved by considering multiple networks capturing different aspects of the response, as proposed in several works (Govindjee and Simo, 1991; Machado et al., 2014; Khiêm and Itskov, 2017). To better link the model parameters to the composition, the stretch localisation rule could be refined to reflect filler rigidity, for example introducing strain amplification effects linked to the filler concentration (Govindjee and Simo, 1991; Qi and Boyce, 2004).

6.8 Dissemination

The work in this Chapter features in the publication: "G. Kumar, L. Brassart *An anisotropic full-network model with damage surface for the Mullins effect in filled rubbers.* International Journal of Solids and Structures 304 (2024): 113030."

Chapter 7

Conclusions

7.1 Summary

The overarching objective of this thesis has been to investigate and extend the micromechanical approach to rubber elasticity to complex elastomer systems under generic loading conditions and loading histories. To this end, a series of micromechanics-based constitutive models for filled rubbers and thermoplastic elastomers have been proposed which link mechanical behaviours to microstructural and compositional parameters. The necessary assumptions in the micromechanical approach for achieving good agreement with experimental data have also been investigated.

A general framework for modelling two-phase elastomers is presented in Chapter 3. The framework generalises the behaviour of a wide range of elastomer systems which are usually modelled using disparate approaches. The framework is specialised firstly to filled rubbers in Section 3.3, which undergo large deformations and display the Mullins effect, and subsequently thermoplastic polyurethanes in Section 3.4, which in addition show plastic and viscous behaviour. The model is compared to experimental data for both filled rubbers and thermoplastic elastomers and is able to explain changes in the stress-stretch response under cyclic uniaxial tension with moderate changes in hard phase volume fraction for each material. Deficits of the model in predicting the material response under equibiaxial tension from the uniaxial tensile response are demonstrated. Predictions of

Mullins softening with changes in loading direction are also analysed and found to deviate from experimental observations.

Following the poor prediction of the equibiaxial response by the filled rubber model, in Chapter 4 the role of the tube model in the micromechanical approach is investigated as this has previously been found to achieve good fitting performance for rubbers under uniaxial, equibiaxial and pure shear loading simultaneously. Tube models are categorised into those where the tube diameter varies with the macroscopic line-stretch and those where the diameter varies with the the macroscopic area-stretch. Comparisons of power-law models of each type are made against experimental data for general biaxial loading; uniaxial tension and equibiaxial tension; and uniaxial tension and uniaxial compression. In the phenomenological theory, good fitting performance has been associated with dependence of the free energy function on the invariant I_2. We find that area-stretch tube models achieve good fitting performance and link the area contraction to the invariant I_2. In contrast, line-stretch models only achieve good fitting performance when used in combination with the three-chain averaging and show very poor fitting performance when used in the full-network scheme.

A further framework is developed for the constitutive behaviour of thermoplastic elastomers displaying a cylinder-forming morphology in Chapter 5. The framework explains the mechanical response of these TPEs based on the behaviour of the hard phase and the soft segments, which display plastic and elastic-viscoelastic behaviour respectively. Micro-macro transitions are proposed following a decomposition of TPE microstructure into the grains that compose it and a further decomposition of the grains into the hard cylinders and soft segments. The model again is confronted to experimental data for the large deformation and cyclic uniaxial responses of a family of TPEs of different hard phase volume fractions. The model is able to capture the monotonic uniaxial response of the material up to a stretch of 20 at higher volume fractions but underpredicts the response at lower volume fractions. The cyclic response is reasonably well predicted. An analysis of the contributions of grains of different orientations counter-intuitively reveals that the

most compliant grains contain cylinders oriented at 47° degrees to the loading direction, which is in agreement with experimental investigations of single grain TPEs.

The shortcomings of the filled rubber model in predicting the Mullins softening following changes in stretching direction motivate us to develop a novel phenomenological approach to modelling the Mullins effect in Chapter 6. The approach introduces a second-order tensor to describe the damage state in the full-network framework. The tensile part of this tensor projected in the reference orientation of the chain gives the chain level damage. Damage surfaces (in the driving force space) are introduced to control the anisotropic evolution of the damage tensor. The model is compared to experimental data with changes in loading direction and accurately captures the response of the material when loaded perpendicular to the original stretching direction. Furthermore, the model is implemented as a user subroutine in the finite element software ABAQUS and is used to simulate the loading of a plate with a central hole in sequentially different directions.

7.2 Future work

One of most immediate directions for this work in the future is in improving the fitting performance of the filled rubber and TPU models presented in Chapter 3. While the models were able to capture the general features of the mechanical response of these materials across several volume fractions, the detailed mechanical response was not captured fully. There remains some uncertainty in the true response of the material however, as limited single test experimental data are available in the literature, such that it cannot directly be concluded that model shows poor quantitative fitting performance from this analysis alone. Future experiments that are repeated and validated would benefit modelling efforts. Nevertheless, the existing data are the best estimate available for the true material response and the comparisons conducted in Section 3.4.2 indicate that the model performance may have room for improvement. As mentioned in Section 3.4.2, the cyclic hysteresis and rate sensitivity could likely be improved through the addition of a second viscoelastic branch (associated with different relaxation processes taking place on

different timescales). Taking an empirical point of view, as the experimental data show much more rate-sensitivity during loading than during unloading, the branch may need to deviate significantly from linear behaviour to fit the data. Another improvement in fitting performance may arise from a more sophisticated plastic contribution as the current choice (log-linear elastic with linear hardening plasticity) is highly idealised. It might be possible to link the plastic contribution to the morphology of the hard phase and derive an expression for the contribution following an assumed microscale plastic mechanism.

An alternative (potentially concurrent) explanation for the deviation between the model performance and the experimental data lies in the model calibration procedure. It is possible that the model is able to capture the material response sufficiently accurately but was not found to do so here due to deficiencies in the material parameter identification procedure. As discussed in Section 3.4.2, a heuristic fitting procedure was followed where parameters were altered to improve fitting performance based on considerations of the model deformation mechanisms and visual inspection of the model fit. As discussed in Section 3.4.2, re-visiting the model evaluation using a rigorous fitting procedure (featuring a suitable objective function and optimisation method) would enable a more reliable analysis of the model. A challenge arises in the number of parameters used in the model but this may be tackled by fitting the model mechanism-by-mechanism to specific parts of the material response if this is possible, or by using high-dimensional optimisation methods if it is not (see e.g. Balázs et al. (2021)).

While it has been shown that incorporating the tube model in micromechanical models significantly improves fitting performance, so far we have not presented a generalised framework with the tube model. Some issues arise in developing tube model frameworks for filled rubbers and TPEs. Following our findings in Chapter 4, a framework featuring area-stretch dependence would be required. Though some simple kinematic arguments can be used to derive stretch amplification factors where the chain end-to-end vector stretch is the only microscale deformation measure, the derivation of area-based amplification factors is less straightforward. Furthermore, the impact of damage on the tube

contribution needs to be investigated and model validation is challenging as there are limited experimental data considering filled rubbers of different volume fractions subjected to multiaxial loading conditions.

These issues could be resolved through combined modelling and experimental approaches. Expressions for area-based amplification factors could be investigated on theoretical grounds. Mullins damage could be seen to affect these amplification factors, or alter the tube contribution through a microstructural parameter such as the number of Kuhn segments per chain (which appears in the tube free energy and, as discussed in Section 2.5, is a common damage parameter in the phantom contribution to the free energy). An experimental campaign would need to be conducted to establish the behaviour of filled rubbers and TPEs in this setting for a series of different volume fractions including the unfilled rubber. By fitting an unamplified tube model to the data at each volume fraction and then by analysing how these parameters change with volume fraction (identifying the tube and phantom network contributions separately), the effects of stretch amplification on the tube contribution could be inferred and modelling assumptions could be verified.

So far in modelling TPEs and filled rubbers, we have considered modelling damage, plasticity and viscous behaviour. Focussing on filled rubbers, it is well-recognised that Mullins damage can be fully recovered by holding the damaged material at an elevated temperature for a sufficient period of time (Diaz et al., 2014). An extension of the existing modelling framework to capture this could in future be explored. This would require the development of coupled thermomechanical framework featuring a temperature-dependent contribution to the free energy function related to healing. Such a framework may also be relevant to modelling healing in TPEs within a certain temperature range. The behaviour of TPEs above the glass transition temperature of the hard phase is vastly different from that of the filled rubbers and generalisation above this temperature may not be possible, though a distinct model (potentially featuring chain diffusion mechanisms) could be developed.

In Chapter 6, an anisotropic Mullins effect model is presented in the full-network frame-

work. The model performs reasonably well in capturing many aspects of the anisotropy of the Mullins effect however it features many phenomenological ingredients including the damage variable, the free energy contributions and the damage surface. Some more physical aspects could be introduced to the model, including those outlined in the general framework of Chapter 3. The stretch amplification concept could be incorporated to capture volume fraction effects and a physical hypothesis could be attached to the damage mechanism. Attaching a physical mechanism to the damage process would allow better identification of the damage variable and additionally both of the elastic and damage parts of the free energy function. Fully reconciling the general framework of Chapter 3 also remains as future work. To maintain the computational benefits (and anisotropic predictions) of the Chapter 6 model, it would perhaps make sense to adapt the generalised framework to feature tensorial variables to describe all chain level internal variables (removing the need to store internal variables at each microsphere integration point).

There are some general questions surrounding the micromechanical approach that remain to be addressed. One problem lies in model calibration. As molecular information is quite often limited, the parameters of micromechanical models are often found through curve fitting. Through this procedure, there is no guarantee of any closeness of the fitted parameters to the quantities which they are supposed to represent. For industrial applications, this treatment of a physical model as a phenomenological one is not in itself a problem but from the perspective of a researcher this means comparisons to experimental data are not necessarily a good indicator of the efficacy of the model. It becomes unclear if the model succeeds because of careful modelling of physical mechanisms, or because the model just happens to contain enough degrees of freedom to capture whatever behaviours the material happens to display.

Taking a broader perspective, there remains a significant gap in the literature on mesoscale modelling approaches for both TPEs and filled rubbers. Insight from such approaches could significantly improve the development of micromechanical models. A number of

simplifying assumptions are made in modelling filled rubbers and TPEs in the micromechanical approach. In particular, the complexity of the microstructure of filled rubbers is neglected in many models, with somewhat *ad hoc* simplifying treatments in the form of network decompositions and stretch amplification factors being commonplace in the literature. In the real materials, filler particles are typically nanometre-sized and agglomerate together, forming hard domains of similar characteristic size to the presumed reference end-to-end distance of typical rubbery chains. Mesoscale modelling approaches which can take into account this level of detail of the material microstructure would allow comparisons between micromechanical models with a form of ground truth, so that they can be evaluated on an appropriate level rather than through comparisons to experimental data where other physical processes make it challenging to decipher the impact of specific modelling assumptions. Discrete network (DN) simulations are one potential mesoscale modelling approach that could fill this gap (see e.g. the recent work of Araujo et al. (2024)). In a DN, chains are represented as springs joined which are joined together at crosslinking sites. By enforcing mechanical equilibrium at crosslinks, the response of the network can be predicted by from only a chain model and knowledge of the material microstructure. The existing DN framework would need to be modified to incorporate filler particles and would ideally take into account chemical and physical interactions between filler particles and polymer chains. These interactions are believed to be significant in the mechanics of filled rubbers but are challenging to analyse experimentally, and some interesting knowledge could be gain from *in silico* investigations.

The pursuit of mesoscale approaches could further aid in material design and optimisation. One area currently being addressed in the TPE community is the development of TPEs from sustainable resources with mechanical properties on par with those derived from fossil fuels (Gregory et al., 2020). There are many variables which can be controlled in the synthesis of TPE molecules: the molecular architecture or shape, the molecular weights of the respective block, the chemical properties of the block (e.g. their phase separation characteristics, the presence of hydrogen bonding groups), the mechanical properties of the blocks (e.g. whether or not they crystallise). In the model developed in this thesis,

the only compositional variables that appear are the molecular weights of each block (the hard phase volume fraction can be derived from these quantities) and the morphology of the TPE is pre-supposed, though in reality it follows from a complex combination of molecular characteristics. The self-consistent field theory of Helfand and Sapse (1975) was developed for determining the microstructure of TPEs based on the balance of driving forces for phase separation and chain stretching. It takes in only molecular information as an input and could be developed in future to predict the impact of altering chain characteristics on the mechanical response.

Regardless of its deficits, the micromechanical approach offers a framework for describing material behaviour that reasonably balances physical meaning and analytical tractability. As the approach features parameters and mechanisms with microstructural interpretation, it can naturally be extended to model other processes and phenomena such as degradation, curing and strain-induced crystallisation, which are much harder to access through phenomenological approaches. Furthermore, while phenomenological models can make wildly inaccurate predictions of material behaviour outside the range of the data they are calibrated against, the predictions of micromechanical models are usually reasonable. As the approach often leads to closed form expressions of the free energy function, the impact of specific material parameters can be elucidated without significant computational expense. As such, the micromechanical approach continues to offer a solid foundation for the development of constitutive models for a variety of rubber-like materials in the future.

Bibliography

Aboudi, J. and Gilat, R. (2022), 'Microbuckling of composites prediction by enhancing the high-fidelity generalized method of cells micromechanics', *International Journal of Solids and Structures* **234–235**, 111275.

Alamé, G. and Brassart, L. (2020), 'Effect of topological defects on the elasticity of near-ideal polymer networks', *Journal of Applied Mechanics* **87**(12).

Alkhoury, K., Ivko, R., Hossain, M., Nadimpalli, S. and Chester, S. A. (2024), 'Experiments and modeling of the coupled viscoelasticity and Mullins effect in filled rubber materials', *Journal of the Mechanics and Physics of Solids* **188**, 105650.

Amores, V. J., Nguyen, K. and Montáns, F. J. (2021), 'On the network orientational affinity assumption in polymers and the micro–macro connection through the chain stretch', *Journal of the Mechanics and Physics of Solids* **148**, 104279.

Angela Mihai, L. and Goriely, A. (2020), 'A pseudo-anelastic model for stress softening in liquid crystal elastomers', *Proceedings of the Royal Society A: Mathematical, Physical and Engineering Sciences* **476**(2243), 20200558.

Anssari-Benam, A. (2023), 'Large Isotropic Elastic Deformations: On a Comprehensive Model to Correlate the Theory and Experiments for Incompressible Rubber-Like Materials', *Journal of Elasticity* **153**(2), 219–244.

Anssari-Benam, A., Akbari, R. and Dargazany, R. (2023), 'Extending the theory of pseudo-elasticity to capture the permanent set and the induced anisotropy in the Mullins effect', *International Journal of Non-Linear Mechanics* **156**, 104500.

Anssari-Benam, A., Bucchi, A. and Saccomandi, G. (2021), 'On the central role of the invariant I2 in nonlinear elasticity', *International Journal of Engineering Science* **163**, 103486.

Anssari-Benam, A. and Hossain, M. (2024), 'A unified pseudo-elastic model of continuous and discontinuous softening in the finite deformation of isotropic soft solids', *International Journal of Solids and Structures* p. 112670.

Aoyagi, T. (2016), Thermoplastic Elastomers, *in* J. A. f. Chemical Innovation, ed., 'Computer Simulation of Polymeric Materials: Applications of the OCTA System', Springer, Singapore, pp. 249–267.

Araujo, L. M., Kryven, I. and Brassart, L. (2024), 'Micromechanical modelling of rubbery networks: The role of chain pre-stretch', *International Journal of Non-Linear Mechanics* **166**, 104834.

Arruda, E. M. and Boyce, M. C. (1993), 'A three-dimensional constitutive model for the large stretch behavior of rubber elastic materials', *Journal of the Mechanics and Physics of Solids* **41**(2), 389–412.

Balázs, C., van Beekveld, M., Caron, S., Dillon, B. M., Farmer, B., Fowlie, A., Garrido-Merchán, E. C., Handley, W., Hendriks, L., Jóhannesson, G., Leinweber, A., Mamužić,

J., Martinez, G. D., Otten, S., de Austri, R. R., Scott, P., Searle, Z., Stienen, B., Vanschoren, J., White, M. and The DarkMachines High Dimensional Sampling Group (2021), 'A comparison of optimisation algorithms for high-dimensional particle and astrophysics applications', *Journal of High Energy Physics* **2021**(5), 108.

Bates, F. S. and Fredrickson, GH. (2000), 'Block copolymers-designer soft materials', *Physics today* **52**.

Bažant, P. and Oh, B. (1986), 'Efficient numerical integration on the surface of a sphere', *ZAMM-Journal of Applied Mathematics and Mechanics/Zeitschrift für Angewandte Mathematik und Mechanik* **66**(1), 37–49.

Beatty, M. F. (2003), 'An average-stretch full-network model for rubber elasticity', *Journal of Elasticity* **70**, 65–86.

Bechir, H., Chevalier, L., Chaouche, M. and Boufala, K. (2006), 'Hyperelastic constitutive model for rubber-like materials based on the first Seth strain measures invariant', *European Journal of Mechanics-A/Solids* **25**(1), 110–124.

Bergstrom, J. S. and Boyce, M. C. (1999), 'Mechanical behavior of particle filled elastomers', *Rubber chemistry and technology* **72**(4), 633–656.

Bergström, J. S. and Boyce, M. C. (2000), 'Large strain time-dependent behavior of filled elastomers', *Mechanics of Materials* **32**(11), 627–644.

Birkes, D. and Dodge, Y. (2011), *Alternative methods of regression*, John Wiley & Sons.

Bleiler, C., Castañeda, P. P. and Röhrle, O. (2021), 'Tangent second-order homogenisation estimates for incompressible hyperelastic composites with fibrous microstructures and anisotropic phases', *Journal of the Mechanics and Physics of Solids* **147**, 104251.

Brassart, L. and Stainier, L. (2012), 'On convergence properties of variational constitutive updates for elasto-visco-plasticity', *GAMM-Mitteilungen* **35**(1), 26–42.

Bresolin, F. and Vassoler, J. (2022), 'A variational full-network framework with anisotropic damage and viscoelasticity induced by deformation', *Journal of the Mechanics and Physics of Solids* **160**, 104777.

Buckley, CP., De Focatiis, DSA. and Prisacariu, C. (2011), 'Unravelling the mysteries of cyclic deformation in thermoplastic elastomers', *Constitutive Models for Rubber VII* pp. 3–10.

Budiansky, B. (1965), 'On the elastic moduli of some heterogeneous materials', *Journal of the Mechanics and Physics of Solids* **13**(4), 223–227.

Bueche, F. (1960), 'Molecular basis for the Mullins effect', *Journal of Applied Polymer Science* **4**(10), 107–114.

Bueche, F. (1961), 'Mullins effect and rubber–filler interaction', *Journal of applied polymer Science* **5**(15), 271–281.

Carroll, M. (2011), 'A strain energy function for vulcanized rubbers', *Journal of Elasticity* **103**, 173–187.

Castañeda, P. P. and Tiberio, E. (2000), 'A second-order homogenization method in finite elasticity and applications to black-filled elastomers', *Journal of the Mechanics and Physics of Solids* **48**(6-7), 1389–1411.

Chagnon, G., Verron, E., Gornet, L., Marckmann, G. and Charrier, P. (2004), 'On the relevance of continuum damage mechanics as applied to the Mullins effect in elastomers', *Journal of the Mechanics and Physics of Solids* **52**(7), 1627–1650.

Chagnon, G., Verron, E., Marckmann, G. and Gornet, L. (2006), 'Development of new constitutive equations for the Mullins effect in rubber using the network alteration theory', *International Journal of Solids and Structures* **43**(22-23), 6817–6831.

Cho, H., Mayer, S., Pöselt, E., Susoff, M., in 't Veld, P. J., Rutledge, G. C. and Boyce, M. C. (2017), 'Deformation mechanisms of thermoplastic elastomers: Stress-strain behavior and constitutive modeling', *Polymer* **128**, 87–99.

Ciesielski, A. (1999), *An introduction to rubber technology*, Rapra Technology, Shawbury.

Coleman, B. D. and Noll, W. (1974), The Thermodynamics of Elastic Materials with Heat Conduction and Viscosity, *in* W. Noll, ed., 'The Foundations of Mechanics and Thermodynamics: Selected Papers', Springer, Berlin, Heidelberg, pp. 145–156.

Dal, H., Açıkgöz, K. and Badienia, Y. (2021), 'On the performance of isotropic hyperelastic constitutive models for rubber-like materials: A state of the art review', *Applied Mechanics Reviews* **73**(2).

Daniel, C., Hamley, IW. and Mortensen, K. (2000), 'Effect of planar extension on the structure and mechanical properties of polystyrene–poly (ethylene-co-butylene)–polystyrene triblock copolymers', *Polymer* **41**(26), 9239–9247.

Dannenberg, E. M. (1975), 'The effects of surface chemical interactions on the properties of filler-reinforced rubbers', *Rubber Chemistry and Technology* **48**(3), 410–444.

Dannenberg, E. M. and Brennan, J. J. (1966), 'Strain energy as a criterion for stress softening in carbon-black-filled vulcanizates', *Rubber Chemistry and Technology* **39**(3), 597–608.

Darabi, E. and Itskov, M. (2021), 'A generalized tube model of rubber elasticity', *Soft Matter* **17**(6), 1675–1684.

Dargazany, R. and Itskov, M. (2009), 'A network evolution model for the anisotropic Mullins effect in carbon black filled rubbers', *International Journal of Solids and Structures* **46**(16), 2967–2977.

Dargazany, R. and Itskov, M. (2013), 'Constitutive modeling of the Mullins effect and cyclic stress softening in filled elastomers', *Physical Review E* **88**(1), 012602.

Dechnarong, N., Kamitani, K., Cheng, C.-H., Masuda, S., Nozaki, S., Nagano, C., Fujimoto, A., Hamada, A., Amamoto, Y., Kojio, K. et al. (2021), 'Microdomain structure change and macroscopic mechanical response of styrenic triblock copolymer under cyclic uniaxial and biaxial stretching modes', *Polymer Journal* **53**(6), 703–712.

Destrade, M., Saccomandi, G. and Sgura, I. (2017), 'Methodical fitting for mathematical models of rubber-like materials', *Proceedings of the Royal Society A* **476**(2198), 20160811.

Diani, J., Brieu, M. and Vacherand, JM. (2006), 'A damage directional constitutive model for Mullins effect with permanent set and induced anisotropy', *European Journal of Mechanics-A/Solids* **25**(3), 483–496.

Diani, J., Fayolle, B. and Gilormini, P. (2009), 'A review on the Mullins effect', *European Polymer Journal* **45**(3), 601–612.

Diani, J. and Le Tallec, P. (2019), 'A fully equilibrated microsphere model with damage for rubberlike materials', *Journal of the Mechanics and Physics of Solids* **124**, 702–713.

Diaz, R., Diani, J. and Gilormini, P. (2014), 'Physical interpretation of the Mullins softening in a carbon-black filled SBR', *Polymer* **55**(19), 4942–4947.

Doi, M. and Edwards, S. F. (1988), *The Theory of Polymer Dynamics*, Vol. 73, oxford university press.

Domurath, J., Saphiannikova, M. and Heinrich, G. (2017), 'The Concept of hydrodynamic amplification infilled Elastomers'.

Dorfmann, A. and Ogden, R. W. (2004), 'A constitutive model for the Mullins effect with permanent set in particle-reinforced rubber', *International Journal of Solids and Structures* **41**(7), 1855–1878.

Dorfmann, A. and Pancheri, F. Q. (2012), 'A constitutive model for the Mullins effect with changes in material symmetry', *International Journal of Non-Linear Mechanics* **47**(8), 874–887.

Drozdov, A. D. (2006), 'Constitutive equations for the nonlinear viscoelastic and viscoplastic behavior of thermoplastic elastomers', *International Journal of Engineering Science* p. 22.

Drozdov, AD. and Christiansen (2007), 'Cyclic viscoplasticity of thermoplastic elastomers', *Acta mechanica* **194**(1), 47–65.

Edwards, S. (1967), 'The statistical mechanics of polymerized material', *Proceedings of the Physical Society* **92**(1), 9–16.

Ehret, A. E. (2015), 'On a molecular statistical basis for Ogden's model of rubber elasticity', *Journal of the Mechanics and Physics of Solids* **78**, 249–268.

Einstein, A. (1906), 'A new determination of molecular dimensions', *Ann. Phys.* **19**, 289–306.

Fernandes Arruebarrena, V. A. (2016), 'Manifestations of the Mullins effect in filled elastomers. PhD thesis, University of Nottingham.'.

Ferreira, J. P. S., Parente, M. P. L., Jabareen, M. and Jorge, R. M. N. (2017), 'A general framework for the numerical implementation of anisotropic hyperelastic material models including non-local damage', *Biomechanics and Modeling in Mechanobiology* **16**(4), 1119–1140.

Fletcher, R. R. (1987), *Practical methods of optimization*, Chichester ; New York : Wiley.

Fliege, J. and Maier, U. (1999), 'The distribution of points on the sphere and corresponding cubature formulae', *IMA Journal of Numerical Analysis* **19**(2), 317–334.

Fried, E. (2002), 'An elementary molecular-statistical basis for the Mooney and Rivlin–Saunders theories of rubber elasticity', *Journal of the Mechanics and Physics of Solids* **50**(3), 571–582.

Furer, J. and Castañeda, P. P. (2020), 'Reinforced elastomers: Homogenization, macroscopic stability and relaxation', *Journal of the Mechanics and Physics of Solids* **136**, 103689.

Gaylord, R. J. (1979), 'Entanglement and excluded volume effects in rubber elasticity', *Polymer Engineering and Science* **19**(4), 263–266.

Gaylord, R. J. (1982), 'The constant volume tube model of rubber elasticity', *Polymer Bulletin* **8**(7), 325–329.

Gent, A. N. (1996), 'A new constitutive relation for rubber', *Rubber Chemistry and Technology* **69**(1), 59–61.

Gent, A. N. and Thomas, A. G. (1958), 'Forms for the stored (strain) energy function for vulcanized rubber', *Journal of Polymer Science* **28**(118), 625–628.

Gent, AN. (2005), 'Extensibility of rubber under different types of deformation', *Journal of Rheology* **49**(1), 271–275.

Germain, P., Suquet, P. and Nguyen, Q. S. (1983), 'Continuum thermodynamics', *ASME Journal of Applied Mechanics* **50**, 1010–1020.

Geuzaine, C. and Remacle, J.-F. (2009), 'Gmsh: A 3-D finite element mesh generator with built-in pre- and post-processing facilities', *International Journal for Numerical Methods in Engineering* **79**(11), 1309–1331.

Ghosh, K., Shrimali, B., Kumar, A. and Lopez-Pamies, O. (2021), 'The nonlinear viscoelastic response of suspensions of rigid inclusions in rubber: I—Gaussian rubber with constant viscosity', *Journal of the Mechanics and Physics of Solids* p. 104544.

Göktepe, S. and Miehe, C. (2005), 'A micro–macro approach to rubber-like materials. Part III: The micro-sphere model of anisotropic Mullins-type damage', *Journal of the Mechanics and Physics of Solids* **53**(10), 2259–2283.

Govindjee, S. (1997), 'An Evaluation of Strain Amplification Concepts via Monte Carlo Simulations of an Ideal Composite', *Rubber Chemistry and Technology* **70**(1), 25–37.

Govindjee, S. and Simo, J. (1991), 'A micro-mechanically based continuum damage model for carbon black-filled rubbers incorporating Mullins' effect', *Journal of the Mechanics and Physics of Solids* **39**(1), 87–112.

Govindjee, S., Zoller, M. J. and Hackl, K. (2019), 'A fully-relaxed variationally-consistent framework for inelastic micro-sphere models: Finite viscoelasticity', *Journal of the Mechanics and Physics of Solids* **127**, 1–19.

Green, M. S. and Tobolsky, A. V. (1946), 'A New Approach to the Theory of Relaxing Polymeric Media', *The Journal of Chemical Physics* **14**(2), 80–92.

Gregory, G. L., Sulley, G. S., Carrodeguas, L. P., Chen, T. T. D., Santmarti, A., Terrill, N. J., Lee, K.-Y. and Williams, C. K. (2020), 'Triblock polyester thermoplastic elastomers with semi-aromatic polymer end blocks by ring-opening copolymerization', *Chemical Science* **11**(25), 6567–6581.

Guth, E. (1945), 'Theory of Filler Reinforcement', *Journal of Applied Physics* **16**(1), 20–25.

Guth, E. and Gold, O. (1938), 'On the hydrodynamical theory of the viscosity of suspensions', *Physical Review* **53**, 322.

Halphen, B. and Son Nguyen, Q. (1975), 'Sur les matériaux standard généralisés', *Journal de Mécanique* **14**(1), 39–63.

Hanson, D. E., Hawley, M., Houlton, R., Chitanvis, K., Rae, P., Orler, E. B. and Wrobleski, D. A. (2005), 'Stress softening experiments in silica-filled polydimethylsiloxane provide insight into a mechanism for the Mullins effect', *Polymer* **46**(24), 10989–10995.

Harwood, JAC., Mullins, L. and Payne, A. R. (1965), 'Stress softening in natural rubber vulcanizates. Part II. Stress softening effects in pure gum and filler loaded rubbers', *Journal of Applied Polymer Science* **9**(9), 3011–3021.

Hashin, Z. and Shtrikman, S. (1963), 'A variational approach to the theory of the elastic behaviour of multiphase materials', *Journal of the Mechanics and Physics of Solids* **11**(2), 127–140.

Heinrich, G., Straube, E. and Helmis, G. (1988), Rubber elasticity of polymer networks: Theories, *in* 'Polymer Physics', Springer, pp. 33–87.

Helfand, E. and Sapse, A. M. (1975), 'Theory of unsymmetric polymer–polymer interfaces', *The Journal of Chemical Physics* **62**(4), 1327–1331.

Hill, R. (1963), 'Elastic properties of reinforced solids: Some theoretical principles', *Journal of the Mechanics and Physics of Solids* **11**(5), 357–372.

Holden, G. (2011), Thermoplastic elastomers, *in* 'Applied Plastics Engineering Handbook', Elsevier, pp. 77–91.

Holzapfel, G. A. (2010), *Nonlinear Solid Mechanics: A Continuum Approach for Engineering*, repr edn, Wiley, Chichester Weinheim.

Honeker, C. C. and Thomas, E. L. (1996), 'Impact of morphological orientation in determining mechanical properties in triblock copolymer systems', *Chemistry of materials* **8**(8), 1702–1714.

Horgan, C. O., Ogden, R. W. and Saccomandi, G. (2004), 'A theory of stress softening of elastomers based on finite chain extensibility', *Proceedings of the Royal Society of London. Series A: Mathematical, Physical and Engineering Sciences* **460**(2046), 1737–1754.

Horgan, C. O. and Smayda, M. G. (2012), 'The importance of the second strain invariant in the constitutive modeling of elastomers and soft biomaterials', *Mechanics of Materials* **51**, 43–52.

Hossain, M., Amin, AFMS. and Kabir, M. N. (2015), 'Eight-chain and full-network models and their modified versions for rubber hyperelasticity: A comparative study', *Journal of the Mechanical Behavior of Materials* **24**(1-2), 11–24.

Hossain, M. and Steinmann, P. (2013), 'More hyperelastic models for rubber-like materials: Consistent tangent operators and comparative study', *Journal of the Mechanical Behavior of Materials* **22**(1-2), 27–50.

Hotta, A., Clarke, S. M. and Terentjev, E. M. (2002), 'Stress Relaxation in Transient Networks of Symmetric Triblock Styrene-Isoprene-Styrene Copolymer', *Macromolecules* **35**(1), 271–277.

Itskov, M. (2016), 'On the accuracy of numerical integration over the unit sphere applied to full network models', *Computational Mechanics* **57**(5), 859–865.

Itskov, M. and Knyazeva, A. (2016), 'A rubber elasticity and softening model based on chain length statistics', *International Journal of Solids and Structures* **80**, 512–519.

James, H. and Guth, E. (1943), 'Theory of the elastic properties of rubber', *Journal of Chemical Physics* **11**, 455–481.

Johnson, M. A. and Beatty, M. F. (1993), 'A constitutive equation for the Mullins effect in stress controlled uniaxial extension experiments', *Continuum Mechanics and Thermodynamics* **5**(4), 301–318.

Kaliske, M. and Heinrich, G. (1999), 'An extended tube-model for rubber elasticity: Statistical-mechanical theory and finite element implementation', *Rubber Chemistry and Technology* **72**(4), 602–632.

Kawabata, S., Matsuda, M., Tei, K. and Kawai, H. (1981), 'Experimental survey of the strain energy density function of isoprene rubber vulcanizate', *Macromolecules* **14**(1), 154–162.

Kearsley, E. (1989), 'Note: Strain Invariants Expressed as Average Stretches', *Journal of Rheology* **33**(5), 757–760.

Kearsley, E. A. and Zapas, L. J. (1980), 'Some Methods of Measurement of an Elastic Strain-Energy Function of the Valanis-Landel Type', *Journal of Rheology* **24**(4), 483–500.

Keller, A. and Odell, JA. (1985), The interrelation between microstructure and properties of block copolymers, *in* 'Processing, Structure and Properties of Block Copolymers', Springer, pp. 29–74.

Ken-Ichi, K. (1984), 'Distribution of directional data and fabric tensors', *International Journal of Engineering Science* **22**(2), 149–164.

Khiêm, V. N. and Itskov, M. (2016), 'Analytical network-averaging of the tube model:: Rubber elasticity', *Journal of the Mechanics and Physics of Solids* **95**, 254–269.

Khiêm, V. N. and Itskov, M. (2017), 'An averaging based tube model for deformation induced anisotropic stress softening of filled elastomers', *International Journal of Plasticity* **90**, 96–115.

Klüppel, M. and Schramm, J. (2000), 'A generalized tube model of rubber elasticity and stress softening of filler reinforced elastomer systems', *Macromolecular Theory and Simulations* **9**(9), 742–754.

Kodama, H., Morita, H. and Kotani, M. (2024), 'A mathematical model of thermoplastic elastomers for analysing the topology of microstructures and mechanical properties during elongation', *Proceedings of the Royal Society A: Mathematical, Physical and Engineering Sciences* **480**(2286), 20230389.

Kraus, G. (1978), 'Reinforcement of Elastomers by Carbon Black', *Rubber Chemistry and Technology* **51**(2), 297–321.

Kroon, M. (2011), 'An 8-chain Model for Rubber-like Materials Accounting for Non-affine Chain Deformations and Topological Constraints', *Journal of Elasticity* **102**(2), 99–116.

Lemaitre, J. and Chaboche, J.-L. (1994), *Mechanics of Solid Materials*, Cambridge University Press.

Linder, C., Tkachuk, M. and Miehe, C. (2011), 'A micromechanically motivated diffusion-based transient network model and its incorporation into finite rubber viscoelasticity', *Journal of the Mechanics and Physics of Solids* **59**(10), 2134–2156.

Lopez-Pamies, O. (2010), 'A new I1-based hyperelastic model for rubber elastic materials', *Comptes Rendus Mecanique* **338**(1), 3–11.

Lopez-Pamies, O., Garcia, R., Chabert, E., Cavaillé, J.-Y. and Ponte Castañeda, P. (2008), 'Multiscale modeling of oriented thermoplastic elastomers with lamellar morphology', *Journal of the Mechanics and Physics of Solids* **56**(11), 3206–3223.

Lopez-Pamies, O., Goudarzi, T. and Danas, K. (2013), 'The nonlinear elastic response of suspensions of rigid inclusions in rubber: II—a simple explicit approximation for finite-concentration suspensions', *Journal of the Mechanics and Physics of Solids* **61**(1), 19–37.

Lopez-Pamies, O., Goudarzi, T. and Nakamura, T. (2013), 'The nonlinear elastic response of suspensions of rigid inclusions in rubber: I—an exact result for dilute suspensions', *Journal of the Mechanics and Physics of Solids* **61**(1), 1–18.

Lorenz, B., Persson, B. N. J., Fortunato, G., Giustiniano, M. and Baldoni, F. (2013), 'Rubber friction for tire tread compound on road surfaces', *Journal of Physics: Condensed Matter* **25**(9), 095007.

Lubarda, V. A. and Krajcinovic, D. (1993), 'Damage tensors and the crack density distribution', *International Journal of Solids and Structures* **30**(20), 2859–2877.

Lubliner, J. (1984), 'A maximum-dissipation principle in generalized plasticity', *Acta Mechanica* **52**(3-4), 225–237.

Machado, G., Chagnon, G. and Favier, D. (2012), 'Induced anisotropy by the Mullins effect in filled silicone rubber', *Mechanics of Materials* **50**, 70–80.

Machado, G., Chagnon, G. and Favier, D. (2014), 'Theory and identification of a constitutive model of induced anisotropy by the Mullins effect', *Journal of the Mechanics and Physics of Solids* **63**, 29–39.

Magnus, J. R. (1985), 'On differentiating eigenvalues and eigenvectors', *Econometric Theory* **1**(2), 179–191.

Mai, T.-T., Morishita, Y. and Urayama, K. (2017), 'Induced anisotropy by Mullins effect in filled elastomers subjected to stretching with various geometries', *Polymer* **126**, 29–39.

Mamodia, M., Indukuri, K., Atkins, E. T., De Jeu, W. H. and Lesser, A. J. (2008), 'Hierarchical description of deformation in block copolymer TPEs', *Journal of Materials Science* **43**(22), 7035–7046.

Marckmann, G., Chagnon, G., Le Saux, M. and Charrier, P. (2016), 'Experimental investigation and theoretical modelling of induced anisotropy during stress-softening of rubber', *International Journal of Solids and Structures* **97**, 554–565.

Marckmann, G. and Verron, E. (2006), 'Comparison of hyperelastic models for rubber-like materials', *Rubber chemistry and technology* **79**(5), 835–858.

Marckmann, G., Verron, E., Gornet, L., Chagnon, G., Charrier, P. and Fort, P. (2002), 'A theory of network alteration for the Mullins effect', *Journal of the Mechanics and Physics of Solids* **50**(9), 2011–2028.

Marrucci, G. (1981), 'Rubber elasticity theory. A network of entangled chains', *Macromolecules* **14**(2), 434–442.

McLeish, TCB. (2002), 'Tube theory of entangled polymer dynamics', *Advances in physics* **51**(6), 1379–1527.

Medalia, A. I. (1987), 'Effect of Carbon Black on Ultimate Properties of Rubber Vulcanizates', *Rubber Chemistry and Technology* **60**(1), 45–61.

Merckel, Y., Brieu, M., Diani, J. and Caillard, J. (2012), 'A Mullins softening criterion for general loading conditions', *Journal of the Mechanics and Physics of Solids* **60**(7), 1257–1264.

Merckel, Y., Diani, J., Brieu, M. and Caillard, J. (2013), 'Constitutive modeling of the anisotropic behavior of Mullins softened filled rubbers', *Mechanics of Materials* **57**, 30–41.

Miehe, C. and Göktepe, S. (2005), 'A micro–macro approach to rubber-like materials. Part II: The micro-sphere model of finite rubber viscoelasticity', *Journal of the Mechanics and Physics of Solids* **53**(10), 2231–2258.

Miehe, C., Göktepe, S. and Lulei, F. (2004), 'A micro-macro approach to rubber-like materials—part I: The non-affine micro-sphere model of rubber elasticity', *Journal of the Mechanics and Physics of Solids* **52**(11), 2617–2660.

Mooney, M. (1940), 'A theory of large elastic deformation', *Journal of applied physics* **11**(9), 582–592.

Mulderrig, J., Li, B. and Bouklas, N. (2021), 'Affine and non-affine microsphere models for chain scission in polydisperse elastomer networks', *Mechanics of Materials* **160**, 103857.

Mullins, L. (1948), 'Effect of stretching on the properties of rubber', *Rubber Chemistry and Technology* **21**(2), 281–300.

Mullins, L. (1969), 'Softening of rubber by deformation', *Rubber Chemistry and Technology* **42**(1), 339–362.

Mullins, L. and Tobin, N. (1965), 'Stress softening in rubber vulcanizates. Part I. Use of a strain amplification factor to describe the elastic behavior of filler-reinforced vulcanized rubber', *Journal of Applied Polymer Science* **9**(9), 2993–3009.

Mullins, L. and Tobin, NR. (1957), 'Theoretical model for the elastic behavior of filler-reinforced vulcanized rubbers', *Rubber chemistry and technology* **30**(2), 555–571.

Neto, E. A. d. S., Peric, D. and Owen, D. R. J. (2011), *Computational Methods for Plasticity: Theory and Applications*, John Wiley & Sons.

Nguyen, N. and Waas, A. M. (2016), 'Nonlinear, finite deformation, finite element analysis', *Zeitschrift für angewandte Mathematik und Physik* **67**(3), 35.

Ogden, R. W. (1972), 'Large deformation isotropic elasticity–on the correlation of theory and experiment for incompressible rubberlike solids', *Proceedings of the Royal Society of London. A. Mathematical and Physical Sciences* **326**(1567), 565–584.

Ogden, R. W. (1997), *Non-Linear Elastic Deformations*, Courier Corporation.

Ogden, R. W. and Roxburgh, D. G. (1999), 'A pseudo–elastic model for the Mullins effect in filled rubber', *Proceedings of the Royal Society of London. Series A: Mathematical, Physical and Engineering Sciences* **455**(1988), 2861–2877.

Ogden, R. W., Saccomandi, G. and Sgura, I. (2004), 'Fitting hyperelastic models to experimental data', *Computational Mechanics* **34**, 484–502.

Ortiz, M. and Stainier, L. (1999), 'The variational formulation of viscoplastic constitutive updates', *Computer Methods in Applied Mechanics and Engineering* **171**(3-4), 419–444.

Pakula, T., Saijo, K., Kawai, H. and Hashimoto, T. (1985), 'Deformation behavior of styrene-butadiene-styrene triblock copolymer with cylindrical morphology', *Macromolecules* **18**(6), 1294–1302.

Peña, E. and Doblaré, M. (2009), 'An anisotropic pseudo-elastic approach for modelling Mullins effect in fibrous biological materials', *Mechanics Research Communications* **36**(7), 784–790.

Plagge, J. and Klüppel, M. (2017), 'A physically based model of stress softening and hysteresis of filled rubber including rate- and temperature dependency', *International Journal of Plasticity* **89**, 173–196.

Prisacariu, C. (2011), *Polyurethane Elastomers: From Morphology to Mechanical Aspects*, Springer Science & Business Media.

Puso, M. (2003), Mechanistic Constitutive Models for Rubber Elasticity and Viscoelasticity, PhD thesis, University of California, Davis.

Qi, H. J. and Boyce, M. C. (2005), 'Stress–strain behavior of thermoplastic polyurethanes', *Mechanics of materials* **37**(8), 817–839.

Qi, HJ. and Boyce, MC. (2004), 'Constitutive model for stretch-induced softening of the stress–stretch behavior of elastomeric materials', *Journal of the Mechanics and Physics of Solids* **52**(10), 2187–2205.

Rault, J., Marchal, J., Judeinstein, P. and Albouy, PA. (2006), 'Stress-induced crystallization and reinforcement in filled natural rubbers: 2H NMR study', *Macromolecules* **39**(24), 8356–8368.

Read, D. J., Duckett, R. A., Sweeney, J. and McLeish, T. C. B. (1999), 'The chevron folding instability in thermoplastic elastomers and other layered materials', *Journal of Physics D: Applied Physics* **32**(16), 2087–2099.

Reese, S. and Govindjee, S. (1998), 'A theory of finite viscoelasticity and numerical aspects', *International Journal of Solids and Structures* **35**(26), 3455–3482.

Reyes, S. I., Vassiliou, M. F. and Konstantinidis, D. (2024), 'Experimental characterization and constitutive modeling of thermoplastic polyurethane under complex uniaxial loading', *Journal of the Mechanics and Physics of Solids* **186**, 105582.

Ricker, A., Gierig, M. and Wriggers, P. (2023), 'Multiplicative, Non-Newtonian Viscoelasticity Models for Rubber Materials and Brain Tissues: Numerical Treatment and Comparative Studies', *Archives of Computational Methods in Engineering* **30**(5), 2889–2927.

Ricker, A. and Wriggers, P. (2023), 'Systematic Fitting and Comparison of Hyperelastic Continuum Models for Elastomers', *Archives of Computational Methods in Engineering* **30**(3), 2257–2288.

Rivlin, RS. and Saunders, DW. (1951), 'Large Elastic Deformations of Isotropic Materials. VII. Experiments on the Deformation of Rubber', *Philosophical Transactions of the Royal Society of London. Series A, Mathematical and Physical Sciences* pp. 251–288.

Robertson, C. G. and Hardman, N. J. (2021), 'Nature of carbon black reinforcement of rubber: Perspective on the original polymer nanocomposite', *Polymers* **13**(4), 538.

Rubinstein, M., Colby, R. H. et al. (2003), *Polymer Physics*, Vol. 23, Oxford University Press New York.

Rubinstein, M. and Panyukov, S. (1997), 'Nonaffine deformation and elasticity of polymer networks', *Macromolecules* **30**(25), 8036–8044.

Scetta, G., Ju, J., Selles, N., Heuillet, P., Ciccotti, M. and Creton, C. (2021), 'Strain induced strengthening of soft thermoplastic polyurethanes under cyclic deformation', *Journal of Polymer Science* **59**(8), 685–696.

Shariff, M. H. B. M. (2000), 'Strain Energy Function for Filled and Unfilled Rubberlike Material', *Rubber Chemistry and Technology* **73**(1), 1–18.

Shariff, M. H. B. M. (2006), 'An anisotropic model of the Mullins effect', *Journal of Engineering Mathematics* **56**(4), 415–435.

Shariff, M. H. B. M. (2014), 'Direction dependent orthotropic model for Mullins materials', *International Journal of Solids and Structures* **51**(25), 4357–4372.

Simo, J. C. (1987), 'On a fully three-dimensional finite-strain viscoelastic damage model: Formulation and computational aspects', *Computer Methods in Applied Mechanics and Engineering* **60**(2), 153–173.

Smith, M. (2009), 'ABAQUS/Standard User's Manual, Version 6.9'.

Steck, J., Kim, J., Kutsovsky, Y. and Suo, Z. (2023), 'Multiscale stress deconcentration amplifies fatigue resistance of rubber', *Nature* **624**(7991), 303–308.

Steinmann, P., Hossain, M. and Possart, G. (2012), 'Hyperelastic models for rubber-like materials: Consistent tangent operators and suitability for Treloar's data', *Archive of Applied Mechanics* **82**(9), 1183–1217.

Sui, T., Baimpas, N., Dolbnya, I. P., Prisacariu, C. and Korsunsky, A. M. (2015), 'Multiple-length-scale deformation analysis in a thermoplastic polyurethane', *Nature Communications* **6**(1), 6583.

Sui, T., Salvati, E., Ying, S., Sun, G., Dolbnya, I. P., Dragnevski, K., Prisacariu, C. and Korsunsky, A. M. (2017), 'Strain softening of nano-scale fuzzy interfaces causes Mullins effect in thermoplastic polyurethane', *Scientific Reports* **7**(1), 916.

Tkachuk, M. and Linder, C. (2012), 'The maximal advance path constraint for the homogenization of materials with random network microstructure', *Philosophical Magazine* **92**(22), 2779–2808.

Treloar, L. R. G. (1943), 'The elasticity of a network of long-chain molecules—II', *Trans. Faraday Soc.* **39**(0), 241–246.

Treloar, L. R. G. (1975), *The Physics of Rubber Elasticity*, Oxford University Press.

Treloar, LRG. (1954), 'The photoelastic properties of short-chain molecular networks', *Transactions of the Faraday Society* **50**, 881–896.

Valanis, K. C. and Landel, R. F. (1967), 'The Strain-Energy Function of a Hyperelastic Material in Terms of the Extension Ratios', *Journal of Applied Physics* **38**(7), 2997–3002.

Verron, E. (2015), 'Questioning numerical integration methods for microsphere (and microplane) constitutive equations', *Mechanics of Materials* **89**, 216–228.

Wales, D. J. and Doye, J. P. K. (1997), 'Global Optimization by Basin-Hopping and the Lowest Energy Structures of Lennard-Jones Clusters Containing up to 110 Atoms', *The Journal of Physical Chemistry A* **101**(28), 5111–5116.

Wang, S. and Chester, S. A. (2018), 'Modeling thermal recovery of the Mullins effect', *Mechanics of Materials* **126**, 88–98.

Wang, Y., Luo, W., Huang, J., Peng, C., Wang, H., Yuan, C., Chen, G., Zeng, B. and Dai, L. (2020), 'Simplification of Hyperelastic Constitutive Model and Finite Element Analysis of Thermoplastic Polyurethane Elastomers', *Macromolecular Theory and Simulations* **29**(4), 2000009.

Weiss, J. A., Maker, B. N. and Govindjee, S. (1996), 'Finite element implementation of incompressible, transversely isotropic hyperelasticity', *Computer Methods in Applied Mechanics and Engineering* **135**(1), 107–128.

Wineman, A. (2005), 'Some results for generalized neo-Hookean elastic materials', *International Journal of Non-linear Mechanics* **40**(2-3), 271–279.

Wu, P. and Van Der Giessen, E. (1993), 'On improved network models for rubber elasticity and their applications to orientation hardening in glassy polymers', *Journal of the Mechanics and Physics of Solids* **41**(3), 427–456.

Xiao, R., Mai, T.-T., Urayama, K., Gong, J. P. and Qu, S. (2021), 'Micromechanical modeling of the multi-axial deformation behavior in double network hydrogels', *International Journal of Plasticity* **137**, 102901.

Yoda, R. (1998), 'Elastomers for biomedical applications', *Journal of Biomaterials Science, Polymer Edition* **9**(6), 561–626.

Yu, Z. Q., Ma, Q., Su, X. M., Lai, X. M. and Tibbenham, P. C. (2010), 'Constitutive modeling for large deformation behavior of thermoplastic olefin', *Materials & Design* **31**(4), 1881–1886.

Zhan, L., Qu, S. and Xiao, R. (2024), 'A review on the mullins effect in tough elastomers and gels', *Acta Mechanica Solida Sinica* .

Zhan, L., Wang, S., Qu, S., Steinmann, P. and Xiao, R. (2023*a*), 'A general continuum damage model for soft composites', *Journal of the Mechanics and Physics of Solids* **175**, 105290.

Zhan, L., Wang, S., Qu, S., Steinmann, P. and Xiao, R. (2023*b*), 'A new micro–macro transition for hyperelastic materials', *Journal of the Mechanics and Physics of Solids* **171**, 105156.

Zhan, L. and Xiao, R. (2022), 'A Microstructural Damage Model toward Simulating the Mullins Effect in Double-Network Hydrogels', *Acta Mechanica Solida Sinica* **35**(4), 682–693.

Appendix A

Incremental variational formulation of inelastic full-network framework

For the purposes of numerical implementation, we re-cast the model presented in Chapter 3 in an incremental variational setting. Incremental variational formulations of constitutive updates were first put forward by Ortiz and Stainier (1999) for viscoplasticity and have recently been extended to micromechanical rubber models by Göktepe and Miehe (2005); Govindjee et al. (2019); Bresolin and Vassoler (2022). In the variational setting, the internal state of the material is given by the solution of a minimisation problem, which can be solved through any optimisation method (numerical or analytical). In addition to providing a convenient framework for updating the internal state, a major benefit of this mathematical structure is that the incremental stress-strain relationship has the same structure as it does in hyperelasticity. Stresses derive from a single incremental potential that is a function of observable state variables only, and the consistent tangent operator follows from the second derivative. This allows numerical methods or approaches developed in a hyperelastic setting to be extended to the inelastic setting with relative ease, for example the extension of non-affine micro-macro transition schemes for rubber models e.g. Miehe et al. (2004); Tkachuk and Linder (2012) to viscoelasticity (Govindjee et al., 2019) and/or damage (Bresolin and Vassoler, 2022). Having introduced a continuous variation principle, it remains to formulate the constitutive updates in a discretised or incremental setting to ensure the advantages earlier described. We use the following incremental

variation principle, again inspiring from Ortiz and Stainier (1999); Bresolin and Vassoler (2022):

$$W_\Delta(\boldsymbol{F}_{n+1}) = \inf_{\xi_{n+1}} J_\Delta\left(\boldsymbol{F}_{n+1}, \xi_{n+1}\right), \tag{A.1}$$

where J_Δ is defined:

$$J_\Delta\left(\boldsymbol{F}_{n+1}, \xi^j_{i,n+1}\right) := \sum_j c^j \left(\psi(\lambda^j_{n+1}, \xi^j_{i,n+1}) - \psi(\lambda^j_n, \xi^j_{i,n}) + \phi\left(\frac{\Delta\xi_i}{\Delta t}, \xi_{i,n+\theta}\right)\Delta t\right). \tag{A.2}$$

The incremental variational principle features discretisation over the unit sphere in addition to temporal discretisation. We use superscript $()^j$ to denote a quantity evaluated at a specific integration point j on the unit sphere and a subscript $()_n$ for a quantity at timestep n (for quantities which already feature a subscript index, the timestep features as a secondary subscript). The subscript $()_{n+\theta}$ denotes a quantity at an interpolated timestep e.g. $\xi_{i,n+\theta} = \theta\xi_{i,n+1} + (1-\theta)\xi_{i,n}$ and $\Delta() = ()_{n+1} - ()_n$. In the definition of the incremental potential J_Δ we have replaced the integral over the unit sphere with a summation:

$$\frac{1}{4\pi}\int_{\mathcal{S}} () d\mathcal{S} \to \sum_j ()^j c^j. \tag{A.3}$$

The following Euler-Lagrange equation is found:

$$\frac{\partial\psi}{\partial\xi^j_{i,n+1}} + \frac{\partial\phi}{\partial\dot{\xi}^j_i} + \theta\Delta t\frac{\partial\phi}{\partial\xi^j_i} = 0. \tag{A.4}$$

It can be shown that the first Piola-Kirchhoff stress at timestep $n+1$ can be determined from the derivative $\partial W_\Delta/\partial\boldsymbol{F}_{n+1}$. Expressing this in terms of J_Δ:

$$\frac{\partial W_\Delta}{\partial\boldsymbol{F}_{n+1}} = \frac{\partial J_\Delta}{\partial\boldsymbol{F}_{n+1}} + \frac{\partial J_\Delta}{\partial\xi^j_{i,n+1}}\frac{\partial\xi^j_{i,n+1}}{\partial\boldsymbol{F}_{n+1}} + \frac{\partial J_\Delta}{\partial\xi^j_{i,n+1}}\frac{\partial\xi^j_{i,n+1}}{\partial\boldsymbol{F}_{n+1}}, \tag{A.5}$$

where summation takes place over all i and j. Due to the stationary conditions, the

derivatives of J_Δ with respect to $\xi^j_{i,n+1}$ are zero, such that:

$$\frac{\partial W_\Delta}{\partial \boldsymbol{F}_{n+1}} = \frac{\partial J_\Delta}{\partial \boldsymbol{F}_{n+1}}, \tag{A.6}$$

$$= \frac{\partial \Psi}{\partial \boldsymbol{F}_{n+1}} \tag{A.7}$$

which determines the non-hydrostatic part of stress. Thus the macroscopic stress can be written in terms of the incremental potential W_Δ, incorporates the updates of internal variables by construction:

$$\boldsymbol{P}_{n+1} = \frac{\partial W_\Delta(\boldsymbol{F}_{n+1})}{\partial \boldsymbol{F}_{n+1}} - P_{n+1}\boldsymbol{F}^{-T}_{n+1}, \tag{A.8}$$

which is analogous to the hyperelastic stress-strain relation.

Appendix B

Equivalence of plastic dissipation potential to yield function

The choice of of the dissipation potential (3.46) in Section 3.4.1 can be shown to recover a one-dimensional yield surface theory of plasticity. As mentioned in Section 3.4.1, the variational principle requires minimisation of the following functional to determine the evolution of plastic strain:

$$J(\dot{p}, N, \Pi) = \lambda^{e1} \frac{\partial \psi^{(2)}}{\partial \lambda^{e1}} (d - \dot{p}N) + (\sigma_y + hp)\, \dot{p} + \Pi \left(|N| - 1 \right), \tag{B.1}$$

where $\dot{p} \geq 0$. The corresponding Euler-Lagrange equations read:

$$\frac{\partial J}{\partial \dot{p}} = -\lambda^{e1} \frac{\partial \psi^{(2)}}{\partial \lambda^{e1}} N + \sigma_y + hp = 0, \tag{B.2}$$

$$\frac{\partial J}{\partial N} = -\lambda^{e1} \frac{\partial \psi^{(2)}}{\partial \lambda^{e1}} \dot{p} + \Pi \frac{N}{|N|} = 0, \tag{B.3}$$

$$\frac{\partial J}{\partial \Pi} = |N| - 1 = 0. \tag{B.4}$$

Consider the case where $\dot{p} > 0$ and examine Eq. (B.2). As $\partial \phi / \partial \dot{p} = \sigma_y + hp \geq 0$ by definition, the quantity $-\lambda^{e1} \left(\partial \psi^{(2)} / \partial \lambda^{e1} \right) N$ must be equal to or less than zero. Due to the constraint on the magnitude of N, which is expressed in Eq. (B.4), it follows that N

must have the opposite sign from $\lambda^{e1}\partial\psi^{(2)}/\partial\lambda^{e1}$, i.e.:

$$N = \text{sgn}\left(\lambda^{e1}\frac{\partial\psi^{(2)}}{\partial\lambda^{e1}}\right). \tag{B.5}$$

Inserting the expression for N into Eq. (B.2) and making use of some basic identities between magnitudes and signs, we find that:

$$-\left|\lambda^{e1}\frac{\partial\psi^{(2)}}{\partial\lambda^{e1}}\right| + \sigma_y + hp = 0, \tag{B.6}$$

when $\dot{p} > 0$. In the solution of the variational problem the current state (in this case defined by λ, λ^p and p) is presumed and the rate of change of the internal state (described by $\dot{\lambda}^p$ and $\dot{p}$) is determined for a given change in the observable state (described by $\dot{\lambda}$). Noting that $\dot{p}$ does not appear in Eq. (B.6) and that the current state of the system may not satisfy Eq. (B.6), we must return to the functional to determine the value of $\dot{p}$. If $\partial J/\partial\dot{p} < 0$, the variational principle dictates that $\dot{p} \to \infty$ as this minimises J. Plastic flow occurs instantaneously and brings the state of the system to the state described by Eq. (B.6). If $\partial J/\partial\dot{p} > 0$, the condition $\dot{p} \geq 0$ implies that no plastic flow occurs ($\dot{p} = 0$). Based on this analysis, a yield function f_y equal to the negative of the left hand side of Eq. (B.6) can be introduced:

$$f_y := \left|\lambda^{e1}\frac{\partial\psi^{(2)}}{\partial\lambda^{e1}}\right| - \sigma_y - hp, \tag{B.7}$$

which acts as an indicator for when plastic flow occurs: $f_y < 0$ implies no plastic flow occurs; $f_y = 0$ implies plastic flow may occur. Thus we arrive at the conditions:

$$f_y \leq 0, \quad \dot{p} \geq 0, \quad f_y\dot{p} = 0, \tag{B.8}$$

as stated in Eq. (3.49).

Appendix C

Analytic full network averaging

C.1 Variance of line-stretch in terms of invariant

The variance of the chain stretch over all orientations of chains is given by:

$$\langle \left(\bar{\lambda}^2 - \langle \bar{\lambda}^2 \rangle\right)^2 \rangle = \langle \bar{\lambda}^4 \rangle - \langle \bar{\lambda}^2 \rangle^2, \tag{C.1}$$

where

$$\langle \bar{\lambda}^2 \rangle = \frac{I_1}{3}. \tag{C.2}$$

Recalling that $\bar{\lambda} = |\boldsymbol{F}\boldsymbol{n}|$, we can calculate:

$$\begin{aligned}
\langle \bar{\lambda}^4 \rangle &= \langle (\bar{\lambda}^2)(\bar{\lambda}^2) \rangle, && \text{(C.3)}\\
&= \langle |\boldsymbol{F}\boldsymbol{n}|^2 |\boldsymbol{F}\boldsymbol{n}|^2 \rangle, && \text{(C.4)}\\
&= \langle (\boldsymbol{n}\boldsymbol{C}\boldsymbol{n})(\boldsymbol{n}\boldsymbol{C}\boldsymbol{n}) \rangle, && \text{(C.5)}\\
&= \boldsymbol{C} : \langle \boldsymbol{n} \otimes \boldsymbol{n} \otimes \boldsymbol{n} \otimes \boldsymbol{n} \rangle : \boldsymbol{C}, && \text{(C.6)}
\end{aligned}$$

where $\boldsymbol{C}$ is the right Cauchy-Green strain tensor: $\boldsymbol{C} = \boldsymbol{F}^T\boldsymbol{F}$. Note the result from Ken-Ichi (1984); Lubarda and Krajcinovic (1993):

$$\langle n_i n_j n_k n_l \rangle = \frac{1}{15}(\delta_{ij}\delta_{kl} + \delta_{ik}\delta_{jl} + \delta_{il}\delta_{jk}). \tag{C.7}$$

Then, direct calculation and using the definitions of I_1 and I_2:

$$\langle \bar{\lambda}^4 \rangle = \frac{1}{15}(I_1^2 + 2tr(\boldsymbol{C}^2)) = \frac{1}{15}(3I_1^2 - 4I_2). \tag{C.8}$$

Using results (C.2) and (C.8), the variance becomes:

$$\langle \left(\bar{\lambda}^2 - \langle \bar{\lambda}^2 \rangle\right)^2 \rangle = \frac{4}{15}(I_1^2 - 3I_2). \tag{C.9}$$

If three-chain averaging is used instead, the variance is given by:

$$\langle \left(\bar{\lambda}^2 - \langle \bar{\lambda}^2 \rangle\right)^2 \rangle_{3C} = \frac{1}{3}\sum_{i=1}^{3}(\lambda_i^2 - \langle \bar{\lambda}^2 \rangle)^2, \tag{C.10}$$

$$= \frac{1}{3}\left((\lambda_1^4 + \lambda_2^4 + \lambda_3^4) - \frac{I_1^2}{3}\right). \tag{C.11}$$

It is readily verified that:

$$\sum_{i=1}^{3}\lambda_i^4 = I_1^2 - 2I_2. \tag{C.12}$$

Combining the above results:

$$\langle \left(\bar{\lambda}^2 - \langle \bar{\lambda}^2 \rangle\right)^2 \rangle_{3C} = \frac{2}{9}(I_1^2 - 3I_2). \tag{C.13}$$

C.2 Variance of the area-stretch in terms of invariants

The variance on the area-stretch is given by:

$$\langle (\bar{\nu}^2 - \langle \bar{\nu}^2 \rangle)^2 \rangle = \langle \bar{\nu}^4 \rangle - \langle \bar{\nu}^2 \rangle^2. \tag{C.14}$$

Recall the result:

$$\langle \bar{\nu}^2 \rangle = \frac{I_2}{3}. \tag{C.15}$$

From the definition of the area-stretch $\bar{\nu} = |\boldsymbol{F}^{-T}|\boldsymbol{n}$, we obtain:

$$\langle \bar{\nu}^4 \rangle = \boldsymbol{C}^{-1} : \langle \boldsymbol{n} \otimes \boldsymbol{n} \otimes \boldsymbol{n} \otimes \boldsymbol{n} \rangle, \tag{C.16}$$

$$= \boldsymbol{C}^{-1} : \frac{1}{5}\mathcal{I} : \boldsymbol{C}^{-1}, \tag{C.17}$$

where $\mathcal{I}_{ijkl} = \frac{1}{3}(\delta_{ij}\delta_{kl} + \delta_{ik}\delta_{jl} + \delta_{il}\delta_{jk})$ (Ken-Ichi, 1984; Lubarda and Krajcinovic, 1993). Note the equality:

$$\boldsymbol{C}^{-1} : \frac{1}{5}\mathcal{I} : \boldsymbol{C}^{-1} = \frac{1}{15}\left(\left(\boldsymbol{C}^{-1} : \boldsymbol{1} \right)^2 + 2\boldsymbol{C}^{-1} : \boldsymbol{C}^{-1} \right). \tag{C.18}$$

From the Cayley-Hamilton theorem, we have:

$$\boldsymbol{C}^3 - I_1\boldsymbol{C}^2 + I_2\boldsymbol{C} - I_3\boldsymbol{1} = \boldsymbol{0} \implies I_3\boldsymbol{C}^{-1} = \boldsymbol{C}^2 - I_1\boldsymbol{C} + I_2\boldsymbol{1}, \tag{C.19}$$

so that:

$$\boldsymbol{C}^{-1} : \boldsymbol{1} = \boldsymbol{C}^2 : \boldsymbol{1} - I_1^2 + 3I_2 = I_2, \tag{C.20}$$

$$\boldsymbol{C}^{-1} : \boldsymbol{C}^{-1} = \boldsymbol{C}^{-1} : \left(\boldsymbol{C}^2 - I_1\boldsymbol{C} + I_2\boldsymbol{1} \right) = I_1 - 3I_1 + I_2^2. \tag{C.21}$$

Substituting Eqs (C.20)-(C.21) into Eq. (C.18), and that result in turn into (C.14), we find:

$$\langle (\bar{\nu}^2 - \langle \bar{\nu}^2 \rangle)^2 \rangle = \frac{4}{45}\left(I_2^2 - 3I_1 \right). \tag{C.22}$$

If three-chain averaging is used, the variance is given by:

$$\langle \left(\bar{\nu}^2 - \langle \bar{\nu}^2 \rangle \right)^2 \rangle_{3C} = \frac{1}{3}\sum_{i=1}^{3} (\Gamma_i - \langle \Gamma \rangle)^2, \tag{C.23}$$

$$= \frac{1}{3}\left((\nu_1^4 + \nu_2^4 + \nu_3^4) - \frac{I_2^2}{3} \right), \tag{C.24}$$

where $\Gamma_i = \nu_i^2$. It is readily verified that:

$$\sum_{i=1}^{3} \nu_i^4 = I_2^2 - 2I_1. \tag{C.25}$$

Combining the above results:

$$\langle \left(\bar{\nu}^2 - \langle \bar{\nu}^2 \rangle\right)^2 \rangle_{3C} = \frac{2}{9}(I_2^2 - 3I_1). \tag{C.26}$$

Appendix D

Series expansions of the full-network tube free energy

λ-based full-network model. Express the tube free energy $\psi_c^{(\lambda)}$ as a function of the squared line-stretch: $w_c^{(\lambda)}(\Lambda) := \psi_c^{(\lambda)}(\bar{\lambda})$, with $\Lambda := \bar{\lambda}^2$. The Taylor series expansion of the tube energy about $\langle\Lambda\rangle$ writes, to the second order:

$$w_c^{(\lambda)}(\Lambda) = w_c^{(\lambda)}(\langle\Lambda\rangle) + \frac{dw_c^{(\lambda)}}{d\Lambda}(\langle\Lambda\rangle)(\Lambda - \langle\Lambda\rangle) + \frac{1}{2}\frac{d^2w_c^{(\lambda)}}{d\Lambda^2}(\langle\Lambda\rangle)(\Lambda - \langle\Lambda\rangle)^2 + \text{h.o.t.}. \quad \text{(D.1)}$$

Note the following results for the average squared line-stretch and its variance (see Appendix C.1 for derivation details):

$$\langle\Lambda\rangle = \frac{I_1}{3}, \quad \langle(\Lambda - \langle\Lambda\rangle)^2\rangle = \frac{4}{45}(I_1^2 - 3I_2). \quad \text{(D.2)}$$

Taking the average of Eq. (D.1) over all chain orientations and using the above results then gives:

$$\langle w_c^{(\lambda)}(\Lambda)\rangle = w_c^{(\lambda)}\left(\frac{I_1}{3}\right) + \frac{2}{45}\frac{d^2w_c^{(\lambda)}}{d\Lambda^2}\left(\frac{I_1}{3}\right)(I_1^2 - 3I_2) + \text{h.o.t.}. \quad \text{(D.3)}$$

Note that the first-order derivative of the free energy plays no role in Eq. (D.3) since $\langle\Lambda - \langle\Lambda\rangle\rangle = 0$.

ν-based full-network model. The series expansion is obtained following similar steps as for the λ-based model. Define the squared area-stretch as $\Gamma := \bar{\nu}^2$, and express the tube free energy as $w_c^{(\nu)}(\Gamma) := \psi_c^{(\nu)}(\bar{\nu})$. The Taylor series expansion of the tube energy about $\langle\Gamma\rangle$ writes, to the second order:

$$w_c^{(\nu)}(\Gamma) = w_c^{(\nu)}(\langle\Gamma\rangle) + \frac{dw_c^{(\nu)}}{d\Gamma}(\langle\Gamma\rangle)(\Gamma - \langle\Gamma\rangle) + \frac{1}{2}\frac{d^2w_c^{(\nu)}}{d\Gamma^2}(\langle\Gamma\rangle)(\Gamma - \langle\Gamma\rangle) + \text{h.o.t.}. \tag{D.4}$$

The average and variance of the squared area-stretch are given by (see Appendix C.2 for details):

$$\langle\Gamma\rangle = \frac{I_2}{3}, \quad \langle(\Gamma - \langle\Gamma\rangle)^2\rangle = \frac{4}{45}(I_2^2 - 3I_1). \tag{D.5}$$

Taking the average of Eq. (D.4) over all chain orientations and using the above results gives

$$\langle w_c^{(\nu)}(\Gamma)\rangle = w_c^{(\nu)}\left(\frac{I_2}{3}\right) + \frac{2}{45}\frac{d^2w_c^{(\nu)}}{d\Gamma^2}\left(\frac{I_2}{3}\right)(I_2^2 - 3I_1) + \text{h.o.t.}. \tag{D.6}$$

Three-chain models. Similar series expansion of the average tube energy can be obtained when three-chain averaging is used, instead of full-network averaging. First introduce the following notation: $\langle\cdot\rangle_{3C} = \frac{1}{3}\sum_{i=1}^{3}(\cdot)_i$. We find, for the three-chain average and variance of the squared line-stretch:

$$\langle\Lambda\rangle_{3C} = \frac{I_1}{3}, \quad \langle(\Lambda - \langle\Lambda\rangle_{3C})^2\rangle_{3C} = \frac{2}{9}(I_1^2 - 3I_2), \tag{D.7}$$

and, for the three-chain average and variance of the squared area-stretch:

$$\langle\Gamma\rangle_{3C} = \frac{I_2}{3}, \quad \langle(\Gamma - \langle\Gamma\rangle_{3C})^2\rangle_{3C} = \frac{2}{9}(I_2^2 - 3I_1). \tag{D.8}$$

See Appendices C.1 and C.2 for details. Series expansions of the average energies can then be expressed as:

$$\langle w_c^{(\lambda)}\rangle_{3C} = \psi_c^{(\lambda)}\left(\sqrt{\frac{I_1}{3}}\right) + \frac{1}{9}\frac{d^2w_c^{(\lambda)}}{d\Lambda^2}\left(\frac{I_1}{3}\right)(I_1^2 - 3I_2) + \text{h.o.t.}, \tag{D.9}$$

and:

$$\langle w_c^{(\nu)}\rangle_{3C} = \psi_c^{(\nu)}\left(\sqrt{\frac{I_2}{3}}\right) + \frac{1}{9}\frac{d^2 w_c^{(\nu)}}{d\Gamma^2}\left(\frac{I_2}{3}\right)(I_2^2 - 3I_1) + \text{h.o.t.}. \tag{D.10}$$

Numerical verification. Series expansions (D.3) and (D.6) of the full-network λ-based and ν-based tube energies are compared to numerical estimates of the expressions that the series seek to approximate in Fig. D.1 (a) and (b). The reference numerical results are exact for the three-chain case (given by the analytical expressions (4.57) and (4.58)) and only deviate from the exact solution in the full-network case due to the error in discretisation over the unit sphere. In the figures, the macroscopic energy $\Psi = n\langle w_c\rangle$ has been normalised by (kn). The tube exponent is set as $\beta = -1$ for the λ-based model and $\beta = 1$ for the ν-based model. Different loading modes are considered, namely uniaxial tension (UT), pure shear (PS) and equibiaxial tension (EBT). The series expansions are accurate at small stretches, but significantly deviate from the reference numerical solution at moderate to large stretches (not shown). We note that the series expansion of the ν-based model is more accurate than that of the λ-based model. The switch in concavity of the free energy between λ-based and ν-based model is consistent with the sign of the tube modulus (4.28) when the sign of the exponent β changes.

The series expansions of the macroscopic free energy obtained using three-chain averaging, Eqs (D.9) and (D.10), are compared to reference numerical results in Figs D.1 (c) and (d) for the same values of the tube exponent β. Compared to the full-network case, the series expansions are less accurate than their full-network counterparts in this range of deformation. For the considered values of β, the three-chain models are identical in their λ-based and ν-based forms, as confirmed by the numerical results. The series expansions are however not identical, and appear slightly more accurate when the expansion is taken about the squared area-stretch than about the squared line-stretch.

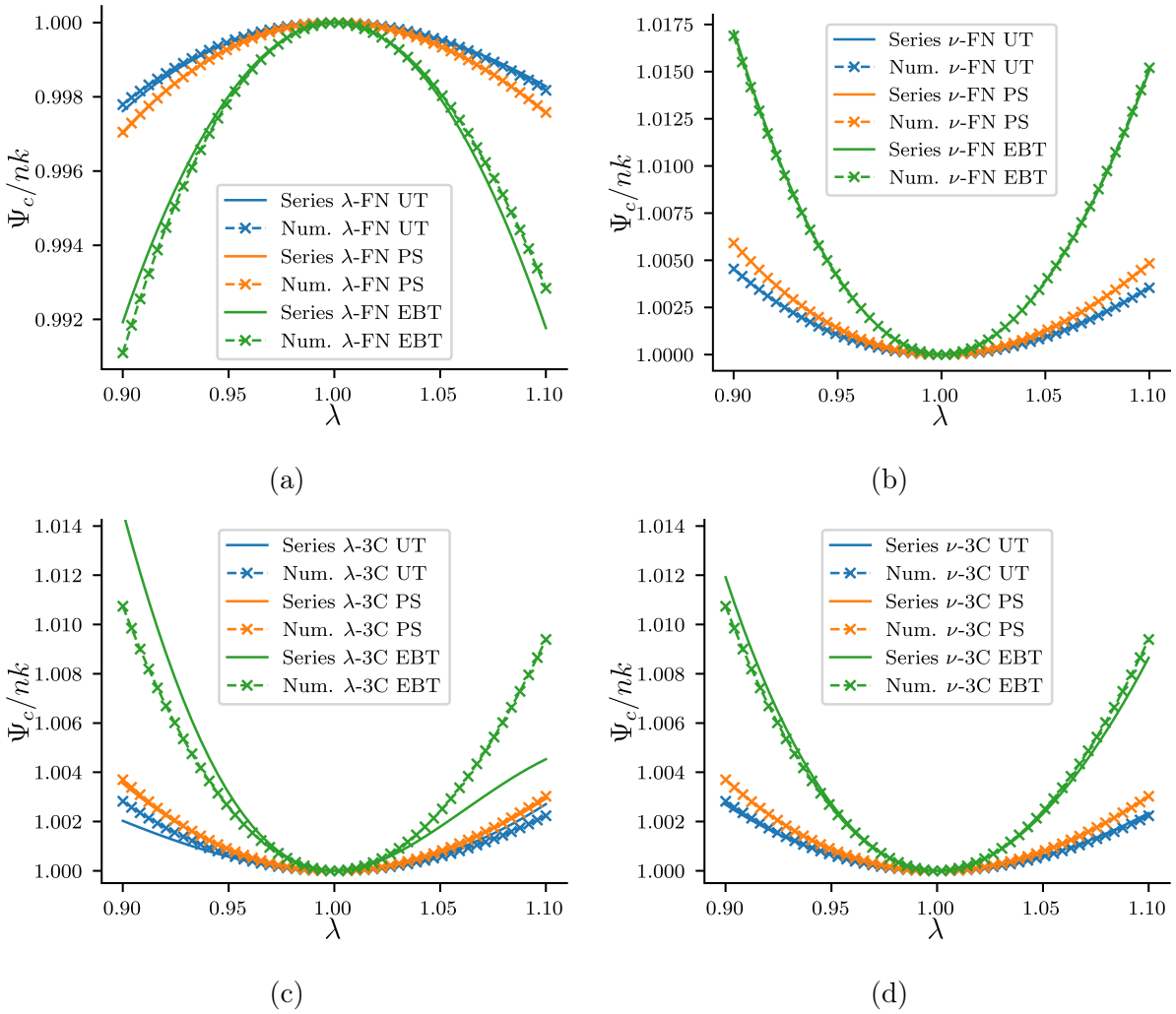


Figure D.1: Comparison between the series expansion approximations of the tube contribution to the macroscopic free energy and the reference solution obtained by numerical integration. (a) λ-based full-network model, Eq. (D.3); (b) ν-based full-network model, Eq. (D.6), (c) λ-based three-chain model, Eq. (D.9) and (d) ν-based three-chain model, Eq. (D.10). The tube exponent is set as $\beta = -1$ in the λ-based models, and as $\beta = 1$ in the ν-based models. Three loading conditions are considered: uniaxial tension (UT), pure shear (PS) and equibiaxial tension (EBT).

Appendix E

Anisotropic Mullins effect model

E.1 Equivalent formulation based on a variational principle

In this section, we show that the general constitutive equations previously obtained using the concept of the damage surface can alternatively be obtained as the solution of a variational problem subjected to kinematic constraints on the flow rule. The variational approach outlined below is similar to the formulation of Ortiz and Stainier (1999), see also Brassart and Stainier (2012).

As before, we describe the state of the material with two tensorial variables: the strain $\boldsymbol{C}$ and the damage tensor $\boldsymbol{A}$. Within the framework of Generalised Standard Materials (Halphen and Son Nguyen, 1975), the constitutive relations derive from two thermodynamic potentials: a free energy $\Psi(\boldsymbol{C}, \boldsymbol{A})$ and a dissipation potential $\Phi(\dot{\boldsymbol{A}})$. Contrarily to classical formulations, here no damage function is explicitly introduced. Instead, we postulate a damage flow rule of the form:

$$\dot{\boldsymbol{A}} = \sum_{i=1}^{p} \dot{\alpha}^{(i)} \boldsymbol{M}^{(i)} \otimes \boldsymbol{M}^{(i)}, \tag{E.1}$$

where $\dot{\alpha}^{(i)}$ are damage amplitudes, $\boldsymbol{M}^{(i)} \otimes \boldsymbol{M}^{(i)}$ are damage directions, and p is the number of tensile principal stretches. Thus, the rank of $\dot{\boldsymbol{A}}$ is equal to the number of

tensile principal stretches p. The vectors $\boldsymbol{M}^{(i)}$ are further subjected to the following kinematic constraints:

$$\boldsymbol{M}^{(i)} \cdot \boldsymbol{M}^{(i)} = 1. \tag{E.2}$$

The free energy Ψ is taken of the form (6.11), together with the localisation rules (6.12) and (6.13). As before, the driving force associated with damage is given by the state law:

$$\boldsymbol{Z} = -\frac{\partial \Psi}{\partial \boldsymbol{A}}, \tag{E.3}$$

and $\boldsymbol{Z} = \hat{\boldsymbol{Z}}$, which follows from the damage localisation rule (6.13). The dissipation potential Φ is given by:

$$\Phi(\dot{\alpha}^{(i)}) = \begin{cases} 0 & \dot{\alpha}^{(i)} \geq 0,\ i \in (1,p) \\ +\infty & \text{otherwise.} \end{cases} \tag{E.4}$$

We next introduce the following functional:

$$\dot{J}(\dot{\boldsymbol{C}}, \dot{\alpha}^{(i)}, \boldsymbol{M}^{(i)}) = \dot{\Psi}(\dot{\boldsymbol{C}}, \dot{\boldsymbol{A}}(\dot{\alpha}^{(i)}, \boldsymbol{M}^{(i)})) + \Phi(\dot{\alpha}^{(i)}) \tag{E.5}$$

$$= \frac{\partial \Psi}{\partial \boldsymbol{C}} : \dot{\boldsymbol{C}} + \frac{\partial \Psi}{\partial \boldsymbol{A}} : \dot{\boldsymbol{A}}(\dot{\alpha}^{(i)}, \boldsymbol{M}^{(i)}) + \Phi(\dot{\alpha}^{(i)}). \tag{E.6}$$

The constitutive model outlined in Section 6.2 is equivalent to the following variational principle:

$$W(\dot{\boldsymbol{C}}) = \inf_{\dot{\alpha}^{(i)}, \boldsymbol{M}^{(i)}} \dot{J}(\dot{\boldsymbol{C}}, \dot{\alpha}^{(i)}, \boldsymbol{M}^{(i)}), \quad i \in (1,p), \tag{E.7}$$

under the constraints (E.2). We note that the minimisation on the flow directions corresponds to maximising the dissipation at constant $\dot{\alpha}^{(i)}$, which parallels the maximum dissipation principle invoked in the previous section. Minimisation w.r.t. the $\boldsymbol{M}^{(i)}$ accounting for the constraints (E.2) can be carried out using Lagrange multipliers, which directly shows that the directions $\boldsymbol{M}^{(i)}$ are the principal directions of $\boldsymbol{Z}$. Stationarity of

the functional $\dot{J}$ w.r.t. $\dot{\alpha}^{(i)}$ leads to:

$$-\boldsymbol{Z} : \boldsymbol{M}^{(i)} \otimes \boldsymbol{M}^{(i)} + \frac{\partial \Phi}{\partial \dot{\alpha}^{(i)}} = 0, \quad i \in (1, p), \tag{E.8}$$

where $\frac{\partial \Phi}{\partial \dot{\alpha}^{(i)}}$ is to be interpreted as a subdifferential of Φ for $\dot{\alpha}^{(i)} = 0$. Note that:

$$\boldsymbol{Z} : (\boldsymbol{M}^{(i)} \otimes \boldsymbol{M}^{(i)}) = \nu^{(i)} = f^{(i)}. \tag{E.9}$$

Thus, the stationary condition (E.8) is equivalent to the damage criterion:

$$\dot{\alpha}^{(i)} = 0 \;\Leftrightarrow f^{(i)} \leq 0 \tag{E.10}$$

$$\dot{\alpha}^{(i)} > 0 \;\Leftrightarrow f^{(i)} = 0 \tag{E.11}$$

and negative values of $\dot{\alpha}^{(i)}$ are prohibited by the specific form of the dissipation potential. Thus, the variational principle (E.7) is equivalent to the model presented in the previous section. Finally, taking the stationarity conditions into account, it can be seen that $\dot{W}$ acts as a potential for the stress.

E.2 Consistent tangent operator

We recall Eq. (6.55), where all quantities are evaluated at t_{n+1} otherwise indicated (subscripts $n+1$ omitted for conciseness):

$$\frac{d^2\Psi}{d\boldsymbol{C}^2} = \frac{\partial^2 \Psi}{\partial \boldsymbol{C}^2} + \frac{\partial^2 \Psi}{\partial \boldsymbol{C} \partial \boldsymbol{A}} : \sum_{i=1}^{p} \left(\boldsymbol{M}^{tr(i)} \otimes \boldsymbol{M}^{tr(i)} \frac{\partial \Delta\alpha^{(i)}}{\partial \boldsymbol{C}} + \Delta\alpha^{(i)} \frac{\partial \boldsymbol{M}^{tr(i)} \otimes \boldsymbol{M}^{tr(i)}}{\partial \boldsymbol{C}} \right). \tag{E.12}$$

The partial derivatives of the free energy are given by:

$$\frac{\partial \Psi}{\partial \boldsymbol{C}} = \left\langle \frac{1}{2\lambda}\frac{\partial \psi}{\partial \lambda}\boldsymbol{n}\otimes\boldsymbol{n}\right\rangle + \left\langle \frac{\partial \psi}{\partial \xi}\boldsymbol{n}\otimes\boldsymbol{n}\right\rangle : \left(\boldsymbol{A} : \frac{\partial \mathcal{N}}{\partial \boldsymbol{C}}\right), \tag{E.13}$$

$$\begin{aligned}\frac{\partial^2 \Psi}{\partial \boldsymbol{C}\partial \boldsymbol{C}} = &\left\langle \frac{1}{4\lambda^2}\left(\frac{\partial^2 \psi}{\partial \lambda^2} - \frac{1}{\lambda}\frac{\partial \psi}{\partial \lambda}\right)\boldsymbol{n}\otimes\boldsymbol{n}\otimes\boldsymbol{n}\otimes\boldsymbol{n}\right\rangle \\ &+ \left\langle \frac{1}{2\lambda}\frac{\partial \psi^2}{\partial \xi \partial \lambda}\left(\boldsymbol{n}\otimes\boldsymbol{n}\otimes\boldsymbol{n}\otimes\boldsymbol{n} : \left(\boldsymbol{A} : \frac{\partial \mathcal{N}}{\partial \boldsymbol{C}}\right) + \boldsymbol{n}\otimes\boldsymbol{n} : \left(\boldsymbol{A} : \frac{\partial \mathcal{N}}{\partial \boldsymbol{C}}\right)\otimes\boldsymbol{n}\otimes\boldsymbol{n}\right)\right\rangle \\ &+ \left\langle \frac{\partial^2 \psi}{\partial \xi^2}\boldsymbol{n}\otimes\boldsymbol{n} : \left(\boldsymbol{A} : \frac{\partial \mathcal{N}}{\partial \boldsymbol{C}}\right)\otimes\boldsymbol{n}\otimes\boldsymbol{n} : \left(\boldsymbol{A} : \frac{\partial \mathcal{N}}{\partial \boldsymbol{C}}\right)\right\rangle \\ &+ \left\langle \frac{\partial \psi}{\partial \xi}\boldsymbol{n}\otimes\boldsymbol{n} : \left(\boldsymbol{A} : \frac{\partial^2 \mathcal{N}}{\partial \boldsymbol{C}\partial \boldsymbol{C}}\right)\right\rangle,\end{aligned} \tag{E.14}$$

$$\begin{aligned}\frac{\partial^2 \Psi}{\partial \boldsymbol{A}\partial \boldsymbol{C}} = &\mathcal{N} : \left\langle \frac{1}{2\lambda}\frac{\partial^2 \psi}{\partial \xi \partial \lambda}\boldsymbol{n}\otimes\boldsymbol{n}\otimes\boldsymbol{n}\otimes\boldsymbol{n}\right\rangle + \mathcal{N} : \left\langle \frac{\partial^2 \psi}{\partial \xi^2}\boldsymbol{n}\otimes\boldsymbol{n}\otimes\boldsymbol{n}\otimes\boldsymbol{n}\right\rangle : \left(\boldsymbol{A} : \frac{\partial \mathcal{N}}{\partial \boldsymbol{C}}\right) \\ &+ \left\langle \frac{\partial \psi}{\partial \xi}\boldsymbol{n}\otimes\boldsymbol{n}\right\rangle : \left(\frac{\partial \mathcal{N}}{\partial \boldsymbol{C}}\right).\end{aligned} \tag{E.15}$$

The derivatives of the principal damage values can be computed from differentiation of the damage function. Either $\Delta\alpha^{(i)} = 0$ and $\partial \Delta\alpha^{(i)}/\partial \boldsymbol{C} = \boldsymbol{0}$ or :

$$\Delta\alpha^{(i)} \neq 0 \implies \frac{\partial f^{(i)}}{\partial \boldsymbol{C}} + \sum_{j=1}^{p}\frac{\partial f^{(i)}}{\partial \Delta\alpha^{(j)}}\frac{\partial \Delta\alpha^{(j)}}{\partial \boldsymbol{C}} = \boldsymbol{0}. \tag{E.16}$$

In the case where damage is only occurring in one direction, the only non-zero principal damage increment derivative is:

$$\frac{\partial \Delta\alpha^{(1)}}{\partial \boldsymbol{C}} = -\frac{\frac{\partial f^{(1)}}{\partial \boldsymbol{C}}}{\frac{\partial f^{(1)}}{\partial \Delta\alpha^{(1)}}}. \tag{E.17}$$

If damage is occurring in two directions simultaneously with $\nu^{tr(1)} \neq \nu^{tr(2)}$, then the derivatives are found from inversion of a 2×2 system:

$$\begin{pmatrix}\frac{\partial \Delta\alpha^{(1)}}{\partial \boldsymbol{C}} \\ \frac{\partial \Delta\alpha^{(2)}}{\partial \boldsymbol{C}}\end{pmatrix} = \begin{pmatrix}\frac{\partial f^{(1)}}{\partial \Delta\alpha^{(1)}} & \frac{\partial f^{(1)}}{\partial \Delta\alpha^{(2)}} \\ \frac{\partial f^{(2)}}{\partial \Delta\alpha^{(1)}} & \frac{\partial f^{(2)}}{\partial \Delta\alpha^{(2)}}\end{pmatrix}^{-1}\begin{pmatrix}\frac{\partial f^{(1)}}{\partial \boldsymbol{C}} \\ \frac{\partial f^{(2)}}{\partial \boldsymbol{C}}\end{pmatrix}. \tag{E.18}$$

If $p = 2$ and $\nu^{tr(1)} = \nu^{tr(2)}$, then:

$$\frac{\partial \Delta\alpha^{(1,2)}}{\partial \boldsymbol{C}} = -\frac{\frac{\partial f^{(1,2)}}{\partial \boldsymbol{C}}}{\frac{\partial f^{(1,2)}}{\partial \Delta\alpha^{(1,2)}}}, \tag{E.19}$$

where $f^{(1,2)}$ is given by Eq. (6.52). In the previous expressions, the relevant partial derivatives $\frac{\partial f^{(i)}}{\partial \Delta\alpha^{(j)}}$ are given by Eqs (6.47), (6.51) and (6.54), respectively. For $p = 1, 2$ and distinct $\nu^{tr(i)}$, the partial derivatives of the damage functions w.r.t. $\boldsymbol{C}$ are given by:

$$\frac{\partial f^{(i)}}{\partial \boldsymbol{C}} = \boldsymbol{M}^{tr(i)} \otimes \boldsymbol{M}^{tr(i)} : \frac{\partial \boldsymbol{Z}}{\partial \boldsymbol{C}} + (\boldsymbol{M}^{tr(i)} \otimes \boldsymbol{M}^{tr(i)}) : \sum_{j=1}^{p} \frac{\partial \boldsymbol{Z}}{\partial \boldsymbol{A}} : \Delta\alpha^{(j)} \frac{\partial \boldsymbol{M}^{tr(j)} \otimes \boldsymbol{M}^{tr(j)}}{\partial \boldsymbol{C}} + \boldsymbol{Z} : \frac{\partial \boldsymbol{M}^{tr(i)} \otimes \boldsymbol{M}^{tr(i)}}{\partial \boldsymbol{C}}, \tag{E.20}$$

whereas in the case where $p = 2$ and $\nu^{tr(1)} = \nu^{tr(1)} = \nu^{tr(1,2)}$, we obtain:

$$\frac{\partial f^{(1,2)}}{\partial \boldsymbol{C}} = (\boldsymbol{1} - \boldsymbol{n}^{(3)} \otimes \boldsymbol{n}^{(3)}) : \frac{\partial \boldsymbol{Z}}{\partial \boldsymbol{C}} - (\boldsymbol{1} - \boldsymbol{n}^{(3)} \otimes \boldsymbol{n}^{(3)}) : \frac{\partial \boldsymbol{Z}}{\partial \boldsymbol{A}} : \Delta\alpha^{(1,2)} \frac{\partial (\boldsymbol{n}^{(3)} \otimes \boldsymbol{n}^{(3)})}{\partial \boldsymbol{C}} - \boldsymbol{Z} : \frac{\partial (\boldsymbol{n}^{(3)} \otimes \boldsymbol{n}^{(3)})}{\partial \boldsymbol{C}}. \tag{E.21}$$

The partial derivatives of the driving force are given by:

$$\frac{\partial \boldsymbol{Z}}{\partial \boldsymbol{A}} = -\mathcal{N} : \left\langle \frac{\partial^2 \psi}{\partial \xi^2} \boldsymbol{n} \otimes \boldsymbol{n} \otimes \boldsymbol{n} \otimes \boldsymbol{n} \right\rangle : \mathcal{N}, \tag{E.22}$$

$$\frac{\partial \boldsymbol{Z}}{\partial \boldsymbol{C}} = -\frac{\partial^2 \Psi}{\partial \boldsymbol{A} \partial \boldsymbol{C}}. \tag{E.23}$$

The derivatives of the (well-defined) damage directions can be found by applying the chain rule:

$$\frac{\partial \boldsymbol{M}^{tr(i)} \otimes \boldsymbol{M}^{tr(i)}}{\partial \boldsymbol{C}} = \frac{\partial \boldsymbol{M}^{tr(i)} \otimes \boldsymbol{M}^{tr(i)}}{\partial \boldsymbol{Z}^{tr}} : \frac{\partial \boldsymbol{Z}^{tr}}{\partial \boldsymbol{C}}. \tag{E.24}$$

Note that the derivative $\partial \boldsymbol{Z}^{tr} / \partial \boldsymbol{C}$ can be evaluated using the same formula as $\partial \boldsymbol{Z} / \partial \boldsymbol{C}$ (setting $\Delta\alpha^{(i)} = 0$).

Partial derivatives of the projection operator $\mathcal{N}$ w.r.t. $\boldsymbol{C}$ are also needed:

$$\frac{\partial \mathcal{N}_{klmn}}{\partial C_{qr}} = \left(\sum_{i=1}^{p} \frac{\partial N_k^{(i)} N_m^{(i)}}{\partial C_{qr}}\right)\left(\sum_{j=1}^{p} N_l^{(j)} N_n^{(j)}\right) + \left(\sum_{j=1}^{p} N_k^{(j)} N_m^{(j)}\right)\left(\sum_{i=1}^{p} \frac{\partial N_l^{(i)} N_n^{(i)}}{\partial C_{qr}}\right) \tag{E.25}$$

and:

$$\begin{aligned}\frac{\partial^2 \mathcal{N}_{klmn}}{\partial C_{qr}\partial C_{st}} = &\left(\sum_{i=1}^{p} \frac{\partial^2 N_k^{(i)} N_m^{(i)}}{\partial C_{qr}\partial C_{st}}\right)\left(\sum_{i=1}^{p} N_l^{(j)} N_n^{(j)}\right) + \left(\sum_{i=1}^{p} \frac{\partial N_k^{(i)} N_m^{(i)}}{\partial C_{qr}}\right)\left(\sum_{i=1}^{p} \frac{\partial N_l^{(j)} N_n^{(j)}}{\partial C_{st}}\right) \\ &+ \left(\sum_{i=1}^{p} \frac{N_k^{(j)} N_m^{(j)}}{\partial C_{st}}\right)\left(\sum_{i=1}^{p} \frac{\partial N_l^{(i)} N_n^{(i)}}{\partial C_{qr}}\right) + \left(\sum_{i=1}^{p} N_k^{(j)} N_m^{(j)}\right)\left(\sum_{i=1}^{p} \frac{\partial^2 N_l^{(i)} N_n^{(i)}}{\partial C_{qr}\partial C_{st}}\right).\end{aligned} \tag{E.26}$$

It remains to express the derivatives of the principal stretch directions w.r.t. $\boldsymbol{C}$. We have the identity (Magnus, 1985):

$$\frac{\partial \boldsymbol{n}^{(i)}}{\partial \boldsymbol{C}} = \sum_{j,j\neq i} \frac{\boldsymbol{n}^{(j)} \otimes \left(\boldsymbol{n}^{(j)} \otimes \boldsymbol{n}^{(i)} + \boldsymbol{n}^{(i)} \otimes \boldsymbol{n}^{(j)}\right)}{2((\lambda^{(i)})^2 - (\lambda^{(j)})^2)}. \tag{E.27}$$

We also find that:

$$\frac{\partial \boldsymbol{n}^{(i)} \otimes \boldsymbol{n}^{(i)}}{\partial \boldsymbol{C}} = 2\sum_{j,j\neq i} \frac{\left(\boldsymbol{n}^{(i)} \otimes \boldsymbol{n}^{(j)}\right)^s \otimes \left(\boldsymbol{n}^{(i)} \otimes \boldsymbol{n}^{(i)}\right)^s}{(\lambda^{(i)})^2 - (\lambda^{(j)})^2}. \tag{E.28}$$

where we have introduced the notation $\boldsymbol{D}^s := \frac{1}{2}\left(\boldsymbol{D} + \boldsymbol{D}^T\right)$ for the symmetric part of a second order tensor. The second derivative can be found by differentiating the above expression to yield:

$$\begin{aligned}\frac{\partial^2 \boldsymbol{n}^{(i)} \otimes \boldsymbol{n}^{(i)}}{\partial \boldsymbol{C}\partial \boldsymbol{C}} = &2\sum_{j,j\neq i} \frac{1}{((\lambda^{(i)})^2 - (\lambda^{(j)})^2)} \frac{\partial\left(\left(\boldsymbol{n}^{(i)} \otimes \boldsymbol{n}^{(j)}\right)^s \otimes \left(\boldsymbol{n}^{(j)} \otimes \boldsymbol{n}^{(j)}\right)^s\right)}{\partial \boldsymbol{C}} \\ &- \frac{\left(\boldsymbol{n}^{(i)} \otimes \boldsymbol{n}^{(j)}\right)^s \otimes \left(\boldsymbol{n}^{(i)} \otimes \boldsymbol{n}^{(j)}\right)^s}{((\lambda^{(i)})^2 - (\lambda^{(j)})^2)^2} \otimes \frac{\partial\left((\lambda^{(i)})^2 - (\lambda^{(j)})^2\right)}{\partial \boldsymbol{C}},\end{aligned} \tag{E.29}$$

where:

$$\frac{\partial \left(N^{(i)}N^{(j)}\right)^s_{kl}\left(N^{(j)}N^{(j)}\right)^s_{mn}}{\partial C_{qr}} = N^{(i)}_k N^{(i)}_m \frac{\partial N^{(j)}_l N^{(j)}_n}{\partial C_{qr}} + \frac{\partial N^{(i)}_k N^{(i)}_m}{\partial C_{qr}} N^{(j)}_l N^{(j)}_n + N^{(i)}_k N^{(i)}_n \frac{\partial N^{(j)}_l N^{(j)}_m}{\partial C_{qr}} + \frac{\partial N^{(i)}_k N^{(i)}_n}{\partial C_{qr}} N^{(j)}_l N^{(j)}_m + N^{(i)}_l N^{(i)}_m \frac{\partial N^{(j)}_k N^{(j)}_n}{\partial C_{qr}} + \frac{\partial N^{(i)}_l N^{(i)}_m}{\partial C_{qr}} N^{(j)}_k N^{(j)}_n + N^{(i)}_l N^{(i)}_n \frac{\partial N^{(j)}_k N^{(j)}_m}{\partial C_{qr}} + \frac{\partial N^{(i)}_l N^{(i)}_n}{\partial C_{qr}} N^{(j)}_k N^{(j)}_m, \tag{E.30}$$

$$\frac{\partial (\lambda^{(i)})^2}{\partial \boldsymbol{C}} = \boldsymbol{n}^{(i)} \otimes \boldsymbol{n}^{(i)}. \tag{E.31}$$

Note that we only use the above expressions for computing the derivatives of well-defined principal stretching directions (corresponding to non-repeated principal stretches) for which they are valid even though the repeated stretching directions appear in the expressions for these derivatives. We will begin by considering the first order derivatives. In the case where $p = 1$ and there are repeated stretches, only the derivatives of the direction $\boldsymbol{n}^{(1)} \otimes \boldsymbol{n}^{(1)}$ are needed. The expression for the first derivative features a summation of two terms in j where the denominators of each terms are equal as $\lambda^{(2)} = \lambda^{(3)}$. This means that the summation can be carried out over the numerators. By using the identity $\sum_{i=1}^{3} \boldsymbol{n}^{(i)} \otimes \boldsymbol{n}^{(i)} = \boldsymbol{1}$, the summations over j of the repeated stretching directions can be replaced by $\boldsymbol{1} - \boldsymbol{n}^{(1)} \otimes \boldsymbol{n}^{(1)}$ which indicates that the expression gives a well-defined value for the derivative. In the case where $p = 2$ and $\lambda^{(1)} = \lambda^{(2)}$, only the derivatives of the $\boldsymbol{n}^{(3)} \otimes \boldsymbol{n}^{(3)}$ are needed. A parallel argument to that of the $\boldsymbol{n}^{(1)} \otimes \boldsymbol{n}^{(1)}$ case can be followed to show that our use of these formulae in this case is also valid. Finally, for the second order derivatives note that rearrangement of Eq. (E.31) allows one to express the second derivative in terms of well defined stretching directions and their first derivatives, meaning our use of it in our model is also valid.

Finally, we also recognise that $\partial(\boldsymbol{M}^{tr(i)} \otimes \boldsymbol{M}^{tr(i)})/\partial \boldsymbol{Z}^{tr}$ is similarly an eigenvector derivative (i.e. $\boldsymbol{Z}^{tr} = \sum_{i=1}^{3} \nu^{tr(i)} \boldsymbol{M}^{tr(i)} \otimes \boldsymbol{M}^{tr(i)}$), which implies this derivative may be found

analogously:

$$\frac{\partial \boldsymbol{M}^{tr(i)} \otimes \boldsymbol{M}^{tr(i)}}{\partial \boldsymbol{Z}^{tr}} = \sum_{j,j\neq i} \frac{\left(\boldsymbol{M}^{tr(j)} \otimes \boldsymbol{M}^{tr(i)} + \boldsymbol{M}^{tr(i)} \otimes \boldsymbol{M}^{tr(j)}\right) \otimes \left(\boldsymbol{M}^{tr(j)} \otimes \boldsymbol{M}^{tr(i)} + \boldsymbol{M}^{tr(i)} \otimes \boldsymbol{M}^{tr(j)}\right)}{2\left(\nu^{tr(i)} - \nu^{tr(j)}\right)}. \tag{E.32}$$

Compressible regularisation Following the compressible regularisation of the model, the tangent operator is split into isochoric-volumetric contributions following from the split of the free energy function. Considering only the isochoric part and omitting subscripts $n+1$ for conciseness, the material tangent $2d\boldsymbol{S}/d\boldsymbol{C}$ is then found from (Steinmann et al., 2012; Holzapfel, 2010):

$$\frac{d\boldsymbol{S}^{iso}}{d\boldsymbol{C}} = \mathbb{P} : \frac{d\bar{\boldsymbol{S}}}{d\bar{\boldsymbol{C}}} : \mathbb{P}^T + \frac{2}{3}\bar{\boldsymbol{S}} : \bar{\boldsymbol{C}}\bar{\mathbb{P}} - \frac{2}{3}\left(\boldsymbol{C}^{-1} \otimes \boldsymbol{S}^{iso} + \boldsymbol{S}^{iso} \otimes \boldsymbol{C}^{-1}\right), \tag{E.33}$$

where the projections $\mathbb{P}$ and $\bar{\mathbb{P}}$ are defined as:

$$\mathbb{P} := \mathbb{I} - \frac{1}{3}\boldsymbol{C}^{-1} \otimes \boldsymbol{C}, \tag{E.34}$$

$$\bar{\mathbb{P}} := \boldsymbol{C}^{-1} \odot \boldsymbol{C}^{-1} - \frac{1}{3}\boldsymbol{C}^{-1} \otimes \boldsymbol{C}^{-1}, \tag{E.35}$$

where again we use the notation $\odot$ for the tensor operation $(\boldsymbol{A} \odot \boldsymbol{B})_{ijkl} := A_{ik}B_{jl}$ and the stress $\bar{\boldsymbol{S}}$ is defined as:

$$\bar{\boldsymbol{S}} := 2\frac{\partial \Psi^{iso}}{\partial \bar{\boldsymbol{C}}}. \tag{E.36}$$

The volumetric part is given by (Steinmann et al., 2012; Holzapfel, 2010):

$$\frac{d\boldsymbol{S}^{vol}}{d\boldsymbol{C}} = \frac{\partial \boldsymbol{S}^{vol}}{\partial \boldsymbol{C}} = \left(J\frac{\partial \Psi^{vol}}{\partial J} + J^2\frac{\partial^2 \Psi^{vol}}{\partial J^2}\right)\boldsymbol{C}^{-1} \otimes \boldsymbol{C}^{-1} - 2J\frac{\partial \Psi^{vol}}{\partial J}\boldsymbol{C}^{-1} \odot \boldsymbol{C}^{-1}. \tag{E.37}$$

ABAQUS implementation ABAQUS defines the consistent tangent DDSDDE through the Jaumann rate (denoted $\overset{\nabla}{(\cdot)}$) of the Kirchhoff stress viz.:

$$\overset{\nabla}{\boldsymbol{\tau}} = J(\text{DDSDDE}) : \boldsymbol{D}, \tag{E.38}$$

where $\boldsymbol{D}$ is the symmetric part of the velocity gradient $\boldsymbol{L}$ which has a skew-symmetric part $\boldsymbol{W}$ (the spin tensor):

$$\boldsymbol{L} = \dot{\boldsymbol{F}}\boldsymbol{F}^{-1}, \quad \boldsymbol{D} = \frac{1}{2}(\boldsymbol{L} + \boldsymbol{L}^T), \quad \boldsymbol{W} = \frac{1}{2}(\boldsymbol{L} - \boldsymbol{L}^T), \tag{E.39}$$

and $\boldsymbol{\tau}$ is the Kirchhoff stress. The Jaumann rate is defined:

$$\boldsymbol{\tau} = J\boldsymbol{\sigma}, \quad \overset{\nabla}{\boldsymbol{\tau}} = \dot{\boldsymbol{\tau}} + \boldsymbol{\tau}\boldsymbol{W} - \boldsymbol{W}\boldsymbol{\tau}. \tag{E.40}$$

It can be shown (see Nguyen and Waas (2016)) that DDSDDE relates to the material tangent via:

$$\text{DDSDDE} = \frac{2}{J}\boldsymbol{F} \odot \boldsymbol{F} : \frac{d\boldsymbol{S}}{d\boldsymbol{C}} : (\boldsymbol{F} \odot \boldsymbol{F})^T + \frac{1}{2}\left(\boldsymbol{\sigma} \odot \boldsymbol{1} + \boldsymbol{1} \odot \boldsymbol{\sigma} + (\boldsymbol{\sigma} \odot \boldsymbol{1})^t + (\boldsymbol{1} \odot \boldsymbol{\sigma})^t\right), \tag{E.41}$$

where again $()^t$ pertains to the transpose in the final two indices. As the compressible regularisation leads to an additive split of the stress and material tangent into isochoric and volumetric parts, the isochoric and volumetric contributions to DDSDDE can also be calculated separately:

$$\text{DDSDDE} = \text{DDSDDE}^{iso} + \text{DDSDDE}^{vol}, \tag{E.42}$$

$$\begin{aligned}\text{DDSDDE}^{(a)} = \frac{2}{J}\boldsymbol{F} \odot \boldsymbol{F} : \frac{d\boldsymbol{S}^{(a)}}{d\boldsymbol{C}} : (\boldsymbol{F} \odot \boldsymbol{F})^T + \frac{1}{2}\Big(&\boldsymbol{\sigma}^{(a)} \odot \boldsymbol{1} + \boldsymbol{1} \odot \boldsymbol{\sigma}^{(a)} + \\ &\left(\boldsymbol{\sigma}^{(a)} \odot \boldsymbol{1}\right)^t + \left(\boldsymbol{1} \odot \boldsymbol{\sigma}^{(a)}\right)^t\Big),\end{aligned} \tag{E.43}$$

for $^{(a)}$ corresponding to the isochoric or volumetric part. For the isochoric part, the push forward of $d\boldsymbol{S}^{iso}/d\boldsymbol{C}$ yields:

$$\boldsymbol{F}\odot\boldsymbol{F}:\frac{d\boldsymbol{S}^{iso}}{d\boldsymbol{C}}:(\boldsymbol{F}\odot\boldsymbol{F})^T=\mathbb{I}^{dev}:\boldsymbol{F}\odot\boldsymbol{F}:\frac{d\bar{\boldsymbol{S}}}{d\bar{\boldsymbol{C}}}:(\boldsymbol{F}\odot\boldsymbol{F})^T:\mathbb{I}^{dev}$$
$$+\frac{2}{3}(J\bar{\boldsymbol{\sigma}}:\mathbf{1})\mathbb{I}^{dev}-\frac{2}{3}(\mathbf{1}\otimes J\bar{\boldsymbol{\sigma}}+J\bar{\boldsymbol{\sigma}}\otimes\mathbf{1}), \tag{E.44}$$

Incorporating the isochoric stress into Eq. (E.41) yields the isochoric contribution DDSDDE^{iso}. The volumetric contribution is most easily evaluated by returning to the free energy function Ψ^{vol} and computing the the contribution to the Kirchhoff stress (and the Jaumann rate) directly:

$$\boldsymbol{\tau}^{vol}=\frac{1}{2}K\frac{\partial(\log J)^2}{\partial\boldsymbol{F}}\boldsymbol{F}^T=K\log J\mathbf{1},\quad \overset{\nabla}{\boldsymbol{\tau}}{}^{vol}=KJ\mathbf{1}\otimes\mathbf{1}:\boldsymbol{D}, \tag{E.45}$$

which yields the following contribution to DDSDDE:

$$\text{DDSDDE}^{vol}=K\mathbf{1}\otimes\mathbf{1}. \tag{E.46}$$

E.3 Finite element implementation

In this Section, we detail the finite element implementation of our model applied to the loading of a holed plate in sequentially different directions.

E.3.1 Compressible regularisation

For the purpose of finite element implementation, we regularise the incompressible model to a nearly-incompressible model (Neto et al., 2011), bypassing the need for a mixed pressure-displacement formulation and associated numerical problems. We follow the isochoric-volumetric split of the deformation gradient, see (Steinmann et al., 2012; Holzapfel, 2010):

$$\boldsymbol{C}=J^{-\frac{2}{3}}\bar{\boldsymbol{C}}, \tag{E.47}$$

and decompose the free energy into isochoric and volumetric contributions:

$$\Psi(\boldsymbol{C}, \boldsymbol{A}) = \Psi^{iso}(\bar{\boldsymbol{C}}, \boldsymbol{A}) + \Psi^{vol}(J). \tag{E.48}$$

The free energy function introduced in Sections 6.2 and 6.3 makes up the isochoric contribution and we choose a simple log-quadratic term for the volumetric term:

$$\Psi^{iso}(\bar{\boldsymbol{C}}) = \Psi^{e}(\bar{\boldsymbol{C}}, \boldsymbol{A}) + \Psi^{d}(\boldsymbol{A}), \quad \Psi^{vol}(J) = \frac{1}{2}K(\log J)^2. \tag{E.49}$$

Setting the modulus K to a large value relative to the other material moduli makes the material behave with near incompressibility. The corresponding 2^{nd} Piola-Kirchhoff stress splits into isochoric and volumetric parts:

$$\boldsymbol{S} = \underbrace{2\frac{\partial \Psi^{iso}}{\partial \boldsymbol{C}}}_{\boldsymbol{S}^{iso}} + \underbrace{2\frac{\partial \Psi^{vol}}{\partial \boldsymbol{C}}}_{\boldsymbol{S}^{vol}}. \tag{E.50}$$

This leads the following expression for the Cauchy stress which is split into a deviatoric part depending only on the isochoric contribution to the free energy, and a spherical part depending only on the volumetric contribution to the free energy:

$$\boldsymbol{\sigma} = \mathbb{I}^{dev} : \bar{\boldsymbol{\sigma}} + \frac{\partial \Psi^{vol}}{\partial J}\mathbf{1}, \quad J\bar{\boldsymbol{\sigma}} = 2\bar{\boldsymbol{F}}\frac{\partial \Psi^{iso}}{\partial \bar{\boldsymbol{C}}}\bar{\boldsymbol{F}}^T. \tag{E.51}$$

We continue to follow the state update algorithm outlined in Section 6.4 with the difference that the isochoric part of the the right Cauchy-Green tensor replaces the full tensor $\boldsymbol{C}$. The compressible regularisation modifies the consistent tangent operator in that it now also follows a split into isochoric and volumetric parts:

$$\frac{d\boldsymbol{S}_{n+1}}{d\boldsymbol{C}_{n+1}} = \frac{d\boldsymbol{S}^{iso}_{n+1}}{d\boldsymbol{C}_{n+1}} + \frac{d\boldsymbol{S}^{vol}_{n+1}}{d\boldsymbol{C}_{n+1}}. \tag{E.52}$$

The isochoric part is related to the consistent tangent calculated for the fully incompressible model outlined previously, and we can calculate the volumetric contribution separately - details are provided in E.2.

E.3.2 Simulation of plate with central hole under sequential stretching

We simulate the loading of a square plate with a central hole sequentially loaded in two orthogonal directions. The dimensions of the plate are $5 \times 5 \times 0.405$ units and the hole radius measures 1 unit. Owing to the symmetries of the structure, only one-eighth of the full domain is represented. The partial domain is discretised using 7000 first-order tetrahedron (C3D4) elements. This example is simply to illustrate the use of the model in an FE problem and it should be noted that the reported results may not be representative of a real world scenario as this choice of element type often gives rise to volumetric locking problems in near-incompressible regimes (Smith, 2009). We have conducted a mesh-convergence study to confirm that the number of elements is sufficient to obtain converged results, and that no softening-induced strain localisation occurs. The mesh, generated in the software Gmsh (Geuzaine and Remacle, 2009), is shown in Fig. E.1 with appropriate symmetry conditions labelled. The plate is subjected to a maximum displacement of the top face of 0.35 in the $\boldsymbol{e}_2$-direction during the first cycle and a displacement of the left face of -0.35 in the $\boldsymbol{e}_1$-direction during the second cycle. We label two points on the surface of the hole A and B in Fig. E.1. We present stress-strain histories for elements at these locations to illustrate the performance of the model under different loading conditions. The model parameters used in the simulation are the following: $G = 0.3$ MPa, $\eta_0 = 0.1$, $\kappa = 0.2$ MPa and $K = 10$ MPa.

Figs E.2(a)-(b) show contour plots of the components A_{11} and A_{22} of the damage tensor at the end of the loading. Damage occurs primarily in regions where the material is most stretched (as expected). At the surface of the hole, due to the traction-free condition and near plane-stress conditions, the stress state is almost uniaxial. During stretching in the $\boldsymbol{e}_2$- direction, this results in the 22-component of the damage tensor growing around point A of the hole. During subsequent stretching in the $\boldsymbol{e}_1$-direction, at point B the 11-component of the damage tensor grows as this region is now under tensile stretching.

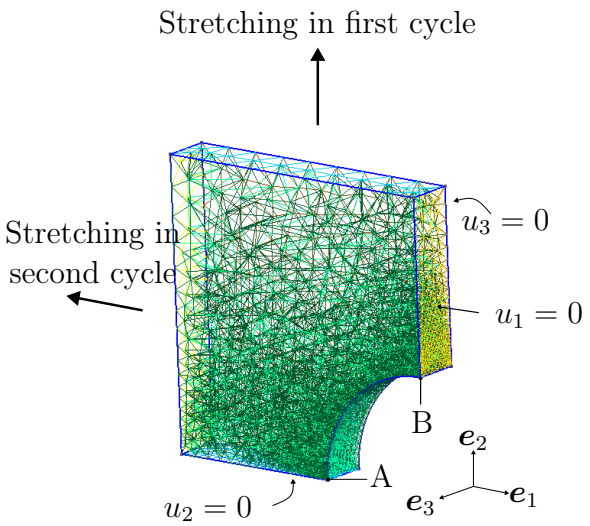


Figure E.1: Finite element mesh generated in Gmsh (Geuzaine and Remacle, 2009) with boundary conditions for sequential uniaxial tensile tests labelled.

Fig. E.2(c) shows the principal stress-principal stretch curves at point A (during the first loading only) and point B (during the second loading only). The local stress-stretch response shows small but visible Mullins effect, which is due to the relatively small deformation applied to the plate. Interestingly, the maximum principal stretch seen by point B during the second loading is smaller than the maximum principal stretch seen by point A during the first loading. We attribute this effect to the softening generated throughout the plate during the first loading cycle, which reduces the strain concentration at point B. Fig. E.2(d) shows the time evolution of the maximum principal value of the damage tensor $A^{(1)}$ at points A and B. During the first loading, $A^{(1)} \approx A_{22}$ at point A, and grows monotonously until reaching a constant value and stays constant during unloading, whereas damage at point B is negligible during the first loading. During the second loading, point A does not experience further damage, whereas at point B, we have $A^{(1)} \approx A_{11}$, which grows with the applied deformation. The maximum value of $A^{(1)}$ at

point B is lower than the maximum value of $A^{(1)}$ at point B, which is related to the fact that point B does not reach the same maximum principal stretch.

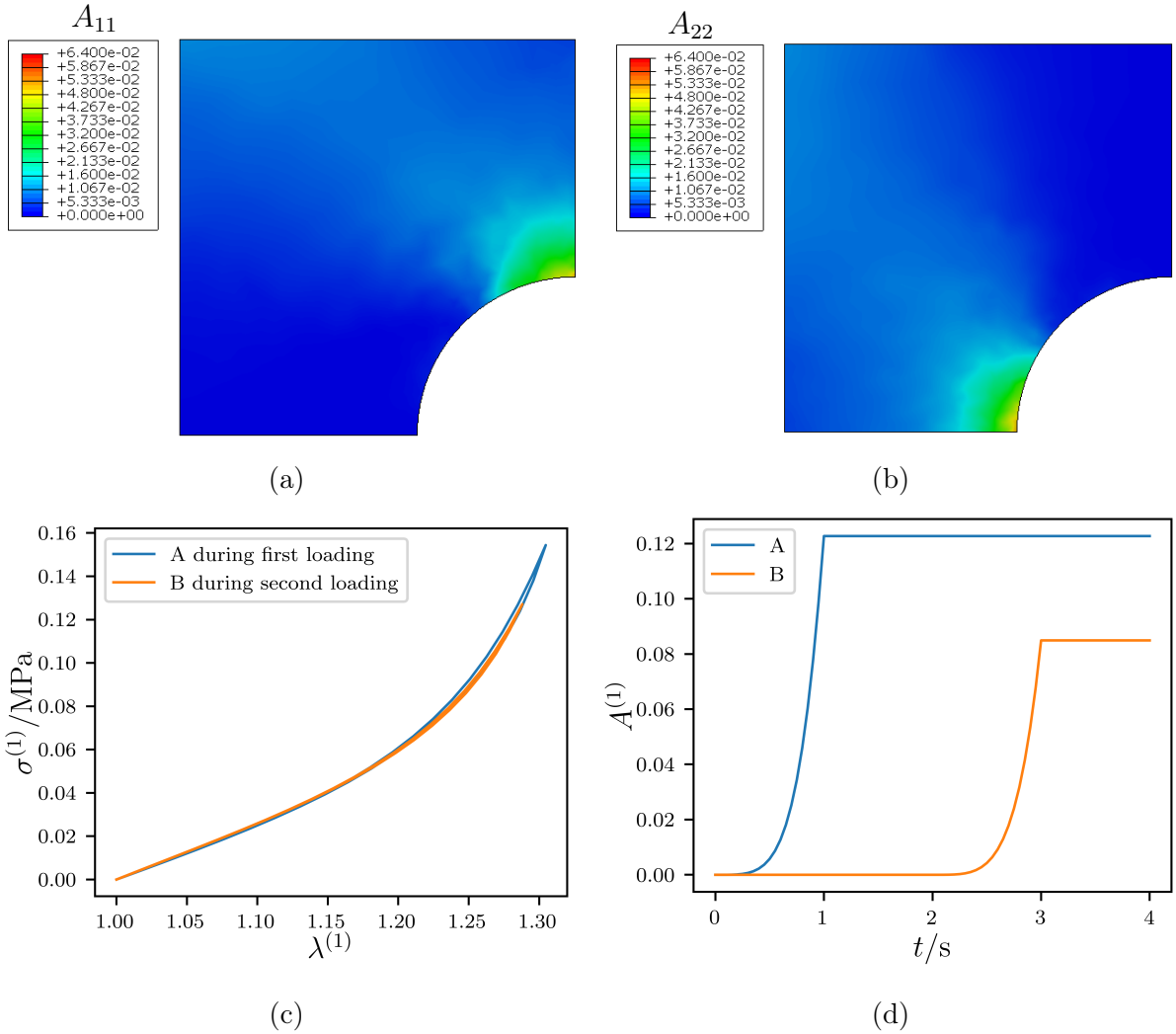


Figure E.2: Final components of the damage tensor predicted by finite element simulations of a plate with a hole undergoing uniaxial tension in the $\boldsymbol{e}_2$-direction followed by uniaxial tension in the $\boldsymbol{e}_1$-direction. (a) and (b) show the A_{11} and A_{22} components respectively plotted on a logarithmic scale to highlight large variation in the damage tensor; (c) provides the principal stress-stretch response at point A during the first loading and B during the second loading; (d) shows the history of the maximum principal component of the damage tensor at points A and B.